Universidade de Lisboa

Faculdade de Ciências

Departamento de Química e Bioquímica

Estudo de Fulerenos e de Monocamadas Auto-Montadas por Simulação Computacional

Rui Pedro da Silva Fartaria

Doutoramento em Química

Especialidade de Química-Física

2007

Universidade de Lisboa

Faculdade de Ciências

Departamento de Química e Bioquímica

Estudo de Fulerenos e de Monocamadas Auto-Montadas por Simulação Computacional

Rui Pedro da Silva Fartaria

Tese orientada pelos Professores Doutor Fernando Manuel Sebastião Silva Fernandes e Doutora Filomena de Fátima Martins Freitas

Dissertação submetida à Faculdade de Ciências da Universidade de Lisboa para obtenção do grau de Doutor em Química na especialidade de Química-Física

Doutoramento em Química

Especialidade de Química-Física

2007

Este trabalho foi realizado no Grupo de Simulação Molecular, presentemente integrado no Centro de Ciências Moleculares e Materiais da Faculdade de Ciências da Universidade de Lisboa.

Dedicado a Anabela,
minha querida esposa

Agradecimentos

Desejo agradecer em primeiro lugar aos meus supervisores, Professores Doutores Fernando Manuel Sebastião Silva Fernandes e Filomena de Fátima Martins Freitas, pela orientação científica, ajuda e incentivo permanentes que me levaram a progredir neste trabalho e pela compreensão e paciência nos momentos mais difíceis.

Um agradecimento especial, também, à Professora Doutora Luísa Abrantes, por todo o apoio, estímulo e sugestões relativamente aos trabalhos de adsorção e automontagem.

Ao Doutor Pedro Rodrigues pelo apoio e disponibilidade, e pelas proveitosas e agradáveis discussões.

Aos colegas Rodrigo e Diogo pelo companheirismo e boa disposição, fundamentais na manutenção de um ambiente de trabalho agradável. Agradeço ainda ao Diogo pela colaboração prestada nos últimos dias da conclusão desta tese.

À minha esposa Anabela pelo carinho que sempre me dedicou, pela compreensão dada nos momentos de maior ausência e pelo seu apoio e incentivo.

Ao meu filho David que, na sua condição especial, me mostra novas formas de ver o mundo que nos rodeia.

Aos meus pais, António e Conceição, que na minha adolescência me compraram o meu primeiro computador, um Amstrad 8086, e pela paciência durante as horas e horas que passava em frente ao computador. Pelo seu exemplo, incentivo e presença permanentes, nos bons e nos maus momentos, e pela segurança e tranquilidade que me proporcionaram.

Aos meus sogros, Alcino e Judite, pelo seu apoio e compreensão, e pelos agradáveis momentos de serenidade, passados na sua casa em Ribas.

Aos meus irmãos e famíla pelo sua boa disposição e incentivo constantes.

Aos meus amigos Paulo, Xana, Pedro, Sandra, Tiago, Neia, Tó Zé e Sílvia pelo seu apoio, optimismo e boa disposição. À pequerrucha, Madalena, pelos seus sorrisos traquinas.

Finalmente, desejo agradecer ao Departamento de Química e Bioquímca da FCUL pela disponibilização das instalações e recursos para a realização do trabalho e à Fundação para a Ciência e a Tecnologia pela atribuição da Bolsa de Doutoramento SFRH/BD/10405/2002.

Conteúdo

Resumo

Nesta dissertação apresentam-se os resultados de simulações dos diagramas de fase de fulerenos e da adsorção e auto-montagem do 1-decanotiol numa superfície Au(111) a partir de uma solução em etanol.

O objectivo principal do estudo sobre os fulerenos é contribuir para a interpretação do diagrama de fase do C_{60} e de outros fulerenos no que se refere à existência, ou não, de equilíbrios liquido-vapor estáveis para estes sistemas. Efectuaram-se simulações, por técnicas de Monte Carlo, para os equilíbrios líquido-vapor, sólido-vapor e sólido-líquido, determinando-se as respectivas linhas de coexistência p vs. T e T vs. ρ. Identificaram-se os pontos críticos e triplos e as zonas de meta-estabilidade das fases líquidas. Calcularam-se, também, as entalpias de sublimação de alguns fulerenos, as quais estão em excelente acordo com os valores experimentais. Os resultados apontam para existência de uma fase líquida estável para o C_{60}, assim como para outros fulerenos, embora num estreito intervalo de temperaturas, de acordo com os resultados de outros autores. O interesse do estudo de fulerenos, no contexto geral desta dissertação, prende-se com a possibilidade de os introduzir quimicamente em cadeias orgânicas auto-montadas com vista, por exemplo, ao desenvolvimento de biosensores e materiais fotosensíveis.

Relativamente à adsorção do 1-decanotiol em eléctrodos de ouro estudou-se o mecanismo da aproximação da molécula à superfície do eléctrodo. Efectuaram-se simulações de Monte Carlo, no ensemble NVT, calculando-se os perfis de densidade do etanol, a densidade superficial relativa das molécula adsorvidas, o ângulo de inclinação e o comprimento médio da molécula de tiol. Determinaram-se, também, as contribuições do eléctrodo e do solvente para o potencial de força média, o qual guia a aproximação da molécula de tiol ao eléctrodo. O estudo partiu de modelos simples, com moléculas rígidas e potenciais globais de interacção com a superfície, que foram sucessivamente refinados. Propõe-se um campo de forças para a interacção etanol-Au(111) com a influência explícita da corrugação da superfície. Este campo de forças baseou-se nos valores de energia de interacção calculados através da teoria do funcional da densidade. Para o ajuste da função de potencial a estes valores recorreu-se a algoritmos genéticos. Analisam-se os efeitos dos refinamentos que foram sendo efectuados nos modelos, principalmente no que diz respeito às estruturas das camadas de adsorção do solvente e ao comportamento da molécula de tiol durante o processo de adsorção.

Apresentam-se, ainda, alguns resultados para a adsorção do fenol e água em eléctrodos de ouro, efectuados em colaboração com outro grupo de investigação. Estes estudos foram realizados em simultâneo com os da adsorção do tiol, utilizando a mesma metodologia.

Abstract

Computer simulation results for the phase diagrams of fullerenes and for the adsorption and self-assembly of the 1-decanethiol on Au(111) surfaces, from an ethanol solution, are presented.

The main objective of the fullerenes study is to contribute for the interpretation of the phase diagram of C_{60}, and of other fullerenes, in what concerns the existence, or not, of stable liquid-vapour equilibria for these systems. Simulations by Monte Carlo techniques for the liquid-vapour, solid-vapour and solid-liquid equilibria were performed and the respective p vs. T and T vs. ρ coexistence lines, as well as critical and triple points, were determined. The metastability regions of the liquid phases were identified. The enthalpies of sublimation for some fullerenes were also worked out which are in very good agreement with experimental data. Overall, the results indicate the existence of stable liquid phases for C_{60} and other fullerenes, though in narrow temperature intervals, in accordance with the results of other authors. The interest of the fullerenes study in the general context of this dissertation is concerned with the possibility of chemically introducing them into self-assembled organic chains regarding, for example, biosensors and photovoltaic developments.

As for the adsorption of the 1-decanethiol on gold electrodes the mechanism of approach of the molecule to the electrode surface was studied. From NVT Monte Carlo simulations the density profiles of the ethanol, the relative surface density of the adsorbed molecules, the tilt angles and the average length of the thiol molecule were calculated. The contributions of the electrode and the solvent to the potential of mean force, which drives the thiol molecule towards the electrode, were also worked out. The study started from simple models, constituted by rigid molecules and global potentials for the interactions with the surface, which were progressively refined. A force field for the interaction of ethanol-Au(111) is proposed, taking explicitly into account the surface corrugation. This force field is based on the interaction energy values calculated by density functional theory. Genetic algorithms were used for the fitting of the potential function to those values. The effects of the models refinements are analyzed mainly in respect to the structures of the adsorbed solvent layers and the behaviour of the thiol molecule during the adsorption process.

Furthermore, some results for the adsorption of phenol and water on gold electrodes, obtained in collaboration with another research group, are presented. These

studies were simultaneously realized with the ones for the adsorption of the thiol, using the same methodology.

Capítulo 1

Introdução

1.1 Química Computacional e Simulação Molecular

A química computacional é um campo muito vasto que engloba todas as técnicas computacionais utilizadas não só no estudo teórico das propriedades físico-químicas a nível molecular, mas também no tratamento, classificação e estruturação de resultados experimentais. De facto, a quantidade de informação experimental é tão grande que se torna praticamente impossível analisar os fenómenos estudados sem recorrer a técnicas computacionais.

Uma das principais componentes da investigação em química computacional é a modelação molecular, isto é, a representação e manipulação das estruturas moleculares e o cálculo das propriedades dependentes da estrutura. Neste aspecto, as mecânicas molecular e quântica [1, 2], bem como a computação gráfica, desempenham um papel crucial. Um tópico directamente relacionado é, certamente, a informática molecular [3]. Trata-se de um termo relativamente novo, usualmente considerado como englobando duas disciplinas: quimioinformática e bioinformática, as quais têm como objectivo fundamental o armazenamento, recuperação e manipulação de informação molecular em gigantescas bases de dados com vista, por exemplo, à síntese orientada de novos materiais ou medicamentos e à determinação do genoma humano. Essas disciplinas estão, por sua vez, associadas a métodos específicos para o reconhecimento de estruturas químicas, análise quantitativa de misturas complexas, determinação da origem de uma amostra, classificação automática de reacções químicas e previsão de propriedades ou actividades de compostos químicos ou materiais com interesse tecnológico, constituindo outras disciplinas bem

identificadas: quimiometria, química combinatorial e redes neuronais artificiais, por exemplo.

Uma vez determinadas as estruturas e propriedades de um dado tipo de moléculas é necessário simular as propriedades emergentes de um conjunto (ou *ensemble*) dessas moléculas, uma vez que as propriedades observáveis são, em geral, a consequência de ensembles moleculares e não de uma única molécula. Este é o objectivo do que designaremos por simulação molecular, a qual se baseia em modelos teóricos da mecânica estatística quântica e/ou clássica. É claro que a simulação molecular, tal como a definimos, tem estreita ligação com a modelação molecular. Estes termos são, frequentemente, considerados equivalentes. Nestas definições, é bom que se diga, não há critérios absolutos. O mesmo se passa com o termo ensemble. Trata-se de um neologismo aceite internacionalmente. Alguns autores preferem, no entanto, os termos equivalentes: conjunto, colectividade ou assembleia.

Posto isto, identificamos os trabalhos desenvolvidos na presente tese com o âmbito particular da modelação e simulação moleculares.

A simulação molecular, através dos métodos de Dinâmica Molecular [4–7] e de Monte Carlo [4–6, 8], teve o seu início na década de 50, do século passado, com as primeiras simulações de sistemas condensados. Desde essa altura, observou-se um considerável desenvolvimento sendo hoje uma das metodologias mais utilizadas no estudo de sistemas químicos, a par do rápido desenvolvimento tecnológico dos computadores. Até aos anos 80 só era possível realizar experiências deste tipo em alguns computadores, restritos a um pequeno número de investigadores. Hoje em dia, qualquer computador pessoal tem capacidade para realizar inúmeras experiências, tanto na investigação como no ensino.

O uso de computadores veio providenciar mais um meio de fazer investigação científica. Os métodos de simulação molecular possibilitam o estudo de uma grande variedade de sistemas e a determinação de algumas propriedades que são inacessíveis ou difíceis de obter por métodos experimentais. Virtualmente qualquer sistema molecular, real ou puramente conceptual, pode ser explorado por estes métodos. Os aspectos técnicos a enfrentar num projecto desta natureza são, entre outros:

- Capacidade de processamento - relacionada, principalmente, com a velocidade e o número de processadores disponíveis. Depende, também, das infra-estruturas de comunicação entre os processadores pois, frequentemente, os cálculos são particionados e distribuídos entre estes.

- Capacidade de memória - relacionada com a memória virtual disponível para

o manuseamento dos dados necessário à prossecução dos cálculos em execução, mas também com a capacidade de armazenamento dos resultados das simulações, fundamentalmente para análise posterior.

Estes factores devem ser sempre tomados em conta pelo investigador em simulação molecular. Este deve ser conhecedor do funcionamento básico dos computadores, infra-estruturas utilizadas, e das linguagens de programação disponíveis para a elaboração do software necessário para as simulações. Neste aspecto, a vida dos químicos computacionais tem vindo a ser facilitada com a disponibilização de múltiplos pacotes de software, alguns deles comerciais, com a possibilidade de contribuições livres, amigáveis ao utilizador ("user friendly"), capazes de efectuar muitas das simulações que o investigador possa necessitar. Sempre que o rumo da investigação siga para áreas inexploradas, em termos do tipo de simulações a efectuar, ou o sistema a explorar contenha situações não contempladas pelos programadores de tais pacotes de software, o químico computacional terá que "colocar as mãos na massa" e, ou modificar o programa em questão, o que nem sempre é possível, ou escrever um de raiz.

Os estudos por simulação molecular, como foi já referido, fundamentam-se essencialmente na mecânica estatística e como tal estabelecem a ligação entre as propriedades microscópicas, e individuais, das moléculas com as propriedades macroscópicas dos sistemas compostos por essas moléculas. Assim, dado um modelo molecular, caracterizado por interacções intermoleculares bem definidas, é possível estudar o comportamento de um sistema complexo com um dado número de moléculas, através dos métodos de Monte Carlo e de dinâmica molecular, nas mais variadas condições de temperatura, pressão, densidade e potencial químico. Aquele número é reduzido, em comparação com o número de moléculas num sistema macroscópico (da ordem de 10^{23}) mas torna-se-à gradualmente maior à medida que as capacidades dos computadores forem aumentando. Note-se que, hoje em dia, esse número é da ordem de 10^6 e em 1953 era da ordem de 10^2.

Uma das principais utilizações da simulação molecular é a exploração e validação de teorias moleculares por comparação dos resultados teóricos com os produzidos por simulação. Por outro lado, no caso dos resultados das simulações se aproximarem dos valores experimentais, então, a simulação molecular complementa os métodos experimentais e pode ser utilizada na estimativa de propriedades de difícil ou impossível acesso experimental.

Introduzidos os aspectos gerais da química computacional, importa referir que

na produção dos resultados apresentados nesta tese, aplicou-se essencialmente o método de Monte Carlo clássico. Este é um método estocástico, em que se gera uma cadeia de configurações do sistema (cadeia de Markov) sobre a qual são calculadas as médias das propriedades pretendidas. Utilizou-se, também, a Teoria do Funcional da Densidade [9–11] para a determinação de energias de interacção entre moléculas de etanol e água e as superfícies Au(111) e Au(210), respectivamente.

Seguidamente, identificaremos os sistemas principais tratados nesta tese.

1.2 Fulerenos

O C_{60}, é uma molécula de forma esférica, de diâmetro ∼1 nm, composta por 60 átomos de carbono distribuídos em hexágonos e pentágonos como se ilustra na Figura 1.1.

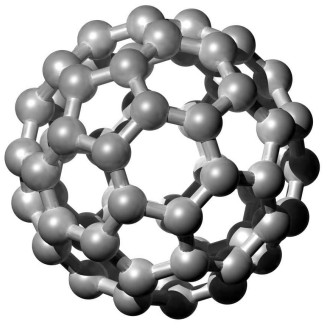

Figura 1.1: Molécula de C_{60}

Após a sua descoberta, em 1985, por Robert Curl (USA), Harold Kroto (UK) e Richard Smalley (USA), o estudo da família de moléculas do C_{60}, os fulerenos (em honra de Buckminster Fuller), captou a atenção dos químicos por todo o mundo. De facto, a gama de aplicações destas moléculas e seus derivados é vasta, indo desde os lubrificantes, às baterias, transístores, sensores (destaque para os bio-sensores), etc., como se pode ver num artigo de revisão de Birkett [12]. À medida que a síntese de C_{60}, na forma cristalina, se desenvolveu, as pesquisas sobre as propriedades dos fulerenos proliferaram um pouco por todos os ramos da química. Isto levou à descoberta de novos materiais, como os nano-tubos por exemplo, uma promessa na industria da electrónica, ou a construção de estruturas supramoleculares com moléculas de C_{60} ligadas entre si por meio de outras moléculas ou distribuídas sobre camadas auto-montadas (SAMs), por exemplo, de alquiltióis sobre superfícies metálicas (nomeadamente de ouro). Os sais de C_{60} exibem propriedades supercondutoras que se manifestam até temperaturas de 117 K [13], o que os torna particularmente interessantes no estudo dos fenómenos de supercondutividade a temperaturas relativamente elevadas.

Uma das formas da aplicação do C_{60}, a que queremos dar destaque, é a sua utilização em monocamadas auto-montadas de forma a produzir superfícies metálicas modificadas, para aplicação em biosensores e materiais fotosensíveis. Nestas aplica-

ções, as moléculas de C_{60} são ligadas, por exemplo, às extremidades de alquiltióis funcionalizados pela introdução de um grupo amina na extremidade da cadeia. Estes compostos formam as monocamadas auto-montadas bem organizadas que, por sua vez, proporcionam a formação de superfícies bem estruturadas de C_{60} [14–17].

O interesse pelos diagramas de fase de fulerenos surge da possibilidade da sua utilização como lubrificantes de altas temperaturas e devido à importância teórica em explicar o comportamento de substâncias em que as interacções intermoleculares são de muito curto alcance. É o caso da molécula de C_{60}, em que o potencial intermolecular é muito negativo para a distância de equilíbrio, mas tende para valores muito próximos de zero à distância intermolecular de apenas 1,6 diâmetros moleculares [18–20]. As substâncias com este tipo de interacção não apresentam sempre uma fase líquida estável. Este efeito foi investigado, no caso do C_{60}, por simulação molecular [21] e outras técnicas [22], tendo os resultados iniciais sido inconclusivos em relação à existência de uma fase líquida estável para esta substância. O estudo do diagrama de fases do C_{60}, apresentado nesta tese, realizou-se com o objectivo de contribuir para o esclarecimento desta questão. Ao mesmo tempo, estes cálculos são úteis relativamente à caracterização e validação de potenciais de interacção, que podem ser utilizados noutros sistemas, por exemplo, na descrição das interacções entre moléculas de fulerenos em monocamadas auto-montadas.

1.3 Monocamadas auto-montadas

A auto-montagem consiste na organização espontânea de moléculas em novos agregados, mais complexos e estruturados. Este é um fenómeno natural, cujo estudo se iniciou na década de 1980, utilizado pelos sistemas vivos na manutenção e fabrico dos seus organismos.

Especificamente, a formação de monocamadas auto-montadas (SAMs - *Self-Assembled Monolayers*) consiste na adsorção de moléculas com formação espontânea de agregados moleculares estruturados, sobre uma superfície sólida [23]. Estas moléculas têm, normalmente, uma estrutura em cadeia, com um grupo funcional com especial afinidade para ligação à fase sólida, como no caso da molécula de alquiltiol (Figura 1.2a) e a sua afinidade para adsorção em superfícies de ouro. A auto-montagem destas moléculas em superfícies de ouro (principalmente no plano (111)) revelou-se uma técnica vantajosa na obtenção de monocamadas organizadas e versáteis, com uma estrutura e composição bem definidas. É a espontaneidade da reacção, com a formação de espécies quimicamente adsorvidas (com uma energia de

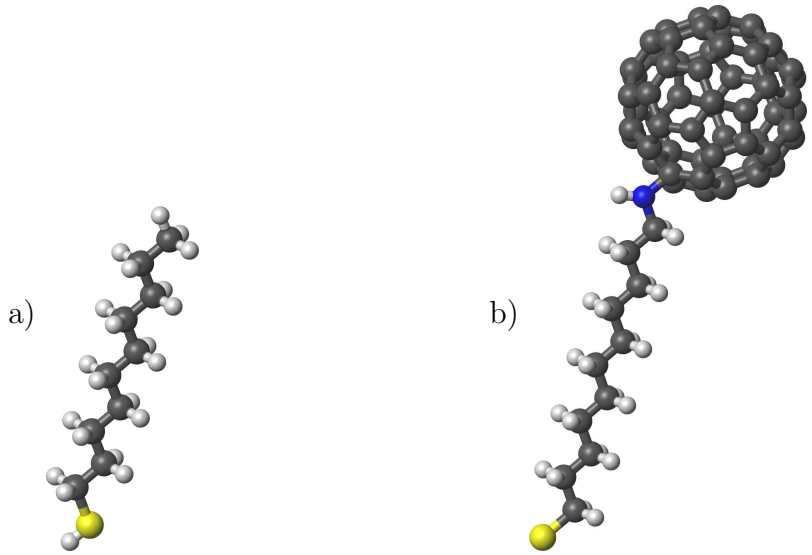

Figura 1.2: a) molécula de 1-decanotiol; b) Molécula de tiol funcionalizada com adição de uma molécula de C_{60} através de um grupo amina.

ligação da ordem de ∼28 kcal mol^{-1}) que leva à formação de camadas compactas em que as forças de van der Waals adquirem importância levando à reorganização e empacotamento das cadeias alifáticas. Os SAMs encontram muitas aplicações nas mais variadas áreas tecnológicas, que vão desde a nanotecnologia ao desenvolvimento de biosensores, entre outras. Uma revisão recente sobre os SAMs e suas aplicações pode encontrar-se em Frank Schreiber [24]. A grande versatilidade das monocamadas baseia-se na possibilidade de funcionalização através da substituição por, ou adição de, grupos funcionais nas extremidades das cadeias alifáticas destas moléculas como, por exemplo, a funcionalização por adição de uma molécula de C_{60} (ver Figura 1.2b). Na produção de monocamadas com funcionalidades úteis a nível tecnológico é necessário conhecer o seu comportamento ao nível molecular. Uma forma de obter informação deste tipo é através da simulação molecular. Com a construção de potenciais de interacção, cada vez mais refinados e adaptados a este tipo de sistemas, será possível obter uma descrição bastante pormenorizada da formação e comportamento dos SAMs. Os modelos de interacção molécula-superfície mais utilizados baseiam-se, frequentemente, na interacção das moléculas em que a informação da estrutura da superfície do eléctrodo se encontra condensada num potencial de interacção que apenas depende da distância da molécula à superfície do eléctrodo [25–32]. Neste caso, as estruturas verificadas nos SAMs dependem unicamente das interacções laterais entre as moléculas, ignorando-se os efeitos das preferências de adsorção em determinados sítios das superfícies metálicas. Além

disso, uma parte considerável das simulações referidas na literatura começam com monocamadas já formadas, montadas numa configuração de acordo com dados experimentais, e seguem a partir daí para o estudo das propriedades desses SAMs. Neste contexto, contribuimos nesta tese com um estudo da adsorção do 1-decanotiol numa superfície Au(111), a partir de uma solução de etanol, recorrendo ao método de Monte Carlo e à teoria do funcional da densidade.

1.4 Estrutura geral da tese

Considerando que uma parte substancial do trabalho realizado já se encontra publicada, optou-se por incluir cópias de alguns artigos em inglês adaptadas, no entanto, ao formato geral da tese.

Neste capítulo procurou-se fazer uma apresentação sucinta dos principais sistemas estudados.

O Capítulo 2, contém uma descrição dos fundamentos teóricos dos métodos computacionais utilizados e dos detalhes técnicos da implementação desses métodos.

Nos Capitulos 3, 4 e 5, apresentam-se as cópias de alguns artigos já publicados, em inglês, dos trabalhos sobre o desenvolvimento de métodos computacionais em mecânica estatística, diagramas de fases de fulerenos e adsorção e auto-montagem de moléculas orgânicas em superfícies Au(111). Nas Secções 5.1 e 5.2 do Capítulo 5 apresentam-se, também, os últimos resultados, ainda não publicados, referentes à continuação do estudo da adsorção e auto-montagem.

O Capítulo 6 contém as cópias de dois artigos, em inglês, referentes à adsorção do fenol e água em superfícies Au(210). Estes trabalhos foram realizados em colaboração com o Instituto de Química de S. Carlos, Univ. de S. Paulo, Brasil e têm uma estreita relação com os desenvolvidos no Capítulo 5 no que diz respeito aos modelos e técnicas utilizadas.

As conclusões e perspectivas futuras são apresentadas no Capítulo 7.

Finalmente, deve esclarecer-se que o autor da presente tese teve a contribuição maioritária na produção e análise dos resultados, em todos os artigos publicados, presentes nos Capítulos 3, 4 e 5. Quanto aos artigos em colaboração com o Brasil, a participação dos autores portugueses foi 50%.

Bibliografia

[1] F. Jensen: *Introduction to Computational Chemistry*, John Wiley & Sons (1999).

[2] J. N. Murrel, S. Carter, S. C. Farantos, P. Huxley and A. J. C. Varandas: *Molecular Potential Energy Functions*, John Wiley & Sons (1984).

[3] A. R. Leach: *Molecular Modelling. Principles and Applications*, Prentic Hall, London, 2nd ed. (2001).

[4] M. Allen and D. Tildesley: *Computer Simulation of Liquids*, Claredon Press, Oxford, U.K., 1st ed. (1987).

[5] D. Frenkel and B. Smit: *Understanding Molecular Simulations: From Algorithms to Applications*, Academic Press, 2nd ed. (2002).

[6] R. J. Sadus: *Molecular Simulation of Fluids - Theory, Algorithms and Object-Orientations*, Elsevier Science (2002).

[7] D. Rapaport: *The Art of Molecular Dynamics Simulation*, pages 57–58, Cambridge University Press (1995) .

[8] D. P. Landau and K. Binder: *A guide to Monte Carlo simulations in statistical physics*, Cambridge University Press, United Kingdom (2000).

[9] J. P. Perdew and S. Kurth: *A Primer in Density Functional Theory*, chap. 1. Density Functionals for Non-relativistic Coulomb Systems in the New Century, Spriger-Verlag Berlin Heidelberg (2003) .

[10] W. Koch and M. C. Holthausen: *A Chemist's Guide to Density Functional Theory*, Wiley-VCH (2001).

[11] R. G. Parr and W. Yang: *Density-Functional Theory of Atoms and Molecules*, Oxford University Press, New York (1989).

[12] P. R. Birkett: Fullerenes, *Annu. Rep. Prog. Chem., Sect. A* 99 (2003) 431–451.

[13] M. Hasegawa and K. Ohno: Can the visual molecular configuration in computer simulations locate solid–fluid phase boundaries? the case of C_{60}, *J. Chem. Phys.* 113 (2000) 4315.

[14] R. R. Sahoo and A. Patnaik: Binding of fullerene C_{60} to gold surface functionalized by self-assembled monolayers of 8-amino-1-octane-thiol: a structure elucidation., *J. Colloid Interface Sci.* 268 (2003) 43–49.

[15] T. Gu, J. K. Whitesell and M. A. Fox: Electrochemical charging of a fullerene-functionalized self-assembled monolayer on Au(111), *J. Org. Chem.* 69 (2004) 4075–4080.

[16] R. R. Sahoo and A. Patnaik: Surface confined self-assembled fullerene nanoclusters: a microscopic study, *Appl. Surf. Sci.* 245 (2005) 26–38.

[17] T. Kondo and K. Uosaki: Self-assembled monolayers (SAMs) with photofunctionalities, *J. Photochem. Photobio. C: Photochem. Rev.* 8 (2007) 1–17.

[18] L. A. Girifalco: Interaction potential for carbon (C_{60}) molecules, *J. Phys. Chem.* 95 (1991) 5370.

[19] L. A. Girifalco: Molecular properties of fullerene in the gas and solid phases, *J. Phys. Chem.* 96 (1992) 858.

[20] J. M. Pacheco and J. P. P. Ramalho: First-principles determination of the dispersion interaction between fullerenes and their intermolecular potential, *Phys. Rev. Lett.* 79 (1997) 3873.

[21] M. H. J. Hagen, E. J. Meijer, G. C. A. M. Mooij, D. Frenkel and H. N. W. Lekkerkerker: Does C_{60} have a liquid phase?, *Lett. to Nature* 365 (1993) 425.

[22] A. Cheng, M. Klein and C. Caccamo: Prediction of the phase diagram of rigid C_{60} molecules, *Phys. Rev. Lett.* 71 (1993) 1200–1203.

[23] L. M. Abrantes, M. Kalaji and A. S. Viana: Eléctrodos modificados por monocamadas auto-montadas, *Química* 74 (1999) 16.

[24] F. Schreiber: Self-assembled monolayers: from 'simple' model systems to biofunctionalized interfaces, *J. Phys.: Condens. Matter* 16 (2004) R881–R900.

[25] J. Hautman and M. L. Klein: Simulation of a monolayer of alkyl thiol chains, *J. Chem. Phys.* 91 (1989) 4994–5001.

[26] J. I. Siepmann and I. R. McDonald: Monte-Carlo study of the properties of self-assembled monolayers formed by adsorption of $CH_3(CH_2)_{15}SH$ on the (111) surface of gold, *Mol. Phys.* 79 (1993) 457–473.

[27] Z. Zhang, T. L. Beck, J. T. Young and F. J. Boerio: Molecular structure of monolayers from thiol-terminated polyimide model compounds on gold. 2. Molecular dynamics simulations, *Langmuir* 12 (1996) 1227–1234.

[28] A. F. Sadreev and Y. V. Sukhinin: Phase transitions in a system of $CH_3(CH_2)_{n-1}$ self-assembled on the Au(111) crystal surface, *Phys. Rev. B* 54 (1996) 17966–17973.

[29] Y. V. Sukhinin: Phase transitions in self-assembled monolayers of alkanethiols containing the polar group, *J. Experimental and Theoretical Physics* 87 (1998) 115–122.

[30] A. J. Pertsin and M. Grunze: Computer simulation of water near the surface of oligo(ethylene glycol)-terminated alkanethiol self-assembled monolayers, *Langmuir* 16 (2000) 8829–8841.

[31] R. D. Mountain, J. B. Hubbard, C. W. Meuse and V. Simons: Molecular dynamics study of partial monolayer ordering of chain molecules, *J. Phys. Chem. B* 105 (2001) 9503–9508.

[32] N. Gronbech-Jensen, A. N. Paikh, K. M. Beardmore and R. C. Desai: Rigid molecular model for the assembly characteristics and optimal structure in molecular monolayers of alkanethiols on Au(111), *Langmuir* 19 (2003) 1474–1485.

Capítulo 2

Metodologia

2.1 Conceitos de mecânica estatística

No trabalho realizado recorreu-se essencialmente ao método de Monte Carlo (MC) clássico. Dado que este método se baseia na mecânica estatística achou-se conveniente abordar alguns dos seus conceitos fundamentais para uma apresentação mais clara das técnicas utilizadas.

Em mecânica estatística, as propriedades macroscópicas podem obter-se através da média das propriedades mecânicas sobre um conjunto de réplicas do sistema, estatisticamente representativo, cada uma correspondendo a um microestado do sistema, mas todas compatíveis com o mesmo estado termodinâmico. O conjunto dos microestados possíveis de um sistema define o que se designa por espaço das fases. Assim, o espaço das fases de um sistema de N moléculas é entendido como um espaço com $2nN$ dimensões, em que n é o número de graus de liberdade de cada molécula. No caso de as moléculas serem monoatómicas (o que, por facilidade de exposição, consideraremos na presente revisão de conceitos) o espaço das fases terá $6N$ dimensões. As $6N$ dimensões são usualmente distribuídas por $3N$ coordenadas de momento linear - $p_{\{xi,yi,zi\}}$ - que definem o espaço dos momentos, e $3N$ coordenadas posicionais - $\{x_i, y_i, z_i\}$ - que definem o espaço das posições (ou espaço configuracional). Um microestado clássico do sistema pode, então, ser geometricamente representado por um ponto do espaço das fases

$$X = (x_1,\, y_1,\, z_1,\, p_{x1},\, p_{y1},\, p_{z1},\ \ \ldots,\, x_N,\, y_N,\, z_N,\, p_{xN},\, p_{yN},\, p_{zN})\,. \tag{2.1}$$

No caso de moléculas poliatómicas terão de incluir-se as coordenadas para os graus de liberdade adicionais.

O sistema irá descrever, ao longo do tempo, uma trajectória no espaço das fases. Pressupõe-se que o sistema pode revisitar "aproximada e grosseiramente" todos os microestados, ou mais correctamente todas as regiões do espaço fásico (hipótese quasi-ergódica).

O método MC, ao contrário do método DM, não requer a determinação da trajectória temporal no espaço das fases, mas sim o conhecimento da f.d.p (função densidade de probabilidade) que nos dá a probabilidade de cada microestado possível de um sistema sujeito a determinados constrangimentos. Estes são expressos por variáveis termodinâmicas como a temperatura, pressão, densidade, potencial químico, etc. O conjunto de cópias virtuais de um dado sistema real, todas no mesmo estado termodinâmico definido pelos constrangimentos, mas não necessariamente no mesmo microestado, designa-se por ensemble representativo do sistema real.

De um modo geral, o método MC gera, de forma estocástica, ensembles de microestados e determina as propriedades observáveis, $\langle A \rangle$, através de uma média de ensemble definida por

$$\langle A \rangle = \sum A_i P_i \tag{2.2}$$

onde A_i é o valor da propriedade do microestado i e P_i é a probabilidade deste microestado, a qual depende do ensemble (constrangimentos) considerado. A média anterior pressupõe que a propriedade A está definida para cada microestado, ou seja, que se trata de uma propriedade mecânica (energia, pressão, etc).

Os ensembles utilizados nos trabalhos apresentados são o canónico (NVT) e o isotérmico-isobárico (NpT). No que se segue adoptaremos o formalismo referente ao ensemble canónico (NVT) [1–3].

Neste ensemble a probabilidade de um sistema se encontrar num microestado i com energia total E_i vem dada por

$$P_i = \frac{\exp\left(-E_i/k_B T\right)}{\sum_j \exp\left(-E_j/k_B T\right)} \tag{2.3}$$

onde k_B é a constante de Boltzmann e T a temperatura absoluta. A média de ensemble de uma dada propriedade A será, então, dada por

$$\langle A \rangle = \frac{\sum_i A_i \exp\left(-E_i/k_B T\right)}{\sum_j \exp\left(-E_j/k_B T\right)} \tag{2.4}$$

de acordo com a equação (2.2). Uma vez que a energia cinética de um sistema é o somatório de termos unimoleculares, a sua média pode ser calculada analiticamente

pelo que a expressão anterior, para a energia, pode reescrever-se como

$$\langle E \rangle = \frac{3}{2} N k_B T + \frac{\sum_i U_i \exp\left(-U_i/k_B T\right)}{\sum_j \exp\left(-U_j/k_B T\right)} \tag{2.5}$$

onde $3/2\, N k_B T$ é a energia cinética média clássica (para um sistema de moléculas monoatómicas) e U_i é a energia potencial. Do mesmo modo, a média de qualquer propriedade observável será constituída por uma parte ideal e por uma parte configuracional (ou de excesso) e traduzida pela expressão

$$\langle A \rangle = A^{id} + A^{exc} = A^{id} + \frac{\sum_i A_i^{exc} \exp\left(-U_i/k_B T\right)}{\sum_j \exp\left(-U_j/k_B T\right)} \tag{2.6}$$

onde A^{id} é a contribuição ideal (que pode ser determinada analiticamente) e A^{exc} a contribuição de excesso da propriedade A. Assim, se gerarmos, aleatoriamente, o número suficiente de microestados, apenas no espaço configuracional, poderemos obter médias para as propriedades observáveis desse sistema. Se esses microestados forem gerados com distribuição uniforme, por uma amostragem do espaço configuracional, grande parte deles irão ter um factor de Boltzmann ($\exp\left(-U_i/k_B T\right)$) muito baixo (devido às frequentes sobreposições moleculares e correspondentes energias muito elevadas). Um factor de Boltzmann muito baixo implica uma pequena contribuição para o valor da média da propriedade observável e, portanto, o número de configurações que seria necessário gerar para obter médias fiáveis seria tão grande que tornaria o processo de simulação completamente inútil. Este efeito deve-se a que a f.d.p da equação (2.3) é uma função muito "afilada", com valores muito altos próximo do valor médio da energia, mas que rapidamente tende para valores muito pequenos quando se afasta ligeiramente desse valor. Um outro aspecto, que conduz mesmo à impossibilidade da aplicação da amostragem uniforme é a necessidade do conhecimento prévio do valor do denominador do segundo membro da equação (2.3), designado por função de partição, o qual é impossível determinar para a maior parte dos sistemas com interesse químico. Assim, foi desenvolvido um outro processo, designado por "importance sampling", em que são seleccionadas, com maior probabilidade, as configurações com factores de Boltzmann mais elevados.

2.2 Método de Monte Carlo em simulação molecular

2.2.1 Monte Carlo de Metropolis

A ineficiência da amostragem uniforme pode ser eliminada gerando configurações com um factor de Boltzmann elevado conforme Metropolis et al. [4] demonstraram. O processo consiste, basicamente, em gerar configurações com probabilidade proporcional a $\exp(-U_i/k_BT)$ sendo as médias de ensemble das propriedades mecânicas determinadas por média aritmética sobre estas configurações. É importante notar que, pelo contrário, no eventual processo de geração uniforme de configurações o valor médio das propriedades seria determinado por média ponderada, em que $\exp(-U_i/k_BT)$ seriam os pesos das configurações.

O método de Metropolis constrói um cadeia de estados (cadeia de Markov) em que cada estado é construído a partir do anterior. Esta cadeia de estados obedece a algumas regras bem definidas:

- A aceitação, ou não, de uma nova configuração só depende da informação contida nas duas configurações, antiga e nova.

- O número de transições para um dado estado tem de ser igual ao número de transições que partem desse estado (reversibilidade microscópica). Este princípio traduz-se pela equação

$$P(\mathrm{o}) \cdot \pi(\mathrm{o} \rightarrow \mathrm{n}) = P(\mathrm{n}) \cdot \pi(\mathrm{n} \rightarrow \mathrm{o}) \tag{2.7}$$

  onde $P(\mathrm{o})$ é a probabilidade de o sistema se encontrar no estado "o" (equação (2.3)) e $\pi(\mathrm{o} \rightarrow \mathrm{n})$ é a probabilidade de transição do estado "o" para o estado "n", sendo $P(\mathrm{n})$ e $\pi(\mathrm{n} \rightarrow \mathrm{o})$ as probabilidades para a transição inversa.

Como construir então uma cadeia de estados que obedeça a estas regras? Operacionalmente, a transição $\mathrm{o} \rightarrow \mathrm{n}$ é a combinação dos acontecimentos: escolha-tentativa da transição $\mathrm{o} \rightarrow \mathrm{n}$ e aceitação dessa transição com probabilidades $\alpha(\mathrm{o} \rightarrow \mathrm{n})$ e $acc(\mathrm{o} \rightarrow \mathrm{n})$, respectivamente. Estas operações (escolha e aceitação) são feitas de forma independente pelo que

$$\pi(\mathrm{o} \rightarrow \mathrm{n}) = \alpha(\mathrm{o} \rightarrow \mathrm{n}) \times acc(\mathrm{o} \rightarrow \mathrm{n}) \tag{2.8}$$

e

$$\pi\left(\mathrm{n}\rightarrow\mathrm{o}\right)=\alpha\left(\mathrm{n}\rightarrow\mathrm{o}\right)\times acc\left(\mathrm{n}\rightarrow\mathrm{o}\right). \tag{2.9}$$

Desta forma a equação (2.7) pode ser reescrita como

$$\frac{\mathrm{acc}\left(\mathrm{o}\rightarrow\mathrm{n}\right)}{\mathrm{acc}\left(\mathrm{n}\rightarrow\mathrm{o}\right)}=\frac{\alpha\left(\mathrm{n}\rightarrow\mathrm{o}\right)}{\alpha\left(\mathrm{o}\rightarrow\mathrm{n}\right)}\cdot\frac{P\left(\mathrm{n}\right)}{P\left(\mathrm{o}\right)} \tag{2.10}$$

As probabilidades de aceitação, acc, são escolhidas da seguinte forma:

$$\begin{aligned}\mathrm{acc}\left(\mathrm{o}\rightarrow\mathrm{n}\right) &= 1 && \Leftarrow P\left(\mathrm{n}\right)\geq P\left(\mathrm{o}\right)\\ &= \left[\alpha\left(\mathrm{n}\rightarrow\mathrm{o}\right)/\alpha\left(\mathrm{o}\rightarrow\mathrm{n}\right)\right]\times\left[P\left(\mathrm{n}\right)/P\left(\mathrm{o}\right)\right] && \Leftarrow P\left(\mathrm{n}\right)<P\left(\mathrm{o}\right)\end{aligned} \tag{2.11}$$

o que pode ser representado por

$$\mathrm{acc}\left(\mathrm{o}\rightarrow\mathrm{n}\right)=\min\left(1,\frac{\alpha\left(\mathrm{n}\rightarrow\mathrm{o}\right)}{\alpha\left(\mathrm{o}\rightarrow\mathrm{n}\right)}\cdot\frac{P\left(\mathrm{n}\right)}{P\left(\mathrm{o}\right)}\right) \tag{2.12}$$

pelo que a probabilidade de transição ficará

$$\begin{aligned}\pi\left(\mathrm{o}\rightarrow\mathrm{n}\right) &= \alpha\left(\mathrm{o}\rightarrow\mathrm{n}\right)\times 1 && \Leftarrow P\left(\mathrm{n}\right)\geq P\left(\mathrm{o}\right)\\ &= \alpha\left(\mathrm{o}\rightarrow\mathrm{n}\right)\cdot\left\{\left[\alpha\left(\mathrm{n}\rightarrow\mathrm{o}\right)/\alpha\left(\mathrm{o}\rightarrow\mathrm{n}\right)\right]\times\left[P\left(\mathrm{n}\right)/P\left(\mathrm{o}\right)\right]\right\} && \Leftarrow P\left(\mathrm{n}\right)<P\left(\mathrm{o}\right)\end{aligned}$$

$$\pi\left(\mathrm{o}\rightarrow\mathrm{o}\right) = 1-\textstyle\sum_{j\neq i}\pi\left(\mathrm{o}\rightarrow\mathrm{n}\right) \tag{2.13}$$

onde $\pi\left(\mathrm{o}\rightarrow\mathrm{o}\right)$ representa a probabilidade de o sistema permanecer no estado original.

No método de Metropolis original [4] as operações de escolha-tentativa das transições são efectuadas de forma a que a matriz subjacente, α, seja simétrica ($\alpha\left(\mathrm{o}\rightarrow\mathrm{n}\right)=\alpha\left(\mathrm{n}\rightarrow\mathrm{o}\right)$), o que faz com que este seja um método não "biased". Tendo isto em mente e considerando as equações (2.3 e 2.5) para o ensemble canónico, vemos que a probabilidades de aceitação de uma nova configuração vem dada, neste caso, por

$$\mathrm{acc}\left(\mathrm{o}\rightarrow\mathrm{n}\right)_{NVT}=\min\left(1,\exp\left(-\beta\Delta U\right)\right) \tag{2.14}$$

onde $\beta=1/k_BT$.

Estas equações são o fundamento do método de MC e permitem a sua imple-

mentação computacional.

Algoritmo base

Consideremos um sistema formado por partículas com uma configuração (o) bem definida pelas respectivas posições. Para aplicar o método MC a este sistema começamos por seleccionar aleatoriamente uma das partículas e calculamos, seguidamente, a sua energia potencial relativamente às restantes do sistema. Desloca-se, então, essa partícula (obtendo-se uma nova configuração, "n") recorrendo a um vector deslocamento, gerado aleatoriamente, e calcula-se a energia potencial da partícula na nova posição. Se $\Delta U = U\,(\mathrm{n}) - U\,(\mathrm{o}) < 0$ ($\Leftrightarrow P\,(\mathrm{n}) \geq P\,(\mathrm{o})$) aceita-se a nova configuração, isto é, esta passa a ser a configuração "efectiva" do sistema, senão $\Delta U \geq 0$ e nesse caso a aceitação tem de ser feita com probabilidade $\exp\left(-\beta\Delta U\right)$. Para esse efeito, procede-se da seguinte forma:

1. gera-se um número aleatório, *rand*, entre 0 e 1
2. se $\exp\left(-\beta\Delta U\right) > rand$ aceita-se a nova configuração
3. se $\exp\left(-\beta\Delta U\right) \leq rand$ rejeita-se a nova configuração e contabiliza-se a configuração anterior como sendo a nova configuração (transição $i \rightarrow i$).

O processo repete-se o número de vezes que for necessário de modo a conseguir-se obter uma boa estatística para as propriedades termodinâmicas que se pretendam determinar.

Ensemble *NpT*

A extensão do procedimento anterior ao ensemble NpT é relativamente simples e, neste caso, apenas referimos os pontos fundamentais da mesma [1, 2]. Neste ensemble, além dos movimentos intrínsecos das partículas temos também a variação do volume. Esta é, usualmente, feita de forma isotrópica através de um escalamento das posições dos centros de massa das partículas.

A f.d.p. para o ensemble NpT é proporcional a

$$\exp\left(-\left(U_i + pV_i\right)/k_B T\right) \tag{2.15}$$

onde p é a pressão constrangida do sistema e V_i é o volume da configuração, i. Considerando deslocamentos individuais para as N partículas, a volume constante,

seguidos de variações de volume, temos que as condições de aceitação de cada uma das transformações vêm dadas por

$$\mathrm{acc}\,(\mathrm{o} \rightarrow \mathrm{n})_{NVT} = \min\left(1, \exp\left(-\beta \Delta U\right)\right) \tag{2.16}$$

e

$$\mathrm{acc}\,(\mathrm{o} \rightarrow \mathrm{n})_{vol,NPT} = \min\left(1, \exp\left(-\beta\left(\Delta U + p\Delta V\right)\right)\right) \tag{2.17}$$

respectivamente.

2.2.2 Aplicação ao equilíbrio de fases

2.2.2.1 Método do ensemble de Gibbs

Em 1987 e 1988, Panagiotopoulos [5] e Panagiotopoulos et al. [6] desenvolveram o método de Monte Carlo no Ensemble de Gibbs (GEMC) para a simulação directa da coexistência de uma fase líquida (fase I) e de uma fase gasosa (fase II) à temperatura T. A técnica envolve, basicamente, a construção de duas caixas cúbicas. A primeira contém N^I moléculas no volume V^I e simula uma região no interior da fase I. A segunda contém N^{II} moléculas no volume V^{II} e simula uma região no interior da fase II. Cada caixa é rodeada por imagens periódicas (as condições de fronteira [1]), de modo a evitar efeitos de superfície. A interface física entre as duas fases não é considerada nesta técnica. O número total de moléculas $N = N^I + N^{II}$ e o volume total $V = V^I + V^{II}$ são conservados. As duas caixas, como um todo, formam um sistema representativo do ensemble canónico: N,V,T constantes. A simulação consta de um conjunto de três passos distintos: a) deslocamento das moléculas em cada caixa, b) variação conjugada dos volumes de cada caixa e c) troca de moléculas entre as caixas. A Figura 2.1 serve de ilustração para estas três etapas que irão constituir um ciclo de Monte Carlo.

a) Deslocamento das moléculas em cada caixa

Neste passo as caixas são independentes. Consideremos, por exemplo, a caixa I. Ela é representativa de um ensemble canónico: N^I,V^I,T constantes. Os estados neste ensemble ocorrem com probabilidade proporcional a $\exp\left(-\beta \Delta U^I\right)$ onde $\beta = 1/k_B T$ e U^I é a energia configuracional da fase I. Estes estados podem ser gerados utilizando o algoritmo de Metropolis [1]: a cada partícula da caixa I dá-se um deslocamento aleatório, gerado uniformemente, para uma nova posição na caixa. Gera-se, assim,

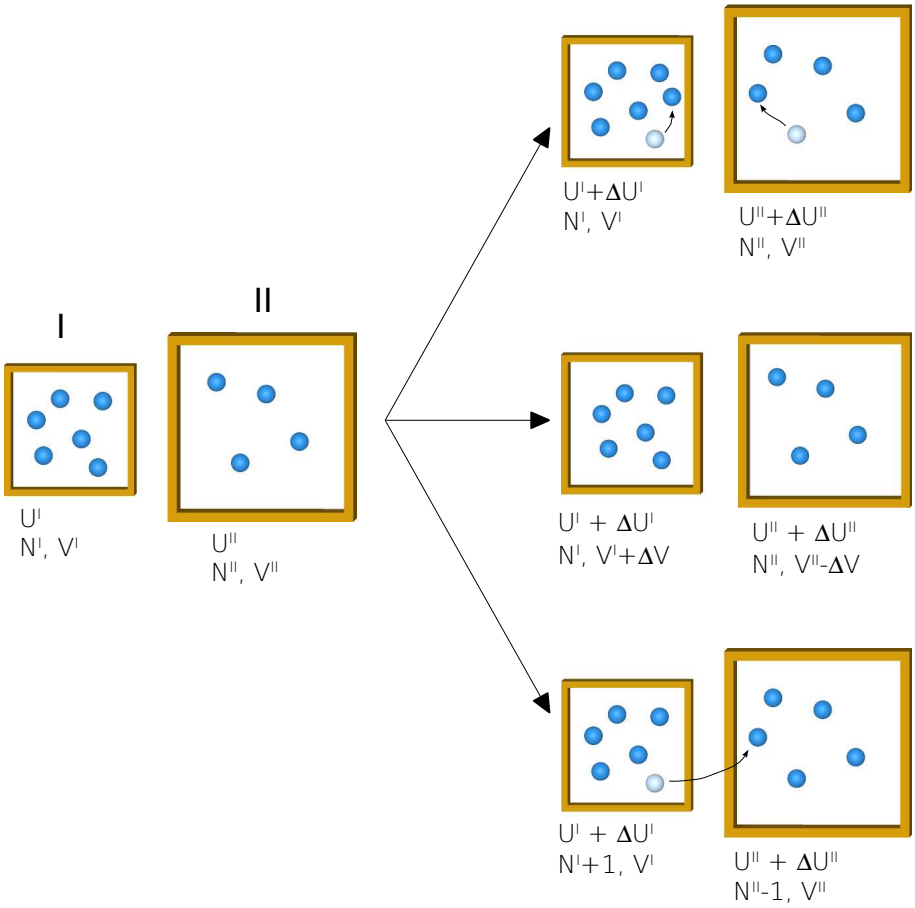

Figura 2.1: Os três passos de um ciclo de Monte Carlo no ensemble de Gibbs.

um novo estado com energia U_n^1 a partir de um estado com energia U_o^I. O novo estado é aceite ou rejeitado de acordo com a probabilidade,

$$acc\,(o \to n)_{NVT} = \min\left(1, \exp\left(-\beta \Delta U^I\right)\right) \tag{2.18}$$

onde ΔU^I é a variação da energia configuracional correspondente ao deslocamento da molécula. Se o novo estado for rejeitado, então, o estado original é recontado constituindo um elemento repetido do ensemble. Um procedimento análogo é aplicado à caixa II. Os deslocamentos máximos para as moléculas são ajustados de modo a obter uma taxa de aceitação da ordem de 50%. Note-se que a temperatura imposta a cada caixa é a mesma, o que corresponde a uma das condições do equilíbrio entre fases coexistentes.

b) Variação dos volumes de cada caixa

Neste passo, as alterações dos volumes de cada caixa não são independentes. Considerando a caixa I como parte de um ensemble isotérmico-isobárico, isto é, N^I, p e T constantes, a alteração do seu volume consiste em gerar aleatoriamente uma variação ΔV. O novo volume será, então, $V^I + \Delta V$. A razão das probabilidades dos estados novo e velho é [6],

$$P_{vol}^I = \frac{\exp\left[-\beta p\left(V^I + \Delta V\right) - \beta U_n^I + N^I \ln\left(V^I + \Delta V\right)\right]}{\exp\left[-\beta p V^I - \beta U_o^I + N^I \ln\left(V^I\right)\right]}$$

$$= \exp\left[-\beta p \Delta V - \beta \Delta U^I + N^I \ln\left(V^I + \Delta V\right) - N^I \ln\left(V^I\right)\right] \tag{2.19}$$

Uma vez que o volume total das duas caixas é constante, uma alteração simultânea na caixa II corresponde a um novo volume $V^{II} - \Delta V$ de modo a gerar um ensemble isotérmico-isobárico a N^{II}, p e T constantes. Repare-se que assumimos a igualdade da pressão, p, nas fases I e II, pois este é um dos critérios para a coexistência de duas fases. A probabilidade para a caixa II é, então,

$$P_{vol}^{II} = \exp\left[\beta p \Delta V - \beta \Delta U^{II} + N^{II} \ln\left(V^{II} - \Delta V\right) - N^{II} \ln\left(V^{II}\right)\right] \tag{2.20}$$

A alteração simultânea dos volume das duas caixas é aceite ou rejeitada com a probabilidade conjunta,

$$P_{vol} = P_{vol}^I \times P_{vol}^{II} \tag{2.21}$$

pelo que o novo estado será aceite com probabilidade

$$acc\left(o \to n\right)_{vol,GEMC} \quad =$$

$$\min\left(1, \exp\left\{-\beta\left[\Delta U^I + \Delta U^{II} - N^I kT \ln\frac{V^I + \Delta V}{V^I} - N^{II} kT \ln\frac{V^{II} - \Delta V}{V^{II}}\right]\right\}\right) \tag{2.22}$$

Se esta variação for rejeitada o estado original é recontado, constituindo assim um elemento repetido do ensemble. Ao multiplicar as probabilidades anteriores está-se a pressupor que a amostragem das configurações geradas para cada fase não é afectada pelo facto das variações de volume em cada caixa serem totalmente correlacionadas. Esta aproximação é bastante boa para estados suficientemente afastados do ponto crítico onde, como se sabe, as flutuações de densidade são consideráveis. A estimativa das propriedades críticas é realizada a partir de estados de equilíbrio líquido-vapor

abaixo da temperatura crítica, como veremos adiante. A variação máxima do volume é ajustada de modo a obter-se uma taxa de aceitação da ordem de 50%.

c) Troca de moléculas entre as duas caixas

A troca de partículas está, também, correlacionada. Considerando a caixa I como representativa de um ensemble grande-canónico (μ,V^I,T constantes, onde μ é o potencial químico) tenta-se a introdução de uma nova molécula. A sua posição é escolhida aleatoriamente dentro da caixa I. A razão das probabilidades dos estados novo e velho [6] é dada por

$$P_{int}^{I} = \frac{\exp\left[-\beta U_n^I + \beta\left(N^I+1\right)\mu - \ln\left(N^I+1\right)! - 3\left(N^I+1\right)\ln\Lambda + \left(N^I+1\right)\ln V^I\right]}{\exp\left[-\beta U_o^I + \beta N^I\mu - \ln N^I! - 3N^I\ln\Lambda + N^I\ln V^I\right]}$$

$$= \exp\left[-\beta\Delta U^I + \ln\left(\frac{zV^I}{N^I+1}\right)\right] \tag{2.23}$$

onde $z = \exp\left(\beta\mu\right)/\Lambda^3$ é a actividade e Λ o comprimento de onda térmico de de Broglie.

Dado que o número total de partículas é constante, a tentativa de introdução de uma molécula na caixa I deverá ser acompanhada de uma tentativa simultânea de destruição de uma molécula na caixa II. Ou seja, a caixa II fornece uma molécula à caixa I. A caixa II é, então, representativa de um ensemble grande-canónico a μ,V^{II},T constantes. Repare-se que μ é o mesmo nas duas fases. Escolhe-se, aleatoriamente, uma molécula da caixa II e tenta-se a sua destruição. A probabilidade de destruição [6] é

$$P_{des}^{II} = \exp\left[-\beta\Delta U^{II} + \ln\left(\frac{N^{II}}{zV^{II}}\right)\right] \tag{2.24}$$

A troca da molécula entre as duas caixas é aceite ou rejeitada com a probabilidade conjunta:

$$P_{troca} = P_{int}^{I} \times P_{des}^{II} \tag{2.25}$$

ou seja

$$acc\left(o \to n\right)_{troca,GEMC} = \min\left(1, \exp\left\{-\beta\left[\Delta U^I + \Delta U^{II} + kT\ln\frac{V^{II}\left(N^I+1\right)}{V^I N^{II}}\right]\right\}\right) \tag{2.26}$$

Se a troca for rejeitada, o estado original do sistema é recontado, constituindo então um elemento repetido do ensemble. De modo a satisfazer o princípio da

reversibilidade microscópica as introduções e destruições de moléculas nas caixas I e II devem ser tentadas com probabilidade igual. Assim, durante as simulações, a escolha da caixa onde se tenta a introdução de uma molécula é realizada com probabilidade 0.5. Se a caixa II for escolhida para a tentativa de introdução de uma molécula, então, os índices I e II, na equação anterior, devem ser trocados.

Nada existe na derivação teórica do método que indique qual o número relativo dos passos a), b) e c) que devem ser realizados para uma convergência adequada das propriedades médias. Cada caso é um caso particular e, por isso, perante uma situação nova, o investigador deve estabelecer qual a melhor maneira de conduzir as suas simulações efectuando cálculos exploratórios prévios. Em geral, uma simulação de Monte Carlo no ensemble de Gibbs realiza vários milhares de ciclos, em que cada ciclo consta de tentativas de deslocamentos de cada molécula do sistema, de uma tentativa da variação do volume de cada caixa e de várias tentativas de trocas de moléculas entre as duas caixas, de modo a obter-se uma taxa de aceitação de trocas da ordem de 1%. As propriedades médias são calculadas sobre os diferentes estados gerados.

É importante sublinhar que, neste método, não é necessário pré-especificar os valores da pressão e do potencial químico, mas apenas o valor da temperatura e das densidades iniciais das duas fases. De facto, as condições de igualdade das pressões e dos potenciais químicos do gás e do líquido estão implícitas nas probabilidades dos passos b) e c), respectivamente. No entanto, é conveniente testar, por cálculos independentes, se essas igualdades são obedecidas. Assim, as pressões podem ser calculadas pelo teorema do virial e os potenciais químicos pelo método da inserção de partículas [1].

As propriedades do ponto crítico não podem ser determinadas directamente por simulação em GEMC, pois, nessa região de temperaturas, as flutuações de volume estão muito correlacionadas e, nessa situação, o método não pode ser aplicado. Em vez disso, a estimativa da temperatura e densidade críticas é feita a partir do ajuste dos dados calculados por GEMC, na região de temperaturas abaixo do ponto crítico. Os dados de temperatura versus densidade são então ajustados à lei do parâmetro de ordem,

$$\frac{\rho_L - \rho_V}{2} = B\left(1 - \frac{T}{T_c}\right)^{\beta}, \tag{2.27}$$

e à lei dos diâmetros rectilíneos,

$$\frac{\rho_L + \rho_V}{2} = d_c + A\left(1 - \frac{T}{T_c}\right), \tag{2.28}$$

onde β é o expoente crítico a que é atribuído o valor $\sim$0.33 [7] para o argon e sistemas afins. A estimativa da pressão é feita, através de um ajuste dos dados de pressão versus temperatura à equação de Clausius-Clapeyron. A partir da função resultante calcula-se a pressão correspondente à temperatura crítica que foi estimada pelo ajustes às equações 2.27 e 2.28.

Uma das limitações de GEMC é a difícil convergência das médias para moléculas poliatómicas e estados muito densos. Nesses casos, a aceitação de trocas de moléculas é muito pequena e o método torna-se muito lento para obter uma igualdade dos potenciais químicos das duas fases. Existem, no entanto, técnicas para remediar essas situações como, por exemplo, o método "cavity-biased" [8,9]. A outra limitação, do método GEMC original é a de não permitir a simulação do equilíbrio fluido-sólido. Na verdade, o modo como a técnica é realizada implicaria adições ou remoções aleatórias de moléculas num cristal o que resultaria na criação de defeitos pontuais nos cristais. No entanto, o método foi recentemente extendido ao tratamento desse equilíbrio por Chen et al. [10].

2.2.2.2 Integração "Gibbs-Duhem"

Em 1993 e 1995, Kofke [11] e Agrawal e Kofke [12,13] estabeleceram um método que pode ser utilizado para simular o diagrama de fases completo de qualquer substância. Este método baseia-se na equação de Clapeyron para a variação da pressão, em função da temperatura, ao longo das linhas de coexistência (lc):

$$\left(\frac{\partial \ln p}{\partial \beta}\right)_{lc} = -\frac{\Delta h}{\beta p \Delta v} \tag{2.29}$$

onde Δh e Δv são, respectivamente, as diferenças da entalpia molar e do volume molar das duas fases. Esta equação é deduzida a partir da equação de Gibbs-Duhem admitindo a igualdade dos potenciais químicos das duas fases em equilíbrio.

Uma vez que se conheçam as propriedades de equilíbrio de um ponto em qualquer linha de coexistência pode, por integração numérica da equação anterior, calcular-se a pressão e a temperatura de outros estados na linha de coexistência considerada. Então, tudo o que há a fazer é realizar duas simulações simultâneas nas caixas I e II, por Monte Carlo ou dinâmica molecular (GDMC ou GDMD) no ensemble isotérmico-isobárico (NpT). Dado que que se determinam a pressão e temperatura de equilíbrio, evita-se a troca de partículas entre as duas caixas o que elimina os problemas referidos anteriormente para o equilíbrio fluido-sólido, moléculas poliató-

micas e fases muito densas.

Contudo, um problema de extrema importância na implementação deste método é a definição de um ponto de coexistência de modo a iniciar-se a integração da equação de Clapeyron. Para o equilíbrio líquido-vapor pode utilizar-se qualquer ponto obtido por GEMC. Para o equilíbrio fluido-sólido tal não é possível, pelo que se torna necessário usar outros métodos para o estabelecimento desse ponto.

Agrawal e Kofke [12,13], a partir das propriedades bem conhecidas da coexistência fluido-sólido para um sistema de esferas rígidas, determinaram as propriedades fluido-sólido para um sistema de esferas moles (SSP) no limite de altas temperaturas. Dado um potencial qualquer, $V(r)$, pode encontrar-se um ponto do equilíbrio fluido-sólido através do potencial escalado:

$$S(r,\lambda) = (1-\lambda)\, SSP(r) + \lambda V(r) \tag{2.30}$$

onde λ é um parâmetro entre 0 e 1. Para uma dada temperatura, a equação de Clapeyron modificada para uma variação em λ é:

$$\frac{\partial \ln p}{\partial \lambda} = -\frac{a^I - a^{II}}{z^I - z^{II}} \tag{2.31}$$

onde $a = \partial(\beta\mu)/\partial\lambda$ e $z = \beta pv$. A determinação do estado de equilíbrio para o potencial $V(r)$ faz-se integrando a equação 2.31, pelo método GDMC, variando λ de 0 a 1. A partir desse ponto, calculam-se, por GDMC ou GDMD, os outros estados coexistentes a temperaturas mais baixas.

Uma vez calculadas as linhas fluido-sólido, as propriedades do ponto triplo são estimadas a partir da intersecção da linha de cristalização com a linha de coexistência líquido-vapor. As propriedades do ponto triplo constituem, por sua vez, o ponto de partida para simular o equilíbrio vapor-sólido.

2.2.3 Aplicação a moléculas poliatómicas

A grande maioria das aplicações do método de MC de Metropolis consiste na simulação de sistemas conceptuais (por ex. esferas rígidas) ou de moléculas de estrutura simples (até ∼10 centros de interacção, rígidas e quasi-esféricas). Iremos concentrar-nos na aplicação do método a sistemas moleculares cujas moléculas têm mais de 5 ou 6 átomos, e com uma estrutura tal que obrigue à aplicação de um modelo flexível (com graus de liberdade intra-moleculares) nas simulações. Para isso iremos em seguida ver quais os tipos de movimentos/tentativas de MC que são necessárias para

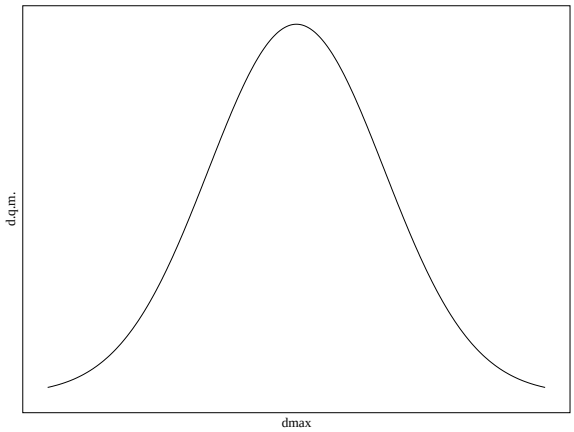

Figura 2.2: Variação do desvio quadrático médio com o deslocamento máximo numa tentativa de translação em MC.

efectuar simulações de tais modelos.

2.2.3.1 Translação

O procedimento geral, para efectuar a translação de uma molécula consiste na geração de um vector aleatório de deslocamento

$$\begin{aligned} x' &= x + d_{max}\,(rand - 0.5) \\ y' &= y + d_{max}\,(rand - 0.5) \\ z' &= z + d_{max}\,(rand - 0.5) \end{aligned} \tag{2.32}$$

onde d_{max} é a maior variação permitida para as variáveis, x, y, ou z, e *rand* é uma função que gera um número pseudo-aleatório entre 0 e 1, com distribuição uniforme nesse intervalo. Move-se a molécula segundo este vector e aceita-se a nova configuração com probabilidade

$$p = min\left[1, \exp\left(-\beta \Delta U\right)\right], \tag{2.33}$$

de acordo com o algoritmo de Metropolis. O valor de d_{max} é ajustado durante a simulação para que se obtenha uma amostragem mais eficaz do espaço das fases. Esta eficácia pode ser relacionada, moderadamente, com o desvio quadrático médio (d.q.m.) das partículas em função do tempo de simulação. Quanto maior este for maior será a eficácia da amostragem configuracional. A Figura 2.2 representa a dependência típica do d.q.m. com o valor de d_{max}. O procedimento mais comum é ajustar d_{max} para que a taxa de aceitação de novas configurações seja de 0.5 mas

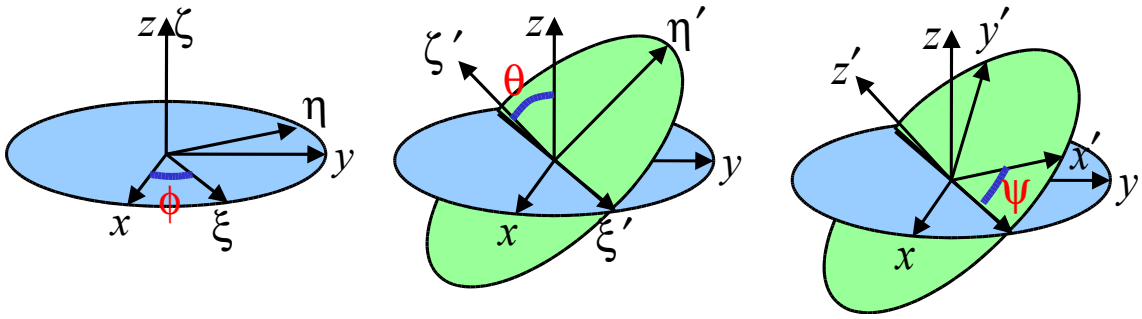

Figura 2.3: Ângulos de Euler: ϕ - rotação em torno do eixo z, θ - rotação em torno do eixo ξ' (imagem do eixo x na rotação ϕ) e ψ - rotação em torno do eixo z' (imagem de z na rotação θ).

este não é necessariamente o valor ideal e depende do tipo de sistemas simulados como é referido em Frenkel e Smit [2].

2.2.3.2 Rotação

Na literatura [1] são discutidos vários métodos de rotação de moléculas. Um dos mais referidos baseia-se em efectuar pequenas variações nos ângulos de Euler ϕ, θ e ψ (Figura 2.3),

$$\begin{aligned} \phi_t &= \phi + \Delta\phi_{max}\,(2\,rand - 1) \\ \cos\theta_t &= \cos\theta + \Delta\,(\cos\theta)_{max}\,(2\,rand - 1) \\ \psi_t &= \psi + \Delta\psi_{max}\,(2\,rand - 1) \end{aligned} \tag{2.34}$$

a partir dos quais se define a orientação molecular, tendo o cuidado de que no caso do ângulo θ as variações sejam feitas em $\cos\theta$, para que as probabilidades de transição sejam bem calculadas. A nova configuração é então aceite com a probabilidade dada pela equação (2.33).

Uma alternativa amplamente adoptada, para evitar a utilização do ângulos de Euler, é o uso de quaterniões. Os quaterniões são vectores num espaço a quatro dimensões em que cada coordenada está relacionada com os ângulos de Euler por relações bem definidas [2]. A rotação da molécula processa-se através da variação do quaternião no espaço a quatro dimensões.

Um processo simples, mas que nos parece bastante apelativo, e de fácil implementação, consiste na geração de um vector unitário $\mathbf{u}$ com distribuição uniforme numa esfera. Existem vários métodos para gerar vectores aleatórios com distribuição uniforme numa esfera de raio unitário. Após a geração daquele vector, gera-se

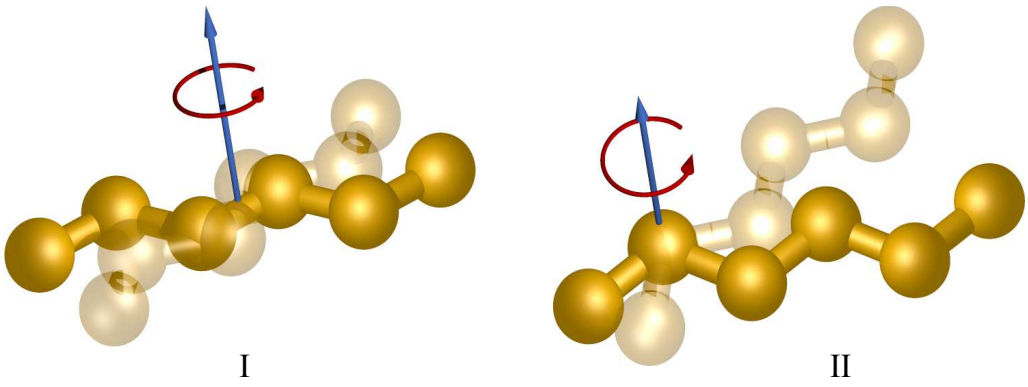

Figura 2.4: I - Rotação em trono do centro de massa. II - Rotação em torno de um centro de interacção da molécula.

aleatoriamente o ângulo de rotação α com

$$\alpha = \Delta\alpha_{max}\,(rand - 0.5) \tag{2.35}$$

em que $\Delta\alpha_{max}$ é o valor máximo do ângulo de rotação, e procede-se à rotação da molécula, em torno de um eixo, **u**, que passe pelo seu centro de massa (ou outro centro escolhido na molécula) como se mostra na Figura 2.4 . A nova configuração é aceite com probabilidade dada pela equação (2.33).

2.2.3.3 Modificação de ângulos entre ligações

Vamos agora considerar a abertura ou fecho de um ângulo formado por duas ligações consecutivas entre os centros de interacção a, b e c como mostra a Figura 2.5 . Nesta rotação, as partes esquerda e direita da molécula, que formam o ângulo, são consideradas estruturas rígidas e rodadas em torno de um eixo que passe pelo centro b, em simultâneo ou individualmente. Para garantir o aleatoriedade das configurações a escolha do tipo de rotação a efectuar (à esquerda, direita ou em simultâneo) deve ser feita com distribuição uniforme de probabilidade ($P = 1/3$). As configurações são aceites com probabilidade dada pela equação (2.33).

2.2.3.4 Modificação de ângulos diedros

Consideremos quatro centros, a, b, c e d, com ligações a—b, b—c e c—d. O ângulo formado pelos planos a—b—c e b—c—d denomina-se ângulo diedro e as transformações deste ângulo efectuam-se por rotação dos elementos a e d em torno do eixo b—c como se pode ver na Figura 2.6 . Também neste caso a escolha

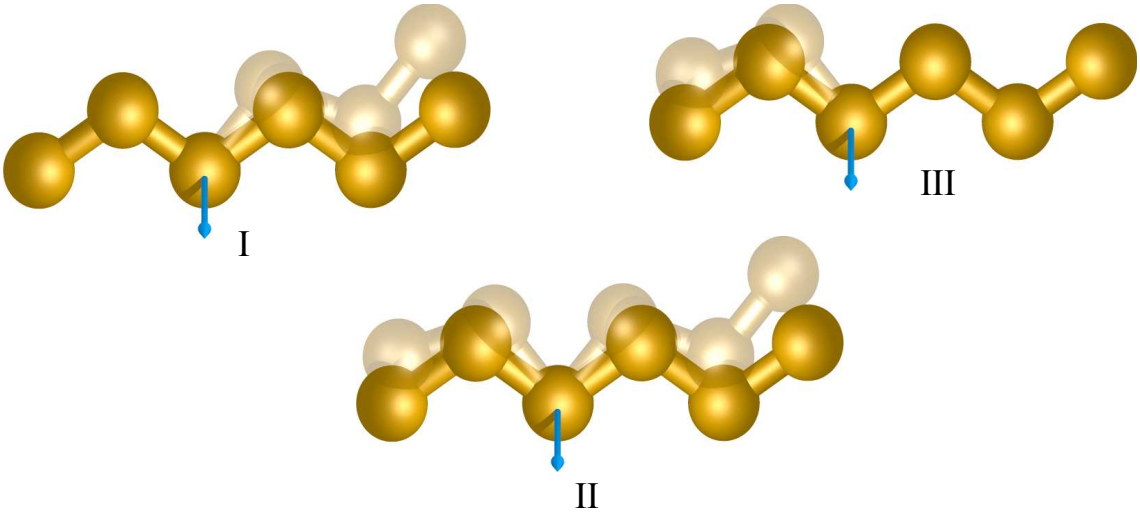

Figura 2.5: Três formas de efectuar uma transformação dum ângulo entre ligações: I - à direita; II - em simultâneo; III - à esquerda.

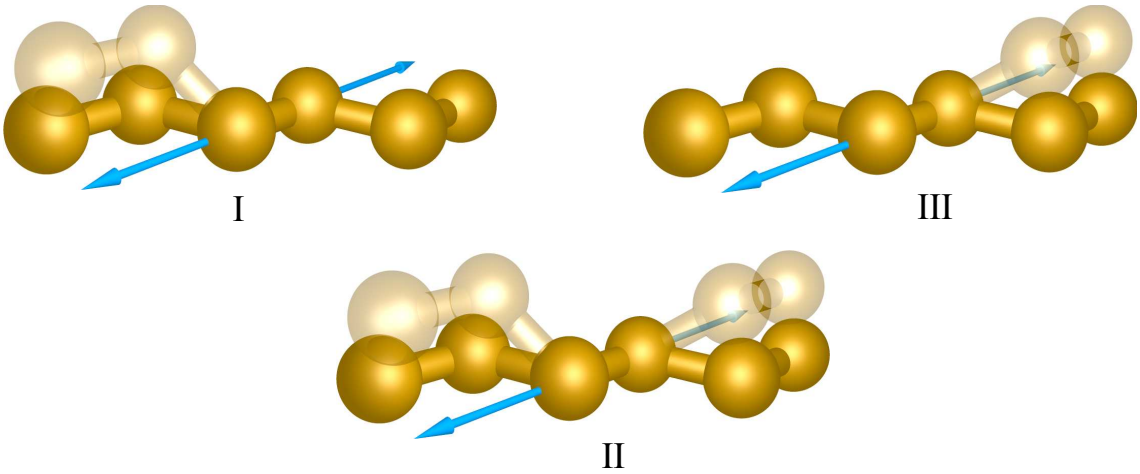

Figura 2.6: Três formas de efectuar uma transformação dum ângulo diedro formado por quatro ligações consecutivas: I - à esquerda; II - em simultâneo; III - à direita.

do tipo de transformação (à esquerda, à direita ou em simultâneo) deve ser feita com distribuição de probabilidade uniforme. A aceitação de configurações faz-se, também, com probabilidade dada pela equação (2.33).

2.2.3.5 Modificação de comprimentos de ligações

Como se pode perceber pela natureza das ligações químicas entre os átomos, os potenciais que descrevem estas interacções são extremamente limitativos no que se refere a desvios da posição de equilíbrio, quando comparados com os potenciais relacionados com as interacções de ângulo diedro ou simples e, ainda mais, com as interacções entre centros não ligados quimicamente. As transformações teriam assim de ser feitas com deslocamentos muito pequenos. Na maior parte dos modelos verifica-se que a extinção destas transformações não altera significativamente os resultados das simulações. Portanto, a não ser que os resultados que se pretendam obter exijam um refinamento muito elevado do modelo computacional do sistema, estas interacções serão "congeladas" fixando os comprimentos das ligações no ponto de energia mínima do potencial.

Estes são os movimentos base necessários para a simulação de moléculas flexíveis. Na literatura, encontra-se uma variedade de possibilidades para estes movimentos [2] de forma a aumentar a eficácia da amostragem dos espaço das fases. No entanto, todos as soluções apresentadas debatem-se com sérias dificuldades quando a dimensão das moléculas aumenta para mais de dez centros de interacção.

Os movimentos que modificam a orientação da molécula no espaço podem ser problemáticos, na medida em que pequenas alterações num dado ponto da molécula provocam movimentos de dimensões exageradas noutro ponto. Por exemplo, na rotação de uma molécula em cadeia, ilustrada na Figura 2.7, apesar de a rotação provocar pequenos movimentos nos pontos próximos do eixo de rotação, os deslocamentos provocados nos extremos da cadeia irão ser de dimensão tal que, na maior parte das vezes, resultarão em sobreposições entre centros de interacção, gerando configurações de altíssima energia, implicando uma elevada taxa de rejeição e deficiente amostragem do espaço das fases. O mesmo efeito ocorre, por exemplo, na modificação de um ângulo diedro no interior da molécula.

A solução, embora parcial, para estes problemas de amostragem surgiu com o desenvolvimento do método "Configurational-bias" que iremos discutir em seguida. Esta melhoria da amostragem do espaço das fases possibilitou a simulação, por MC,

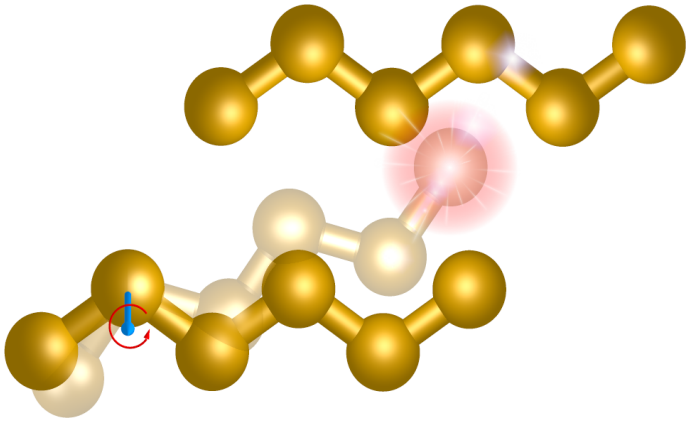

Figura 2.7: Colisão provocada por rotação em torno de um centro de interacção numa molécula em cadeia.

de sistemas de moléculas em cadeia (alcanos, álcoois, tióis, etc) que, de outra forma, seriam impraticáveis pois o número de configurações necessárias para a obtenção de médias estáveis seria muito elevado, sobrepondo-se o custo, em tempo e recursos computacionais, aos proveitos retirados das simulações.

2.2.4 Monte Carlo "configurational-bias"

Na aplicação do método MC a sistemas moleculares surgem, normalmente, problemas de amostragem relacionados com efeitos esterioquímicos que provocam o aparecimento, quase exclusivo, de configurações com factor de Boltzmann muito baixo o que, como já foi referido, irá implicar a sua rejeição. Na literatura podemos encontrar alguns métodos, normalmente para sistemas moleculares específicos, como os algoritmos "Kink-Jump" e "Pivot" [14], desenvolvidos para contornar estes problemas. Contudo, o aparecimento dos métodos de amostragem "biased", no que diz respeito à geração de novas configurações, veio dar um grande impulso à aplicação do método de MC em sistemas moleculares. Estes métodos são especialmente úteis em casos em que não é possível alterar a conformação de uma molécula através de um número pequeno de passos consecutivos.

Nos métodos "biased" utiliza-se a informação estrutural da configuração corrente para gerar a nova configuração, de forma a que esta tenha maior probabilidade de ser aceite. Recorde-se que, no método MC padrão, esta informação só era utilizada na decisão de aceitação da nova configuração. Neste esquema as probabilidades $\alpha(\mathrm{o} \rightarrow \mathrm{n})$ e $\alpha(\mathrm{n} \rightarrow \mathrm{o})$ já não são iguais, pois a produção de configurações deixou de ser feita de forma uniforme. Da equação (2.13) conclui-se que agora a frac-

ção $[\alpha(\mathrm{n} \rightarrow \mathrm{o})/\alpha(\mathrm{o} \rightarrow \mathrm{n})]$ é um factor importante, cuja função é corrigir o "bias" introduzido na escolha de configurações de modo a assegurar a reversibilidade microscópica patente na equação (2.7).

De uma forma geral, nos métodos "biased" a geração de novas configurações faz-se com probabilidades

$$\begin{aligned} \alpha(\mathrm{o} \rightarrow \mathrm{n}) &= \mathrm{f}[U(\mathrm{n})] \\ \alpha(\mathrm{n} \rightarrow \mathrm{o}) &= \mathrm{f}[U(\mathrm{o})] \end{aligned} \tag{2.36}$$

onde f é a função que controla a aceitação de novas configurações com base na informação estrutural das mesmas. Vejamos, então, como será então a regra de aceitação de novas configurações no ensemble NVT, corrigida para ter em conta a geração "biased" de configurações. Substituindo as probabilidade da equação (2.36) nas equações (2.8) e (2.7) ficaremos com

$$\frac{\mathrm{acc}(\mathrm{o} \rightarrow \mathrm{n})}{\mathrm{acc}(\mathrm{n} \rightarrow \mathrm{o})} = \frac{\mathrm{f}[U(\mathrm{o})]}{\mathrm{f}[U(\mathrm{n})]} \frac{P(\mathrm{n})}{P(\mathrm{o})}$$

pelo que a regra para a aceitação de novas configurações será

$$\mathrm{acc}(\mathrm{o} \rightarrow \mathrm{n}) = \min\left(1, \frac{\mathrm{f}[U(\mathrm{o})]}{\mathrm{f}[U(\mathrm{n})]} \frac{P(\mathrm{n})}{P(\mathrm{o})}\right) \tag{2.37}$$

e, portanto, no ensemble canónico

$$\mathrm{acc}(\mathrm{o} \rightarrow \mathrm{n})_{NVT} = \min\left(1, \frac{\mathrm{f}[U(\mathrm{o})]}{\mathrm{f}[U(\mathrm{n})]} \exp\{-\beta \Delta U\}\right). \tag{2.38}$$

Este exemplo traduz, na generalidade, a estratégia adoptada para os esquemas "biased" em MC.

Existem vários algoritmos de MC do tipo "biased" aplicados à rotação, inserção/remoção de moléculas, modelos em rede, etc, que se encontram descritos na literatura [2]. Iremos, em seguida, derivar o método "Configurational-bias" aplicado à amostragem de conformações de moléculas em cadeia considerando as interacções intra- e inter-moleculares.

2.2.4.1 Derivação do método

O método de Monte Carlo "Configurational-bias" (MCCB) [15–17] tem a sua origem no algoritmo proposto por Rosenbluth e Rosenbluth [18] com o objectivo de possibilitar a amostragem de conformações em polímeros. O esquema inicial de Rosenbluth

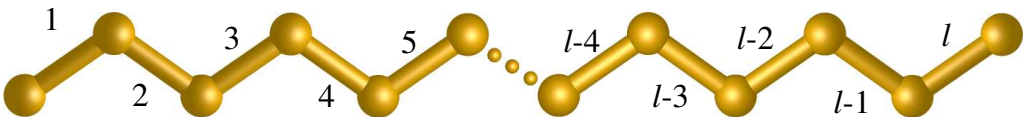

Figura 2.8: Representação de uma cadeia molecular com os segmentos numerados de 1 a l.

consistiu na apresentação de um processo de construção de cadeias moleculares em que os segmentos eram montados sequencialmente sobre uma rede cúbica ou quadrada (a duas dimensões). Para corrigir a parcialidade da amostragem, Rosenbluth e Rosenbluth introduziram um parâmetro de correcção, W, dependente da estrutura das configurações geradas. Batoulis e Kremer [19], numa análise do método de Rosenbluth e Rosenbluth, mostram que o método é eficaz apenas para cadeias relativamente pequenas e que sua eficiência diminui exponencialmente com o aumento do comprimento das cadeias. De modo a melhorar a eficiência da construção de cadeias, no método MCCB, a produção de novas configurações é conduzida ("biased") de forma a que no final se obtenha uma distribuição correcta (de Boltzmann) de conformações de cadeias moleculares.

Consideremos uma molécula em cadeia com l segmentos, como se ilustra na Figura 2.8. O objectivo é gerar conformações da cadeia através da sua reconstrução, total ou parcial, segmento a segmento. Estas conformações têm, no entanto, de ser viáveis no que diz respeito à sua energia potencial de ligação (u^{lig}, ligações químicas, ângulos e diedros) e de par (u^{par}, pares intra- e inter-moleculares) e, para isso, cada segmento da cadeia tem de ser colocado considerando estas contribuições.

Na colocação de um segmento na cadeia, as contribuições para a energia de ligação vêm das interacções entre segmentos vizinhos, e dependem quase sempre da distância entre dois centros consecutivos (correspondente a uma ligação química), do ângulo formado entre ligações sucessivas e dos ângulos diedros em que estão envolvidos. A energia de par corresponde a interacções intramoleculares entre centros mais distantes (normalmente a mais de quatro centros de distância) como se ilustra na Figura 2.9 e a interacções entre centros de diferentes moléculas (interacções inter-moleculares).

Vamos, então, analisar a colocação de um segmento da cadeia. Para cada segmento irá ser produzida uma série de k orientações tentativa (Figura 2.10)

$$\{b\}_k = \{b_1, \ldots, b_k\}$$

com distribuição de probabilidade dependente do factor de Boltzmann associado à

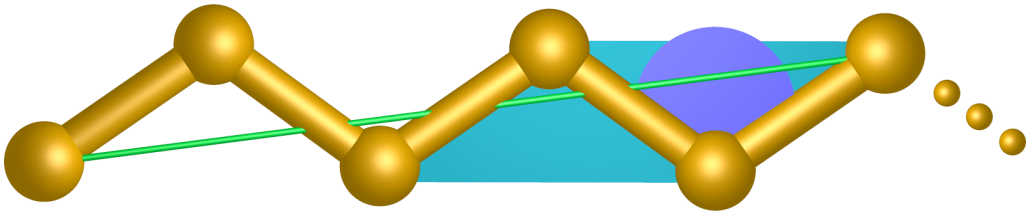

Figura 2.9: Representação das interacções de um segmento (neste caso o segmento mais à direita): azul - ângulo de ligação; ciano - ângulo diedro; verde - interacção de par, entre centros a mais de quatro vizinhos de distância.

energia potencial de ligação para esse segmento

$$P_i^{\text{lig}}(b) \propto \exp\left[-\beta u_i^{\text{lig}}(b)\right]. \tag{2.39}$$

Destas orientações irá ser seleccionada uma com probabilidade dependente da sua contribuição para a energia de par do sistema, dada por

$$P_i^{\text{par}}(b) = \frac{\exp\left[-\beta u^{\text{par}}(b)\right]}{w_i^{\text{par}}\left(\{b\}_k\right)} \tag{2.40}$$

onde o denominador $w_i^{\text{par}}\left(\{b\}_k\right)$ se designa por factor de Rosenbluth e é a soma dos factores de Boltzmann inter-moleculares sobre o conjunto de configurações tentativa $\{b\}_k$,

$$w_i^{\text{par}}\left(\{b\}_k\right) = \sum_{j=1}^{k} \exp\left[-\beta u_i^{\text{par}}(b_j)\right]. \tag{2.41}$$

Com este processo de produção de orientações para o segmento i, em dois passos, consegue-se, então, produzir um segmento que terá uma probabilidade muito maior de ser aceite do que se o processo fosse completamente aleatório. Assim, a probabilidade conjunta de produzir uma determinada orientação b para o segmento i é dada por

$$\alpha_i(\text{o} \to \text{n}) = P_i^{\text{lig}}(b) \cdot P_i^{\text{par}}(b)$$

e, portanto, a probabilidade de gerar uma cadeia com l segmentos será dada por

$$\alpha(\text{o} \to \text{n}) = \prod_{i=1}^{l} \alpha_i(\text{o} \to \text{n}) = \prod_{i=1}^{l} P_i^{\text{lig}}(b) \cdot P_i^{\text{par}}(b). \tag{2.42}$$

Consideremos, agora, o processo de aceitação da transição da conformação de partida "o" da cadeia para a nova conformação "n". Como acabamos de ver os

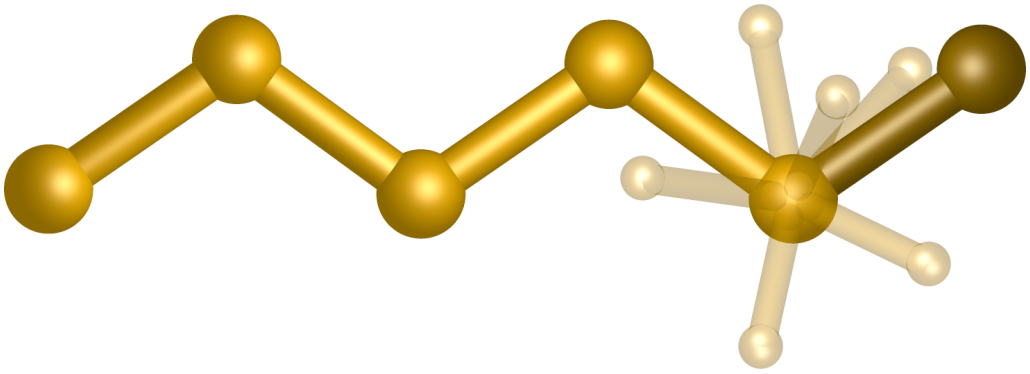

Figura 2.10: Inserção do segmento mais à direita. Em cor mais escura representa-se a orientação de partida. Em cor transparente têm-se as k orientações tentativas das quais uma seria escolhida para a inserção do segmento.

segmentos de cada cadeia são escolhidos de conjuntos de orientações tentativa. Isto é válido para ambas as conformações, pelo que podemos dizer que quaisquer segmentos "o" e "n" são escolhidos de um conjunto de orientações com k elementos $(\{b\}_k^{\mathrm{o}}, \{b\}_k^{\mathrm{n}})$ e definir a probabilidade de gerar um destes conjuntos como:

$$P^{\mathrm{lig}}\left(\{b\}_k^{\mathrm{o}}, \{b\}_k^{\mathrm{n}}\right). \tag{2.43}$$

Recorde-se que as regras de aceitação para as transições $(\mathrm{o} \to \mathrm{n})$ têm como base a equação (2.7). Aplicando esta equação ao esquema MCCB e para apenas um segmento, teremos

$$\begin{aligned} P_i(\mathrm{o}) \cdot \pi_i(\mathrm{o} \to \mathrm{n}) &= P_i(\mathrm{o}) \cdot \alpha_i\left(\mathrm{o} \to \mathrm{n}, \{b\}_{k,i}^{\mathrm{o}}, \{b\}_{k,i}^{\mathrm{n}}\right) \cdot \mathrm{acc}_i\left(\mathrm{o} \to \mathrm{n}, \{b\}_{k,i}^{\mathrm{o}}, \{b\}_{k,i}^{\mathrm{n}}\right) \\ &= C \cdot \exp\left[-\beta u_i(\mathrm{o})\right] \cdot \exp\left[-\beta u_i^{\mathrm{lig}}(\mathrm{n})\right] \cdot \frac{\exp\left[-\beta u_i^{\mathrm{par}}(\mathrm{n})\right]}{w_i^{\mathrm{inter}}\left(\{b\}_{k,i}^{\mathrm{n}}\right)} \\ &\quad \cdot \mathrm{acc}_i\left(\mathrm{o} \to \mathrm{n}, \{b\}_{k,i}^{\mathrm{o}}, \{b\}_{k,i}^{\mathrm{n}}\right) \cdot P_i^{lig}\left(\{b\}_{k,i}^{\mathrm{o}}, \{b\}_{k,i}^{\mathrm{n}}\right) \end{aligned} \tag{2.44}$$

e

$$\begin{aligned} P_i(\mathrm{n}) \cdot \pi_i(\mathrm{n} \to \mathrm{o}) &= P_i(\mathrm{n}) \cdot \alpha_i(\mathrm{n} \to \mathrm{o}, \{b\}_k^{\mathrm{n}}, \{b\}_k^{\mathrm{o}}) \cdot \mathrm{acc}_i(\mathrm{n} \to \mathrm{o}, \{b\}_k^{\mathrm{n}}, \{b\}_k^{\mathrm{o}}) \\ &= C \cdot \exp\left[-\beta u_i(\mathrm{n})\right] \cdot \exp\left[-\beta u_i^{\mathrm{lig}}(\mathrm{o})\right] \cdot \frac{\exp\left[-\beta u_i^{\mathrm{inter}}(\mathrm{o})\right]}{w_i^{\mathrm{inter}}\left(\{b\}_{k,i}^{\mathrm{o}}\right)} \\ &\quad \cdot \mathrm{acc}_i\left(\mathrm{n} \to \mathrm{o}, \{b\}_{k,i}^{\mathrm{n}}, \{b\}_{k,i}^{\mathrm{o}}\right) \cdot P_i^{\mathrm{lig}}\left(\{b\}_{k,i}^{\mathrm{o}}, \{b\}_{k,i}^{\mathrm{n}}\right) \end{aligned} \tag{2.45}$$

onde $u = u^{\mathrm{lig}} + u^{\mathrm{par}}$ é a energia total do segmento em questão e C é uma constante

de normalização. Igualando os termos da transformação directa e inversa, obtemos a regra para a aceitação de novos segmentos

$$\frac{\mathrm{acc}_i\left(\mathrm{n}\rightarrow\mathrm{o},\{b\}^{\mathrm{o}}_{k,i},\{b\}^{\mathrm{n}}_{k,i}\right)}{\mathrm{acc}_i\left(\mathrm{n}\rightarrow\mathrm{o},\{b\}^{\mathrm{n}}_{k,i},\{b\}^{\mathrm{o}}_{k,i}\right)}=\frac{w_i^{\mathrm{par}}\left(\{b\}^{\mathrm{n}}_{k,i}\right)}{w_i^{\mathrm{par}}\left(\{b\}^{\mathrm{o}}_{k,i}\right)} \tag{2.46}$$

onde apenas aparecem os factores de Rosenbluth dos conjuntos de orientações, $\{b\}^{\mathrm{o}}_{k,i}$ e $\{b\}^{\mathrm{n}}_{k,i}$,de onde foram escolhidas as orientações de partida e de chegada, respectivamente.

Para a cadeia completa, o critério de aceitação é o produto dos termos para cada um dos segmentos:

$$\frac{\mathrm{acc}\left[\mathrm{n}\rightarrow\mathrm{o},\left(\{b\}^{\mathrm{n}}_{k,1},\ldots,\{b\}^{\mathrm{n}}_{k,l}\right)\right]}{\mathrm{acc}\left[\mathrm{o}\rightarrow\mathrm{n},\left(\{b\}^{\mathrm{o}}_{k,1},\ldots,\{b\}^{\mathrm{o}}_{k,l}\right)\right]}=\frac{W\left[\mathrm{n},\left(\{b\}^{\mathrm{n}}_{k,1},\ldots,\{b\}^{\mathrm{n}}_{k,l}\right)\right]}{W\left[\mathrm{o},\left(\{b\}^{\mathrm{o}}_{k,1},\ldots,\{b\}^{\mathrm{o}}_{k,l}\right)\right]} \tag{2.47}$$

onde o numerador

$$W\left[\mathrm{n},\left(\{b\}^{\mathrm{n}}_{k,1},\ldots,\{b\}^{\mathrm{n}}_{k,l}\right)\right]=\prod_{i=1}^{l}w_i^{\mathrm{par}}\left(\{b\}^{\mathrm{n}}_{k,i}\right) \tag{2.48}$$

é o factor de Rosenbluth para a nova conformação resultante de todos os segmentos da nova cadeia e o denominador é o mesmo, mas para a conformação de partida. Repare-se que na regra de aceitação não aparecem os termos dependentes da energia potencial intra-molecular e note-se a sua simplicidade tendo em conta as probabilidades de partida associadas às operações deste esquema, que é muito mais complexo que o esquema original do método MC padrão.

2.2.4.2 Algoritmo

Em termos gerais, o algoritmo do método MCCB consiste em seleccionar aleatoriamente uma cadeia (molécula), reconstruir total ou parcialmente essa cadeia gerando assim uma nova conformação, calcular os factores de Rosenbluth para a cadeia antiga e nova e testar a aceitação da nova cadeia pela regra de aceitação da equação (2.47).

A partir das regras de probabilidade, acima definidas, vamos agora descrever, em termos operacionais, como é que os segmentos da cadeia são colocados. Imaginemos que alguns segmentos da cadeia já foram colocados e vamos agora colocar o segmento

i do meio da cadeia. O segmento irá ser colocado da seguinte forma:

1. Gerar k orientações tentativa para o segmento. O número de orientações, k, é escolhido por tentativa e erro de forma a fornecer os melhores resultados. As orientações têm de ser geradas com probabilidade dada pela equação (2.39). Um dos processos para gerar as orientações será:

   (a) Gerar um vector unitário com distribuição uniforme de orientações numa esfera de raio 1. Os métodos para gerar este tipo de distribuição de orientações podem encontrar-se na literatura referida [2].

   (b) Avaliar a contribuição desta orientação para a energia potencial de ligação, u_i^{lig}. Aceitar a orientação gerada com probabilidade

   $$\min\left[1, \exp\left(-\beta u_i^{\text{lig}}\right)\right] \tag{2.49}$$

   (c) Repetir os passos (a) e (b) até que se tenha construído um conjunto com k elementos, $\{b\}_{k,i}^{\text{n}}$.

2. Avaliar a energia potencial de par $u_{j,i}^{\text{par}}$ para cada uma das orientações e calcular o factor de Rosenbluth do conjunto, $w_i^{\text{n}}\left(\{b\}_{k,i}^{\text{n}}\right)$ (equação (2.41)). Seleccionar uma das orientações segundo a probabilidade dada pela equação (2.40). Para isso, gera-se um número aleatório, $rand$, e selecciona-se uma orientação b_s que satisfaça a seguinte condição:

   $$\sum_{j=1}^{s\leq k} \exp\left(-\beta u_{j,i}^{\text{par}}\right) \geq rand \cdot w_i\left(\{b\}_k^{\text{n}}\right). \tag{2.50}$$

   O segmento produzido torna-se, assim, o segmento i da conformação tentativa.

3. Repetir os passos 1, 2 e 3 até que se obtenha uma cadeia completa.

4. Calcular o factor de Rosenbluth da nova conformação, $W\,(\text{n})$ (equação (2.48)).

Agora que construímos a nova conformação e calculámos o factor de Rosenbluth, $W\,(\text{n})$, temos de fazer um rastreio dos segmentos da conformação antiga para determinar o factor de Rosenbluth, $W\,(\text{o})$. O rastreio de um segmento geral i será feito da seguinte forma:

1. Gerar $k-1$ orientações alternativas para o segmento. Essas orientações serão geradas, novamente, com distribuição de probabilidade dada pela equação (2.39). O processo de geração de orientações é análogo ao que foi descrito acima na inserção de novos segmentos. As novas orientações, juntamente com a orientação do segmento, irão formar o conjunto $\{b\}_{k,i}^{\mathrm{o}}$.

2. Para cada uma das orientações do conjunto $\{b\}_{k,i}^{\mathrm{o}}$, calcular a energia potencial de par e determinar o factor de Rosenbluth $w_i^o\left(\{b\}_{k,i}^{\mathrm{o}}\right)$ (equação (2.41)).

3. Calcular o factor de Rosenbluth de toda a cadeia, $W\left(\mathrm{o}\right)$(equação (2.48)) repetindo os passos 1 e 2 para todos os segmentos.

Depois de calculados os factores de Rosenbluth, a nova conformação é aceite com probabilidade

$$\min\left[1, W\left(n\right)/W\left(o\right)\right]. \tag{2.51}$$

Na Figura 2.11 encontra-se a descrição do algoritmo MCCB, para a inserção de segmentos, em linguagem algorítmica.

Ainda sobre a inserção de segmentos há que referir os casos especiais da inserção do primeiro, segundo e terceiro centros de interacção da molécula. No caso do primeiro é de salientar que as contribuições para a energia potencial são exclusivamente inter-moleculares. No caso do segundo, e assumindo que estamos a utilizar um modelo de comprimentos de ligação fixos, também não há contribuições intra-moleculares, o que faz com que com que a distribuição de orientações para este primeiro segmento seja uma distribuição uniforme numa esfera. No caso do terceiro centro (introdução do segundo segmento) as contribuições intra-moleculares vêm da abertura e fecho do ângulo com o primeiro segmento. A partir daqui a inserção de segmentos processa-se normalmente.

A selecção e reconstrução das cadeias pode ser efectuada de vários modos. Normalmente, a selecção de uma cadeia é feita de forma aleatória. A reconstrução da cadeia pode ser total ou parcial. No caso da reconstrução ser total, o primeiro centro de interacção da molécula é colocado através de uma translação como se tratasse de uma partícula simples. No caso da reconstrução não ser total, seleccionam-se, aleatoriamente, um centro e uma direcção de reconstrução. Neste caso, o rastreio da conformação antiga também só se faz a partir do centro e na direcção seleccionados.

Para moléculas mais complexas como, por exemplo, cadeias ramificadas ou cíclicas, o método tem de ser adaptado para lidar com os constrangimentos intra-moleculares. Além disso, existem ainda situações em que os movimentos de algumas

```
W ← 1  Factor de Rosenbluth da cadeia
ciclo i ← n até 1
      sumW ← 0  Factor de Rosenbluth do segmento
      j ← 1
      Gerar conjunto de k configurações:
      ciclo enquanto j ≠ k
            rit é uma variável vector [x,y,z]
            randr() retorna vector aleatório unitário com dist. orient. unif.
            norm() retorna a norma de um vector
            rit ← randr()*norm(ri)
            Uit ← Uang + Udied
            Incluir energia de pares intramoleculares:
            ciclo m ← 1 até n-5
                  Uit ← Uit + Umnt
            fim de ciclo
            ΔUit ← Uit – Ui
            se exp(-β*ΔUit) > rand() então
                  Orientação aceite!
                  j ← j + 1
                  trials[j] ← rit
                  Calcular mudança na energia inter-molecular:
                  ΔUinter ← Uinter_t - Uinter
                  Wtrial[j] ← exp(-βΔUinter)
                  sumW ← sumW + Wtrial[j]
      fim de ciclo
      Seleccionar uma orientação:
      selW ← rand() * sumW
      sw ← Wtrial[1]
      rnd ← rand()
      j ← 1
      ciclo enquanto sw < selW
            j ← j + 1
            sw ← sw + Wtrial[j]
      fim de ciclo
      Orientação de indice j seleccionada!
      W ← W * sumW
      Guardar orientação!
      Tseg[i] ← trials[j]
fim de ciclo
```

Figura 2.11: Algoritmo de construção de uma cadeia a partir do segmento n.

secções das moléculas estão mais limitados (em relação ao resto da cadeia) como no caso de moléculas em cadeia cujos extremos estão fixos por adsorção química em substractos cristalinos. Para moléculas com cadeias muito extensas, como no caso dos polímeros, pode também ser interessante adaptar o método MCCB para que apenas se modifiquem secções intermédias das cadeias num processo denominado de "rebridging". [2, 14]

De uma forma intuitiva, já se percebe que este método deve tornar possível a simulação, por MC, de sistemas moleculares com um grande número de graus de liberdade intra-moleculares que de outra forma só seriam possíveis de simular pelo método DM.

2.3 Potenciais de interacção

Para se poder efectuar qualquer tipo de estudo por simulação molecular clássica é absolutamente necessário possuir uma boa descrição das interacções intra- e intermoleculares em termos de potenciais de interacção. Estas consistem, na maior parte dos casos, em interacções entre pares de átomos, ou centros de interacção, mas podem também incluir-se interacções de multicorpos [1, 2]. No caso de se querer estudar um sistema molecular pode ser necessário, também, utilizar potenciais de interacção na descrição das interacções intramoleculares como, por exemplo, na descrição de ligações químicas, abertura e fecho de ângulos de ligação e torção em torno de uma ligação (abertura e fecho dos ângulos diedros).

Um dos potenciais efectivos frequentemente utilizados em simulação molecular, para as interacções intermoleculares de dispersão e repulsivas, é o potencial de Lennard-Jones (LJ)

$$U\left(r_{ij}\right) = 4\varepsilon\left[\left(\frac{\sigma}{r_{ij}}\right)^{12} - \left(\frac{\sigma}{r_{ij}}\right)^{6}\right] \tag{2.52}$$

onde r_{ij} é a distância entre os centros de interacção, σ é o diâmetro molecular e ε é o valor do mínimo de energia potencial para a interacção. Na presença de cargas eléctricas totais ou parciais, localizadas nos centros de interacção, adiciona-se o potencial de Coulomb

$$U\left(r_{ij}\right) = \frac{q_i q_j}{4\pi\varepsilon_0 r_{ij}} \tag{2.53}$$

onde q_i e q_j são os valores das cargas e ε_0 é a permitividade do vácuo. Desta forma, para um sistema onde só sejam contabilizadas as interacções inter-moleculares a

energia potencial do sistema será dada por:

$$U = \sum_{i>j} 4\varepsilon \left[\left(\frac{\sigma}{r_{ij}} \right)^{12} - \left(\frac{\sigma}{r_{ij}} \right)^{6} \right] + \frac{q_i q_j}{4\pi\varepsilon_0 r_{ij}} \tag{2.54}$$

onde $i > j$ significa que a soma é feita sobre todos os pares distintos de centros de interacção. Esta é a base do desenvolvimento, por exemplo, dos potenciais OPLS [20,21] (Optimized Potentials for Liquid Simulations) utilizados na modelação das interacções etanol-etanol, tiol-tiol e etanol-tiol nos sistemas de auto-montagem apresentados nesta tese.

Uma aproximação para interacções mais complexas é a condensação das interacções relativas às partes individuais, que constituem uma dada estrutura molecular, num potencial mais simples que descreve as interacções entre essas estruturas como um todo. Este é o caso do potencial de Girifalco, para os fulerenos, em especial para o C_{60} [22]. Neste potencial assume-se que a interacção entre duas molécula de C_{60} pode ser aproximada pela interacção entre duas esferas com uma densidade uniforme de átomos de carbono. Utilizando o potencial LJ e integrando sobre a superfície das esferas obtém-se a expressão

$$U(s) = -2\alpha \left[\frac{1}{s(s-1)^3} - \frac{1}{s(s-1)^3} \right] + 2\beta \left[\frac{1}{s(s-1)^9} - \frac{1}{s(s+1)^9} \right]$$

onde $s = r/2a$, com

$$\alpha = N^2 A/12(2a)^6 \qquad \beta = N^2 B/90(2a)^{12}$$

onde N é o número de átomos de carbono (neste caso $N = 60$). As constantes A, B e a são calculadas através do ajuste a dados experimentais para a molécula de C_{60}.

Quando é necessário calcular a interacção de espécies moleculares com uma superfície infinita pode adoptar-se uma estratégia semelhante à anterior. A interacção entre uma molécula e a superfície, separadas por uma dada distância, z, é calculada somando as interacções entre todos os pares molécula-(átomo da superfície). Esta, pode escrever-se [23]

$$U_s(z) = \sum_i U_{ms}(r_i) \tag{2.55}$$

onde U_{ms} é a interacção entre a molécula e um átomo da superfície. Caso U_{ms} seja uma interacção com uma forma analítica simples, por exemplo, o potencial LJ, os átomos da superfície podem ser substituídos por uma distribuição contínua e a

soma substituída por um integral. A integração pode ser feita camada a camada, o que assumindo um potencial LJ(12-6), resulta num potencial LJ(10-4) ou sobre todas as camadas em conjunto resultando num potencial LJ(9-3). Esta é a base do desenvolvimento dos potenciais de interacção tiol-Au(111) de Hautman et al. [24], também utilizados em alguns modelos apresentados nesta tese. Este tipo de procedimento esconde os efeitos de "corrugação" da superfície que deixam de ser calculados explicitamente pois o novo potencial depende apenas da distância z que vai da molécula à superfície. Nos ciclos de simulação molecular é ususal referir este modelo como "de interacção com uma superfície plana e não estruturada", o que não significa, sublinhe-se, que a corrugação da superfíce não é considerada. Esta designação é utilizada ao longo desta tese. Uma forma de melhorar este modelo, introduzindo o factor corrugação de forma explicita, é a inclusão de uma variável extra que localiza a molécula sobre a superfície. Essa variável pode ser, por exemplo, um vector da superfície definido a partir de um ponto de referência. Um exemplo da aplicação desta estratégia são os potenciais de interacção água-platina de Yeh e Berkowitz [25].

Na descrição de interacções intermoleculares com eléctrodos utilizam-se também as superfícies de potencial (PES) calculadas por métodos quânticos. Neste caso, dependendo da extensão da PES disponível podem utilizar-se directamente os valores de energia potencial ou fazer um ajuste da PES a uma função analítica que será depois utilizada nas simulações. Tais métodos foram utilizados por nós para refinar os potenciais de interacção etanol-Au(111) e água-Au(210). Estes modelos são referidos como " de interacção com uma superfície estruturada" dado que a corrugação da superfície é explicitamente considerada.

A descrição de sistemas moleculares, em que é necessário introduzir flexibilidade na estrutura individual das moléculas, implica um maior grau de complexidade no que diz respeito à elaboração de campos de força. Assim, é necessário introduzir potenciais para as interacções intramoleculares. No caso das ligações químicas, em especial nos cálculos de mecânica molecular, pode ser utilizado o potencial harmónico

$$U\left(r_{ij}\right) = \frac{1}{2}k\left(r_{ij} - r_0\right)^2 \tag{2.56}$$

ou o potencial de Morse

$$U\left(r_{ij}\right) = E_0\left[\left\{1 - \exp\left(-k\left(r_{ij} - r_0\right)\right)\right\}^2 - 1\right] \tag{2.57}$$

onde k e E_0 são os parâmetros a ajustar para cada tipo de ligação. Para a descrição dos ângulos de ligação utiliza-se igualmente o potencial harmónico da equação (2.56) em que a variável não é a distância r_{ij}, mas sim o ângulo de ligação, θ. Na rotação em torno de ligações químicas (variação de ângulos diedros) utilizam-se normalmente séries de Fourier com o número de termos necessários para descrever correctamente as variações de energia associadas a esses graus de liberdade [2, 14].

2.3.1 Corte do potencial e correcções de longo alcance

Algumas interacções intermoleculares são de curto alcance, isto é, os respectivos valores de energia decaem para valores próximos de zero em apenas alguns diâmetros moleculares, como é o caso da energia de dispersão traduzida pelo potencial LJ. Nesta situação, é comum considerar somente as interacções cujas distâncias entre partículas caem dentro de uma esfera de raio de corte, r_{cut}. Isto leva a que só uma pequena percentagem das $\frac{1}{2}N\left(N-1\right)$ interacções, necessárias para o cálculo da energia potencial total, sejam efectivamente tidas em conta. A contribuição de energia devida às interacções com partículas que ficam fora da esfera de corte é calculada integrando a função de potencial, considerando uma função de distribuição radial uniforme e unitária, isto é:

$$U^{tot} = \sum_{i<j} U\left(r_{ij} < r_{cut}\right) + \frac{N\rho}{2} \int_{r_{cut}}^{\infty} U\left(r\right)\, 4\pi r^2\, dr \tag{2.58}$$

onde ρ é a densidade do sistema.

Somas de Ewald

No caso do potencial de Coulomb não é possível aplicar um corte análogo ao que discutimos para o potencial LJ. Este potencial decai com uma potência em r^{-1} o que provoca a divergência do integral [2], apresentado na equação (2.58), para as contribuições de longo alcance. No entanto, é comum observar-se na literatura que para simulações de sistemas biológicos de grandes dimensões a estratégia de corte do potencial é muitas vezes utilizada [2]. Isto deve-se à necessidade de diminuir os tempos de cálculo que, para estes sistemas, podem alcançar valores além do que é praticável. Por outro lado, demonstrou-se que em muitos casos a aplicação do corte às interacções de Coulomb introduz erros significantes na simulação [2, 26].

Iremos de seguida analisar aplicação da soma de Ewald a um sistema com condições fronteira periódicas em duas dimensões mas limitado na terceira (geometria

laminar). Este método adequa-se à aplicação em sistemas com interfaces líquido sólido, que são o objecto de estudo de parte dos trabalhos apresentados. O método utilizado, denominado de EW3DC [27], é derivado da aplicação a um sistema periódico nas três dimensões. Um dedução mais rigorosa da aplicação a este tipo de geometria consiste no método EW2D derivado por Parry [28,29] e Heyes et al. [30]. As técnicas de soma de Ewald aplicadas a esta geometria encontram-se discutidas por exemplo em Widmann et al. [31]. Bródka e Grzybowski [32] demonstram analiticamente a aproximação do método EW2D pelo método EW3DC.

A energia de Coulomb total de um sistema, representado por uma caixa de geometria paralelipipédica de lados L_x, L_y e L_z, com condições de fronteira periódicas [1,2], constituído por N partículas pode ser escrita como

$$U_C = \frac{1}{2}{\sum_{\boldsymbol{n}}}' \sum_{i=1}^{N}\sum_{j=1}^{N} \frac{q_i q_j}{|\boldsymbol{r}_{ij} + \boldsymbol{n}L|} \tag{2.59}$$

onde q_i é a carga da partícula i. O vector $\boldsymbol{n} = (n_1, n_2, n_3)$ indica as coordenadas do centro da célula imagem, $\boldsymbol{n}L = (n_1 L_x, n_2 L_y, n_3 L_z)$, sendo que para a célula original $\boldsymbol{n} = (0,0,0)$. A distância entre partículas é dada por $r_{ij,\boldsymbol{n}} = |\boldsymbol{r}_i - \boldsymbol{r}_j + \boldsymbol{n}L|$. A soma acima apresentada converge lentamente e de forma condicionada (i.e. depende da ordem das parcelas) [1], além de que para sistemas muito grandes se torna incomportável, em termos de tempo de cálculo.

A soma de Ewald foi apresentada, em 1921 [33], como uma técnica de soma para as contribuições de longo alcance de um sistema com condições fronteira periódicas. Nesta técnica, a soma da equação (2.59) é dividida em quatro termos [1,2,27]: duas séries rapidamente convergentes, um termo constante, e um termo dependente da geometria da soma, respectivamente,

$$U_{Ewald} = U^r + U^k + U^0 + J\left(\boldsymbol{M}, P\right) \tag{2.60}$$

onde

$$U^r = \frac{1}{2}\sum_{i=1}^{N}\sum_{j=1}^{N}{\sum_{\boldsymbol{n}}}' q_i q_j \frac{\operatorname{erfc}\left(\alpha\,|\boldsymbol{r}_{ij} + \boldsymbol{n}L|\right)}{|\boldsymbol{r}_{ij} + \boldsymbol{n}L|}, \tag{2.61}$$

$$U^k = \frac{1}{2\pi V}\sum_{i=1}^{N}\sum_{j=1}^{N}\sum_{k\neq 0} q_i q_j \left(\frac{4\pi^2}{k^2}\right)\exp\left(-\frac{k^2}{4\alpha^2}\right)\cos\left(\boldsymbol{k}\cdot\boldsymbol{r}_{ij}\right), \tag{2.62}$$

$$U^0 = -\frac{\alpha}{\sqrt{\pi}} \sum_{i=1}^{N} q_i^2. \tag{2.63}$$

A forma do termo $J(\boldsymbol{M}, P)$ será discutida posteriormente. Nestas equações, $V = L_x \cdot L_y \cdot L_z$ é o volume do sistema, $\boldsymbol{k} = 2\pi\left(n_x/L_x, n_y/L_y, n_z/L_z\right)$ é um vector do espaço recíproco e α é um parâmetro da distribuição Gaussiana que determina a dispersão das cargas. Numa simulação, o valor de α e o número de vectores $\boldsymbol{k}$ são parâmetros ajustados empiricamente em função da eficiência computacional e do rigor pretendido.

A soma de Ewald baseia-se na dispersão das cargas pontuais das partículas por uma distribuição Gaussiana de igual magnitude e sinal oposto [26]. As interacções entre as partículas passam a ter um comportamento de curto alcance fazendo com que a soma no espaço real, U^r, convirja rapidamente. Para contrariar o efeito da distribuição Gaussiana, acima referida, é utilizada uma outra, com o mesmo sinal e magnitude, mas fazendo a soma no espaço recíproco utilizando transformadas de Fourier para resolver a equação de Poisson [1, 2]. O resultado é a soma no espaço recíproco, U^k. O termo constante, U^0, é um termo de correcção que elimina os efeitos de, no termo anterior, U^k, se terem considerado as interacções das cargas com elas próprias. Em sistemas moleculares é ainda necessário adicionar um outro termo de correcção, dado por

$$U^{excl} = -\frac{1}{2} \sum_{i,j \in excl} \frac{z_i z_j erf\left(\alpha \left|\boldsymbol{r}_{ij}\right|\right)}{\left|\boldsymbol{r}_{ij}\right|} \tag{2.64}$$

relativo às interacções entre partículas vizinhas nas moléculas, mas que estão excluídas do cálculo das interacções de Coulomb por estarem ligadas por outros tipos de interacção, como ligações químicas, ângulos e diedros, já referidos anteriormente. A função de erro complementar $erfc(x) = 1 - erf(x) = 1 - 2/\sqrt{\pi} \int_0^x e^{-u^2} du$ é uma função que decresce monotonamente para zero e define a dispersão das cargas acima referida.

Como já se disse, o termo $J(\boldsymbol{M}, P)$, depende da geometria da soma (P), sendo $\boldsymbol{M} = \sum z_i r_i$ o momento dipolar total do sistema (com z=carga e $\boldsymbol{r}$=vector posição). A geometria normalmente utilizada para a soma é a esférica, ($P = S$), e nesse caso

$$J(\boldsymbol{M}, S) = \frac{2\pi}{(2\epsilon + 1) V} \left|\boldsymbol{M}\right|^2. \tag{2.65}$$

Se o meio envolvente tiver uma constante dieléctrica, ϵ, infinita (condição "tinfoil"),

este termo anula-se. No caso de o sistema ser isotrópico temos $\boldsymbol{M} = 0$ e portanto $J = 0$.

O método de soma de Ewald exposto até aqui, EW3D, aplica-se a sistemas periódicos nas três dimensões x, y e z. O método EW3DC [27], de aplicação em sistemas periódicos em apenas duas dimensões (*e.g.* x e y),($P = R$), consiste na utilização do esquema EW3D mas fazendo com que o sistema seja muito maior na direcção não periódica, *i.e.* introduzindo um espaço vazio na direcção z, e aplicando um termo de correcção dependente da polarização total do sistema,

$$J\left(\boldsymbol{M}, R\right) = \frac{2\pi}{V} M_z^2 \tag{2.66}$$

onde M_z é a componente z do momento dipolar total do sistema. Em termos de eficiência computacional, Berkowitz e Yeh [27] chegaram à conclusão que o método EW3DC era $\sim$10 vezes mais rápido que a melhor optimização do método EW2D.

2.4 Teoria do Funcional da Densidade (DFT)

A Teoria do Funcional da Densidade é um método mecânico-quântico largamente aplicado ao cálculo das propriedades de sistemas moleculares. DFT fundamenta-se em dois teoremas, demonstrados por Hohenberg Kohn em 1964 [34]:

1. A densidade electrónica determina univocamente o Hamiltoneano do sistema e, portanto, todas as propriedades do sistema.

2. A energia do sistema calculada a partir de uma dada densidade electrónica é mínima se a densidade utilizada corresponder ao estado fundamental do sistema.

Estes teoremas levam a que a função de onda do sistema, que depende de $4N$ coordenadas (três espaciais e uma de spin, sendo N o número de electrões do sistema), possa ser substituída pela densidade electrónica, que depende apenas de três variáveis. Esta substituição, de certa forma, sugere que a função de onda possui, na verdade, mais informação do que a que é necessária para a descrição do sistema [35].

Num sistema molecular a energia passa, assim, a ser escrita como um funcional da densidade electrónica:

$$E\left[\rho\right] = T\left[\rho\right] + E_{ee}\left[\rho\right] + E_{Ne}\left[\rho\right] \tag{2.67}$$

onde ρ é a densidade electrónica, E é a energia total, T é a energia cinética, E_{ee} é a energia resultante da interacção entre electrões e E_{Ne} é a energia da interacção dos electrões com os núcleos atómicos. Os funcionais apresentados podem ser divididos em dois grupos, um dependente da configuração dos núcleos e do número de electrões e outro universal, calculado sempre da mesma forma independentemente do sistema em questão. A parte "dependente" corresponde a E_{Ne} e pode ser escrita como

$$E_{Ne}[\rho] = \int \rho(\boldsymbol{r}) V_{Ne} d\boldsymbol{r} \tag{2.68}$$

onde V_{Ne} é o potencial de interacção núcleo-electrão e $\boldsymbol{r}$ é o vector posição. A parte independente, F_{HK}, designada por funcional de Hohenberg-Kohn, pode apresentar-se como

$$F_{HK}[\rho] = T[\rho] + E_{ee}[\rho]. \tag{2.69}$$

Aplicando o principio variacional, traduzido no segundo teorema, a energia do estado fundamental escreve-se [36]

$$E_0 = \min_{\rho \to N} \left(F_{HK}[\rho] + \int \rho(\boldsymbol{r}) V_{Ne} d\boldsymbol{r} \right). \tag{2.70}$$

A universalidade do funcional F_{HK} é um aspecto importante da teoria DFT pois permite que seja utilizado do mesmo modo quer para um sistema pequeno, como o átomo de hidrogénio, quer para um sistema composto por milhares de átomos como polímeros, biomoléculas ou eléctrodos metálicos. No entanto, a forma explicita deste funcional é completamente desconhecida, sendo este, hoje em dia, um campo muito activo da investigação em química-física fundamental. Se a expressão analítica de F_{HK} fosse conhecida, então seria possível resolver a equação de Shrödinger de forma exacta e, neste caso, portanto seria possível, em princípio, descrever ao pormenor o comportamento de todos os sistemas químicos.

Os teoremas de Hohenberg-Kohn não fornecem nenhuma pista sobre como calcular E_0 a partir de ρ ou sobre a forma dos funcionais nem sobre qualquer processo pelo qual seja possível encontrar esses funcionais. Em 1965, Kohn e Sham [37] elaboraram um processo através do qual é possível aproximar o funcional F_{HK}. Este processo inspira-se na teoria Hartree-Fock e no modelo de electrões não interactuantes que se movem num potencial efectivo. Estes autores introduziram a seguinte formula para o funcional universal, F_{HK} [36]:

$$F_{HK}[\rho] = T_s[\rho(\boldsymbol{r})] + J[\rho(\boldsymbol{r})] + E_{xc}[\rho(\boldsymbol{r})] \tag{2.71}$$

onde $T_s[\rho(\boldsymbol{r})]$ é a energia cinética do sistema não interactuante

$$T_S[\rho] = -\frac{1}{2}\sum_{i}^{N}\langle\varphi_i \mid \bigtriangledown^2 \mid \varphi_i\rangle \tag{2.72}$$

$J[\rho(\boldsymbol{r})]$ é a energia de interacção electrónica clássica

$$J[\rho(\boldsymbol{r})] = \frac{1}{2}\sum_{i}^{N}\sum_{j}^{N}\int\int|\varphi_i(\boldsymbol{r}_1)|^2\frac{1}{r_{12}}|\varphi_j(\boldsymbol{r}_2)|^2 d\boldsymbol{r}_1 d\boldsymbol{r}_2 \tag{2.73}$$

e $E_{xc}[\rho(\boldsymbol{r})]$ é a chamada energia de troca-correlação, da qual não se conhece a forma explicita. Este termo inclui as contribuições electrostáticas não clássicas e a energia de correlação e de troca, além de uma pequena porção da energia cinética [36].

As funções φ_i, $i = 1, 2, ..., N$, denominadas de orbitais de Kohn-Sham são calculadas a partir da resolução das equações monoelectrónicas [35]

$$\hat{F}_{KS}(1)\varphi_i(1) = \varepsilon_{i,KS}\varphi_i(1) \tag{2.74}$$

onde $\hat{F}_{KS}$ é o operador Kohn-Sham

$$\hat{F}_{KS} = -\frac{1}{2}\bigtriangledown_1^2 + \sum_{j=1}^{N}\hat{J}_j(1) + V_{xc}(1) - \sum_{\alpha}\frac{Z_\alpha}{r_{1\alpha}}. \tag{2.75}$$

O último termo desta expressão corresponde ao funcional E_{Ne} da equação (2.67). O potencial de troca-correlação,V_{xc}, é definido como sendo a derivada funcional de E_{xc},

$$V_{xc} = \frac{\delta}{\delta\rho(\boldsymbol{r}_1)}E_{xc}[\rho(\boldsymbol{r}_1)] \tag{2.76}$$

As orbitais de Kohn-Sham, φ_i, não têm significado físico definido além da sua utilização para calcular a densidade electrónica através da expressão

$$\rho = \sum_{i=1}^{N}|\varphi_i|^2. \tag{2.77}$$

A função de onda em DFT não é um determinante de Slater de orbitais-spin (como na teoria Hartree-Fock) e de facto não existe função de onda molecular em DFT. Da mesma forma, as energias de orbitais Kohn-Sham não podem ser interpretadas como sendo energias de orbitais moleculares [35].

Não se conhecendo explicitamente o funcional E_{xc}, os métodos DFT existentes assentam em várias aproximações a este termo. É nestas aproximações que se encontram as principais diferenças entre os métodos DFT hoje utilizados, como a aproximação da densidade local (LDA e LSDA) [36, 38] ou a aproximação generalizada de gradiente (GGA) [36, 38].

A utilização dos métodos DFT veio permitir a exploração de sistemas moleculares de dimensões muito maiores do que os permitidos pelos métodos *ab initio*[1], principalmente quando a correlação electrónica desempenha um papel importante na química das espécies envolvidas.

Nos trabalhos apresentados utilizaram-se os métodos DFT implementados no pacote de software GAUSSIAN98 [39], com principal ênfase no método B3LYP [40]. Este é um método híbrido, que combina as aproximações *ab initio* e DFT. Utiliza o potencial de troca de Hartree-Fock e funcionais de troca DFT, nomeadamente o funcional de troca-correlação desenvolvido por Lee et al. [41].

2.5 Algoritmos Genéticos

Os algoritmos genéticos (GA) são uma família de métodos computacionais inspirados pela selecção natural das espécies e pela genética, da qual herdaram, aliás, muita da linguagem e nomenclatura. O conceito de algoritmo genético aparece em 1975 com os estudos de John Holland e colaboradores [42–44]. Estes algoritmos são muitas vezes referidos no contexto mais amplo (e mais controverso) da denominada inteligência artificial [44]. Refira-se, no entanto, que não existe uma definição rigorosa de GA aceite universalmente na comunidade cientifica que permita distinguir os GAs de outros métodos da chamada área da "computação evolucionária". Uma definição geral para GA poderá ser, segundo Michalewicz [43]:

> ..., a GA performs a multi-directional search by maintaining a population of potential solutions and encourages information formation and exchange between these directions. The population undergoes a simulated evolution: at each generation the relatively "good" solutions reproduce, while the relatively "bad" solutions die. To distinguish different solutions we use an objective (evaluation) function which plays the role of an environment.

[1] O método DFT só não é considerado um método *ab initio* devido às aproximações, de natureza empírica, necessárias para calcular o funcional de troca-correlação.

Segundo esta definição o objectivo dos GAs é a procura da solução de um problema através de uma pesquisa multi-direccional. É esta característica que distingue e fortalece os GAs quando comparados com outros algoritmos de optimização. Nesses, o processo de optimização é executado para uma variedade de pontos iniciais na esperança de alcançar a melhor solução. Isto é assim porque para cada um desses pontos iniciais o algoritmo segue uma linha única de optimização até que se atinja o critério de finalização. Os GAs, quando bem formulados e parametrizados, têm a capacidade de "saltar" soluções locais e procurar a solução óptima. Estes algoritmos foram utilizados com sucesso nas mais variadas áreas, tais como: roteamento, calendarização, controlo adaptativo, jogos de computador, modelação cognitiva, problemas de transportes e distribuição, bases de dados, etc.

Os passos gerais da preparação e execução de um GA são:

1. Codificação da informação referente a cada individuo em "genes" sob a forma numérica.
2. Definição da uma função objectivo. Esta define a forma de classificação ("aptidão") dos "genes".
3. Criação da população inicial, com N elementos, través da geração aleatória de "genes".
4. Avaliação de cada um dos genes e ordenação pela sua classificação.
5. Reprodução cruzada dos genes mais aptos (a percentagem de genes utilizados é um parâmetro do GA).
6. Mutação de alguns genes (a percentagem de genes a mutar é um parâmetro do GA).
7. Selecção da nova geração.
8. Iterar a partir do passo nº 4 até que se atinja o critério de convergência ou que se atinja um dado número de iterações.

Existem vários métodos padrão para a realização da reprodução e mutação e selecção [45]. Por vezes, os GAs podem apresentar alguma tendência para ficar presos em "soluções" locais. Nesse caso pode ser necessário alterar os critérios de selecção dos "genes" e tentar novos processos de cruzamento. O processo de mutação e a percentagem de genes a mutar têm também muita influência no desempenho do GA.

Uma baixa percentagem de mutações leva a um maior apuramento dos indivíduos da população mas favorece a estabilização em "soluções locais". Pelo contrário uma alta percentagem de mutação leva a uma maior variabilidade dos indivíduos em detrimento da qualidade dos mesmos. A escolha da melhor taxa de mutação é um processo empírico de tentativa e erro. Verifica-se, no entanto, que valores de percentagem de mutação baixos (até 5%) produzem, em geral, melhores resultados. Existem vários processos padrão de selecção de novas gerações. Estes distinguem-se principalmente no uso ou não de elitismo. Numa selecção com elitismo garante-se que o melhor indivíduo (ou uma certa quantidade destes) de uma dada geração, passa sempre para a nova geração. Desta forma garante-se preservação da informação e do sucesso já alcançado nas gerações anteriores. O elitismo pode, no entanto, levar à estagnação do algoritmo dificultando a procura da tão ambicionada "solução global".

Nos trabalhos apresentados foram utilizados GAs na optimização de uma função analítica para a descrição de uma superfície de energia potencial (PES) obtida por cálculos DFT. Nestes algoritmos cada indivíduo (representado por um gene) consiste num conjunto de parâmetros da função a optimizar. A função objectivo calcula o desvio quadrático médio do gene (para a função de ajuste em utilização) em relação aos valores de energia, obtidos por DFT para as configurações moleculares consideradas. O valor desta grandeza vai servir para medir a aptidão do referido gene para reprodução e para a passagem à próxima geração.

O software utilizado neste processo foi produzido no âmbito do trabalho desta tese com recurso a uma livraria de GAs, GAlib, escrita em C++ por Mathew Wall [45]. Foram testados vários GAs com diferentes esquemas de selecção, reprodução e mutação. A escolha dos algoritmos a utilizar foi baseada em critérios de estabilidade e consistência da convergência dos resultados.

2.6 Programação orientada por objectos em simulação molecular

No mundo do desenvolvimento de software existem vários paradigmas de programação, cada um com as suas vantagens e desvantagens tendo em conta os variados contextos de desenvolvimento. Iremos abordar aqui o paradigma da programação orientada por objectos (object oriented - OO) no contexto da simulação molecular. [46]

A primeira linguagem orientada por objectos foi o SIMULA-67 desenvolvida

por volta de 1960. No entanto, a primeira linguagem a alcançar o estatuto de linguagem OO por excelência foi o Smalltalk desenvolvido na Xerox PARC nos anos 70. Foi também com esta linguagem que o termo "object oriented programming" ganhou notoriedade nas comunidades de desenvolvimento de software. Nos anos 90 a programação por objectos sofreu uma expansão notável, principalmente devido à popularização de linguagens como o C++ [47] e posteriormente o Java. Hoje em dia, a programação por objectos predomina em praticamente todas as áreas, embora o debate sobre as suas vantagens e desvantagens continue [48].

A programação estruturada por objectos (OO) é um paradigma da programação em que se dá mais ênfase aos dados, passando-se os procedimentos para segundo plano. As linguagens OO estão, também, desenhadas de forma a promover a modularidade[2] e a reutilização de código, sempre que possível. Estas duas características permitem, e promovem, o desenvolvimento faseado e em equipa do software, o que é muito importante quando o projecto de trabalho envolve problemas complexos com milhares, ou milhões, de linhas de código.

A abordagem de um dado problema em OO foca as entidades inerentes a esse problema e as relações entre elas. Assim, a primeira fase do desenvolvimento de um programa em OO é a identificação dos componentes desse problema e da forma como eles comunicam entre si. A partir daí, a construção de um programa OO consiste na montagem de um espaço de entidades que se relacionam entre si, tendo cada uma uma tarefa bem definida, inerente às suas características, de forma a produzir o resultado pretendido.

No centro de toda a programação OO temos, portanto, o *objecto*. Este conceito é crucial no paradigma OO, dado que concentra em si todas as características de um modelo de concepção e desenvolvimento de software [48]. Um *objecto* é um módulo computacional, básico e único, correspondente à representação abstracta de uma entidade autónoma sob a forma de:

- Um identificador único;
- Um conjunto de atributos privados (que definem o estado interno do objecto);
- Um conjunto de operações (denominados de *métodos*) cujas funções são principalmente as de alterar o estado interno ou devolver informações, simples ou transformadas, sobre o *objecto*. Estas operações definem o comportamento total do *objecto*.

[2] Agrupamento de pedaços de código inseridos num mesmo contexto.

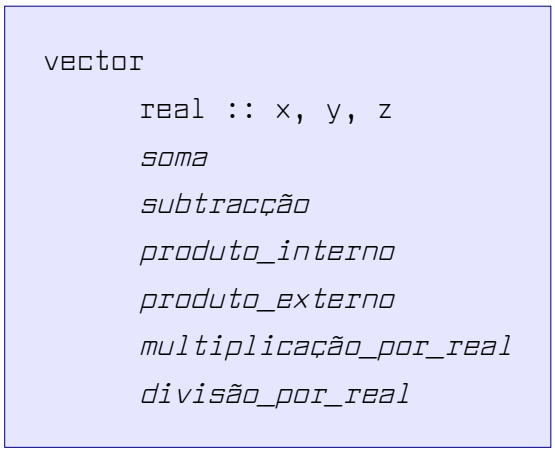

Figura 2.12: Descrição de uma *classe vector* para a representação de vectores num espaço a três dimensões.

Um outro conceito importante é o de *classe*. Uma *classe* é um protótipo de um *objecto*, que pode ser invocado tantas vezes quantas as necessárias para definir novos objectos (pertencentes a essa *classe*). O inicio de um projecto de programação OO consiste essencialmente na definição de classes de objectos.

Como aplicar então a programação OO em simulação molecular? Iremos abordar este assunto, de forma sucinta, com alguns exemplos da construção de classes de objectos para algumas das entidades fundamentais em simulação molecular. A estratégia a seguir desenvolvida tem como objectivo final a construção de uma *classe molécula*, muito simplificada, a partir da qual serão instanciados os objectos-moléculas que irão ser os constituintes fundamentais dos sistemas a simular.

A descrição da posição e velocidade de uma partícula (átomo, ião, molécula, etc) assenta na utilização de vectores num espaço tridimensional. Será portanto necessário definir uma *classe vector*. Cada objecto dessa classe será caracterizado por três elementos do tipo real, x, y e z, que são as coordenadas. Em seguida, teremos de adicionar ao vector métodos que traduzam as operações que se possam querer para esta classe de objectos. Teremos então de definir métodos como a soma e subtracção de vectores, o produto interno e externo, a multiplicação por um escalar, etc. Ficaremos então com uma estrutura, representada esquematicamente na Figura 2.12, de dados e métodos que definem um vector. Essa estrutura pode, em qualquer altura, ser expandida com novas operações, e até elementos, sem que a estrutura anterior (já em funcionamento) seja afectada.

Passaremos agora à definição da classe partícula, representada esquematicamente na Figura 2.13 . Os elementos que definem uma partícula (no contexto da simulação

```
partícula
      vector :: posição
      vector :: velocidade
      vector :: força
      real   :: massa
      real   :: carga
      translação
      rotação_em_torno_de_eixo
```

Figura 2.13: Descrição de uma *classe partícula* com as propriedades e métodos necessários em simulação molecular.

```
molécula
      real :: massa
      real ::centro_de_massa
      array de partícula :: partículas
      translação
      rotação_em_torno_de_eixo
      rotação_em_torno_de_centro_de_massa
```

Figura 2.14: Descrição de uma *classe molécula* com as propriedade e métodos necessários em simulação molecular.

molecular), são a massa, a carga, a posição e a velocidade. Destes, a massa e a carga serão valores do tipo real e a posição e velocidade objectos da *classe vector* já definida. Alguns dos métodos essenciais às partículas serão por exemplo, a translação, rotação em torno de um eixo, etc.

A *classe molécula*, representada esquematicamente na Figura 2.14, irá conter como elementos, a massa, o número de partículas, conjuntos de partículas (denominados de *arrays*) e o centro de massa. Alguns métodos desta *classe* serão a translação, a rotação em torno de um eixo, a rotação em torno de um eixo que passe pelo centro de massa (como caso especial do método anterior), etc.

Como se pode ver, a *classe molécula* é construída sobre as *classes vector* e *partícula* definindo-se automaticamente uma hierarquia de classes. Os métodos das classes mais complexas fazem uso dos métodos das classes suas constituintes. Assim,

ao ser invocado o método translação de uma molécula, vão ser automaticamente accionados os métodos translação de cada uma das partículas que constituem a molécula. Por sua vez, estes irão accionar os métodos de soma com vector dos vectores posição das partículas. A translação de uma molécula, num programa OO, poderá então ser tão simples como "pedir" à molécula que se mova segundo um dado vector de translação.

Com estes exemplos pretendemos ter dado uma ideia de como se pode fazer a aplicação da programação OO em simulação molecular. Richard Sadus, no seu livro *Molecular simulation of Fluids* [14] apresenta uma estratégia de desenvolvimento OO em simulação baseada na linguagem C++. Pedro Rodrigues [49] apresenta também uma estratégia de desenvolvimento OO (programa OMD - *objective molecular dynamics*) direccionando o conceito OO para o desenvolvimento de uma linguagem dirigida para a realização de experiências de simulação molecular (*experiment programing language* - EPL).

Para a realização dos trabalhos apresentados foi desenvolvido um pacote de software essencialmente em Fortran 90/95. Esta não é na realidade uma linguagem OO. No entanto, é possível, através de alguma disciplina na utilização e organização da linguagem, traduzir a maior parte dos conceitos OO para Fortran. A estratégia consiste em utilizar as estruturas de tipos derivados e módulos, existentes nesta linguagem, de forma a mimificar os conceitos de *classe* e *objecto* em OO na mesma linha do que é apresentado no livro de Ed. Akin, "Object-Oriented Programing Via Fortran 90/95" [50]. O pacote de software desenvolvido no âmbito desta tese, implementa o método de MC na simulação de:

- Sistemas simples (partículas):
  - ensembles NVT, NPT e μVT
  - aplicação do método do ensemble de Gibbs
  - integração termodinâmica simples, e acoplada, pelo método Gibbs-Duhem
- Sistemas moleculares:
  - ensemble NVT com moléculas rígidas e flexíveis (pelo método MCCB) com especial ênfase na simulação de interfaces líquido-sólido.
  - aplicação do método do ensemble de Gibbs

O desenvolvimento deste software foi feito em paralelo com os trabalhos de investigação, tendo por isso progredido à medida que se requeriam novas capacidades de simulação. A adopção da estratégia OO, facilitou grandemente o desenvolvimento do software, principalmente no que diz respeito à depuração de erros e implementação progressiva de novas camadas de código, considerando os objectivos a alcançar.

Bibliografia

[1] M. Allen and D. Tildesley: *Computer Simulation of Liquids*, Claredon Press, Oxford, U.K., 1st ed. (1987).

[2] D. Frenkel and B. Smit: *Understanding Molecular Simulations: From Algorithms to Applications*, Academic Press, 2nd ed. (2002).

[3] F. Mandl: *Statistical Physics*, John Wiley & Sons, Ltd, 2nd ed. (1988).

[4] N. Metropolis, A. Rosenbluth, M. Rosenbluth, A. Teller and E. Teller: Equation of state calculations by fast computing machines, *J. Chem. Phys.* 21 (1953) 1087–1092.

[5] A. Z. Panagiotopoulos: Direct determination of phase coexistence properties of fluids by Monte-Carlo simulation in a new ensemble, *Mol. Phys.* 61 (1987) 813–826.

[6] A. Panagiotopoulos, N. Quirke, M. Stapleton and D. Tildesley: Phase-equilibria by simulation in the Gibbs ensemble - alternative derivation, generalization and application to mixture and membrane equilibria, *Mol. Phys.* 63 (1988) 527–545.

[7] H. E. Stanley: *Introduction to Phase Transitions and Critical Phenomena*, Oxford University Press (1971).

[8] M. Mezei: Grand-canonical ensemble Monte Carlo study of dense liquid, *Mol. Phys.* 61 (1987) 565.

[9] D. Boda and K.-Y. C. I. Szalai: Determination of vapour-liquid equilibrium using cavity-biased grand canonical Monte Carlo method, *Mol. Phys.* 92 (1997) 1067.

[10] B. Chen, J. I. Siepmann and M. L. Klein: Direct Gibbs ensemble Monte Carlo simulations for solid-vapor phase equilibria: Applications to Lennard-Jonesium and carbon dioxide, *J. Phys. Chem. B* 105 (2001) 9840.

[11] D. Kofke: Direct evaluation of phase coexistence by molecular simulation via integration along the saturation line, *J. Chem. Phys.* 98 (1993) 4149–4162.

[12] R. Agrawal and D. Kofke: Thermodynamic and structural-properties of model systems at solid-fluid coexistence. 1. fcc and bcc soft spheres, *Mol. Phys.* 85 (1995) 23–42.

[13] R. Agrawal and D. Kofke: Thermodynamic and structural-properties of model systems at solid-fluid coexistence. 2. Melting and sublimation of the Lennard-Jones system, *Mol. Phys.* 85 (1995) 43–59.

[14] R. J. Sadus: *Molecular Simulation of Fluids - Theory, Algorithms and Object-Orientations*, Elsevier Science (2002).

[15] J. J. de Pablo, M. Laso and U. W. Suter: Estimation of the chemical potential of chain molecules by simulation, *J. Chem. Phys.* 96 (1992) 6157.

[16] M. Laso, J. J. de Pablo and U. W. Suter: Simulation of phase equilibria for chain molecules, *J. Chem. Phys.* 97 (1992) 2817.

[17] G. C. A. M. Mooij, D. Frenkel and B. Smit: Direct simulation of phase equilibria of chain molecules, *J. Phys.: Condens. Matter* 4 (1992) L255–L259.

[18] M. N. Rosenbluth and A. W. Rosenbluth: Monte Carlo calculation of the average extention of molecular chains, *J. Chem. Phys.* 23 (1955) 356.

[19] J. Batoulis and K. Kremer: Statistical properties of biased sampling methods for long polimer chains, *J. Phys. A: Math. Gen.* 21 (1988) 127–146.

[20] W. L. Jorgensen: Optimized intermolecular potential functions for liquid alcohols, *J. Phys. Chem.* 90 (1986) 1276–1284.

[21] W. Jorgensen: Intermolecular potential functions and Monte-Carlo simulations for liquid sulfur-compounds, *J. Phys. Chem.* 90 (1986) 6379–6388.

[22] L. A. Girifalco: Interaction potential for carbon (C_{60}) molecules, *J. Phys. Chem.* 95 (1991) 5370.

[23] M. Rigby, E. B. Smith, W. A. Wakeham and G. C. Maitland: *The Forces Between Molecules*, Oxford Science Publications (1986).

[24] J. Hautman and M. L. Klein: Simulation of a monolayer of alkyl thiol chains, *J. Chem. Phys.* 91 (1989) 4994–5001.

[25] I. C. Yeh and M. L. Berkowitz: Structure and dynamics of water at water vertical bar Pt interface as seen by molecular dynamics computer simulation, *J. Electroanal. Chem.* 450 (1998) 313–325.

[26] A. Y. Toukmaji and J. A. B. Jr.: Ewald summation techniques in perspective: a survey, *Comp. Phys. Comm.* 95 (1996) 73–92.

[27] I.-C. Yeh and M. L. Berkowitz: Ewald summation for systems with slab geometry, *J. Chem. Phys.* 111 (1999) 3155–3162.

[28] D. E. Parry: The electrostatic potential in the surface region of an ionic crystal, *Surf. Sci.* 49 (1975) 433.

[29] D. E. Parry: The electrostatic potential in the surface region of an ionic crystal: Errata, *Surf. Sci.* 54 (1976) 195.

[30] D. M. Heyes, M. Barber and J. H. R. Clarke: Molecular dynamics computer simulation of surface properties of crystalline potassium chloride, *J. Chem. Soc. Faraday Trans. II* 73 (1977) 1485.

[31] A. H. Widmann and D. B. Adolf: A comparison of Ewald summation techniques for planar surfaces, *Comp. Phys. Comm.* 107 (1997) 167–186.

[32] A. Bródka and A. Grzybowski: Electrostatic interactions in computer simulations fo a three-dimensional system periodic in two directions: Ewald-type summation, *J. Chem. Phys.* 117 (2002) 8208.

[33] P. Ewald: Die berechnung optischer und elektrostatischer gitterpotentiale, *Ann. Phys.* 64 (1921) 253–87.

[34] P. Hohenberg and W. Kohn: Inhomogeneous electron gas, *Phys. Rev.* 136 (1964) B864.

[35] I. N. Levine: *Quantum Chemistry*, Prentice-Hall, Inc., 4th ed. (1991).

[36] W. Koch and M. C. Holthausen: *A Chemist's Guide to Density Functional Theory*, Wiley-VCH (2001).

[37] W. Kohn and L. J. Sham: Self-consistent equations including exchange and correlation effects, *Phys. Rev.* 140 (1965) A1133.

[38] J. P. Perdew and S. Kurth: *A Primer in Density Functional Theory*, chap. 1. Density Functionals for Non-relativistic Coulomb Systems in the New Century, Spriger-Verlag Berlin Heidelberg (2003) .

[39] M. J. Frisch, G. W. Trucks, H. B. Schlegel, G. E. Scuseria, M. A. Robb, J. R. Cheeseman, V. G. Zakrzewski, J. A. Montgomery, R. E. Stratmann, J. C. Burant, S. Dapprich, J. M. Millam, A. D. Daniels, K. N. Kudin, M. C. Strain, O. Farkas, J. Tomasi, V. Barone, M. Cossi, R. Cammi, B. Mennucci, C. Pomelli, C. Adamo, S. Clifford, J. Ochterski, G. A. Petersson, P. Y. Ayala, Q. Cui, K. Morokuma, D. K. Malick, A. D. Rabuck, K. Raghavachari, J. B. Foresman, J. Cioslowski, J. V. Ortiz, B. B. Stefanov, G. Liu, A. Liashenko, P. Piskorz, I. Komaromi, R. Gomperts, R. L. Martin, D. J. Fox, T. Keith, M. A. Al-Laham, C. Y. Peng, A. Nanayakkara, C. Gonzalez, M. Challacombe, P. M. W. Gill, B. G. Johnson, W. Chen, M. W. Wong, J. L. Andres, M. Head-Gordon, E. S. Replogle and J. A. Pople: *Gaussian 98*, Gaussian Inc., Pittsburgh PA (1998).

[40] A. D. Becke: A new mixing of Hartree-Fock and local density-functional theories, *J. Chem. Phys.* 98 (1993) 1372–1377.

[41] C. Lee, W. Yang and R. G. Parr: Development of the colle-salvetti correlation-energy formula into a functional of the electron-density, *Phys. Rev. B* 37 (1988) 785–789.

[42] D. A. Coley: *An Introduction to Genetic Algorithms for Scientists and Engineers*, World Scientific (1999).

[43] Z. Michalewicz: *Genetic Algorithms + Data Structures = Evolution Programs*, Springer-Verlag, 3rd ed. (1999).

[44] M. Mitchell: *An Introduction to Genetic Algorithms*, MIT Press, Cambridge, MA (1996).

[45] M. Wall: *GAlib - A C++ Library of Genetic Algorithm Components*, Massachusetts Institute of Technology (MIT) (1995), URL `http://lancet.mit.edu/ga/`.

[46] F. Jensen: *Introduction to Computational Chemistry*, John Wiley & Sons (1999).

[47] R. Johnsonbaugh and M. Kalin: *Object-Oriented Programming in C++*, Prentice Hall, Inc. (1995).

[48] F. M. Martins: *Programação Orientada aos Objectos em Java 2*, FCA-Editora de Informática, Lda. (2000).

[49] P. C. R. Rodrigues: *Transições de Fase em sistemas Iónicos, Modelos Teóricos e Simulação Computacional*, Ph.D. thesis, Universidade de Lisboa, Lisboa (2007).

[50] E. Akin: *Object-Oriented Programing Via Fortran 90/95*, Cambridge University Press (2003).

Capítulo 3

Estudo e desenvolvimento de métodos computacionais

Neste capítulo são apresentados, sob a forma de dois artigos, desenvolvimentos metodológicos propostos por nós, os quais complementam os aspectos tratados no capítulo anterior:

- **The starting state in simulations of the fluid-solid coexistence by Gibbs-Duhem integration**
  Fernando M.S. Silva Fernandes, Rui P.S. Fartaria and Filomena F.M. Freitas
  Comp. Phys. Comm. 141 (2001) 403-411

- **A time saving algorithm for the Monte Carlo method of Metropolis**
  Rui P.S. Fartaria, Rodrigo S. Neves, Pedro C.R. Rodrigues, Filomena F.M. Freitas and Fernando M.S. Silva Fernandes
  Comp. Phys. Comm. 175 (2006) 116-121

Comp. Phys. Comm. 141 (2001) 403-411

The starting state in simulations of the fluid-solid coexistence by Gibbs-Duhem integration

Fernando M.S. Silva Fernandes[a,b,1] , Rui P.S. Fartaria[a] and Filomena F.M. Freitas[a,b]

[a] *Department of Chemistry and Biochemistry, Faculty of Sciences, University of Lisbon, Rua Ernesto de Vasconcelos, Bloco C8, 1749-016 Lisboa, Portugal*

[b] *Center of Electrochemistry and Kinetics (CECUL), Faculty of Sciences, University of Lisbon, Rua Ernesto de Vasconcelos, Bloco C8, 1749-016 Lisboa, Portugal*

Abstract

A direct method to determine the starting state in simulations of the fluid-solid coexistence by Gibbs-Duhem integration is presented. It is based on the limiting behaviour of the Gibbs Ensemble vapour-liquid calculations at the lowest temperature range.

The approach estimates the location of the triple point and, from there up, the fluid-solid coexistence properties, at higher temperatures, are calculated by Gibbs-Duhem simulations. The technique is illustrated by tracing the phase diagram of the Lennard-Jones system. The usefulness of the method is discussed in view of our recent study on the phase behaviour of C_{60} [Int. J. Quantum Chem. 84 (2001) 375].

Keywords: Gibbs-Duhem integration, Monte Carlo simulations, Phase Diagram

[1]To whom correspondence should be addressed. E-mail: fsilva@fc.ul.pt

1 Introduction

The major thrust in direct simulation of phase equilibria has been the introduction of the Gibbs Ensemble Monte Carlo method (GEMC) by Panagiotopoulos [1] and Panagiotopoulos et al. [2]. The method enables the direct calculation of the vapour-liquid coexistence properties of pure components and mixtures from a single simulation without need for determining or specifying the chemical potential and pressure. Basically, the technique involves setting up a two-phase thermodynamic system with no physical interface between the two regions and performing the simulation steps (particle displacement, volume rearrangement and particle interchange) according to the acceptance criteria necessary to reach thermodynamic equilibrium. The main limitation of the method is the poor convergence of the averages when dealing with polyatomic molecules and very dense phases. In these cases, successful particle exchanges become rare and phases are slow to equate the chemical potentials. There are a number of techniques to remedy those situations as, for example, the cavity-biased method [3, 4].

The GEMC method, however, can not be used to study fluid-solid coexistence. In fact, mass exchange between the fluid and the solid phase requires the addition or removal of molecules in an otherwise perfect crystal and this would result in the creation of point defects. In order to overcome these limitations, the Gibbs-Duhem Integration method, proposed by Kofke [5] and Agrawal et al. [6, 7], can be used to directly simulate the whole phase diagram of any substance. The method avoids particle exchange. The conditions of coexistence are calculated according to the Gibbs-Duhem equation and simultaneous N,p,T simulations (by Monte Carlo or molecular dynamics) are performed along the coexistence lines.

An important issue in Gibbs-Duhem simulations is the definition of the starting state to initiate the integration of the equation. For the vapour-liquid part of the phase diagram any well defined state obtained by GEMC can be used. For the fluid-solid region Agrawal et al. [6, 7] proposed its determination from the known properties of the soft-sphere potential (SSP), in the limit of high temperature, through the scaled potential:

$$S(r, \lambda) = (1 - \lambda) SSP(r) + \lambda V(r), \tag{1}$$

where λ is a parameter between 0 and 1 and $V(r)$ is the potential of interest. From that point, the other fluid-solid states, at lower temperatures, are determined.

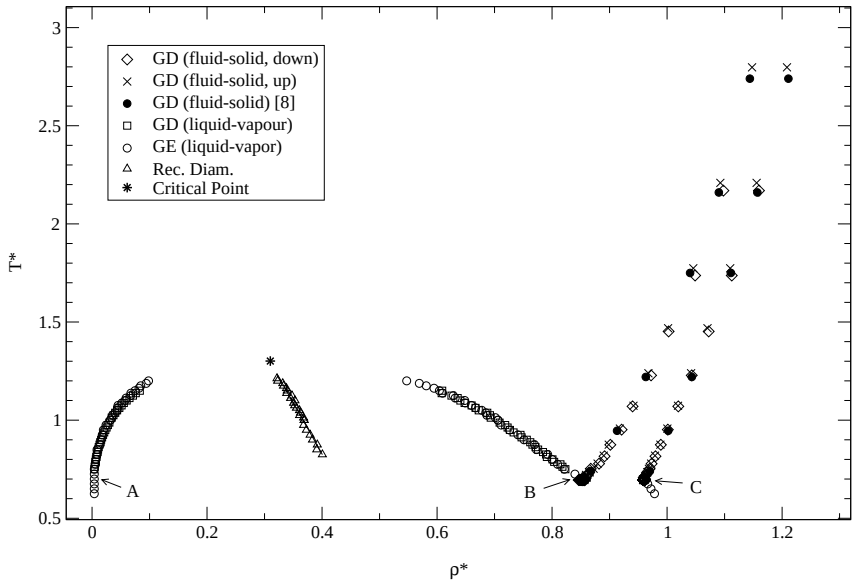

Figure 1: Phase diagram of the Lennard-Jones system.

In this article we suggest an alternative approach. To the best of our knowledge, the technique is new and provides, in a direct and natural way, the location of the triple point. It is based on the limiting behaviour of the GEMC calculations at the lowest temperature range. From that point, the other fluid-solid states, at higher temperatures, are calculated.

In the next section we present the computational details of the method and its application to the phase diagram of the Lennard-Jones system. In Section 3 we discuss the usefulness of the technique in view of our recent study of the phase behaviour of C_{60} [8]. Finally, section 4 contains the conclusions of the present work.

2 Computational details. Phase diagram of the Lennard-Jones system.

The vapour-liquid equilibrium of the Lennard-Jones system was calculated by GEMC and Gibbs-Duhem Integration Monte Carlo (GDMC) methods using the procedures described in the original articles referred to in the previous section. The temperature-density results are plotted in Figure 1 and quoted as "GE" or "GD" respectively for GEMC or GDMC calculations. The critical temperature and density were estimated by fitting the results to the laws of rectilinear diameters and order

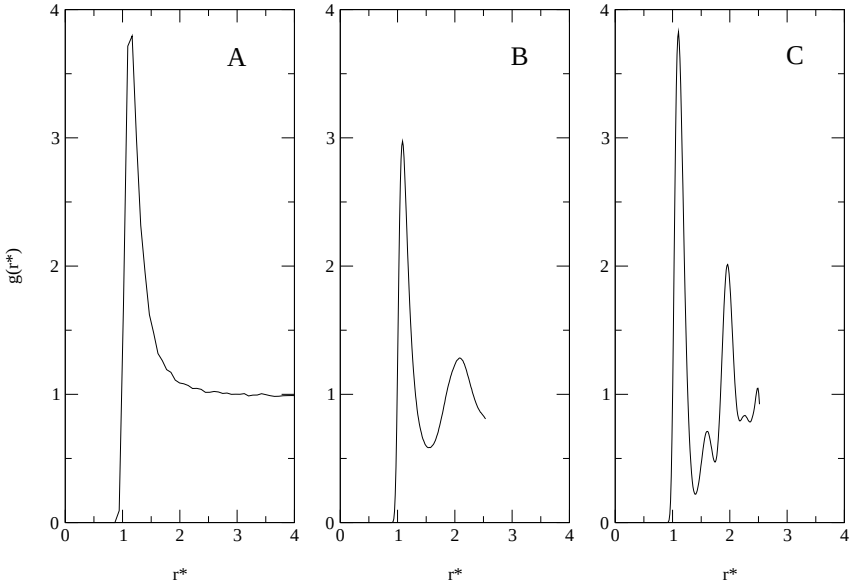

Figure 2: Radial distribution functions of the Lennard-Jones system at the triple point.

parameter scaling [9] with a critical exponent β=0.33. The pressures were fitted to the Clausius-Clapeyron equation.

The potential was truncated at half of the boxes lengths with application of long-range corrections and cubic periodic boundary conditions. Reduced units were used throughout.

If the temperature of the vapour-liquid equilibrium is successively decreased by small steps, when it reaches a value beteween 0.70 and 0.68, the liquid phase is not stable anymore. The system readily assumes a vapour-solid configuration, that is to say, spontaneous freezing is detected in the high-density box. This can be observed in Figure 1 (note the circles below the line A-B-C). That value of temperature, the densities and configurational energies (just before and after freezing) and the vapour pressure are taken as an estimate of the triple point properties. The corresponding vapor, liquid and solid phases are marked, in Figure 1, as A, B and C respectively. Figure 2 shows the radial distribution functions, that seem to support our procedure. From that point we calculated, by GDMC, the other fluid-solid sates at higher temperatures. They are quoted as "GD(up)" in Figure 1. The points quoted as "GD(down)" were obtained using Agrawal et al. [6, 7] procedure from the limit of high temperature. The accordance of the results calculated by the two different paths is excellent. The relevant numerical details of the calculations are presented

ahead.

We must emphasize that the present approach does not mean that the fluid-solid equilibrium can be properly simulated by GEMC. Indeed, what we are only stating is that the Gibbs Ensemble method is able to detect a singular point below which the liquid phase is not stable. Thus the circles bellow the line A-B-C in Figure 1, that were determined by GEMC, must not be understood as corresponding to exact vapour-solid states. In fact they were calculated just to check out that the liquid phase is not stable bellow that line. It is essential that the decreasing of temperature in the region of the triple point be conducted in small steps. In the present study $\Delta T \approx 0.01$. That point can also be detected from the vapour-liquid GDMC calculations. However, a smaller ΔT than in the case of GEMC is required.

It could seem that the present approach should not work in general not being, therefore, very reliable. Indeed, if the temperature is successively decreased towards the triple point we can observe spontaneous freezing in the high-density box below a certain temperature. However, it may be argued that this does not happen at coexistence, but at a supercooling that is large enough to see crystallization during the simulations. What then results is a system with in one box a dilute vapour and, in the other, a defect-rich solid. If so, the method will not generate a solid phase really representative of the equilibrium solid so that the contributions of grain-boundaries, dislocations and vacancies to the solid free-energy are negligible.

In what follows, we suggest that, by the present approach, spontaneous freezing occurs in a very narrow interval of temperatures and the generated solid is not defect-rich, if the conditions of the next algorithm are fulfilled:

a) Set up the vapour-liquid experiment at a temperature, T_i, greater than the triple point temperature, say 0.75 for the Lennard-Jones system. The starting configuration in each box is a face-centred-cubic lattice with the right number of particles ($4uc^3$; uc is the number of unit cells per dimension) and the appropriate densities.

b) Run n (N,V,T) cycles without rearrangement of volumes and exchange of particles, just to destroy the lattices.

c) Run ne (GEMC) equilibration cycles from the last configurations of the previous run.

d) Run *np* (GEMC) production cycles from the last configurations of the previous run. Calculate final average values.

e) Using the equilibrium densities of the previous run, start a new experiment, at temperature T_i-ΔT, with perfect lattices in each box.

f) Repeat steps b) - e)

In the present study, a GEMC cycle consisted of a displacement of each molecule taken sequentially, one rearrangement of volume and a certain number (120-250) of particle interchange attempts. The maximum displacements for particles and volume were adjusted for a rate of acceptance of ∼50%

The algorithm above ensures that the number of particles in each box, although fluctuating, is maintained near the ones of the starting configurations. Thus, we get similar statistics for both phases.

We carried out calculations with 216 and 512 molecules (the starting configurations were always perfect lattices with, respectively, 108 and 256 molecules in each box) varying ΔT, *n* (*N,V,T*), *ne* (GEMC) and *np* (GEMC). The results are practically number independent and we have chosen ΔT= 0.005 - 0.01, *n* (*N,V,T*) = 5000 - 10000, *ne* (GEMC) = 10000 and *np* (GEMC) = 20000.

Table 1 displays some raw data obtained with 512 molecules and $\Delta T = 0.01$. Table 2 shows the results for the same number of molecules and $\Delta T = 0.005$.

Spontaneous freezing is observed for temperatures between 0.70 and 0.69, with $\Delta T = 0.01$. It happens between 0.685 and 0.68, with $\Delta T = 0.005$. Thus, we estimate the triple point temperature between 0.68 and 0.70, within an interval of 0.02, that is the maximum error usually reported for that temperature.

The vapour pressures, densities and configurational energies, just before and after freezing, agree very well, for both cases, within the root mean square deviations.

It is also worth mentioning that after spontaneous freezing the solid phase reached the same number of molecules as the perfect lattice (256). Of course, it rests to be seen whether or not the solid is defect-rich. This can be analysed, for example, either by direct inspection of snapshots or by integrating the radial distribution functions over different coordination shells. Table 3 shows the integration of the triple point solid radial distribution function at different minima. The numbers of particles within successive shells are in excellent agreement with the ones of a face-centred-cubic lattice. Figure 3 displays the radial distribution function of the

Table 1: Lennard-Jones system: reduced configurational energies (u), pressures (p), densities (ρ) and number of particles (N) for the vapour-liquid and vapour-solid at different temperatures with $\Delta T = 0.01$. Spontaneous freezing is observed for temperatures between 0.70 and 0.69. The numbers in parentheses are r.m.s. deviations over the entire production runs, so 5.9080 (0959) means 5.9080± 0.0959.

T	$-u$	p	ρ	N
0.75	0.0395 (0094)	0.0025 (0001)	0.0035 (0001)	294.92 (7.72)
	5.9080 (0959)	0.0022 (3132)	0.8214 (0123)	217.08 (7.72)
0.74	0.0408 (0102)	0.0025 (0001)	0.0035 (0001)	261.97 (7.64)
	5.9602 (0922)	-0.0002 (2928)	0.8273 (0120)	250.03 (7.64)
0.73	0.0369 (0105)	0.0022 (0001)	0.0032 (0001)	228.19 (5.80)
	6.0091 (0862)	0.0059 (2782)	0.8331 (0116)	283.81 (5.80)
0.72	0.0319 (0101)	0.0019 (0001)	0.0027 (0001)	215.60 (4.47)
	6.0225 (0805)	0.0025 (2741)	0.8346 (0108)	296.40 (4.47)
0.71	0.0301 (0091)	0.0017 (0001)	0.0025 (0001)	239.99 (7.17)
	6.0611 (0778)	-0.0017 (2836)	0.8387 (0104)	272.01 (7.17)
0.70	0.0260 (0091)	0.0015 (0001)	0.0021 (0002)	218.68 (16.99)
	6.1087 (0775)	-0.0026 (2759)	0.8441 (0103)	293.32 (16.99)
0.69	0.0263 (0082)	0.0014 (0001)	0.0021 (0001)	256.03 (0.20)
	7.2867 (0705)	0.0025 (3670)	0.9634 (0093)	255.97 (0.20)

solid, at triple point, compared with the one obtained by an independent canonical molecular dynamics run at the same temperature and density. Finally, Figures 4 and 5 show snapshots of the liquid and solid just before and after spontaneous freezing. The snapshots were obtained by projecting the molecules onto the x-y plane. In view of the present results it appears that the generated solid is not defect-rich.

The final triple point properties were assessed by fitting the raw data and intercepting the extention of the vapour-liquid line with the freezing line. The pressure lines are displayed in Figure 6.

The agreement of our results with the ones reported by Agrawal et al. [7], for the Lennard-Jones system, is excellent. A comparison of the triple point and critical properties is presented in Table 4.

Table 2: Lennard-Jones system: reduced configurational energies (u), pressures (p), densities (ρ) and number of particles (N) for the vapour-liquid and vapour-solid at different temperatures with $\Delta T = 0.005$. Spontaneous freezing is observed for temperatures between 0.685 and 0.68. The numbers in parentheses are r.m.s. deviations over the entire production runs, so 0.0260 (0091) means 0.0260±0.0091.

T	$-u$	p	ρ	N
0.70	0.0260 (0091)	0.0015 (0001)	0.0021 (0002)	218.68 (16.99)
	6.1087 (0775)	-0.0026 (2759)	0.8441 (0103)	293.32 (16.99)
0.695	0.0265 (0083)	0.0015 (0001)	0.0022 (0001)	257.16 (5.82)
	6.1307 (0790)	-0.0058 (2939)	0.8462 (0106)	254.84 (5.82)
0.6925	0.0256 (0084)	0.0014 (0001)	0.0021 (0001)	248.90 (5.65)
	6.1402 (0852)	-0.0020 (2904)	0.8474 (0112)	263.10 (5.65)
0.69	0.0242 (0083)	0.0013 (0001)	0.0019 (0001)	238.64 (5.55)
	6.1528 (0853)	0.0082 (2864)	0.8490 (0101)	273.36 (5.55)
0.685	0.0221 (0078)	0.0012 (0001)	0.0018 (0001)	239.01 (9.04)
	6.1814 (0812)	-0.0014 (2841)	0.8519 (0106)	272.98 (9.04)
0.68	0.0222 (0076)	0.0012 (0001)	0.0018 (0001)	256.02 (0.14)
	7.3104 (0719)	0.0123 (3654)	0.9663 (0094)	255.98 (0.14)

Table 3: Integration of the solid radial distribution function at triple point for Lennard-Jones: minima distances (r^*), calculated number of particles (n') and number of particles for a perfect lattice ($n_{f.c.c}$).

r^*	n'	$n_{f.c.c}$
1.398	12.07	12
1.752	17.89	18
2.169	43.48	42
2.362	53.23	54
2.748	80.78	78

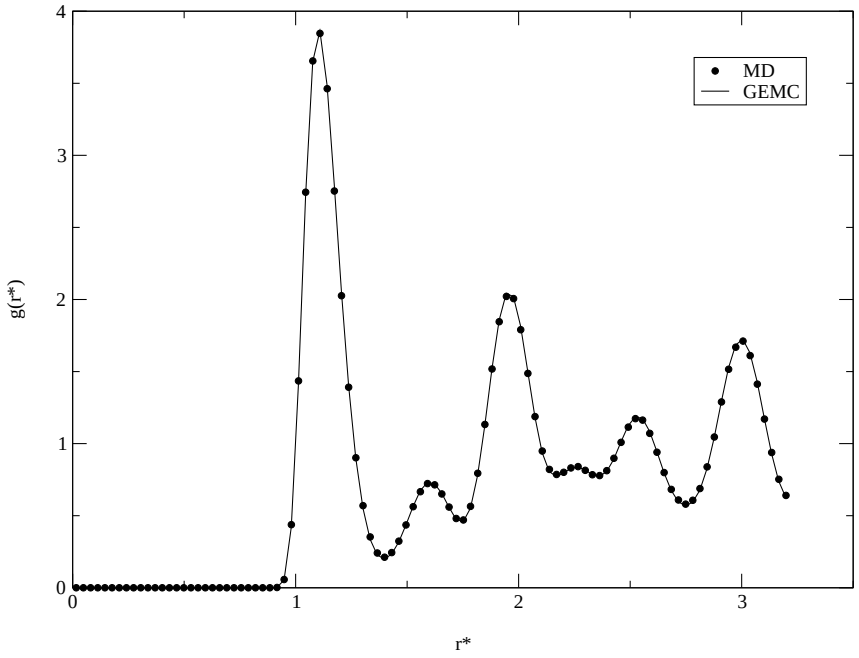

Figure 3: Lennard-Jones system: radial distribution function of the solid at triple point (T^*=0.69, ρ^* =0.96) by GEMC and MD.

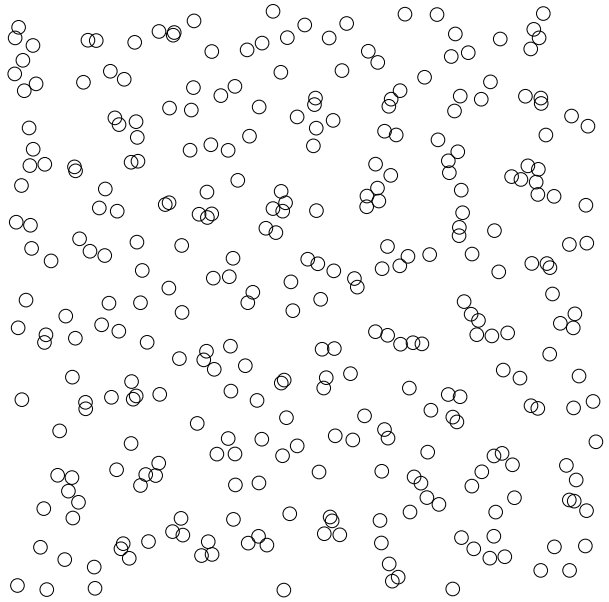

Figure 4: Lennard-Jones system: snapshot of liquid before spontaneous freezing (T^* = 0.7).

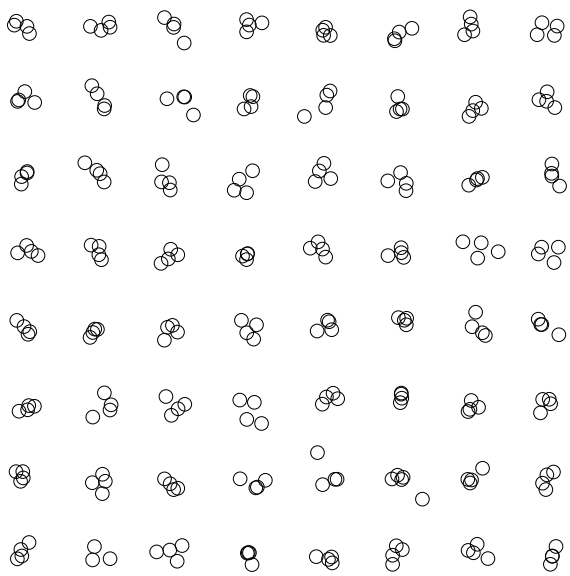

Figure 5: Lennard-Jones system: snapshot of solid after spontaneous freezing (T^* = 0.69).

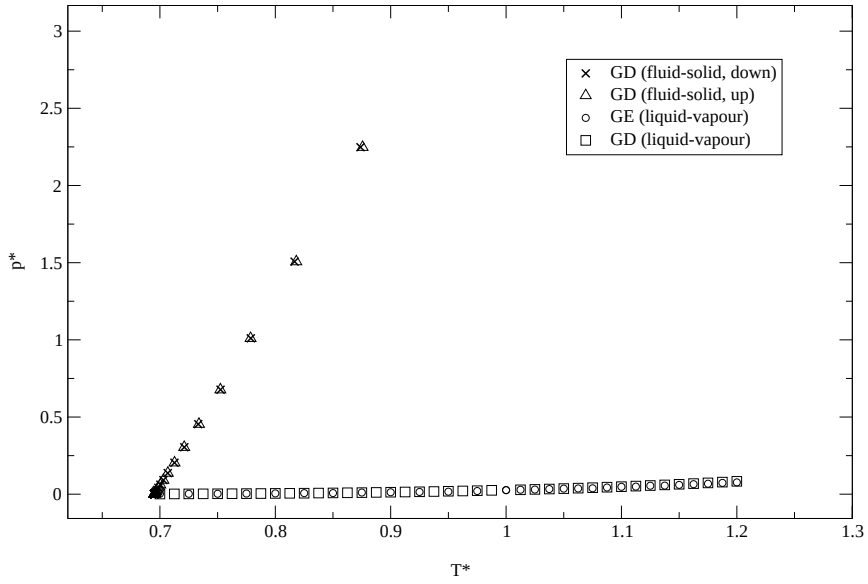

Figure 6: Pressure as a funtion of temperature for the vapour-liquid and fluid-solid coexistence of the Lennard-Jones system.

Table 4: Lennard-Jones system: estimates for some reduced critical and triple point properties.

	T_c	ρ_c	p_c
GE	1.301±0.003	0.309±0.010	0.118±0.001
GD	1.300±0.004	0.316±0.005	0.124±0.001
ref. [5]	1.321±0.004	0.306±0.001	—
	T_{tr}	$\rho_{l,tr}$	p_{tr}
GD (down)	0.690±0.002	0.850±0.003	0.001±0.002
GD (up)	0.690±0.001	0.850±0.002	0.001±0.001
ref. [7]	0.687±0.004	0.850	0.0011

3 Phase behaviour of C_{60}

Recently, we have studied the phase behaviour of C_{60} [8] using a first-principles interaction potential [10]. The works of Hagen et al [11] and Cheng et al. [12] gave rise to a controversial question on the existence of a stable liquid phase for C_{60}. Until our study, the simulation results clearly showed two types of behaviours. Either no triple point was predicted or a triple point was estimated, but a liquid phase remained below it. This contrasts with the theoretical calculations from Hypernetted Mean Spherical Approximation [12] and modified hypernetted chain theory [13] where a conventional triple point is defined below which a liquid phase is not observed. The existence of a stable liquid phase below the triple point is, of course, against the basic concepts of thermodynamics.

In our study, after establishing the thermodynamic stability of the vapour-liquid equilibrium, we performed simulations of the fluid-solid equilibrium, by GDMC, following two different paths as done, in the previous section, for the Lennard-Jones system. For C_{60}, however, the results from the two paths differ significantly. Indeed, the freezing line obtained by the method of Agrawal et al. [6, 7], from the limit of high temperature, intercepts the vapour-liquid line below the critical point, but a stable liquid phase remains below the crossing point. On the contrary, the freezing line calculated by the present method, from the limit of low temperature, starts from a point below which the liquid phase is not stable, predicting a conventional triple point in accordance with the theoretical methods and the basic concepts of thermodynamics.

We detected spontaneous freezing between the temperatures 1570 and 1560 K. The data was analysed by the same procedures as for the Lennard-Jones system.

Table 5: Integration of the solid radial distribution function at triple point for C_{60}: minima distances (r^*), calculated number of particles (n') and number of particles for a perfect lattice ($n_{f.c.c}$).

r^*	n'	$n_{f.c.c}$
1.321	11.9955	12
1.704	17.9957	18
2.037	41.9856	42
2.286	53.9818	54
2.569	78.2952	78

Table 5 presents the integration of the solid radial distribution function at triple point. Figures 7 and 8 show snapshots of the liquid and solid just before and after spontaneous freezing.

Although the results from the two different paths are consistent, we suggested [8] that the calculations starting from the limit of high temperature were constrained to a metastable fluid-solid region of phase space.

The phase behaviour of C_{60} is presumably due to the heavy short range nature of the potential models used [14] as well as to the probed high temperature range.

4 Conclusions

We have presented a direct method to determine the starting state in simulations of the fluid-solid coexistence by Gibbs-Duhem integration. It is based on the limiting behaviour of the Gibbs Ensemble vapour-liquid calculations at the lowest temperature range.

The approach estimates the location of the triple point and, from there up, the fluid-solid coexistence properties, at higher temperatures, are calculated by Gibbs-Duhem simulations. The vapour-solid coexistence properties can also be calculated from that point by decreasing the temperature. The technique was illustrated by tracing part of the phase diagram of the Lennard-Jones system. The results are in excellent agreement with the ones obtained by Agrawal et al. [7]. Thus, it constitutes a possible alternative way to circumvent one of the limitations of the Gibbs-Duhem scheme to trace coexistence curves.

The usefulness of the method was demonstrated by its recent application to C_{60} [8]. In fact, it has enabled to resolve an ambiguity on the phase behaviour of

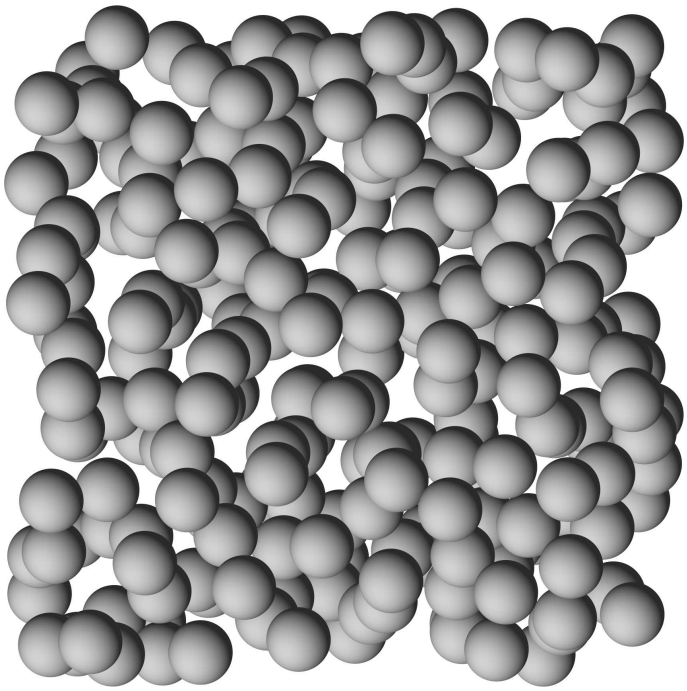

Figure 7: Snapshot of liquid C_{60} before spontaneous freezing ($T \approx 1570$K).

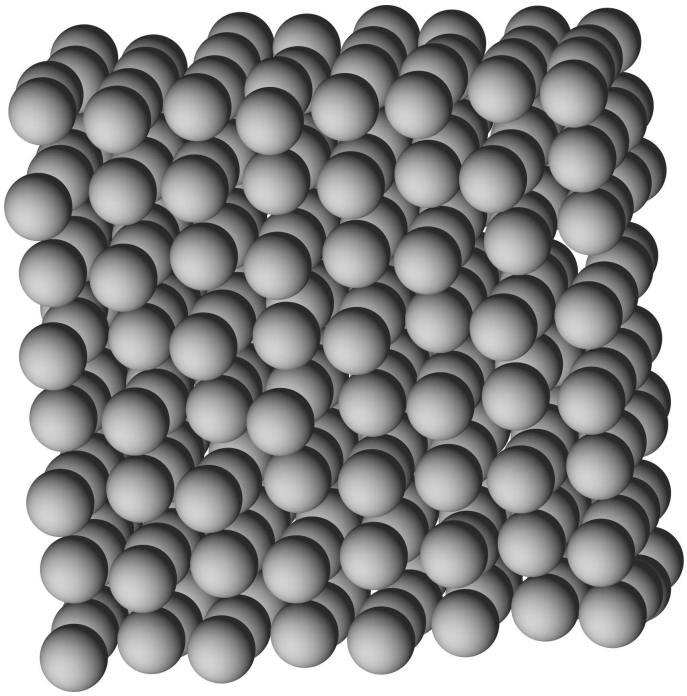

Figure 8: Snapshot of solid C_{60} after spontaneous freezing ($T \approx 1560$K).

that substance.

It would be important to apply the present technique to other molecular systems. Some years ago, we studied the vapour-liquid equilibrium of methyl chloride and iodide [15,16]. Of course, for those systems, when the triple point is approached, the successful particle exchanges become rare and some smarter Monte Carlo methods have to be used. Work along these lines is in progress.

Acknowledgements

Two of us (F. Fernandes and F. Freitas) thank Fundação para a Ciência e Tecnologia (FCT) for financial support. The Computing Services at Faculty of Sciences, University of Lisboa, are also gratefully acknowledged for the allocation of computational resources.

References

[1] A. Z. Panagiotopoulos: Direct determination of phase coexistence properties of fluids by Monte-Carlo simulation in a new ensemble, *Mol. Phys.* 61 (1987) 813–826.

[2] A. Panagiotopoulos, N. Quirke, M. Stapleton and D. Tildesley: Phase-equilibria by simulation in the Gibbs ensemble - alternative derivation, generalization and application to mixture and membrane equilibria, *Mol. Phys.* 63 (1988) 527–545.

[3] M. Mezei: Grand-canonical ensemble Monte Carlo study of dense liquid, *Mol. Phys.* 61 (1987) 565.

[4] D. Boda and K.-Y. C. I. Szalai: Determination of vapour-liquid equilibrium using cavity-biased grand canonical Monte Carlo method, *Mol. Phys.* 92 (1997) 1067.

[5] D. Kofke: Direct evaluation of phase coexistence by molecular simulation via integration along the saturation line, *J. Chem. Phys.* 98 (1993) 4149–4162.

[6] R. Agrawal and D. Kofke: Thermodynamic and structural-properties of model systems at solid-fluid coexistence. 1. fcc and bcc soft spheres, *Mol. Phys.* 85 (1995) 23–42.

[7] R. Agrawal and D. Kofke: Thermodynamic and structural-properties of model systems at solid-fluid coexistence. 2. Melting and sublimation of the Lennard-Jones system, *Mol. Phys.* 85 (1995) 43–59.

[8] R. P. S. Fartaria, F. M. S. S. Fernandes, F. F. M. Freitas and P. C. R. Rodrigues: Phase behavior of C_{60} by computer simulation using ab-initio interaction potential, *Int. J. Quantum Chem.* 84 (2001) 375.

[9] H. E. Stanley: *Introduction to Phase Transitions and Critical Phenomena*, Oxford University Press (1971).

[10] J. M. Pacheco and J. P. P. Ramalho: First-principles determination of the dispersion interaction between fullerenes and their intermolecular potential, *Phys. Rev. Lett.* 79 (1997) 3873.

[11] M. H. J. Hagen, E. J. Meijer, G. C. A. M. Mooij, D. Frenkel and H. N. W. Lekkerkerker: Does C_{60} have a liquid phase?, *Lett. to Nature* 365 (1993) 425.

[12] A. Cheng, M. Klein and C. Caccamo: Prediction of the phase diagram of rigid C_{60} molecules, *Phys. Rev. Lett.* 71 (1993) 1200–1203.

[13] C. Caccamo: Modified-Hypernetted-Chain determination of the phase diagram of rigid C_{60} molecules, *Phys. Rev. B* 51 (1995) 3387–3390.

[14] N. W. Ashcroft: Elusive diffusive liquids, *Nature* 365 (1993) 387.

[15] F. F. M. Freitas and F. M. S. S. Fernandes: in F. Bernardi and J.-L. Rivail (eds.), *Conference proceedings: ECCC1 Computational Chemistry*, 330, American Institute of Physics (1995) page 305.

[16] F. F. M. Freitas, F. M. S. S. Fernandes and B. J. C. Cabral: Vapor-liquid-equilibrium and structure of methyl-iodide liquid, *J. Phys. Chem.* 99 (1995) 5180–5186.

Comp. Phys. Comm. 175 (2006) 116-121

A time saving algorithm for the Monte Carlo method of Metropolis

Rui P.S. Fartaria[a], Rodrigo S. Neves[b], Pedro C.R. Rodrigues[a], Filomena F.M. Freitas[a] and Fernando M.S. Silva Fernandes[a,1]

[a] *Laboratory of Molecular Simulation, Department of Chemistry and Biochemistry, Faculty of Sciences, University of Lisboa, Rua Ernesto de Vasconcelos, Bloco C8, 1749-016 Lisboa, Portugal*

[b] *Instituto de Química de São Carlos, Universidade de São Paulo, Av. do Trabalhador Sancarlense, CP 780, 13560-970 São Carlos-SP, Brazil*

Abstract

A time saving algorithm for the Monte Carlo method of Metropolis is presented. The technique is tested with different potential models and number of particles. The coupling of the method with neighbour lists, linked lists, Ewald sum and reaction field techniques is also analysed. It is shown that the proposed algorithm is particularly suitable for computationally heavy intermolecular potentials.

PACS: 02.50.Tt; 07.05.Tp

Keywords: Monte Carlo, algorithms, molecular simulation

[1]Corresponding author, e-mail: fsilva@fc.ul.pt

1 Introduction

Since the beginning of computer simulation in statistical mechanics, by Monte Carlo and molecular dynamics, it is clear that one of the main operational issues has been the optimization of the computing time spent in the loops for calculating the energy and forces.

From programming in machine language in the initial period [1] to the use of computational tricks, taking advantage of smarter compilers, and of vector or massive parallel computers [2,3], researchers have always looked for the best algorithms to get their results in the shortest time possible. This is important, as the complexity of the systems analyzed by computer simulation increases constantly, requiring runs that cover considerable space and time scales.

Presently, many research groups rely on dedicated stations or PC farms instead of mainframe computers. Now that the memory capacity and processor speed of one PC are many orders of magnitude greater than the ones of old mainframe computers (for example, the famous CDC 7600) an important question is how to get the best performance of such an ubiquitous laboratory tool, in particular within the field of statistical mechanics.

The objective of this paper is to present an algorithm for the Monte Carlo method of Metropolis [4], particularly suitable for computationally heavy intermolecular potentials. The technique is applied to different potential models and number of particles. The coupling of the method with neighbour lists, linked lists, Ewald sum and reaction field techniques is also analysed. The programs were all written in Fortran 90 and were compiled with the Intel Fortran Compiler, Version 8.1 for Linux, with options for optimization and strong inlining of subroutines. The computers used were PC's with "AMD® Athlon XP 1600+" processors and "Intel® P4" processors. Section 2 contains the definition of the algorithm and its behavior. The applications to different potential models and the concluding remarks are presented in section 3.

2 Algorithm

2.1 Definition

In the standard Monte Carlo - Metropolis algorithm (Figure 1) one has to evaluate, in each step, the energy of the "old" and "trial" configurations. The technique presented here aims at speeding up the MC process by reducing the time consumed in the

$E_{old} \leftarrow$ Calculate energy
Build trial configuration
$E_{trial} \leftarrow$ Calculate energy
$\Delta E \leftarrow E_{trial} - E_{old}$

ran() returns a random uniform number between 0 and 1.
if (exp($-\beta\Delta E$) > ran()) **then**
    Accept trial configuration
else
    Reject trial configuration
end if

Figure 1: Algorithm for a standard Monte Carlo step.

energy calculation of the "old" configuration, ideally to "zero", when compared with the time spent on the calculation of the "trial" configuration energy. If accomplished, this means that the updated MC algorithm should be, at its maximum efficiency, two times faster. Somewhere in the standard simulation we have to calculate the energy of the "old" configuration. It is possible, however, to save this energy so that when we need it again one just have to "ask for it". Will it be efficient doing this with a Desktop PC, regarding the memory requirements for this operation?

The "energy saving" operation is, thus, the main issue in the implementation of this idea. We propose using the structure, called "energy-repository" (ER), depicted in Figure 2. This structure can be built as a vector of vectors of diferent sizes or with one indexed vector. The elements of ER will keep track of all pair-energies in the system, so that at any point in the simulation one can simply retrieve the energy of the present ("old") configuration, or even of a particle ("particle" means "atom" or "molecule") of the system, by summing over the required pairs. This should be, for almost all interaction potentials, a much lighter task than evaluating the energy by the usual way. The standard MC algorithm was modified to use this structure and the new one is presented in Figure 3. This algorithm assumes that the ER was already correctly filled with the initial values for the pair-energies of the system. The crucial operations in this scheme are the creation of the vector V_{trial}, which

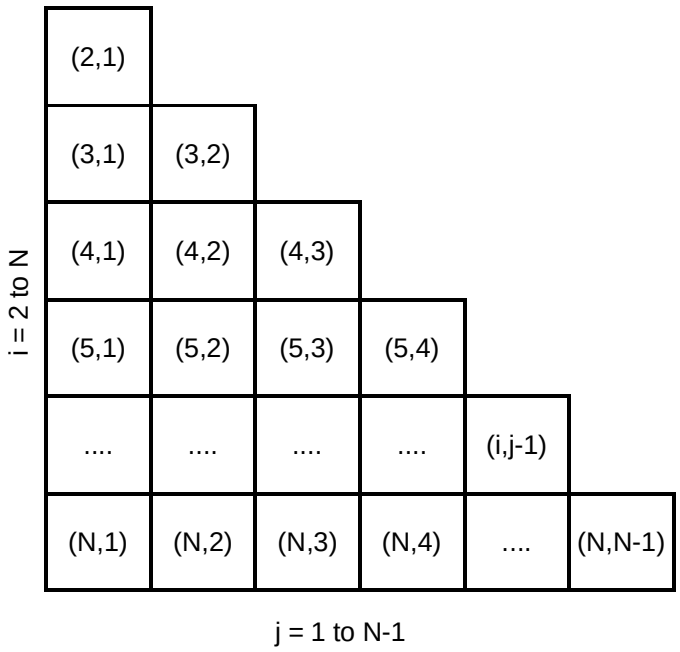

Figure 2: The vector-based structure named energy-repository (ER).

holds the pair-energies for the "trial" configuration, and the registration of the trial values from V_{trial} into the ER structure when the trial configuration is accepted. The implementation of this scheme shall prove to be a simple task in the majority of Monte Carlo software.

The memory requirements for the energy-repository structure, assuming that it only keeps the energy-pairs (it could also keep the virial-pairs), in double precision, is given by

$$M(N)/\text{MB} = \frac{1}{2}N(N-1) * 8/1024^2 \tag{1}$$

where $M\,(N)$ is the used memory in MB and N is the number of particles of the system. The plot in Figure 4 represents the memory used by ER as a function of the number of particles. Thus, a usual Desktop PC with a memory of 512 MB RAM can easily hold a system with 10000 particles.

2.2 Behavior

Let us now analyse the efficiency of this scheme as a function of the number of particles, the weight of the interaction potential and the existence, or not, of a cutoff for the pair distances ($rcut$). To this end model functions are constructed and used to interpret the values obtained experimentally.

Assuming that the energy-repository (ER) is already built.

$E_{old} \leftarrow$ Retrieve energy from ER
Build trial configuration
$V_{trial}[\,] \leftarrow$ Calculate energy pairs
$E_{trial} \leftarrow$ Sum over V_{trial} elements
$\Delta E \leftarrow E_{trial} - E_{old}$

ran() returns a random uniform number between 0 and 1.
if (exp($-\beta\Delta E$) > ran()) **then**
    Accept trial configuration
    Regist V_{trial} elements on the ER
else
    Reject trial configuration
end if

Figure 3: Algorithm for the modified Monte Carlo step using the energy-repository (ER) structure.

The time for a standard MC cycle[2] (ST) should be (apart from minor approximations) given by

$$t_{\mathrm{cycle,ST}} = 2N \cdot (N \cdot t_{\mathrm{rij}} + n_{\mathrm{rcut}} \cdot t) \tag{2}$$

where N is the number of particles in the system, t_{rij} is the time taken to calculate a pair distance (with periodic boundary conditions), n_{rcut} is the number of molecules inside the cutoff sphere, and t_{pot} is the time taken to calculate the interaction potential. The time for a MC cycle using ER should then be given by

$$t_{\mathrm{cycle,ER}} = N \cdot (N \cdot t_{\mathrm{rij}} + n_{\mathrm{rcut}} \cdot t_{\mathrm{pot}} + N \cdot \alpha \cdot t_{\mathrm{acc}}) \tag{3}$$

where t_{acc} is the time taken to access the ER structure when getting old energy pairs or registering the new ones and α is a parameter related to the number of

[2]In the present calculations one cycle corresponds to a trial move of every particle taken sequentially.

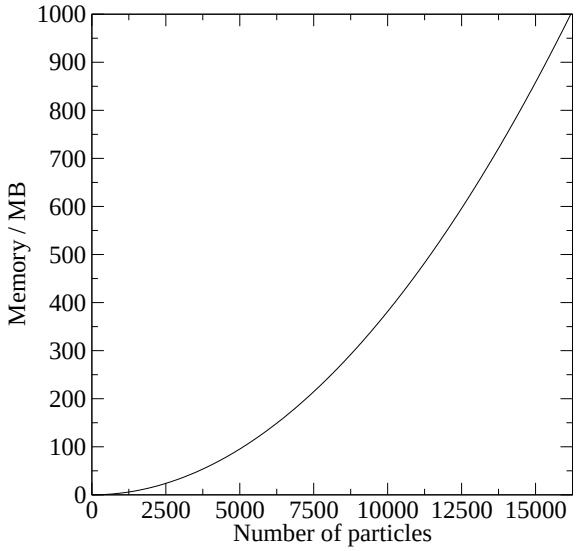

Figure 4: Memory used by the energy-repository as a function of the number of particles.

times that the operation of reading or registering pairs is performed in a step. Thus, the efficiency of ER is evaluated by the ratio

$$\text{ratio} = \frac{t_{\text{cycle,ER}}}{t_{\text{cycle,ST}}} \tag{4}$$

which, in the ideal situation when $t_{\text{acc}} \to 0$ (compared with t_{pot}), will have the value ~ 0.5.

The experimental times were calculated by performing MC simulations in the NVT ensemble for the Lennard-Jones system, with and without ER, using different number of particles and potential weights. They are presented in Table 1. The calculational weight of the potential was increased by adding, to the Lennard-Jones potential, the function

$$\begin{cases} f_1\left(r_{ij}\right) = \exp\left(-20 r_{ij}^2\right) \\ f_{n_{\text{expo}}+1}\left(r_{ij}\right) = \exp\left(f_{n_{\text{expo}}}\left(r_{ij}\right) - 30\right) \end{cases} \tag{5}$$

where r_{ij} is the reduced distance between particles and n_{expo} is the number of exponential functions. As the values of this function are always of the order of 10^{-14} it does not affect the simulation results for the system physical properties, but only the computing time. These simulations were performed at reduced temperature $T^* = 2.0$ and density $\rho^* = 0.65$ with $r_{\text{cut}} = 2.74$ (which implies $n_{\text{rcut}} \sim 56$). It should be noted that the time for calculating the potential in the equations is $t_{\text{pot}} = t_{\text{LJ}} + n_{\text{expo}} t_{\text{expo}}$

Table 1: Time ratios (equation (4)) calculated for a Lennard-Jones system when using (**values in bold**), or not, a cutoff on the potential. N is the number of particles and n_{expo} is the number of exponentials in equation (5).

	N		
n_{expo}	256	1372	4000
0	**0.84**	**1.08**	**2.94**
	0.80	0.92	2.19
5	**0.65**	**0.92**	**2.53**
	0.54	0.56	0.73
10	**0.58**	**0.85**	**2.33**
	0.52	0.54	0.65
20	**0.55**	**0.76**	**2.18**
	0.51	0.50	0.55

where t_{LJ} is the time for computing the LJ potential and t_{expo} is the time to compute one exponential.

The general behaviour of the energy-repository efficiency can be assessed through the analysis of equation (4) as a function of the number of particles, N, and the weight of the potential, t_{pot}, when using, or not, a cutoff on the potential. One should bear in mind that in equations (2) and (3) the parameter t_{rij} is independent of N, but the access time for the ER memory, t_{acc}, is not. When N is small (<2000 in our computers) the memory used by the ER is such that it allows the processor to have a very efficient access to it, but when N becomes larger the memory access efficiency is reduced and so is the ER efficiency in time saving.

When not using a cutoff the potential is always calculated for all pairs in the system and so the ratio should rapidly approach 0.5 as the calculational weight of the potential increases, and it should barely change with the increase of the number of particles. When using a cutoff the ER efficiency is drastically reduced as the potential is only computed for the pairs inside the sphere of radius r_{cut}. In this case the effect of the weight of the potential is heavily reduced and the ratio rapidly increases with the number of particles as more pairs are left out of the cutoff sphere but the same amount of ER memory (as in the case of no cutoff) is probed. This interpretation is supported by the ratios in Table 1. It is clear that (especially in the case of $n_{\mathrm{expo}} = 20$) the ratio increases remarkably with the number of particles when using a cutoff and hardly changes when not using it. Therefore, using ER,

with a good decrease in simulation time, will depend on the characteristics of the simulation regarding the computational weight of the potential and the system size. When the potential is computationally light, the simulation times can be even worse when using ER than when using the standard MC algorithm.

2.3 Energy-repository plus neighbour lists

From the previous discussion one could think that using the ER with short range potentials is not a good strategy, except when the potential is so heavy that it overwhelms the cutoff effect. However, it is possible, by coupling the present ER scheme with neighbour lists to approach the ratios of the "no cutoff" cases referred to before, or even substantially increase the efficiency of the usual neighbour lists technique.

A neighbour list, from now on designated as NL1, is built for each particle, containing references to the particles that are inside the sphere of radius r_{cut} centered on the particle. These lists are then used repeatedly to select the pairs that have to be retrieved from the ER as well as the ones to be registered. When a new configuration is accepted, the lists must be updated accordingly as well as the ER energy pairs involved in the old and new configurations. The algorithm for a MC step using this scheme is presented in Figure 5.

The time spent on a MC step is now

$$t_{\text{cycle,ER+NL1}} = N \cdot (N \cdot t_{\text{rij}} + n_{\text{rcut}} \cdot t_{\text{pot}} + n_{\text{rcut}} \cdot \alpha \cdot t_{\text{acc}}) \tag{6}$$

which should be smaller than $t_{\text{cycle,ER}}$ in equation (3) since $n_{\text{rcut}} \cdot \alpha \cdot t_{\text{acc}} < N \cdot \alpha \cdot t_{\text{acc}}$. In fact this scheme should yield ratios comparable to the ones obtained when using long range potentials (without cutoff).

At this stage one can see that a further improvement is possible: the coupling of ER with the common neighbour lists technique [2,5], from now on designated NL2. For that, a skin over the cutoff sphere is added and one now follows the standard operations of the usual neighbour lists technique. The algorithm (for a MC step) is presented in Figure 6. One should expect that, to some extent, the resulting time saving effects of this scheme (ER+NL2) should be the sum of the ones of ER+NL1

Assuming that the energy-repository (ER) and the nighbour lists (NL) are already built.

$E_{old} \leftarrow$ Retrieve energy from ER using NL
Build trial configuration
$V_{trial}[\,] \leftarrow$ Calculate energy pairs and build trialNL
$E_{trial} \leftarrow$ Sum over V_{trial} elements
$\Delta E \leftarrow E_{trial} - E_{old}$

if (exp($-\beta\Delta E$) > ran()) **then**
    Accept trial configuration
    Regist V_{trial} elements on the ER and update NL using trialNL
else
    Reject trial configuration
end if

Figure 5: Algorithm for the coupling of ER with NL1.

and NL2 techniques. The time spent on a MC step is now

$$\begin{aligned} t_{\mathrm{cycle,ER+NL2}} &= N \cdot [(1-\phi)\,(n_{\mathrm{list}} \cdot t_{\mathrm{rij}} + n_{\mathrm{rcut}} \cdot t_{\mathrm{pot}} + n_{\mathrm{list}} \cdot \alpha \cdot t_{\mathrm{acc}}) + \\ &\quad \phi\,(N \cdot t_{\mathrm{rij}} + n_{\mathrm{rcut}} \cdot t_{\mathrm{pot}} + n_{\mathrm{list}} \cdot \alpha \cdot t_{\mathrm{acc}})] \end{aligned} \tag{7}$$

where $\phi =$ number of list updates/number of MC steps and n_{list} is the average number of particles referenced in a neighbour list. The time spent on a MC step using the common neighbour lists is

$$\begin{aligned} t_{\mathrm{cycle,NL2}} = N \cdot [(2-\phi)\,(n_{\mathrm{list}} \cdot t_{\mathrm{rij}} + n_{\mathrm{rcut}} \cdot t_{\mathrm{pot}} + n_{\mathrm{list}} \cdot \alpha \cdot t_{\mathrm{acc}}) + \\ \phi\,(N \cdot t_{\mathrm{rij}} + n_{\mathrm{rcut}} \cdot t_{\mathrm{pot}} + n_{\mathrm{list}} \cdot \alpha \cdot t_{\mathrm{acc}})]\,. \end{aligned} \tag{8}$$

Comparing $t_{\mathrm{cycle,NL2}}$ with $t_{\mathrm{cycle,ER+NL2}}$ it is easy to conclude (look at the term $(2-\phi)$ in equation 10) that the effect of the ER, when used with NL2, is, again in a ideal situation, to half the NL2 step computing time.

Assuming that the energy-repository (ER) and the neighbour lists (NL) are already built.

$E_{old} \leftarrow$ Retrieve energy from ER using NL
Build trial configuration
NLupdate $\leftarrow$ Test displacement for NL update
if (NLupdate) **then**
    $V_{trial}[\,] \leftarrow$ Calculate energy pairs and build trialNL
else
    $V_{trial}[\,] \leftarrow$ Calculate energy pairs using NL
end if
$E_{trial} \leftarrow$ Sum over V_{trial} elements
$\Delta E \leftarrow E_{trial} - E_{old}$

if (exp($-\beta\Delta E$) > ran()) **then**
    Accept trial configuration
    if (NLupdate) **then**
        Regist V_{trial} elements on the ER and update NL using trialNL
    else
        Regist V_{trial} elements on the ER using trialNL
    end if
else
    Reject trial configuration
end if

Figure 6: Algorithm for the coupling of ER with NL2.

Simulations, in the same conditions as for Table 1, have been conducted for these

Table 2: Time ratios (equations (9) and 10)) calculated for a Lennard-Jones system. Values for $ratio_{ER+NL1}$ are in **bold** characters, values for $ratio_{ER+NL2}$ are in *italic* characters and values for $ratio_{NL2}$ are in standard format characters.

	N			
n_{expo}	256	1372	4000	6912
0	**0.80**	**0.63**	**0.58**	**0.56**
	0.62	*0.26*	*0.16*	*0.14*
	0.69	0.42	0.47	0.60
5	**0.63**	**0.60**	**0.57**	**0.56**
	0.55	*0.32*	*0.20*	0.17
	0.87	0.53	0.50	0.59
10	**0.58**	**0.58**	**0.57**	**0.56**
	0.54	*0.35*	*0.23*	*0.19*
	0.93	0.63	0.54	0.62
20	**0.55**	**0.56**	**0.57**	**0.56**
	0.53	*0.40*	*0.27*	*0.22*
	0.96	0.72	0.60	0.65

last three schemes and the calculated time ratios

$$\text{ratio}_{\text{ER+NL1}} = \frac{t_{\text{cycle,ER+NL1}}}{t_{\text{cycle,ST}}}, \tag{9}$$

$$\text{ratio}_{\text{ER+NL2}} = \frac{t_{\text{cycle,ER+NL2}}}{t_{\text{cycle,ST}}} \tag{10}$$

and

$$\text{ratio}_{\text{NL2}} = \frac{t_{\text{cycle,NL2}}}{t_{\text{cycle,ST}}} \tag{11}$$

are presented in Table 2. These values ascertain the increased effect of ER when the potential computing weight increases and show that, indeed, the effects of ER and NL2 are cumulative. Looking at the case $n_{\text{expo}} = 20$ and $N = 4000$, the ratio for ER+NL2 is nearly half the ratio of NL2.

2.4 Energy-repository plus linked lists

The coupling of ER with the linked lists [2, 5] technique was also studied. The algorithm for a MC step is presented in Figure 7. The times spent on a MC cycle

Assuming that the energy-repository (ER) and the linked lists (LL) are already built.

ocell ← Determine cell where particle is
E_{old} ← Retrieve energy from ER using LL
Build trial configuration
ncell ← Determine cell where particle will possibly be
$V_{trial}[\,]$ ← Calculate energy pairs using LL

E_{trial} ← Sum over V_{trial} elements
$\Delta E \leftarrow E_{trial} - E_{old}$

if (exp($-\beta\Delta E$) > ran()) **then**
  Accept trial configuration
  if (ocell **.ne.** ncell) **then**
    Swap particle cell
  end if
  Regist V_{trial} elements on the ER
else
  Reject trial configuration
end if

Figure 7: Algorithm for the coupling of ER with LL.

with the linked lists technique (LL) and with the ER plus LL are, respectively

$$t_{\mathrm{cycle,LL}} = 2N\left(27 \cdot n_{\mathrm{cell}} \cdot t_{\mathrm{rij}} + n_{\mathrm{rcut}} \cdot t_{\mathrm{pot}}\right) \tag{12}$$

and

$$t_{\mathrm{cycle,ER+LL}} = N\left(27 \cdot n_{\mathrm{cell}} \cdot t_{\mathrm{rij}} + n_{\mathrm{rcut}} \cdot t_{\mathrm{pot}} + 27 \cdot n_{\mathrm{cell}} \cdot \alpha \cdot t_{\mathrm{acc}}\right) \tag{13}$$

where n_{cell} is the average number of particles in a cell. The respective ratios are

$$\mathrm{ratio}_{\mathrm{LL}} = \frac{t_{\mathrm{cycle,LL}}}{t_{\mathrm{cycle,ST}}} \tag{14}$$

Table 3: Time ratios (equations(14) and (15)) calculated for a Lennard-Jones system. Values for $ratio_{ER+LL}$ are in **bold** characters and values for $ratio_{LL}$ are in standard format characters.

	N			
n_{expo}	256	1372	4000	6912
0	**3.21**	**0.64**	**0.21**	**0.09**
	4.00	0.52	0.16	0.07
5	**2.00**	**0.59**	**0.23**	**0.12**
	3.07	0.64	0.25	0.13
10	**1.71**	**0.58**	**0.26**	**0.14**
	2.74	0.70	0.31	0.18
20	**1.47**	**0.56**	**0.30**	**0.18**
	2.53	0.88	0.41	0.26

and

$$\text{ratio}_{\text{ER+LL}} = \frac{t_{\text{cycle,ER+LL}}}{t_{\text{cycle,ST}}} \tag{15}$$

Analyzing equations (12) and (13) it is seen that the ER efficiency increases, in this scheme, only when the term $(27 \cdot n_{\text{cell}} \cdot \alpha \cdot t_{\text{acc}})$ becomes very small in comparison with the term $(27 \cdot n_{\text{cell}} \cdot t_{\text{rij}} + n_{\text{rcut}} \cdot t_{\text{pot}})$, and that this will happen only by an increase of the potential weight t_{pot}.

Simulations have been carried out (in the same conditions as before) and the time ratios (equations (14) and (15)) are presented in Table 3. The results show that, indeed, ER+LL only becomes useful (comparing with the LL case) when the potential computational weight increases.

3 Applications and concluding remarks

The efficiency of the energy-repository was tested by performing simulations using different intermolecular potential models, and by evaluating the simulations time ratios given by equation (4). The results are presented in Table 4. and the thermodynamic conditions for the simulations are in Table 5. In Table 4 EWALDSUM1 means the technique involving the real and reciprocal spaces sums with cutoff [2, 5, 12, 13]. EWALDSUM2 refers to the method of Adams and Dubey [14] which involves Kubic harmonics and no cutoff. The results agree with the predictions of the previous section. The LJ and C_{60}, with cutoff, require the use of the ER plus neighbour lists

Table 4: Experimental time ratios (equation (4)) for various models. The ratios for the LJ and C_{60} models were obtained using the ER plus neighbour lists technique. For the other models the standard ER technique was used.

N	**ratio**
Lennard-Jones [6] (LJ) (cutoff)	
256	0.62
1372	0.26
4000	0.16
C_{60} - Girifalco [7] (cutoff)	
256	0.53
1372	0.20
4000	0.09
Water TIP4P [8] (no EWALDSUM; no cutoff in Coulomb; cutoff in LJ)	
216	0.52
512	0.57
1000	0.56
Water TIP4P (EWALDSUM1)	
216	0.52
512	0.54
1000	0.54
CH_3I [9] (EWALDSUM2)	
256	0.53
864	0.54
1372	0.65
Ethanol [10] (no EWALDSUM; cutoff LJ; no cutoff Coulomb)	
216	0.55
512	0.54
1000	0.53
CH_2F_2 [11] (cutoff LJ; Coulomb-reaction field)	
216	0.51
512	0.55
1000	0.64

for an increase of time saving but for the molecular ones, with and without Ewald sum, the use of the simple ER technique yields always good time ratios.

Table 5: Simulated thermodynamic conditions for the models presented in Table 4.

Lennard-Jones (LJ) (cutoff)
$T^* = 2.0$; $\rho^* = 0.65$; $rcut^* = 2.74$
C_{60} - Girifalco (cutoff)
$T = 2200$K; $\rho = 0.8$ nm^{-3}; $rcut^* = 2.67$
Water TIP4P (no EWALDSUM; no cutoff in Coulomb; cutoff in LJ)
$T = 298$K; $\rho = 0.98$ g cm^{-3}; $rcut^*_{LJ} = 2.4$
Water TIP4P (EWALDSUM1)
$T = 298.15$K; $\rho = 0.999$ g cm^{-3}; $rcut_{LJ} = 7.5$Å
CH_3I (EWALDSUM2)
$T = 303$K; $\rho = 2.254$ g cm^{-3}; $rcut_{LJ} = 15$ Å
Ethanol (no EWALDSUM; cutoff LJ; no cutoff Coulomb)
$T = 298$K; $\rho = 0.879$ g cm^{-3}; $rcut_{LJ} = 14$ Å
CH_2F_2 (cutoff LJ; Coulomb - reaction field (with cutoff))
$T = 220$K; $\rho = 1.0$ g cm^{-3}; $rcut = 15$ Å

The faster the access to the RAM the better the results we should expect with the present algorithm. It is also shown that the method is suitable for the simultaneous use of other Monte Carlo acceleration techniques like Verlet's neighbour lists or linked lists.

In view of these results we can conclude that the use of the energy-repository is feasible in most Monte Carlo simulations and we hope that the application of this algorithm to other models will reveal its full capacities.

Recently, we have applied the technique to an extensive study of the adsorption of water on gold electrodes [15] with an excellent saving of computing time.

Acknowledgements

Rui Fartaria acknowledges the support from Fundação para a Ciência e Tecnologia (PhD. grant SFRH/BD/10405/2002). Pedro Rodrigues tanks the institutional support of the Department of Chemistry and Biochemistry (FCUL) during his research work.

References

[1] A. Rahman: Correlations in motion of atoms in liquid argon, *Phys. Rev.* 136 (1964) A405.

[2] M. Allen and D. Tildesley: *Computer Simulation of Liquids*, Claredon Press, Oxford, U.K., 1st ed. (1987).

[3] D. J. Tildesley: Molecular simulation: A view from the bond, *Faraday Discuss.* 100 (1995) C29–C45.

[4] N. Metropolis, A. Rosenbluth, M. Rosenbluth, A. Teller and E. Teller: Equation of state calculations by fast computing machines, *J. Chem. Phys.* 21 (1953) 1087–1092.

[5] D. Frenkel and B. Smit: *Understanding Molecular Simulations: From Algorithms to Applications*, Academic Press, 2nd ed. (2002).

[6] J. E. Lennard-Jones: On the determination of molecular fields. i. From the variation of the viscosity of a gas with temperature, *Proc. Roy. Soc.* A106 (1924) 441–463.

[7] L. A. Girifalco: Molecular properties of fullerene in the gas and solid phases, *J. Phys. Chem.* 96 (1992) 858.

[8] W. L. Jorgensen and J. D. Madura: Temperature and size dependence for Monte-Carlo simulations of TIP4P water, *Mol. Phys.* 56 (1985) 1381–1392.

[9] F. F. M. Freitas, F. M. S. S. Fernandes and B. J. C. Cabral: Vapor-liquid-equilibrium and structure of methyl-iodide liquid, *J. Phys. Chem.* 99 (1995) 5180–5186.

[10] W. L. Jorgensen: Optimized intermolecular potential functions for liquid alcohols, *J. Phys. Chem.* 90 (1986) 1276–1284.

[11] P. Jedlovszky and M. Mezei: Computer simulation study of liquid CH_2F_2 with a new effective pair potential model, *J. Chem. Phys.* 110 (1999) 2991–3002.

[12] P. Ewald: Die berechnung optischer und elektrostatischer gitterpotentiale, *Ann. Phys.* 64 (1921) 253–87.

[13] A. Y. Toukmaji and J. A. B. Jr.: Ewald summation techniques in perspective: a survey, *Comp. Phys. Comm.* 95 (1996) 73–92.

[14] D. J. Adams and G. S. Dubey: Taming the Ewald sum in the computer-simulation of charged systems, *J. Comput. Phys.* 72 (1987) 156–176.

[15] R. S. Neves, R. P. S. Fartaria, F. M. S. S. Fernandes and A. J. Motheo: *J. Electroanal. Chem. (to be submitted)* .

Capítulo 4

Diagramas de fases e entalpias de sublimação de fulerenos

Neste capítulo apresentam-se os resultados do estudo dos fulerenos sob a forma de três artigos:

- **Monte Carlo Simulation of the Phase Diagram of C_{60} Using Two Interaction Potentials. Enthalpies of Sublimation**
  Rui P.S. Fartaria, Fernando M.S. Silva Fernandes, Filomena F.M. Freitas
  J. Phys. Chem. B 106 (2002) 10227-10232

- **Phase Diagrams and Sublimation Enthalpies of Model $C_{n\geq 60}$ Fullerenes. A Comparative Study by Computer Simulation**
  Fernando M.S. Silva Fernandes, Filomena F.M. Freitas, Rui P.S. Fartaria
  J. Phys. Chem. B 107 (2003) 276-281

- **Phase Diagram and Sublimation Enthalpies of Model C_{60}Revisited**
  Fernando M.S. Silva Fernandes, Filomena F.M. Freitas, Rui P.S. Fartaria
  J. Phys. Chem. B 108 (2004) 9251-9255

J. Phys. Chem. B 106 (2002) 10227-10232

Monte Carlo Simulation of the Phase Diagram of C_{60} Using Two Interaction Potentials. Enthalpies of Sublimation.

Rui P.S. Fartaria, Fernando M.S. Silva Fernandes[1], Filomena F.M. Freitas
Laboratory of Molecular Simulation and CECUL, Department of Chemistry and Biochemistry, Faculty of Science, University of Lisboa, Rua Ernesto de Vasconcelos, Bloco C8, Piso 3, 1749-016 Lisboa, Portugal

Abstract

A first-principles interaction potential proposed by Pacheco and Ramalho (PRP) and the effective potential of Girifalco (GP) have been used to model the whole phase diagram of C_{60} by Gibbs ensemble and Gibbs-Duhem integration Monte Carlo methods. The triple-point properties were determined by a direct method recently proposed by us [Comp. Phys. Commun. **2001**, 141, 403]. It is based on the behavior of the Gibbs ensemble vapor-liquid simulations at the low-temperature limit and it does not involve free-energy calculations. A stable liquid phase for temperatures between 1570±20 K and 2006±27 K is predicted with the PRP model and for temperatures between 1529±36 K and 1951±28 K with the GP model. According to these results, the liquid phase for C_{60} extends over ∼450 K, a temperature range considerably wider than the ones reported by other authors on the basis of free-energy calculations and density functional approaches. Nonetheless, the present results are in good agreement with the theoretical predictions from the hypernetted mean spherical approximation, the modified hypernetted chain theory and a correlative self-consistent field method, as well as, with some molecular dynamics simulations. The reported free-energy data for the fluid-solid region are reproduced here, strictly by computer simulation. According to them the liquid phase of C_{60} extends over ∼100 K. A discussion on the apparent conflicting triple-point data is presented. The calculated enthalpies of sublimation at 700 K (163±9 kJmol^{-1} for

[1]To whom correspondence should be addressed (e-mail: fsilva@fc.ul.pt)

PRP and 170±12 kJmol^{-1} for GP) are in good agreement with the available experimental results. The estimated standard enthalpies are also within the recommended values and the third-law enthalpies are in excellent agreement with experimental and theoretical data. This suggests that at least the simulated triple-point properties, in the low-temperature limit, should approach that of real C_{60}. The radial distribution functions and the self-diffusion coefficients, in the liquid pockets predicted for the two models, are also consistent with a normal liquid state and no sign of liquid supercooling was observed. On the whole, the differences between the present interaction potentials do not induce significant qualitative changes in the phase behavior of the two models. However, the differences are clearly reflected in the location of the coexistence lines, the critical and triple-point properties as well as in the enthalpies of sublimation. Finally, as a further test of the reliability of our method for the determination of triple-point properties, we also report preliminary results for the triple-point temperature and the standard enthalpy of sublimation of C_{70}. They are in excellent agreement with theoretical and experimental data.

1 Introduction

Recently, we have reported the vapor-liquid and fluid-solid coexistence properties of a C_{60} model [1, 2] using a first-principles interaction potential (PRP) proposed by Pacheco and Ramalho [3]. The pioneering works of Hagen et al. [4] and Cheng et al. [5], in 1993, based on an effective potential (GP) proposed by Girifalco [6, 7] gave rise to a controversial question on the existence of a stable liquid phase for C_{60}. The first group, using a combination of simulation and free-energy methods, concluded that C_{60} does not have a stable liquid phase since the sublimation line was located 35 K above the critical temperature at 1798 K. The second group, used the hypernetted mean spherical approximation (HMSA) combined with molecular dynamics, predicting a stable liquid phase between 1774 and 1900-2050 K.

Since then, part of the simulation and free-energy calculations [8–12], as well as, some density functional approaches [13–15] presented two types of behavior. Either no triple point was predicted or a triple point was estimated, but a liquid phase remained below it. If the liquid there is metastable, then no conflict with thermodynamics exists. However, the extensive Gibbs ensemble vapor-liquid simulations of Caccamo et al. [16] suggest that the liquid phase is stable below the triple-points estimated from the free-energy based calculations. Moreover, the theoretical studies based on the hypernetted mean spherical approximation (HMSA) [5], the modified hypernetted chained theory (MHNC) [17, 18] and a correlative self-consistent method [19], as well as, some molecular dynamics simulations [20] point to the existence of lower triple-points temperatures than the ones from free-energy studies. Such behaviors were the object of our work referred above in which it was demonstrated, strictly by computer simulation, that a model of C_{60} is able to reproduce two sets of apparent conflicting triple-point properties: one, in the high-temperature limit, according to the free-energy results; the other, in the low-temperature limit, according to the findings of HMSA and MHNC theories.

Our simulations were carried out by the Gibbs ensemble Monte Carlo (GEMC) [21, 22] and the Gibbs-Duhem integration Monte Carlo (GDMC) [23] methods. Furthermore, we have proposed [24] a new approach to estimate the location of the triple point. The method is based on the limiting behavior of the Gibbs ensemble vapor-liquid calculations for the lowest temperature range. It provides, in a direct and natural way, a starting state (the triple point) for the simulation of the fluid-solid coexistence by GDMC. Also, it constitutes an alternative to the perturbation technique proposed by Agrawal and Kofke [25, 26] to circumvent one of the limitations

of the Gibbs-Duhem scheme to trace coexistence curves.

In this work, we present results from GEMC and GDMC simulations of the whole phase diagram of C_{60} using PRP and GP. Indeed, most of the simulations carried out hitherto have used these interaction models. The main objectives of the present article are: i) to extend our previous work to the vapor-solid coexistence properties of C_{60}; ii) to assess the effect of the differences between the interaction potentials on the phase behavior; iii) to compare the respective enthalpies of sublimation with the available experimental results. We also reaffirm that it is possible to estimate, strictly by computer simulation, conventional triple-points for the two models in accordance with some theoretical predictions and the basic concepts of thermodynamics.

Whether or not the present simulation results correspond to the whole phase diagram of real C_{60} is a matter that can be settled only with further experimental and theoretical investigation. In fact, molecular dynamics simulations [27, 28] predict that an isolated C_{60} molecule is stable up to ∼4500 K. However, some experiments [11,16,29] show that C_{60} molecules in the solid phase are unstable against polymerization or amorphization well below the temperatures of interest (∼2000 K). Nevertheless, we believe that the present work shed light on the main aspects of the present potential models for C_{60} and that it may be useful in the experimental field. In fact, we shall see that the simulated enthalpies of sublimation are in good agreement with the available experimental data, suggesting that at least the triple-point properties, in the low-temperature limit, should approach those of real C_{60}. Moreover, those properties seem to be consistent with a kind of "corresponding state" rule for fullerenes recently reported by Abramo et al. [29].

In the next section we present the potential models and computational details. The results are shown and discussed in sections 3 and 4. The final section contains the conclusions of this work.

2 Potential Models and Computational Details

The *ab initio* PRP [3] is composed by a short-range term,

$$M(r) = M_0 \exp\left[\tau\left(1 - \frac{r}{d_0}\right)\right]\left\{\exp\left[\tau\left(1 - \frac{r}{d_0}\right)\right] - 2\right\} \tag{1}$$

a long-range term,

$$W(r) = -\frac{C_6}{r^6} - \frac{C_8}{r^8} - \frac{C_{10}}{r^{10}} - \frac{C_{12}}{r^{12}} \tag{2}$$

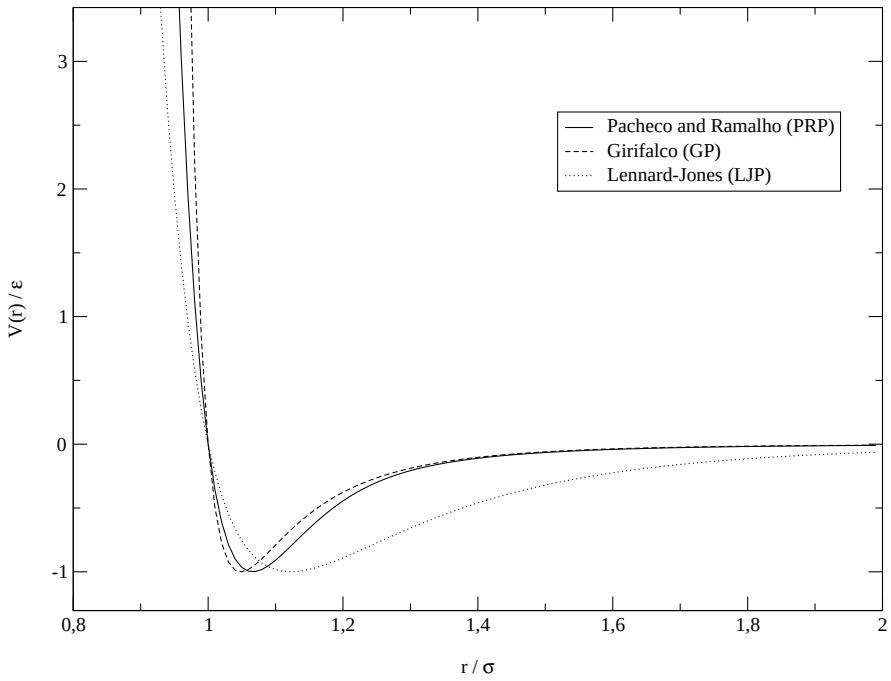

Figure 1: Comparison of PRP and GP with LJP (ε is the well depth and σ the effective molecular diameter)

and a Fermi-type crossover function,

$$F(r) = \left\{1 + \exp\left[\frac{r-\mu}{\delta}\right]\right\}^{-1} \tag{3}$$

The final form of the potential is:

$$V(r) = F(r) \times M(r) + [1 - F(r)] \times W(r) \tag{4}$$

with the parameters given in the original article. GP [6, 7] has the form:

$$V(r) = -\alpha\left[\frac{1}{s(s-1)^3} + \frac{1}{s(s+1)^3} - \frac{2}{s^4}\right] + \beta\left[\frac{1}{s(s-1)^9} + \frac{1}{s(s+1)^9} - \frac{2}{s^{10}}\right] \tag{5}$$

with the parameters given in the original articles.

PRP is softer than GP, but they both are significantly harder and narrower, and decay much more rapidly to zero, than the Lennard-Jones potential (LJP) as can be seen in Figure 1. These aspects could be the origins of the apparent anomalous behavior detected in the fluid-solid region of C_{60} when compared with the well-

behaved trend observed in the diagram of the LJ system. Either PRP or GP seem to be, at least as a first step, appropriate to model C_{60}. However, PRP reproduces the experimental pressure-volume isotherm at high pressures more accurately than GP [3].

Although PRP is a first-principles accurate potential, it depicts (as GP does) V(r) for an r measured from the center of the approximately spherical C_{60} molecule. This may mask the true nature of the interactions responsible for the convexity properties of the free energy. Indeed, they may arise from a more cooperative interaction of clusters. Ashcroft [30], for example, touches upon the problem in an interesting note commenting on the results of Hagen et al. [4] and Cheng et al. [5]. That is a serious suggestion not taken into account in the present study.

The rationale for essentially noble gas models is, above all, the use of the simplest and plausible ab initio and effective potentials to probe the phase behavior of C_{60}. This may well turn out, however, as a crude approximation, at least for some regions of the phase diagram.

The potentials were truncated at half of the simulation boxes lengths. This distance was always larger than 2σ (σ is the effective diameter of the molecule). Long range corrections (LRC) were not included, because the potentials rapidly decay to zero for distances greater than 2σ. Nonetheless, taking into account the study of Hasegawa and Ohno [15], we have verified that the truncation distances that were used have negligible effects on the phase behavior. For distances smaller than 0.3σ the potentials were switched to ∞ because at these values of proximity the potential energy is very high and the configurations would always be rejected. Also, for separations smaller than 0.2σ, PRP reaches high negative values and any configuration would be accepted. The usual cubic periodic boundary conditions were always applied.

The vapor-liquid coexistence curves were obtained by GEMC simulations. The first point was set up by placing the molecules in face-centered cubic (fcc) lattices with 256 molecules in each box, at appropriate densities, and running the convenient number of cycles for a complete relaxation of the system. The other points were calculated starting from fcc lattices with 256 molecules in each box, at the equilibrium densities of the previous runs. Equilibration runs of 3,000 - 10,000 cycles were followed by production runs of 20,000 - 40,000 cycles. A GEMC cycle consisted of random displacements of each molecule, a random rearrangement of the volume of each box (keeping the total volume constant) and a number of trials to transfer a molecule from one box to another, with a rate of acceptance of $\sim$1% of the total

number of trials.

The liquid-solid and vapor-solid coexistence curves were calculated by the GDMC method. It consisted of successive and simultaneous NpT simulations in two boxes (each containing 256 molecules) combined with a predictor-corrector scheme to estimate the temperature, as a function of pressure, for the next point along the coexistence line. The coupling procedure described by Kofke [23] was applied in some calculations.

An important issue in fluid-solid simulations by the GDMC method is the definition of the starting state to initiate the integration of the Clapeyron equation. In the present study two methods were applied. The first one is an adaptation of Agrawal and Kofke's method [25, 26]. From the known properties of the soft-sphere potential (SSP), in the limit of high-temperature, we determined the starting phase points through the scaled potential:

$$V(r, \lambda) = (1 - \lambda)\ SSP(r) + \lambda\, V(r) \tag{6}$$

where λ is a parameter between 0 and 1 and $V(r)$ is the potential of interest. From that points, we calculated the other points at lower temperatures.

The second method is the one proposed by us. The full computational details of the method can be seen in the original article [24]. In short, it consists of decreasing the temperature of the GEMC vapor-liquid equilibrium by small steps (ΔT ~10 K) until a temperature is reached below which the liquid phase is not stable anymore. The system readily assumes a vapor-solid configuration, that is to say, spontaneous freezing is detected in the high density box. Those values of temperature, the densities and configurational energies (just before and after freezing) and the vapor pressure are taken as an estimation of the triple point properties. From that point, in the low-temperature limit, we successively calculated the fluid-solid lines by increasing the temperature and the vapor-solid lines by decreasing the temperature.

It may be argued that this method does not have the reliability that would warrant anything more than a qualitative conclusion regarding the true freezing temperature. We should mention, however, that in the original article [24] ample evidence was given of the quantitative correctness of the method. In particular, it was demonstrated that the method does not lead to the supercooling of the liquid, if the conditions of the respective computational algorithm are fulfilled. Furthermore, it is able to determine the triple-point temperature in a very narrow interval ($\pm$10 K for C_{60}), within the maximum error usually reported for that property.

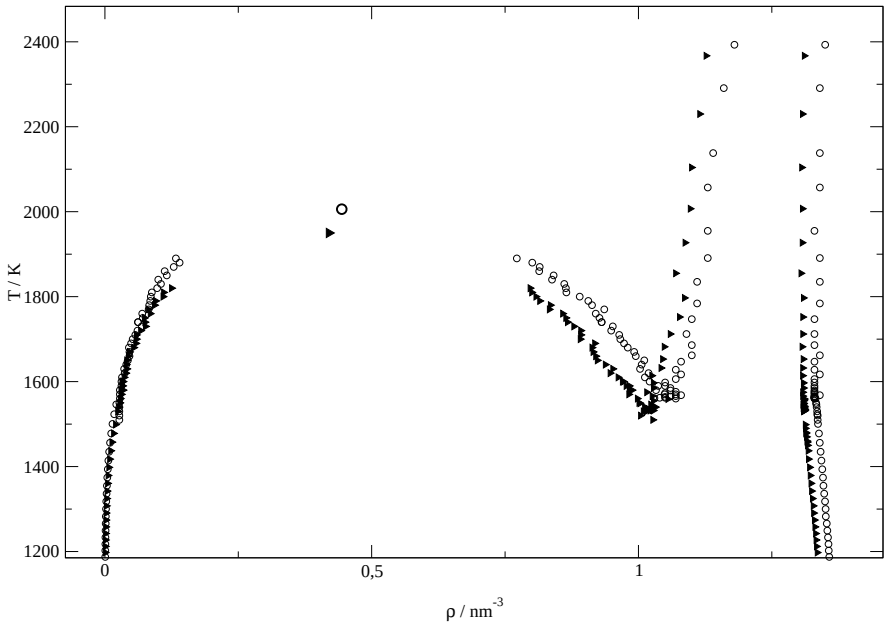

Figure 2: Temperature-density phase diagram. Empty circles - PRP; dark triangles - GP (the fluid-solid and vapor-solid lines were obtained from the starting state defined by our method [1, 24]).

The results obtained by the two methods are significantly different as we shall see in the following section.

3 Phase Diagrams

The whole temperature-density phase diagram of C_{60} obtained from the two potential models is presented in Figure 2. The fluid-solid and vapor-solid coexistence lines were obtained from the starting state defined by our method.

Figure 3, displays part of the diagram with the fluid-solid coexistence lines calculated from the starting state defined by Agrawal and Kofke's method. Although they have already been reported in our previous article [1] it is important to include them here regarding the discussion ahead.

Table 1 displays some critical and triple point properties obtained by various authors for PRP and GP.

The critical temperatures and densities were estimated by fitting the vapor-liquid data to the laws of rectilinear diameters and order parameter scaling [31] with a critical exponent $\sim$0.33. The pressures were fitted to the Clapeyron equation. The final triple point properties were assessed by fitting the fluid-solid raw data and

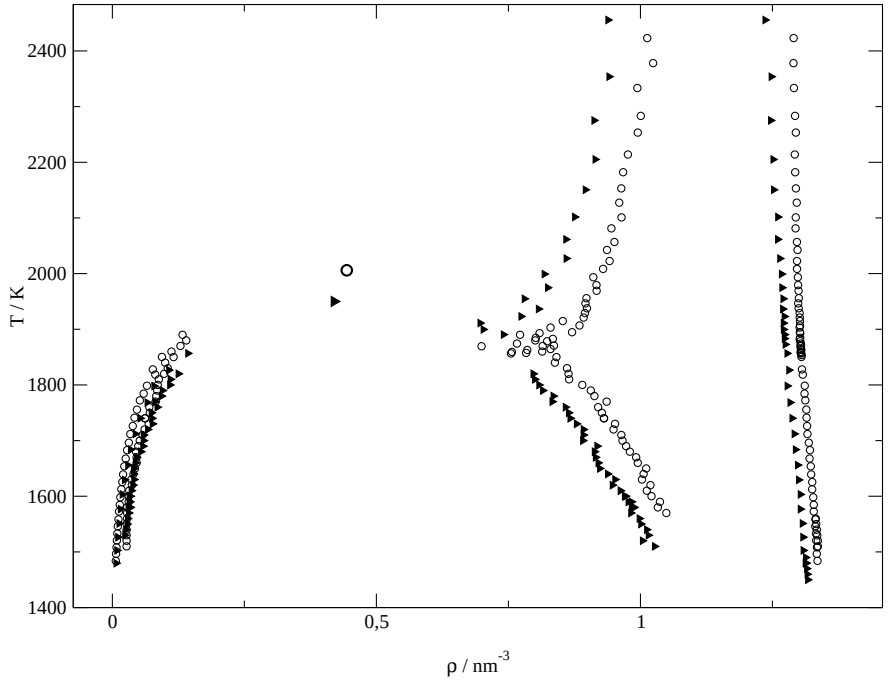

Figure 3: Part of the temperature-density phase diagram. Empty circles - PRP; dark triangles - GP (the fluid-solid lines were obtained from the starting state defined by Agrawal and Kofke's method [25, 26]).

intersecting the extension of the vapor-liquid lines with the freezing lines. The pressure-temperature diagrams are displayed in Figure 4.

The vapor-liquid curves show the usual behavior (see Figure 2). As expected, the order parameter $(\rho_L - \rho_V)$ for PRP is greater than the one for GP, giving rise to a higher critical temperature and density: 2006±27 K; 0.444±0.003 nm^{-3} for PRP and 1951±28 K; 0.423±0.003 nm^{-3} for GP. This clearly reflects the softer nature of PRP. These values compare well with the data of Ferreira et al. [10] for PRP, and of Caccamo et al. [16] and Hasegawa and Ohno [11] for GP.

Regarding the discussion ahead, it is very important to point out that the vapor-liquid properties were checked against thermodynamic stability. This was done by confirming the equality of the chemical potentials and pressures, at all the simulated points of the coexistence curves. Additionally, the analysis of the probability plots, recommended by Frenkel and Smit [32], was also carried out.

The fluid-solid curves obtained with PRP are located at a higher density region than the ones from GP (see Figure 2). This also seems to reflect the softer nature of PRP . The estimated triple-point temperatures and liquid densities are: 1570±20 K; 1.05±0.01 nm^{-3} for PRP and 1529±36 K; 1.02±0.01 nm^{-3} for GP. The values

Table 1: Estimates of critical and triple point properties for PRP and GP. (AK means Agrawal and Kofke's method [26]; FFF means our method [24])

		T_c/K	ρ_c/nm^{-3}	p_c/bar
PRP	(ref. [1])	2006±27	0.444±0.003	35±6
	(ref. [10])	2011.7±1.1	0.4676±0.0007	
GP	this work	1951±28	0.423±0.003	33±9
	(ref. [4])	1798±10	∼0.41	
	(ref. [5])	1900 - 2050	0.56	
	(ref. [17])	1920	∼0.60	
	(ref. [11])	1980	0.44	
	(ref. [16])	1924 - 1941	0.39 - 042	29

		T_{tr}/K	ρ_{tr}/nm^{-3}	p_{tr}/bar
PRP	(ref. [1])	1570±20	1.05±0.01	5±16
	(ref. [1])	1858±32	0.81±0.01	19±10
	(ref. [10])	1881.2±0.1	0.8447±0.0003	
GP	this work (FFF)	1529±36	1.02±0.01	4±19
	this work (AK)	1898±21	0.69±0.01	26±3
	(ref. [5])	1540	1.097	
		1774	0.944	14
	(ref. [17])	1620	1.0	∼5
	(ref. [11])	1880	0.74	
	(ref. [16])	∼1700	∼0.91	
		∼1500	∼1.0	
	(ref. [19])	∼1460		∼1

for GP are in excellent agreement with the data of Caccamo et al. [16] obtained by a combination of simulation and theory. It is also worth mentioning that in a theoretical study, based on a correlative self-consistent field method, Zubov et al. [19] estimated the triple-point temperature at ∼1460 K from GP.

The results obtained using the method of Agrawal and Kofke [25,26] are, however, significantly different (see Figure 3). Thus, our estimated triple point temperatures and liquid densities by that method are: 1858±32 K; 0.81±0.01 nm^{-3} for PRP and 1898±21 K; 0.69±0.01 nm^{-3} for GP. They also agree with the data of Ferreira et al. [10] and of Hasegawa and Ohno [11] obtained by a combination of simulation and free-energy calculations. Below those points, though, a stable liquid phase is

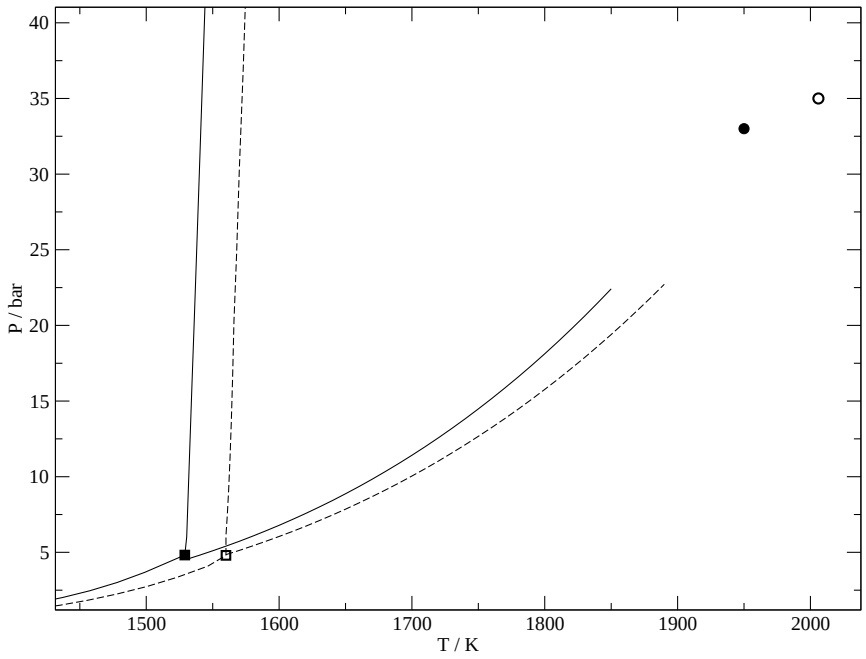

Figure 4: Pressure-temperature phase diagram. Dashed line - PRP (empty square - triple point; empty circle - critical point); straight line - GP (dark square - triple point; dark circle - critical point);

observed (see Figure 3). As referred above, we have checked the thermodynamic stability along the vapor-liquid coexistence curves. On the basis of the values of the fluid-solid relative chemical potentials for PRP we suggested [1] that this behavior corresponds to metastable states in the fluid-solid region. Table 2 shows the fluid-solid relative chemical potentials, $\Delta(\beta\mu)$, for GP obtained by Agrawal and Kofke's method "GD(AK)" and by our method "GD(FFF)". The respective values for PRP and the calculation details were already reported [1]. No errors bars were determined. Even so, the coincidence of the relative chemical potentials for the fluid and solid within each set of simulations is remarkable, indicating that both calculations are consistent.

The results for GP confirm the same behavior as detected for PRP. It seems that the GD(AK) calculations were constrained to a metastable fluid-solid region of phase space. In fact, the relative chemical potentials along the two sets of fluid-solid lines show a hint of local minima for the Gibbs free energy.

As far as structural properties are concerned we have noted the presence of shoulders in the second peak of the liquid and fluid radial distribution functions for the PRP model [1]. They were also reported by Cheng et al. [5] from molecular

Table 2: Relative chemical potentials for fluid-solid coexistence from GDMC with GP by two different paths.

GD (AK)			GD (FFF)		
	Fluid	Solid		Fluid	Solid
T / K	$\Delta(\beta\mu)$	$\Delta(\beta\mu)$	T / K	$\Delta(\beta\mu)$	$\Delta(\beta\mu)$
2353	0.00	0.00	2374	0.00	0.00
2275	-0.57	-0.56	2105	-2.50	-2.50
2205	-1.09	-1.07	1924	-4.62	-4.60
2150	-1.53	-1.50	1798	-6.31	-6.27
2101	-1.92	-1.89	1712	-7.58	-7.53
2061	-2.25	-2.22	1653	-8.52	-8.47
2027	-2.54	-2.51	1613	-9.20	-9.14
1999	-2.79	-2.75	1585	-9.69	-9.61
1974	-3.00	-2.96	1566	-10.02	-9.95
1954	-3.18	-3.14	1554	-10.25	-10.17
1936	-3.34	-3.29	1545	-10.40	-10.32
1923	-3.46	-3.41	1539	-10.51	-10.43
1911	-3.57	-3.52	1535	-10.58	-10.50
1899	-3.67	-3.62	1530	-10.68	-10.60

dynamics of GP. We confirm the existence of these shoulders for GP in Figure 5. They indicate the presence of solid or glasslike features. This may be an interesting point regarding the suggestion of a more cooperative interaction of clusters in C_{60} referred above.

Radial distribution functions at different points inside the liquid pockets, determined from the low-temperature limit, were also calculated showing patterns typical of the liquid state. Additionally, we have performed canonical molecular dynamics simulations, in the regions of the low-temperature triple-points, with 256, 864 and 2048 molecules. The self-diffusion coefficients were always of the order of 10^{-5} cm^2s^{-1}, an order of magnitude consistent with a normal liquid phase [20,29]. No sign of liquid supercooling was observed. Finally, it is worth mentioning that the solid generated by the spontaneous freezing, detected in our method, is a quasi-perfect, not defect-rich, face-centered-cubic lattice [24].

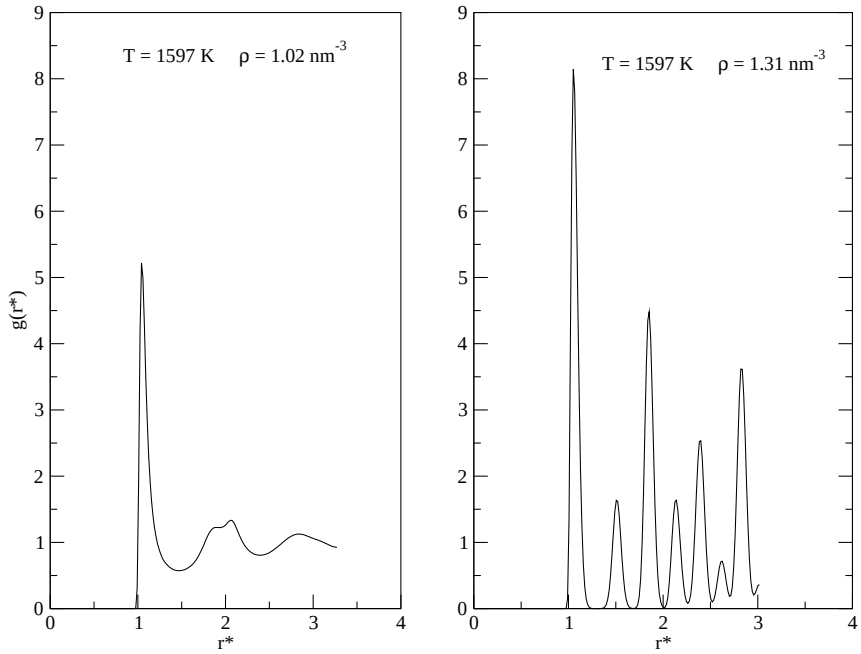

Figure 5: Radial distribution functions for the liquid-solid coexistence at 1597 K (near the triple point) with GP

4 Enthalpies of Sublimation. Prediction of enthalpies of vaporization and melting

From the vapor-solid coexistence calculations we worked out the enthalpies of sublimation, as a function of temperature, for the two models. They are displayed in Figure 6. The simulation results were fitted to equation [33]

$$\Delta_{sub}H = ZRT^2 \frac{d \ln p}{d T} \tag{7}$$

with

$$\ln p = A + \frac{B}{T} + C \ln T + DT^E \tag{8}$$

The values at 700 K are 163±9 kJmol^{-1} for PRP and 170±12 kJmol^{-1} for GP. They compare well with the experimental data, at about the same temperature, reported in the NIST Database [34]. From a direct extrapolation of our results to 298.15 K and 1 bar, we estimated the standard enthalpies of sublimation: 166±9 kJmol^{-1} for PRP and 173±12 kJmol^{-1} for GP. However, using the correction from 700 K to 298.15 K calculated by Diogo et al. [35] (47.3 kJmol^{-1}) the estimated stan-

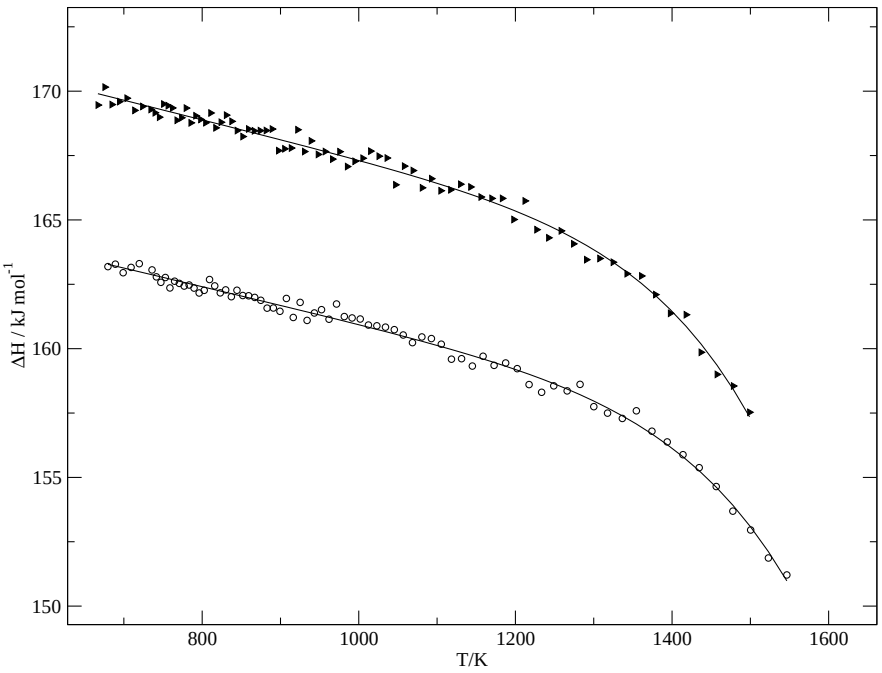

Figure 6: Enthalpies of sublimation as a function of temperature (empty circles - PRP; dark triangles - GP; straight lines - fitting to equation 7)

dard enthalpies of sublimation for PRP and GP to be, respectively, 210 kJmol^{-1} and 217 kJ mol^{-1}. Both sets of values, though, interpolate the reported experimental standard enthalpies of sublimation. Moreover, in a very recent review Markov et al. [36] recommend the following experimental values: 181±2 kJmol^{-1} for the standard enthalpy of sublimation and 175±14 kJmol^{-1} for the third law enthalpy. An extrapolation of our results to absolute zero gives 167 kJmol^{-1} for PRP and 174 kJmol^{-1} for GP which, within the error, coincide with the experimental value. Also, the value for GP is in excellent agreement with the theoretical result (174.2 kJmol^{-1}) obtained by Zubov et al. [19] with the same potential.

Although, to the best of our knowledge, there are no experimental data for the enthalpies of melting and vaporization we can predict them from the simulated phase diagrams. For example, for GP at 1600 K (near the triple-point) we estimate ∼53 kJ mol^{-1} for the melting enthalpy and ∼97 kJ mol^{-1} for the vaporization enthalpy. The respective values for PRP at 1700 K (also near the triple- point) are ∼45 kJ mol^{-1} and ∼89 kJ mol^{-1}. The full analysis of the predicted enthalpies of melting and vaporization will be reported soon [37].

The higher enthalpy values for GP reflect that its potential well is narrower and slightly deeper than the PRP well. This is not totally visible in Figure 1 because

the plots are in reduced units.

Finally, it is worth mentioning that we have completed [37] a systematic study of the enthalpies of sublimation of model $C_{n\geq 70}$ fullerenes with GP. As a further test of the reliability of our method for the determination of the triple-point properties, the preliminary result for the triple-point temperature of C_{70} is 1670-1680 K, in excellent agreement with the value (1650 K) recently reported by Abramo et al. [29] obtained through a combination of simulation and theory. The estimated standard enthalpy of sublimation is 194.4 kJmol^{-1}, also in excellent accordance with the available experimental value, 200±6 kJmol^{-1} [34].

5 Conclusions

From the results and discussion of the last sections the following general conclusions can be drawn. The GEMC vapor-liquid coexistence curve determined with PRP has an order parameter ($\rho_L - \rho_V$) greater than the one obtained from GP, reflecting the softer nature of PRP. Thus, the critical temperature (2006±27 K) is greater than the temperature estimated with GP (1951±28 K). These values are in good agreement with the ones from other authors.

Two sets of simulations were performed for the fluid-solid coexistence. The results are significantly different. One set was carried out by setting up the starting points in the limit of high temperature. From those points, decreasing the temperature, a series of coexistent states were calculated by GDMC. We found a triple point temperature of 1858±32 K for PRP and 1898±21 K for GP. According to these results the stable liquid phase of C_{60} extends over ∼150 K for PRP and ∼50 K for GP. These values agree well with results of other authors that were based on free-energy calculations. Nevertheless, either their results or ours show a liquid phase below the triple points. This may be thermodynamically questionable because the liquid there appears to be stable. However, the fluid-solid relative chemical potentials seem to suggest that this set of simulations corresponds to local minima of the Gibbs free-energy.

The origin of this apparent anomalous behavior may presumably be ascribed to the heavy short-range nature of the potentials models and to their narrow and deep wells. In the limit of high temperatures the kinetics is violently collisional and the system eventually approaches a hard-sphere behavior. On the contrary, in the limit of low temperatures the system probably samples the narrow and deep potential wells approaching the usual behavior of attractive potentials.

In the second set of calculations we decreased the temperature of the Gibbs ensemble vapor-liquid simulations by small steps until a temperature was reached below which the liquid phase is not stable anymore and the system assumed a vapor-solid configuration. From that state, in the limit of low temperature (taken as the triple point) a series of coexistent fluid-solid states were simulated by GDMC increasing the temperature of the system. From these calculations we estimated the triple point temperatures at 1570±20 K for PRP and 1529±36 K for GP. Below these points, though, a liquid phase is not observed and from there up the fluid-solid lines display the conventional behavior, in accordance with some theoretical methods and thermodynamics. Moreover, the fluid-solid relative chemical potentials seem to suggest that this set of simulations corresponds to the global minima of the Gibbs free-energy. Also, the radial distribution functions and the self-diffusion coefficients inside the liquid pockets, determined from these triple-points, are consistent with a normal liquid phase and no sign of liquid supercooling was observed. Therefore, we predict a stable liquid phase, for the PRP model, in the range of temperatures 1570±20 K to 2006±27 K. For the GP model, a stable liquid phase between 1529±36 K and 1951±28 K is predicted. Thus, according to these results, the liquid phase of C_{60}, extends over almost 450 K, a temperature range considerably wider than the ones found by other authors based on free-energy calculations.

Taking the previous triple points as starting states and successively decreasing the temperature, we simulated the vapor-solid coexistence lines by GDMC. This enabled the calculation of the enthalpies of sublimation as a function of temperature. The values at 700 K are: 163±9 $kJmol^{-1}$ for PRP and 170±12 $kJmol^{-1}$ for GP, in good agreement with the available experimental results at the same temperature. Additionally, the estimated standard enthalpies of sublimation interpolate the reported experimental values and the third-law enthalpies are in excellent agreement with experimental and theoretical data. Thus, considering the way the simulations were conducted, that is to say, starting from the triple-points determined by our method, we believe that at least the low-temperature triple-point properties should approach those of real C_{60}. We are well-aware that some experiments show that solid C_{60} is unstable at ∼1200 K. Therefore, our conjecture that the low-temperature triple-point properties should approach real C_{60} only can be confirmed or dismissed if there are any experimental means to prevent the decomposition of fullerite. We have also predicted a few values for the enthalpies of melting and vaporization.

We point out that the present fluid-solid simulations performed by the method of Agrawal and Kofke, from the high-temperature limit, reproduce very well the results

reported hitherto from free-energy calculations. The excellent equality of simulated relative chemical potentials of the fluid and solid confirms the consistency of those results. Thus, we believe that both sets of triple-point data are credible as far as the present additive models are concerned. It would be very important to retrace the evolution of the absolute free-energy in the whole density and temperature ranges of interest. Would the low-temperature behaviors detected in the present simulations not also turn out? Calculations in this direction are in progress.

On the whole, the differences between the present interaction potentials do not induce significant qualitative changes in the phase behavior of the two models. However, the differences are clearly reflected in the location of the coexistence lines, the values of the critical and triple point properties as well as in the enthalpies of sublimation.

Finally, it would be interesting to investigate the role of three-body forces on the PRP model. Some years ago, we showed [38] that those forces are of the utmost importance in the vapor-liquid equilibrium of argon. It is expected that they will also induce changes in the critical and triple-point properties of this C_{60} model. Indeed, because such forces are on average repulsive, the order parameter of the vapor-liquid line will presumably decrease. Thus, it seems that the critical temperature should be lower than the one predicted by the present PRP additive model. Work along these lines is also in progress.

Acknowledgments

We would like to thank Professors J.A. Martinho Simões and M.E. Minas Piedade for providing useful references and helpful discussions on the enthalpies of sublimation. Fundação para a Ciência e a Tecnologia (FCT) is gratefully acknowledged for financial support.

References

[1] R. P. S. Fartaria, F. M. S. S. Fernandes, F. F. M. Freitas and P. C. R. Rodrigues: Phase behavior of C_{60} by computer simulation using ab-initio interaction potential, *Int. J. Quantum Chem.* 84 (2001) 375.

[2] R. P. S. Fartaria, F. M. S. S. Fernandes, F. F. M. Freitas and P. C. R. Rodrigues: Erratum: Phase behavior of C_{60} by computer simulation using ab-initio interaction potential, *Int. J. Quantum Chem.* 88 (2002) 355.

[3] J. M. Pacheco and J. P. P. Ramalho: First-principles determination of the dispersion interaction between fullerenes and their intermolecular potential, *Phys. Rev. Lett.* 79 (1997) 3873.

[4] M. H. J. Hagen, E. J. Meijer, G. C. A. M. Mooij, D. Frenkel and H. N. W. Lekkerkerker: Does C_{60} have a liquid phase?, *Lett. to Nature* 365 (1993) 425.

[5] A. Cheng, M. Klein and C. Caccamo: Prediction of the phase diagram of rigid C_{60} molecules, *Phys. Rev. Lett.* 71 (1993) 1200–1203.

[6] L. A. Girifalco: Interaction potential for carbon (C_{60}) molecules, *J. Phys. Chem.* 95 (1991) 5370.

[7] L. A. Girifalco: Molecular properties of fullerene in the gas and solid phases, *J. Phys. Chem.* 96 (1992) 858.

[8] M. Tau, A. Parola, D. Pini and L. Reatto: Differential theory of fluids below the critical temperature: Study of the Lennard-Jones fluid and of a model of C_{60}, *Phys. Rev. E* 52 (1995) 2644–2656.

[9] J. Q. Broughton, J. V. Lill and J. K. Johnson: C60s phase diagram: A full free-energy analysis, *Phys. Rev. B* 55 (1997) 2808–2817.

[10] A. L. C. Ferreira, J. M. Pacheco and J. P. Prates-Ramalho: Phase diagram of C_{60} from ab initio intermolecular potential, *J. Chem. Phys.* 113 (2000) 738.

[11] M. Hasegawa and K. Ohno: Monte Carlo simulation study of the high-temperature phase diagram of model C_{60} molecules, *Journal of Chemical Physics* 111 (1999) 5955–5963.

[12] M. Hasegawa and K. Ohno: Can the visual molecular configuration in computer simulations locate solid–fluid phase boundaries? the case of C_{60}, *J. Chem. Phys.* 113 (2000) 4315.

[13] L. Mederos and G. Navascués: High-temperature phase diagram of the fullerene C_{60}, *Phys. Rev. B* 50 (1994) 1301.

[14] M. Hasegawa and K. Ohno: Density functional theory for the phase diagram of rigid C-60 molecules, *Phys. Rev. E* 54 (1996) 3928.

[15] M. Hasegawa and K. Ohno: The dependence of the phase diagram on the range of the attractive intermolecular forces, *J. Phys.: Condens. Matter* 9 (1997) 3361.

[16] C. Caccamo, D. Costa and A. Fucile: A Gibbs ensemble Monte Carlo study of phase coexistence in model C_{60}, *J. Chem. Phys.* 106 (1997) 255–263.

[17] C. Caccamo: Modified-Hypernetted-Chain determination of the phase diagram of rigid C_{60} molecules, *Phys. Rev. B* 51 (1995) 3387–3390.

[18] C. Caccamo: Integral equation theory description of phase equilibria in classical fluids, *Phys. Rep.* 274 (1996) 1.

[19] V. I. Zubov, J. F. Sanchez-Ortiz, J. N. T. Rabelo and I. V. Zubov: Theoretical study of the saturated vapor pressure and enthalpy of sublimation of C60s fullerite, *Phys. Rev. B* 55 (1997) 6747–6749.

[20] M. C. Abramo and G. Coppolino: Molecular-dynamics study of the Girifalco-model C_{60} at two high-temperature isotherms, *Phys. Rev. B* 58 (1998) 2372.

[21] A. Z. Panagiotopoulos: Direct determination of phase coexistence properties of fluids by Monte-Carlo simulation in a new ensemble, *Mol. Phys.* 61 (1987) 813–826.

[22] A. Panagiotopoulos, N. Quirke, M. Stapleton and D. Tildesley: Phase-equilibria by simulation in the Gibbs ensemble - alternative derivation, generalization and application to mixture and membrane equilibria, *Mol. Phys.* 63 (1988) 527–545.

[23] D. Kofke: Direct evaluation of phase coexistence by molecular simulation via integration along the saturation line, *J. Chem. Phys.* 98 (1993) 4149–4162.

[24] F. M. S. S. Fernandes, R. P. S. Fartaria and F. F. M. Freitas: The starting state in simulations of the fluid-solid coexistence by Gibbs-Duhem integration, *Comp. Phys. Comm.* 141 (2001) 403.

[25] R. Agrawal and D. Kofke: Thermodynamic and structural-properties of model systems at solid-fluid coexistence. 1. fcc and bcc soft spheres, *Mol. Phys.* 85 (1995) 23–42.

[26] R. Agrawal and D. Kofke: Thermodynamic and structural-properties of model systems at solid-fluid coexistence. 2. Melting and sublimation of the Lennard-Jones system, *Mol. Phys.* 85 (1995) 43–59.

[27] C. Z. Wang, C. H. Xu, C. T. Chan and K. M. Ho: Disintegration and formation of C-60, *J. Phys. Chem.* 96 (1992) 3563–3565.

[28] S. Serra, S. Sanguinetti and L. Colombo: Solid-to-liquid phase change and fragmentation in C_{60}, *J. Chem. Phys.* 102 (1995) 2151–2155.

[29] M. C. Abramo, C. Caccamo, D. Costa and G. Pellicane: Phase diagram of model $C_{n\geq 70}$ fullerenes, *Europhys. Lett.* 54 (2001) 468.

[30] N. W. Ashcroft: Elusive diffusive liquids, *Nature* 365 (1993) 387.

[31] H. E. Stanley: *Introduction to Phase Transitions and Critical Phenomena*, Oxford University Press (1971).

[32] D. Frenkel and B. Smit: *Understanding Molecular Simulations: From Algorithms to Applications*, Academic Press, 1st ed. (1996).

[33] H. P. Diogo, R. C. Santos, P. M. Nunes and M. E. M. da Piedade: Ebulliometric apparatus for the measurement of enthalpies of vaporization, *Thermochim. Acta* 249 (1995) 113–120.

[34] P. J. Linstrom and W. G. Mallard (eds.): *NIST Chemistry WebBook, NIST Standard Database Number 69*, National Institute of Standards and Technology, Gaithersburg MD, 20899 (http://webbook.nist.gov) (2001), URL `http://webbook.nist.gov`.

[35] H. P. Diogo, M. E. M. Piedade, T. J. S. Dennis, J. P. Hare, H. W. Kroto, R. Taylor and D. R. M. Walton: Enthalpies of formation of buckminsterfullerene (C_{60}) and of the parent ions C_{60}^{+}, C_{60}^{2+}, C_{60}^{3+} and C_{60}^{-}, *J. Chem. Soc. Faraday Trans.* 89 (1993) 3541.

[36] V. Y. Markov, O. V. Boltalina and L. N. Sidorov: Saturated vapor pressure and the enthalpy of sublimation of fullerenes, *Russian J. Phys. Chem.* 75 (2001) 1.

[37] F. M. S. S. Fernandes, F. F. M. Freitas and R. P. S. Fartaria: Phase diagrams and sublimation enthalpies of model $C_{n\geq 60}$ fullerenes: A comparative study by computer simulation, *J. Phys. Chem. B* 107 (2003) 276–281.

[38] S. P. J. Rodrigues and F. M. S. S. Fernandes: Vapor-liquid-equilibrium of argon - simulation with nonadditive potentials, *J. Phys. Chem.* 98 (1994) 3917.

J. Phys. Chem. B 107 (2003) 276-281

Phase Diagrams and Sublimation Enthalpies of Model $C_{n\geqslant 60}$ Fullerenes. A Comparative Study by Computer Simulation

Fernando M.S. Silva Fernandes[1], Filomena F.M. Freitas, Rui P.S. Fartaria
Laboratory of Molecular Simulation and CECUL, Department of Chemistry and Biochemistry, Faculty of Science, University of Lisboa, Rua Ernesto de Vasconcelos, Bloco C8, Piso 3, 1749-016 Lisboa, Portugal

Abstract

A comparative study, strictly by computer simulation, of the phase diagrams and sublimation enthalpies of model $C_{n\geqslant 60}$ fullerenes is presented. Gibbs ensemble and Gibbs-Duhem integration Monte Carlo simulations were carried out with the effective potentials of Girifalco. The triple-point properties were determined by a direct method recently proposed by us. It is based on the behavior of the Gibbs ensemble simulations at the lowest temperature limit and it does not involve free-energy calculations or any other theoretical approach. According to the present results the liquid phases of the studied fullerenes (C_{60}, C_{70}, C_{76} and C_{84}) extend over ∼450 K. No sign of liquid supercooling was observed. The triple-point temperatures increase from C_{60} to C_{84}. This, and the simultaneous effect of molecular size, cause a relative dislocation of the phase diagrams to higher critical temperatures and lower densities. The simulated enthalpies of sublimation increase from C_{60} to C_{84} and they are in very good agreement with the available experimental data. It is suggested that at least the predicted triple-point properties should also approach the real fullerenes. There is a strong correlation between the phase properties and the details of the interaction potentials, clearly reflected in the relative location of the phase diagram and enthalpy curves. On the whole, the simulated results are in good accordance with the ones recently reported by Abramo et al. [*Europhys. Lett.* **2001**, 54, 468] from a combination of simulation, Modified Hypernetted Chain (MHNC) theory and a kind of "corresponding state" rule, and confirm the consistency of the MHNC

[1]To whom correspondence should be addressed (e-mail: fsilva@fc.ul.pt)

theoretical approach. The reduced properties, which also include the critical and triple-point pressures as well as the sublimation enthalpies, also confirm that some kind of corresponding states rule may be established for fullerenes. On the basis of that, the enthalpy of sublimation of C_{96} is predicted.

1 Introduction

Computer Simulation in Statistical Mechanics is a powerful tool to produce quasi-experimental results for a molecular model. It serves two main purposes. On the one hand, it is able to test a theoretical approach unambiguously. On the other hand, it can confirm, correct or reject a given model against experimental evidence. Therefore, if it is possible to study a molecular model, strictly by computer simulation, then we presumably get the "two sides of the coin". This is the spirit of the present article.

In a recent letter, Abramo et al. [1] reported a systematic study of the phase behavior of model fullerenes based on Girifalco's potential (GP) [2,3]. Monte Carlo simulations were combined with the Modified Hypernetted Chain (MHNC) theoretical approach, to obtain the vapor-liquid coexistence curve, the freezing line, the critical and the triple-point temperatures and densities of C_{70}. Structural and dynamic properties were also calculated in the predicted liquid pocket, showing that the results are consistent with a normal liquid state. No sign of liquid supercooling was observed. From a kind of "corresponding state" rule for fullerenes, the critical and triple-point temperatures and densities for C_{76}, C_{84} and C_{96} were predicted. They concluded that the model fullerenes have liquid phases that extend over almost 500 K, a temperature range considerably wider than the one found for C_{60} ($\sim$90 K).

The mentioned temperature interval of $\sim$90 K for the existence of liquid C_{60} seems, however, to be a matter of choice between two sets of apparent conflicting triple-point data: one, from free-energy Monte Carlo calculations [4], that estimate a triple-point temperature considerably higher than the other, based on simulation combined with the Hypernetted Mean Spherical Approximation and the Modified Hypernetted Chain theories [5–8].

In recent articles [9–11] based on two different simulation approaches to estimate the triple point and using a first-principles interaction potential (PRP) [12] and Girifalco's potential (GP), we have shown that both interaction models for C_{60} are able to reproduce two sets of triple-point properties: one, in which triple point is approached from high temperatures, agrees with free-energy-based calculations; the other, in which the triple point is approached from lower temperatures, is in accordance with the findings of HMSA and MHNC theoretical approaches. The high-temperature set indicates that the liquid phase for C_{60} extends over $\sim$100 K, and the low-temperature one, that the liquid extends over $\sim$450 K. Moreover, we

suggested that the high-temperature results correspond to local minima of the Gibbs free-energy, whereas the low-temperature results correspond to the free-energy global minima. Then, from the low-temperature triple-points we simulated the vapor-solid and liquid-solid coexistence properties. The enthalpies of sublimation, in particular, are in very good agreement with the available experimental data.

The low-temperature triple-point properties were determined by a direct approach recently proposed by us [13]. It is based on the behavior of the Gibbs ensemble vapor-liquid simulations at the lowest temperature limit and it does not involve free-energy calculations or any other theoretical approach.

The main objectives of the present work are: i) to trace the whole phase diagrams of C_{70}, C_{76} and C_{84}, on the basis of GP and using the same techniques as in our previous articles for C_{60}, that is, strictly by computer simulation. ii) to compare the simulated critical and triple-point properties with the ones reported by Abramo et al. [1] for the same potential models, which will be an independent test of the reliability of the MHNC theory used by those authors and of their suggestion on a "corresponding state" rule for fullerenes; iii) to compare the predicted enthalpies of sublimation with the available experimental data, which will assess the reality of the present models; and iv) to correlate the simulated results with the main characteristics of the potential models, which is directly connected to the possibility of establishing a corresponding states rule for fullerenes.

To this end, we also include some of our results for C_{60} reported elsewhere [11].

In the next section we present the potential model and the computational details. The results are shown and discussed in sections 3 and 4. The final section contains the conclusions of this work.

2 Interaction Potentials and Computational Details

The potential of Girifalco (GP) [3] has the form:

$$V(r) = -\alpha\left[\frac{1}{s(s-1)^3} + \frac{1}{s(s+1)^3} - \frac{2}{s^4}\right] + \beta\left[\frac{1}{s(s-1)^9} + \frac{1}{s(s+1)^9} - \frac{2}{s^{10}}\right] \quad (1)$$

where $s = r/R$, $\alpha = N^2A/12R^6$ and $\beta = N^2B/90R^{12}$; N and R are, respectively, the number of carbon atoms and the diameter of the fullerene molecules; A = 32×10^{-60}erg cm^6. and B = 55.77×10^{-105}erg cm^{-12} are constants entering the

Table 1: Parameters of Girifalco's Potential.

	R / nm	R_0 / nm	$-\epsilon/k_B$	α / 10^{-15}erg	β / 10^{-18}erg
C_{60}	0.71	0.9599	3218	74.94	135.95
C_{70}	0.762	1.011	3653	66.7	79.23
C_{76}	0.7991	1.048	3808	59.2	52.87
C_{84}	0.8401	1.0890	4081	53.56	35.42

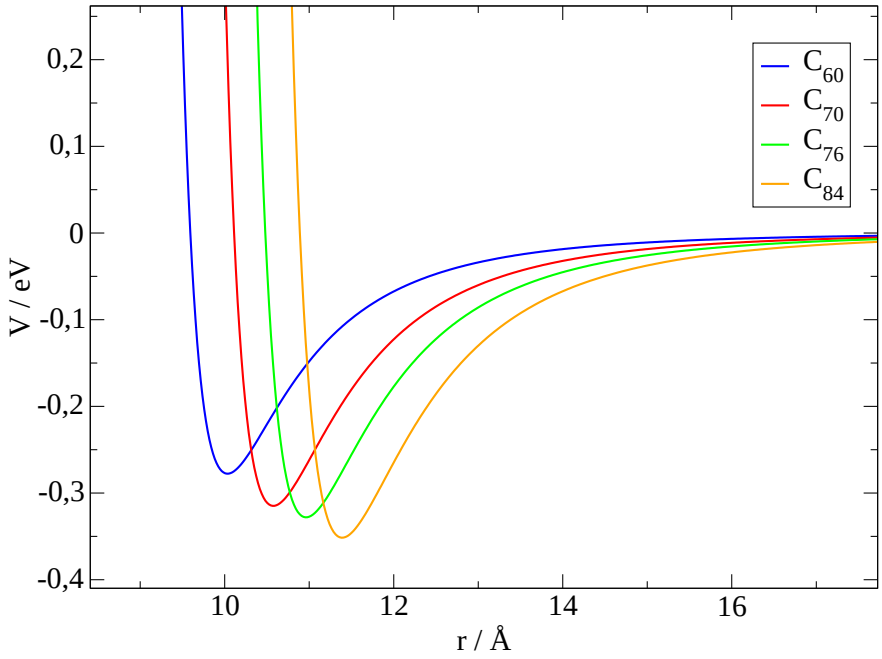

Figure 1: Girifalco's potentials.

Lennard-Jones 12-6 potential through which two carbon sites on different spherical-ized molecules are assumed to interact. The specific parameters for the different fullerenes, presented in Table 1, are the ones given by Abramo et al. [1] and Zubov et al [14].

GP is a very useful interaction potential since it can be easily adapted to fullerenes with a different number of carbon atoms. In addition, our present and previous work, suggest that it is also a good effective potential, at least for some phase properties in the lower temperature limit. Indeed, it is able to reproduce very well the experimental enthalpies of sublimation of the studied C_n fullerenes.

Figure 1, displays the potentials for the fullerenes analyzed in this work. They are all very hard and short-ranged, decaying rapidly to zero for distances greater than

$2R_0$ (R_0 is the effective diameter of the molecules). The repulsive parts have similar trends with the location of R_0 reflecting the molecular size. Also, the potential depths increase significantly from C_{60} to C_{84}. It is important to point out these aspects regarding the discussion in the next sections.

The potentials were truncated at half of the simulation boxes lengths. As these distances were always greater than $2R_0$, long range corrections were not included. Nonetheless, taking into account the study of Hasegawa and Ohno [15], we have verified that the used truncation distances have negligible effects on the phase diagrams. The usual cubic periodic boundary conditions were applied.

The vapor-liquid coexistence curves were obtained by Gibbs ensemble Monte Carlo (GEMC) simulations [16, 17]. The first point was set up by placing the molecules in face-centered-cubic (fcc) lattices with 256 molecules in each box, at appropriate densities, and running the convenient number of cycles for a complete relaxation of the system. The other points were calculated starting from fcc lattices with 256 molecules in each box, at the equilibrium densities of the previous runs. Equilibration runs with 3,000-10,000 cycles were followed by five independent production runs, with 20,000-40,000 cycles each. A GEMC cycle consisted of random displacements of the molecules in each box by considering the boxes independently, by a random rearrangement of the volume of each box in such a way that the total volume remains constant, and by using a number of trials to transfer a molecule virtually from one box to another. The virtual exchange of particles is performed as follows. One of the two boxes is chosen, with equal probability, to receive one particle. Suppose it is box 1. Then, simultaneously in box 2, a randomly chosen particle is destroyed. Thus, the total number of particles in the system remains constant. The joint probabilities of creating/destroying a particle and of the volume changes are given elsewhere. [16–18] It turns out that these probabilities are explicitly independent of the pressures and chemical potentials. Therefore, there is no need to specify the pressures and chemical potentials in GEMC simulations. Even so, we have always calculated them (from the virial theorem and the particle insertion method, respectively) to verify the thermodynamic stability of the vapor-liquid equilibrium. Additionally, the analysis of the probability plots, recommended by Frenkel and Smit [19], was also carried out in some simulations.

The liquid-solid and vapor-solid coexistence curves were obtained by the Gibbs-Duhem Integration Monte Carlo (GDMC) method [20–22]. It consisted of successive and simultaneous NpT simulations in two boxes (each containing 256 molecules) combined with a predictor-corrector scheme to estimate (from the Clapeyron equa-

tion) the temperature, as a function of pressure, for the next point along the coexistence line. The coupling procedure described by Kofke [20] was applied in some calculations. A similar statistics to the GEMC simulations was also carried out. Also, in GDMC calculations, the chemical potentials do not explicitly appear in the final formulation of the method. Despite the explicit absence of the chemical potentials in Gibbs MC simulations, the powerful hand of the free energy is always present, however invisible. Thus, those simulations should ultimately be equivalent to the so-called free-energy calculations referred to in the abstract and in the body of the present article. The heart of the matter in such calculations is the explicit determination of the free energies for interacting systems from the well-known free energies of the ideal gas and the Einstein crystal. [18]

An important issue in fluid-solid simulations by the GDMC method is the definition of the starting state to initiate the integration of the Clapeyron equation. In the present work, we defined that point through the approach recently proposed by us [13]. The full computational details of the method can be seen in the original article. A discussion of the differences between our approach and other alternative proposed by Agrawal and Kofke [21, 22] was presented elsewhere [9, 11]. In short, the method consists of decreasing the temperature of the GEMC vapor-liquid equilibrium by small steps (ΔT$\sim$10K) until a temperature is reached below which the liquid phase is not stable anymore. The system readily assumes a vapor-solid configuration, that is, spontaneous freezing is detected in the high density box. Those values of temperature, the densities and configurational energies (just before and after freezing) and the vapor pressure are taken as an estimate of the triple-point properties. From that point, we successively calculated the liquid-solid lines by increasing the temperature and the vapor-solid lines by decreasing the temperature. We should mention that, if the conditions of the respective computational algorithm are fulfilled, the method does not lead to the supercooling of the liquid and it is able to determine the triple-point temperature in a very narrow interval ($\sim$10K for fullerenes), within the maximum error usually reported for that property. Moreover, the solid generated by the spontaneous freezing is a quasi-perfect, not defect-rich, face-centered-cubic lattice.

In order to test the reliability of the fluid-solid simulations, we calculated, from the raw data for each phase, the relative chemical potentials, $\Delta(\beta\mu)$, by applying a simple trapezoidal rule to the Gibbs-Duhem equation:

$$d(\beta\mu) = h\, d\beta + \beta p/\rho\, d\, lnp \tag{2}$$

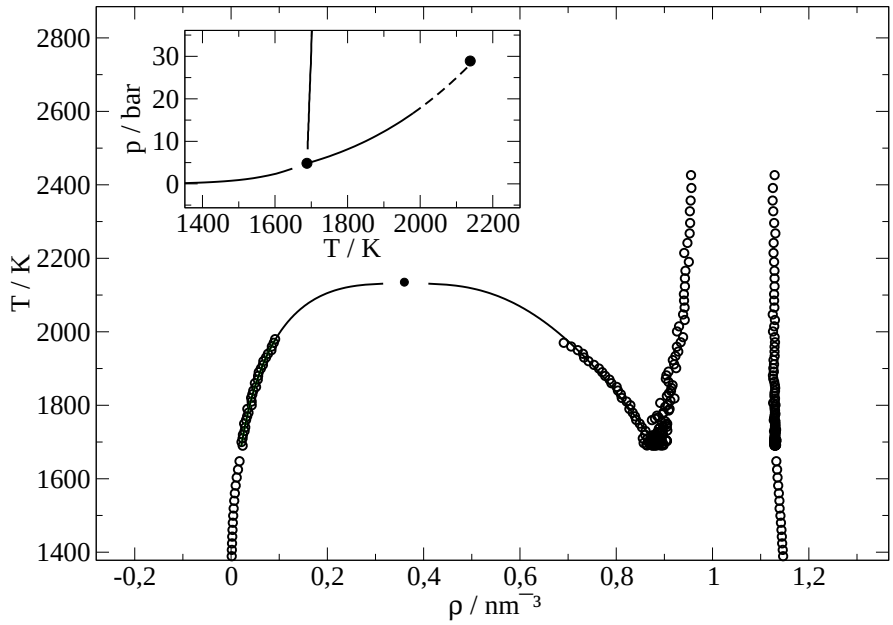

Figure 2: Temperature-density and pressure-temperature (inset) phase diagrams of C_{70}.

where $h = u + p/\rho$ is the molar enthalpy and $\beta = 1/k_B T$.

The critical temperatures and densities were estimated by fitting the vapor-liquid data to the laws of rectilinear diameters and order parameter scaling [23] with a critical exponent $\sim$0.33. The pressures were fitted to the Clapeyron equation. The final triple-point properties were assessed by fitting the fluid-solid raw data and intersecting the vapor-liquid lines with the freezing lines.

3 Phase Diagrams

Figure 2, displays the temperature-density and pressure-temperature phase diagrams of C_{70}. Table 2, presents numerical data for the vapor-liquid equilibrium and Table 3, the relative chemical potentials for the fluid-solid equilibrium.

The equality of the pressures and chemical potentials, within the error bars, of the vapor-liquid simulations suggests a good thermodynamic stability for this region of the phase diagram. Regarding the relative chemical potentials of the fluid-solid equilibrium, no error bars were determined. Even so, their coincidence in both phases is remarkable, showing the consistency of the simulations.

Figure 3, shows the radial distribution functions for the liquid-solid coexistence near the triple-point of C_{70}. They indicate the usual behavior of a liquid and a face-

Table 2: Vapor-liquid coexistence of C_{70}: densities, ρ, pressures, p, and chemical potentials, μ. (The numbers in parenthesis are rms deviations calculated from five independent runs with 20,000 MC cycles each.)

T / K	ρ_V / nm^{-3}	ρ_L / nm^{-3}	p_V / bar	p_L / bar	$-\mu_V$ / 10^{-13}erg	$-\mu_L$ / 10^{-13}erg
1980	0.091(0.005)	0.667(0.021)	16.83(0.54)	18.24(2.81)	8.26(0.05)	8.33(0.12)
1920	0.067(0.003)	0.742(0.006)	13.09(0.41)	12.03(3.03)	8.49(0.05)	8.58(0.12)
1890	0.057(0.003)	0.771(0.004)	11.45(0.50)	10.41(2.05)	8.63(0.08)	8.55(0.31)
1800	0.043(0.002)	0.829(0.004)	8.47(0.36)	9.73(2.93)	8.78(0.08)	8.51(0.20)
1770	0.033(0.002)	0.839(0.005)	6.76(0.40)	7.28(1.90)	9.06(0.12)	9.10(0.67)
1710	0.024(0.002)	0.865(0.005)	4.88(0.31)	5.76(2.10)	9.37(0.14)	8.94(0.27)
1690	0.024(0.000)	0.882(0.004)	4.85(0.07)	4.55(4.71)	9.26(0.02)	9.26(0.27)

Table 3: Relative chemical potentials for fluid-solid coexistence of C_{70}.

	Fluid	Solid
T / K	$\Delta(\beta\mu)$	$\Delta(\beta\mu)$
2501	0.00	0.00
2267	-2.34	-2.34
2084	-4.24	-4.25
1959	-5.73	-5.74
1872	-6.85	-6.87
1812	-7.67	-7.68
1771	-8.25	-8.27
1743	-8.65	-8.67
1725	-8.93	-8.95
1712	-9.13	-9.14
1704	-9.26	-9.27
1698	-9.35	-9.36
1694	-9.41	-9.42
1691	-9.45	-9.46
1690	-9.46	-9.48

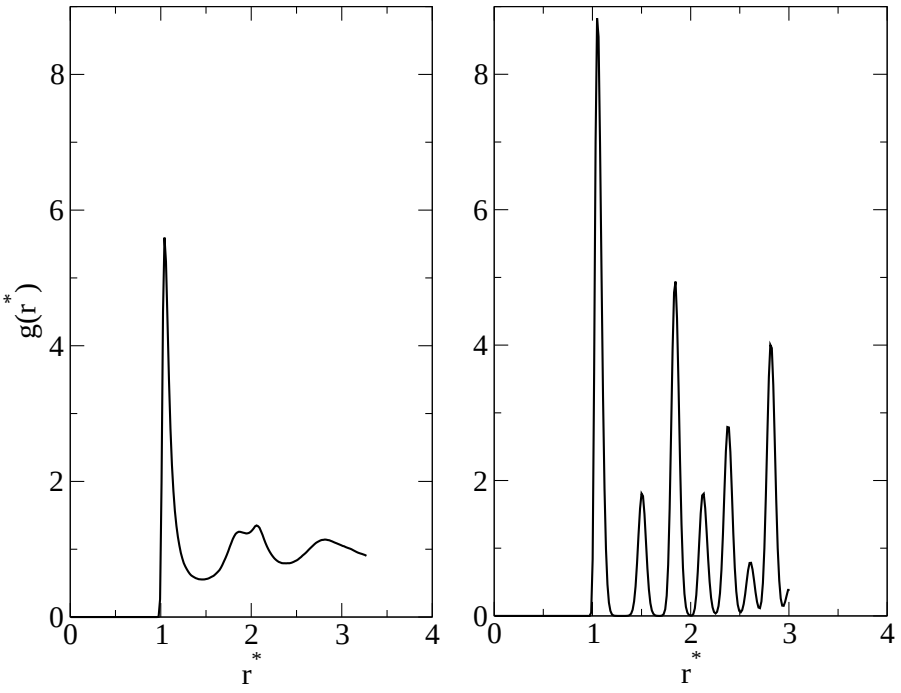

Figure 3: Radial distribution functions for liquid-solid coexistence of C_{70} (1700K, near the triple point).

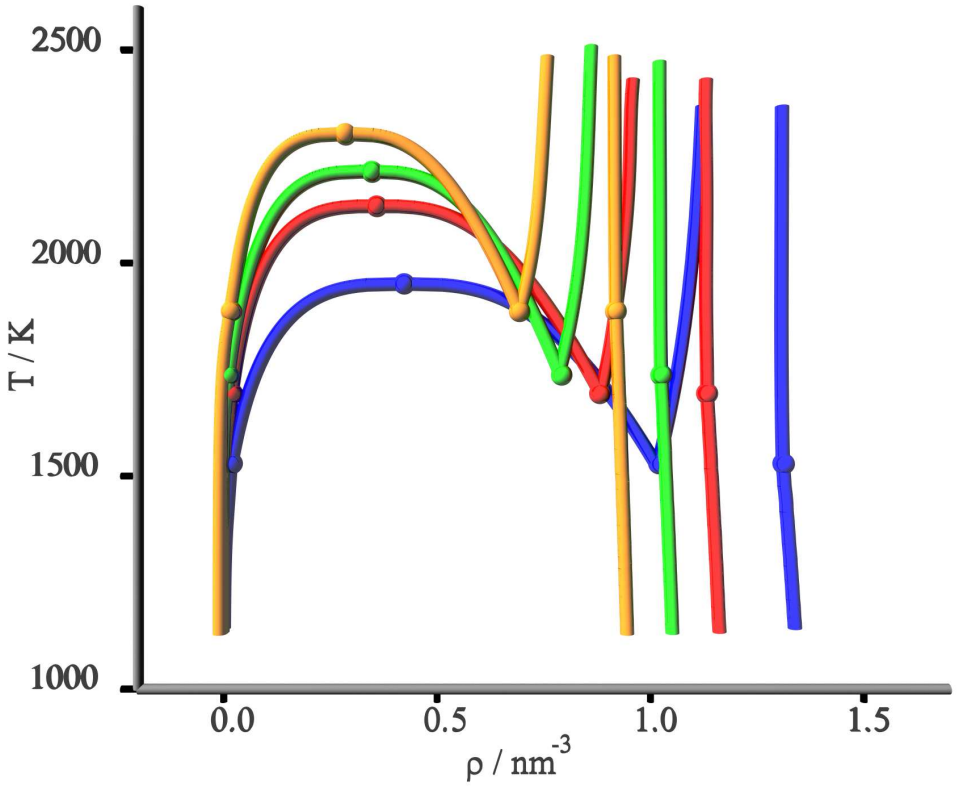

Figure 4: Temperature-density phase diagrams : C_{60} - blue; C_{70} - red; C_{76} - green; C_{84} - orange.

centered-cubic solid lattice respectively. The shoulders in the second peak of the liquid function, also reported and discussed for C_{60} [5, 9, 11], indicate the presence of solid or glasslike clusters.

Figure 4, displays the temperature-density phase diagrams for C_{60}, C_{70}, C_{76} and C_{84} obtained by fitting the simulation raw data. Table 4, contains the respective numerical results for critical and triple-point properties as well as some results recently obtained by Abramo et al. [1]. The results for C_{60} have been reported elsewhere [11].

All of the studied model fullerenes present liquid pockets that extend over ∼450 K. No liquid supercooling was observed. The radial distribution functions inside those pockets show patterns typical of the liquid state. In addition, we calculated, by canonical molecular dynamics, self-diffusion coefficients for some states. They were always of the order of 10^{-5} cm^2 s^{-1}, a magnitude consistent with a normal liquid phase [1, 24].

The rise of the triple-point temperature from C_{60} to C_{84}, reflects the increase of their potential depths (see Figure 1 and 4). This, and the simultaneous effect of

Table 4: Critical and triple-point properties.

		ρ_{cr} / nm^{-3}	T_{cr} / K	p_{cr} / bar	$\rho_{tr,liq}$ / nm^{-3}	T_{tr} / K	p_{tr} / bar
C_{60}	[11]	0.42±0.01	1951±28	33±9	1.02±0.01	1529±36	4±19
	[8]	0.42	1941		1.00	1500	
C_{70}	this work	0.36±0.03	2131±44	29.5±1.3	0.88±0.01	1694±49	4.44±1.31
	[1]	0.376	2140	-	0.88	1650	-
C_{76}	this work	0.35±0.03	2204±59	32.5±1.4	0.79±0.01	1737±34	4.41±2.59
C_{84}	this work	0.29±0.05	2293±60	24.4±1.6	0.69±0.01	1884±50	5.83±2.19
		estimates from "corresponding states" rule.					
C_{70}	[1]	0.36	2190	-	0.85	1703	-
C_{76}	[1]	0.32	2284	-	0.77	1775	-
C_{84}	[1]	0.29	2448	-	0.68	1902	-

Table 5: Triple and critical point properties in reduced units.

	ρ_{cr}^{*}	T_{cr}^{*}	p_{cr}^{*}	$\rho_{tr,liq}^{*}$	T_{tr}^{*}	p_{tr}^{*}
C_{60}	0.37±0.01	0.60±0.01	0.07±0.02	0.90±0.01	0.47±0.01	0.01±0.04
C_{70}	0.37±0.04	0.58±0.01	0.06±0.01	0.90±0.01	0.46±0.01	0.01±0.01
C_{76}	0.40±0.04	0.58±0.01	0.07±0.01	0.91±0.01	0.46±0.01	0.01±0.01
C_{84}	0.38±0.07	0.56±0.01	0.06±0.01	0.89±0.01	0.46±0.01	0.01±0.01

molecular size, causes a relative dislocation of the phase diagrams to higher critical temperatures and lower densities.

As far as the critical and triple-point pressures are concerned, it is expected that they should also significantly increase from C_{60} to C_{84} considering the rise in the temperature. The respective pressures for the different fullerenes are, however, of the same order of magnitude, which seems to reflect the relative decrease in the densities.

Regarding the critical and triple-point properties in reduced units, presented in Table 5, they seem to confirm that some kind of corresponding states rule may be established for fullerenes according to the suggestion of Abramo et al. [1]. Incidentally, the reduced properties were directly obtained from the simulated results by the usual equations: $T^* = T\,k_B/\epsilon$; $\rho^* = \rho\,R_0^3$; $p^* = p\,R_0^3/\epsilon$. In the next section we shall report the reduced enthalpies of sublimation.

Overall, our results agree very well with those of Abramo et al. However, the present simulated critical temperatures are lower than the ones worked out by them from the "corresponding state" rule. This also seems to be in accordance with their mentioned preliminary GEMC simulations of C_{84}. Moreover, the present results confirms the consistency of the MHNC theoretical approach.

4 Enthalpies of Sublimation

From the vapor-solid coexistence simulations, we worked out the enthalpies of sublimation as a function of temperature, starting at the predicted triple-points. They are displayed in Figure 5. The results for C_{60} have been reported elsewhere [11]. The simulation results were fitted to equation [25]:

$$\Delta_{sub}H = ZRT^2\,\frac{d\,\ln p}{d\,T} \tag{3}$$

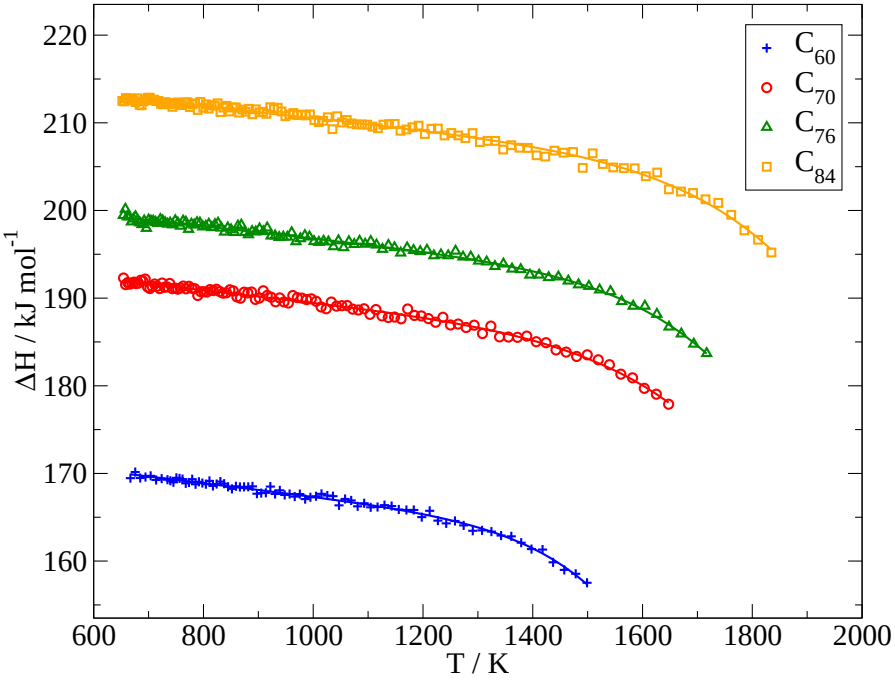

Figure 5: Enthalpies of sublimation as function of temperature (solid lines - fitting to eq. 3).

with

$$\ln p = A + \frac{B}{T} + C \ln T + DT^E \tag{4}$$

Table 6, contains some numerical values. They are in very good agreement with the available experimental data [26, 27]. The enthalpies at 700 K (ΔH_{700}) were directly obtained from the simulated vapor-solid results. The standard (ΔH^o_{298}) and third-law enthalpies (ΔH^o_0) were estimated by an extrapolation of the simulation results to 298.15 and 0 K respectively. The error bars, for the simulated results

Table 6: Enthalpies of sublimation in kJ mol^{-1}.

	simulated results			experimental results		
				NIST [26]	Markov et al. [27]	
	700 K	298 K	0 K	~700 K	298 K	0 K
C_{60}	170±12	173±12	174	176±2	181±2	175±14
C_{70}	191±13	194±13	196	196±7	200±6	-
C_{76}	198±14	201±14	203	-	206±4	-
C_{84}	212±15	215±15	217	-	225±6	-

presented in Table 6, are the maxima of the standard deviations for the sublimation enthalpies of each fullerene at different temperatures.

An increase in the enthalpy of sublimation from C_{60} to C_{84} reflects, once again, the relative increase in their potential depths (see Figure 1). It is worth to point out the relative variation of the enthalpies from C_{60} to C_{84}. In fact, the differences between the potential depths (see Table 1) are: $\Delta\epsilon/k_B$(C_{70}-C_{60})= 435 K; $\Delta\epsilon/k_B$(C_{76}-C_{70})= 155 K and $\Delta\epsilon/k_B$(C_{84}-C_{76}) = 273 K. These differences clearly influence the relative location of the enthalpy curves (see Figure 5). The effect is also clearly visible in the critical and triple-point regions of the phase diagrams (see Figure 4).

We also calculated, for example, the third-law sublimation enthalpies in reduced units. The value is 6.4 for all fullerenes, in excellent accordance with a corresponding states rule. Thus, taking the potential depth indicated by Abramo et al [1] for C_{96}, we predict its third-law enthalpy of sublimation: $\Delta H_0^o = 222$ kJ mol^{-1}.

Finally, the present results for the enthalpies of sublimation constitute a further test of the consistency of our method for the determination of triple-point properties and suggest that at least these properties should also approach the real fullerenes.

5 Conclusions

We have presented a comparative study of the phase diagrams and enthalpies of sublimation of four model C_n fullerenes carried out strictly by computer simulation.

In view of the present results the following general conclusions can be drawn. The liquid pockets for the studied fullerenes extend over ∼450 K. No liquid supercooling was observed. The radial distribution functions and self-diffusion coefficients are consistent with a normal liquid phase.

There is a rise in the triple-point temperatures from C_{60} to C_{84} due to the increase in the respective potential depths. This, and the simultaneous effect of molecular size, cause a relative dislocation of the phase diagrams to higher critical temperatures and lower densities. The respective critical and triple-point pressures, however, are on the same order of magnitude what seems to reflect the relative decreasing in the densities.

Regarding the critical and triple-point properties, as well as the sublimation enthalpies, in reduced units, the results seem to confirm that some kind of corresponding state rule may be established for fullerenes according to the recent suggestion of Abramo et al. On the basis of that, the sublimation enthalpy of C_{96} is predicted.

Overall, our results, obtained strictly by computer simulation, are in good accordance with the ones of Abramo et al., from a combination of simulation and theory, and confirm the consistency of the MHNC theoretical approach.

The enthalpies of sublimation are in excellent agreement with the available experimental data. There is an increase of the sublimation enthalpies from C_{60} to C_{84}, due to the relative increase of the potential depths. The differences between the potential depths are also clearly reflected in the relative location of the phase diagram and enthalpy curves.

Because the calculation of the sublimation enthalpies started from the predicted triple-points, it is suggested that at least the triple-point properties of the present model should also approach those of real fullerenes. Considering that some experiments show that solid C_{60} is unstable at $\sim$1200 K, this suggestion only may be confirmed, or rejected, if there are any experimental means to prevent the decomposition of fullerites.

Finally, we believe that the present results are valuable in two ways: first, they give an estimate of the phase diagrams of an important class of carbon forms, and second, they provide insight into the relation between thermodynamic properties and the underlying potential functions.

Acknowledgments

Fundação para a Ciência e a Tecnologia (FCT) is gratefully acknowledged for financial support.

We are also thankful to Intel Corporation for the free access to their compilers and to the GNU and Linux communities for the invaluable tools they offer.

References

[1] M. C. Abramo, C. Caccamo, D. Costa and G. Pellicane: Phase diagram of model $C_{n\geq 70}$ fullerenes, *Europhys. Lett.* 54 (2001) 468.

[2] L. A. Girifalco: Interaction potential for carbon (C_{60}) molecules, *J. Phys. Chem.* 95 (1991) 5370.

[3] L. A. Girifalco: Molecular properties of fullerene in the gas and solid phases, *J. Phys. Chem.* 96 (1992) 858.

[4] M. Hasegawa and K. Ohno: Monte Carlo simulation study of the high-temperature phase diagram of model C_{60} molecules, *Journal of Chemical Physics* 111 (1999) 5955–5963.

[5] A. Cheng, M. Klein and C. Caccamo: Prediction of the phase diagram of rigid C_{60} molecules, *Phys. Rev. Lett.* 71 (1993) 1200–1203.

[6] C. Caccamo: Modified-Hypernetted-Chain determination of the phase diagram of rigid C_{60} molecules, *Phys. Rev. B* 51 (1995) 3387–3390.

[7] C. Caccamo: Integral equation theory description of phase equilibria in classical fluids, *Phys. Rep.* 274 (1996) 1.

[8] C. Caccamo, D. Costa and A. Fucile: A Gibbs ensemble Monte Carlo study of phase coexistence in model C_{60}, *J. Chem. Phys.* 106 (1997) 255–263.

[9] R. P. S. Fartaria, F. M. S. S. Fernandes, F. F. M. Freitas and P. C. R. Rodrigues: Phase behavior of C_{60} by computer simulation using ab-initio interaction potential, *Int. J. Quantum Chem.* 84 (2001) 375.

[10] R. P. S. Fartaria, F. M. S. S. Fernandes, F. F. M. Freitas and P. C. R. Rodrigues: Erratum: Phase behavior of C_{60} by computer simulation using ab-initio interaction potential, *Int. J. Quantum Chem.* 88 (2002) 355.

[11] R. P. S. Fartaria, F. M. S. S. Fernandes and F. F. M. Freitas: Monte Carlo simulation of the phase diagram of C_{60} using two interaction potentials. enthalpies of sublimation, *J. Phys. Chem. B* 106 (2002) 10227–10232.

[12] J. M. Pacheco and J. P. P. Ramalho: First-principles determination of the dispersion interaction between fullerenes and their intermolecular potential, *Phys. Rev. Lett.* 79 (1997) 3873.

[13] F. M. S. S. Fernandes, R. P. S. Fartaria and F. F. M. Freitas: The starting state in simulations of the fluid-solid coexistence by Gibbs-Duhem integration, *Comp. Phys. Comm.* 141 (2001) 403.

[14] V. I. Zubov, N. P. Tretiakov and I. V. Zubov: Molecular interactions in fullerenes and equilibrium of higher fullerites C_{76} and C_{84} with their vapors, *Eur. Phys. J. B* 17 (2000) 629.

[15] M. Hasegawa and K. Ohno: The dependence of the phase diagram on the range of the attractive intermolecular forces, *J. Phys.: Condens. Matter* 9 (1997) 3361.

[16] A. Z. Panagiotopoulos: Direct determination of phase coexistence properties of fluids by Monte-Carlo simulation in a new ensemble, *Mol. Phys.* 61 (1987) 813–826.

[17] A. Panagiotopoulos, N. Quirke, M. Stapleton and D. Tildesley: Phase-equilibria by simulation in the Gibbs ensemble - alternative derivation, generalization and application to mixture and membrane equilibria, *Mol. Phys.* 63 (1988) 527–545.

[18] D. Frenkel and B. Smit: *Understanding Molecular Simulations: From Algorithms to Applications*, Academic Press, 1st ed. (1996).

[19] D. Frenkel and B. Smit: *Understanding Molecular Simulations: From Algorithms to Applications*, Academic Press, 2nd ed. (2002).

[20] D. Kofke: Direct evaluation of phase coexistence by molecular simulation via integration along the saturation line, *J. Chem. Phys.* 98 (1993) 4149–4162.

[21] R. Agrawal and D. Kofke: Thermodynamic and structural-properties of model systems at solid-fluid coexistence. 1. fcc and bcc soft spheres, *Mol. Phys.* 85 (1995) 23–42.

[22] R. Agrawal and D. Kofke: Thermodynamic and structural-properties of model systems at solid-fluid coexistence. 2. Melting and sublimation of the Lennard-Jones system, *Mol. Phys.* 85 (1995) 43–59.

[23] H. E. Stanley: *Introduction to Phase Transitions and Critical Phenomena*, Oxford University Press (1971).

[24] M. C. Abramo and G. Coppolino: Molecular-dynamics study of the Girifalco-model C_{60} at two high-temperature isotherms, *Phys. Rev. B* 58 (1998) 2372.

[25] H. P. Diogo, R. C. Santos, P. M. Nunes and M. E. M. da Piedade: Ebulliometric apparatus for the measurement of enthalpies of vaporization, *Thermochim. Acta* 249 (1995) 113–120.

[26] P. J. Linstrom and W. G. Mallard (eds.): *NIST Chemistry WebBook, NIST Standard Database Number 69*, National Institute of Standards and

Technology, Gaithersburg MD, 20899 (http://webbook.nist.gov) (2001), URL `http://webbook.nist.gov`.

[27] V. Y. Markov, O. V. Boltalina and L. N. Sidorov: Saturated vapor pressure and the enthalpy of sublimation of fullerenes, *Russian J. Phys. Chem.* 75 (2001) 1.

J. Phys. Chem. B 108 (2004) 9251-9255

Phase Diagram and Sublimation Enthalpies of Model C_{60} Revisited

Fernando M.S. Silva Fernandes[1], Filomena F.M. Freitas, Rui P.S. Fartaria
Laboratory of Molecular Simulation and CECUL, Department of Chemistry and Biochemistry, Faculty of Sciences, University of Lisboa, Rua Ernesto de Vasconcelos, Bloco C8, Piso 3, 1749-016 Lisboa, Portugal

Abstract

The objective of the present paper is to reassess our previous results and conclusions on the simulation of model C_{60}, and other fullerenes, in view of the results recently reported by other authors. We report new sublimation enthalpies in good agreement with the available experimental data and recente theoretical results. A special attention is given to the pressures along the coexistent phases. We also present a comparative study, by NVT and NpT simulations, of supercritical isotherms for Lennard-Jonesium and C_{60}, in order to clarify the Gibbs Ensemble and Gibbs-Duhem Monte Carlo calculations. It is suggested that even in the case of C_{60} the stable fluid-solid transitions can be detected through the visual analysis of the equations of state. Finally, we critically review our previous works on model fullerenes.

[1]To whom correspondence should be addressed (e-mail: fsilva@fc.ul.pt)

1 Introduction

In recent articles [1–4] we have reported the phase diagrams and enthalpies of sublimation of model C_{60} by Gibbs-Ensemble (GE) and Gibbs-Duhem (GD) Monte Carlo simulations based on the Girifalco potential (GP) [5, 6] and on the ab-initio potential (PRP) of Pacheco and Ramalho [7]. Starting from different initial conditions, however using the same simulation procedures, we have suggested that both interaction potentials show the existence of two sets of apparently conflicting triple point properties. One, in which the triple point is approached from fluid-solid states at high temperatures, agrees well with free-energy-based calculations [8, 9]. The other, in which the "triple point" is reached by extending the GE vapor-liquid lines to low temperatures, is in a reasonable accordance with the results of the Modified Hypernetted Chain (MHCN) theory [10, 11] combined with computer simulations and the one-phase freezing criterion (OPFC) [12]. The triple point temperature of the first set is considerably higher than the temperature of the second set. Conversely, the triple point density of the first set is lower than the density of the second one. We have also argued that the high-temperature results correspond to local minima of the Gibbs free energy, whereas the low-temperature results correspond to the free energy global minima. Moreover, the enthalpies of sublimation obtained from the vapor-solid coexistence, starting at the low-temperature "triple point", are in good agreement with the available experimental data.

In recent investigations, Costa and co-workers [9, 13] have suggested an explanation for the discrepancy between the prediction of several structural indicators and the results of full free energy calculations, to locate the fluid phase boundaries. They have calculated the high-temperature phase diagram of the GP model, based on extensive absolute free energies, Monte Carlo simulations and several theoretical approaches. In parallel, the entropy of the fluid phase has also been systematically analysed, given that in their earlier articles [10, 11, 14] the onset of freezing was associated with the vanishing of the residual entropy, ΔS=0, following the prescription of OPFC. They have also reported the freezing line of the hard-sphere fluid corresponding to the C_{60} model, according to the Weeks, Chandler and Andersen (WCA) theory [15]. Some of their conclusions are: i) the model C_{60} has, confidently, a narrow stable liquid phase interval ($\sim$1875-1940 K); ii) due to the strong attractive and rapidly decaying potential well, the onset of the solid-liquid transition is mainly driven by "energetic" rather than entropic effects, resulting in the anticipation of the freezing threshold to lower densities than those predicted by solely structural

conditions and iii) the OPFC freezing line almost coincides with the WCA line, suggesting that the ΔS=0 locus tends to overestimate the coexisting fluid density, thus affecting the location of the triple point.

This scenario has motivated us to reanalyse our previous results and conclusions. Meanwhile, more recently, Chen and co-workers [16] have showed that "the saturated vaporization pressures are higher than the saturated sublimation pressures below the "high-temperature" triple points. Because the chemical potential of the vapor phase increases with pressure, it is obvious that the phase with lower saturation pressure also have the lower Gibbs free energy". This, of course, refutes our arguments regarding the free energies of model fullerenes [3, 4].

The objective of the present article is to reassess our previous results and conclusions on the simulation of model C_{60} in view of the results of the authors referred to above. We report new sublimation enthalpies for the GP and PRP interaction models, now based on the vapor-solid coexistence starting from the high-temperature triple points. A special attention is given to the pressures along the coexistent phases. We also present a comparative study, by NVT and NpT simulations, of supercritical isotherms for Lennard-Jonesium and C_{60}, in order to clarify the Gibbs Ensemble and Gibbs-Duhem Monte Carlo calculations and to show that even in the case of C_{60} the stable fluid-solid transitions can be detected through the visual analysis of the equations of state. Finally, we critically review our previous works on model fullerenes.

2 Phase Diagram, Enthalpies of Sublimation and Pressure lines

The calculations have been carried out using the GP and PRP interaction models and the simulation procedures described elsewhere [3, 4]. Figure 1, displays the whole temperature-density phase diagram of GP. Our previous fluid-solid results corresponding to the low-temperature "triple point" (named as GD-up), and the OPFC and WCA freezing lines of Costa et al. [9] are also included. The fluid-solid results corresponding to the high-temperature triple-point are named as GD-down. The temperature-density phase diagram of PRP is similar to the GP one and it is not represented. Figures 2 and 3, show the enthalpies of sublimation as a function of temperature, calculated from the high and low-temperature triple points for GP

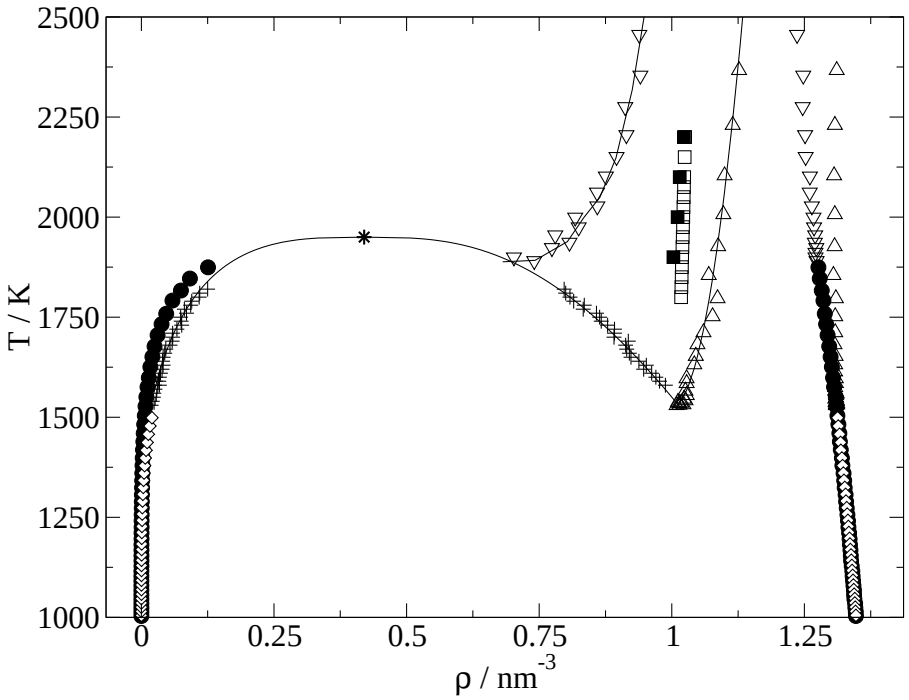

Figure 1: Temperature-density phase diagram of GP model. Estimated critical point (∗); Gibbs-ensemble (vapor-liquid, +). Gibbs-Duhem method: solid-fluid from high-temperature (▽); solid-fluid from low-temperature (△); solid-vapor from high-temperature triple-point (●); solid-vapor from "low-temperature triple-point" (◇). OPFC (■) and WCA (□) from [9]. Solid lines are guides to the eye.

and PRP respectively. The results were fitted to equation [17]:

$$\Delta_{sub}H = ZRT^2 \frac{d \ln p}{dT} \tag{1}$$

with

$$\ln p = A + \frac{B}{T} + C \ln T + DT^E. \tag{2}$$

Table 1, contains some simulated and experimental values. The error bars affecting the simulated results at 700 K are r.m.s. deviations. The values at 298K and 0K are extrapolations of the fitting equation 1.

The results apparently suggest the existence of two sets of triple point properties for the GP and PRP interaction models. However, as we shall see, the low-temperature set is not thermodynamically stable.

The narrow stable liquid phase intervals (1880-1980 K), (1875-1940 K) and (1876±13 - 1946±4 K) predicted respectively by Hasegawa and Ohno [8], Costa et al. [9] and Chen et al. [16] for GP are, within the error bars, in very good agree-

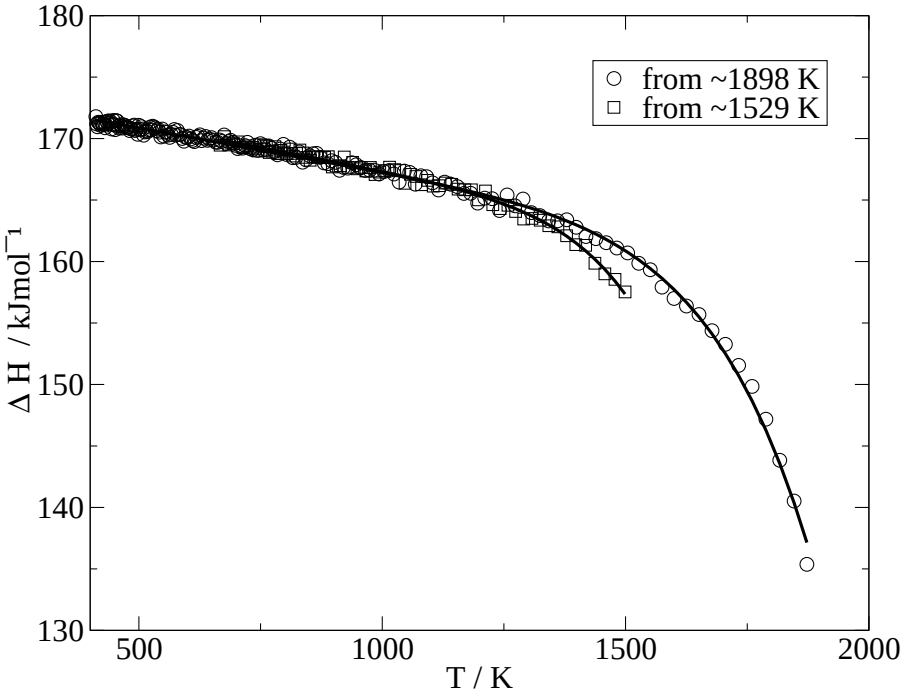

Figure 2: Enthalpies of sublimation as a function of temperature for GP model. Fitting to equation 1 (–).

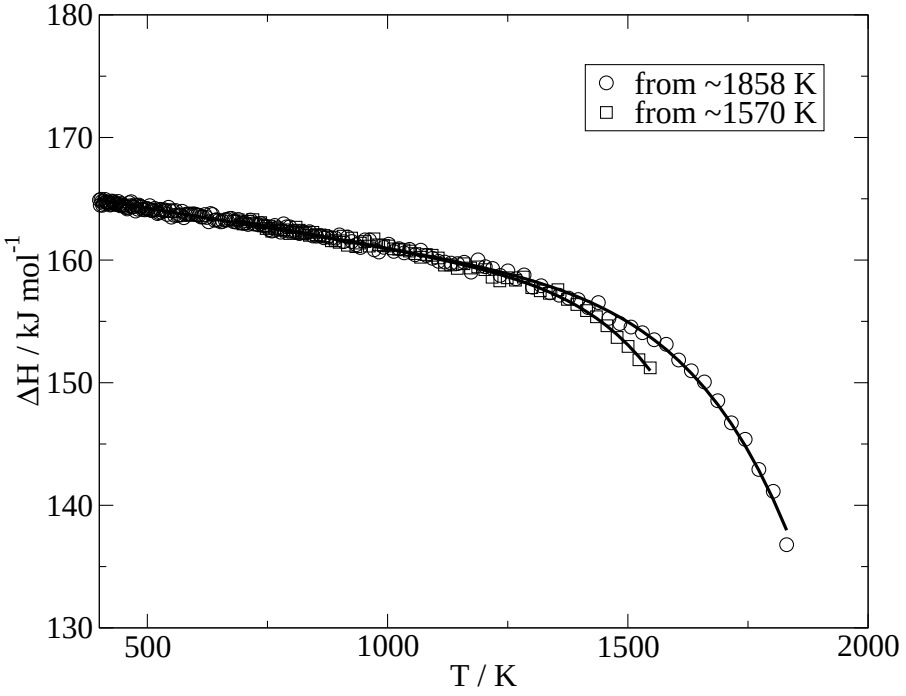

Figure 3: Enthalpies of sublimation as a function of temperature for PRP model. Fitting to equation 1 (–).

Table 1: Enthalpies of sublimation in kJ mol^{-1}.

	simulated results		
	GP		
	700 K	298 K	0 K
from ∼1529	170±12	173	174
from ∼1898	170±12	172	174
	PRP		
	700 K	298 K	0 K
from ∼1570	163±9	166	167
from ∼1858	163±10	166	167
	experimental results		
	NIST [18]	Markov et al. [19]	
	∼700 K	298 K	0 K
	176±2	181±2	175±14

ment with our simulation result [3] corresponding to the high-temperature triple point (1898±21-1951±28 K).

Both freezing lines depend on density and temperature, though the line from the high-temperature triple point spans a wider range of density versus temperature. The GD-up freezing line, does not entirely coincide with the OPFC and WCA lines. Nonetheless, their extrapolation approaches our "low-temperature triple point" density and temperature. The structural indicators do appear to identify a very restricted range of density versus temperature, over which structural reorganization of the fluid phase should be established in order to mainly satisfy entropic demands, as proposed by Costa and co-workers [9, 13].

Hoover and Ree [20], many years ago, determined that the hard-sphere system has a fluid-solid transition for densities, relative to the close-packing, in the range 0.667-0.736. Thus, a fluid of hard-spheres with a diameter of 0.9599 nm (the effective diameter of the C_{60} molecule used in the present simulations) should freeze at a density ∼1.07 nm^{-3}. This value is just inside the range of density versus temperature of the GD-up freezing line. We have overlooked this important result in the conclusions of one of our previous articles [3], where we have suggested the approach to hard-sphere behaviour for the GD-down freezing line.

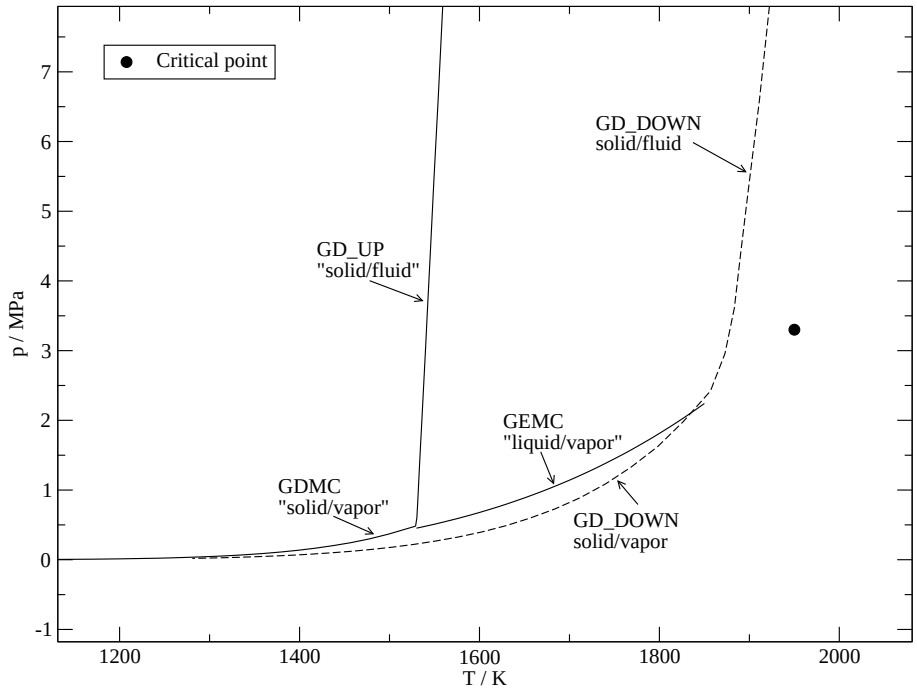

Figure 4: Pressure-temperature phase diagram of GP model.

The present simulations clearly show that the vapor-solid lines, calculated from the two triple points and interaction potentials, coincide for temperatures below ∼1250 K. Consequently, the model sublimation enthalpies are equal below that temperature and they are in good agreement with the available experimental data, particularly the ones corresponding to GP. Thus, the experimental data can not be used to discard one of the simulation triple point estimates contradicting what we have conjectured in our previous articles [3, 4]. Incidentally, Zubov et al. [21] have reported, in a recent theoretical study, sublimation enthalpies in excellent agreement with our simulation results at 700 K. However, the noticeable discrepancy (on the vapor side) of the vapor-solid lines above ∼1250 K (see Figure 1), which is also reflected in the sublimation enthalpies above that temperature (see Figures 2 and 3), called for a further thorough analysis of our pressure-temperature diagrams, displayed in Figure 4 for GP. A similar diagram is observed for PRP. It is clear that the saturated sublimation pressures are systematically less than the saturated vaporization pressures, but below ∼1250 K they coincide. Thus, the corresponding Gibbs free-energies definitely have the inverse order of that we have claimed in our previous articles [3, 4]. This agrees with the Clausius-Clapeyron plots recently reported by Chen et al. [16]. Therefore, the behaviors detected below the high-temperature sublimation curve are metastable or unstable. Indeed, this had already

been suggested, for the first time, in the 1993 pioneering work of Hagen et al. [22].

3 Supercritical isotherms for Lennard-Jonesium and C_{60}

The apparent persistence and reproducibility of the fluid-solid coexistence obtained from the metastable "low-temperature triple point" needs, however, a further investigation in an attempt to trace its origin and meaning. To this end, we have simulated, by NVT and NpT Monte Carlo as well as by NVT molecular dynamics, supercritical isotherms for the Lennard-Jonesium (at reduced temperatures 2.0 and 2.74) and for C_{60} with GP (at 2100 K). For each point of the Lennard-Jonesium, the calculations, with 256 and 108 molecules, started always from face-centered-cubic (fcc) lattices. The density was increased by steps of 0.05, spanning the interval 0.7-1.3. In NpT, the pressure was slowly increased, always from a lattice at density 0.7, spanning the same range of densities. For each point of the C_{60}, the NVT calculations, with 256 and 2048 molecules, always started from fcc lattices, the densities being increased by steps of 0.05 nm^{-3}, spanning the interval 0.6-1.4 nm^{-3}. In NpT, however, two initial conditions were used: fcc lattices at different densities and the last configurations of production runs for previous states. The pressure was slowly increased. Cubic periodic boundary conditions were applied to both systems, with the potential cut-off at half of the simulation box length and applying long-range corrections. A total of 50000 MC cycle production runs followed equilibration runs with 10000 cycles. The canonical MD simulations, with 2048 molecules, were carried out with a similar statistics, a cut-off at about three molecular diameters and using the linked-list technique. The results, displayed in Figures 5 and 6, suggest that:

a) For the Lennard-Jonesium, the fluid-solid transitions are clearly detected by the direct observation of the equation of state, either in NVT or in NpT. The transition at $T^* = 2.74$, for example, is located in the density interval 1.05-1.13, the pressure being $p^* \sim 25$. These values agree well with the results of Street et al. [23] and Hansen and Verlet [24]. The supercooling of the fluid is slight because the starting configurations are fcc lattices. If the initial configurations are disordered, then a pronounced supercooling will be observed, as showed by Street et al. [23] years ago. It appears that the remains of the ordered initial configurations induce the presence of seeds for solidification.

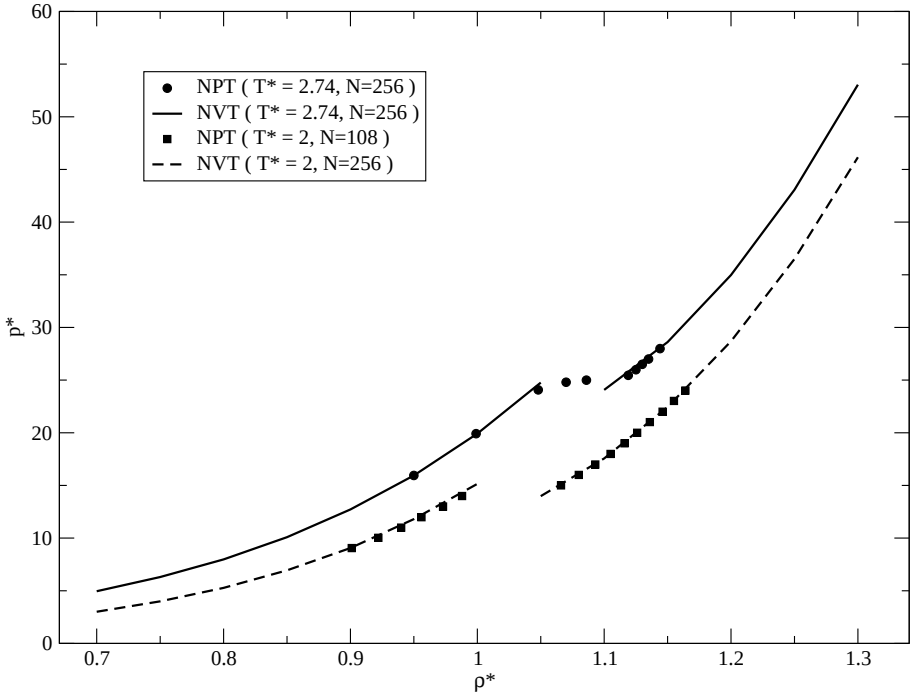

Figure 5: Supercritical equations of state for Lennard-Jonesium.

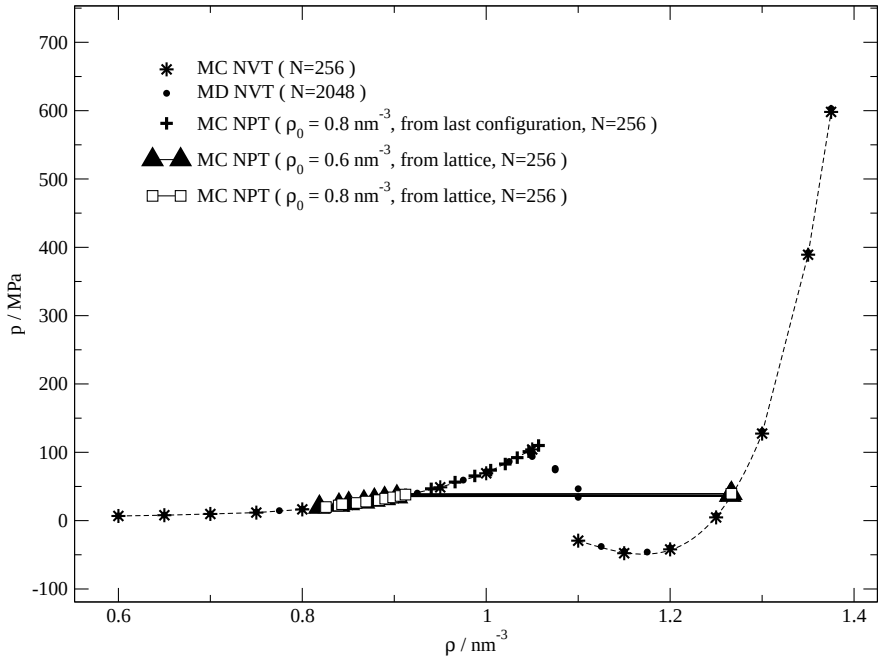

Figure 6: Supercritical equation of state for GP model at 2100 K.

b) As for the C_{60}, two kinds of behavior are detected. In the NVT calculations, even starting always from the lattice, a pronounced supercooling of the fluid is observed and a transition is only detected at density $\sim$1.05 nm^{-3}. This value is in accordance with our GD-up calculations. The equation of state is, also, in excellent agreement with that recently reported by Costa et al. [9] and Hasegawa and Ohno [25]. Incidentally, the production of metastable states by computer simulation is extremely useful in full free energy calculations, for it enables a correct double tangent construction [9], as well as in the study of metastable real systems [26]. The NpT calculations starting from the lattice, though, show a transition at the density interval $\sim$0.9-1.25 nm^{-3} in accordance with our GD-down simulations and full free energy calculations [8, 9]. On the contrary, the NpT simulations starting from disordered configurations present the same pronounced supercooling of the fluid as observed in the NVT calculations. Constraint of fixed volume, and the anticipation of the freezing threshold to lower densities due to the potential form [9], seems to prevent, in the case of C_{60}, a proper sampling of phase space in the NVT calculations. This may explain the reason for Hasegawa and Ohno [25] not having detected the location of the stable fluid-solid boundary in their recent study on the isotherms of C_{60} by NVT Monte Carlo.

We should emphasize that we do not mean, at all, that straight Monte Carlo or molecular dynamics simulations can exactly determine the fluid-solid boundaries. Indeed, these can only be precisely established by appropriate simulation methods, free energy calculations or both. However, it appears that, even in the case of C_{60}, the location of the stable boundaries can approximately be detected by direct observation of the equations of state.

This study indicates that the analogies between Lennard-Jonesium and C_{60}, or other systems that interact through short-range forces, must be taken with care. Furthermore, it clarifies the GE and GD simulations, and it reconfirms that our so-called GD-up "freezing-lines" for C_{60} are metastable. It also recalls the well-known importance of the initial conditions when simulating states not thermodynamically stable.

4 Determination of the triple point by Gibbs-Ensemble

The GD-up "freezing-lines" are based on a method recently proposed by us [27]. The method has its roots in a previous work [1] and it was mainly intended to avoid full free energy calculations. As it worked very well for Lennard-Jonesium [27] we then applied it to C_{60} and other fullerenes [3, 4]. An important detail has, however, been overlooked. That is, the method relies on the Gibbs-ensemble vapor-liquid curve which, for C_{60}, is metastable in the simulated range of temperatures and densities (see Figures 1 and 4). This fact and the results of the previous section seem to suggest that the so-called low-temperature "triple point", and the corresponding "freezing-lines", should mean no more than the limit of metastability and the onset of the absolute instability of the system.

But why has this not turned out in our previous GD-up simulations? Another detail has been overlooked: the importance of the initial conditions. In fact, our original Gibbs-Duhem simulations (up and down) were performed always starting from the last configurations of the production runs for previous state points. We have recalculated the GD-down and GD-up curves, but now starting from lattice configurations. The GD-down curve is totally reproduced (indicating that stable states do not depend on the initial configurations), whereas the GD-up curve is not. In the last case, the "liquid-box", after a few state points, reaches solid configurations. This can be tested, in a simpler way, by performing an independent NpT simulation at a "liquid sate point" on the original "freezing-up line". The "liquid" does not withstand the applied pressure and jumps to a solid.

In view of the present results it should be concluded that our method, in the case of C_{60} and other fullerenes, has just extended the metastable GE vapor-liquid curve down to the point of absolute instability of the system. This point, initially detected with 108 and 256 molecules in each simulation box, has been confirmed by performing simulations wit a larger number of molecules/box, namely 500 and 1000. The method was accepted for publication in July 2001 [1]. At that time, we were not aware of the method by Chen and co-workers [28] published in the same year. Their method allows the direct simulation of the solid-vapor equilibria, in the spirit of extending the Gibbs-Ensemble technique and avoiding full free energy calculations. It appears to be general and robust.

We should also comment on the correlations, that we have previously reported [4], between the intermolecular potentials and the phase properties of C_{60} and other fullerenes, based on a kind of "corresponding states" rule. Apart from the "low-

temperature triple points" being metastable the correlations seem to be valid. Indeed, even the onset of absolute instability should directly depend on the underlying potential functions.

5 Final Remarks

We have critically reviewed our previous works on the phase behavior of C_{60} and other fullerenes. An explanation has been suggested regarding some important aspects that have not turned out in our original calculations.

The simulated sublimation enthalpies are in very good agreement with the available experimental data and recent theoretical results, particularly the enthalpies calculated from the Girifalco potential.

Finally, in view of the present results, it seems that the origin of the discrepancies on the fluid-solid equilibria, previously reported by us, has been resolved.

Acknowledgements

We gratefully thank Dr. Dino Costa, Messina University, Italy, for kindly providing his numerical results of the OPFC and WCA freezing lines. Fundação para a Ciência e a Tecnologia (FCT) is gratefully acknowledged for financial support. Rui P. S. Fartaria contributed to this work within the PhD grant SFRH/BD/10405/2002 of FCT.

References

[1] R. P. S. Fartaria, F. M. S. S. Fernandes, F. F. M. Freitas and P. C. R. Rodrigues: Phase behavior of C_{60} by computer simulation using ab-initio interaction potential, *Int. J. Quantum Chem.* 84 (2001) 375.

[2] R. P. S. Fartaria, F. M. S. S. Fernandes, F. F. M. Freitas and P. C. R. Rodrigues: Erratum: Phase behavior of C_{60} by computer simulation using ab-initio interaction potential, *Int. J. Quantum Chem.* 88 (2002) 355.

[3] R. P. S. Fartaria, F. M. S. S. Fernandes and F. F. M. Freitas: Monte Carlo simulation of the phase diagram of C_{60} using two interaction potentials. enthalpies of sublimation, *J. Phys. Chem. B* 106 (2002) 10227–10232.

[4] F. M. S. S. Fernandes, F. F. M. Freitas and R. P. S. Fartaria: Phase diagrams and sublimation enthalpies of model $C_{n\geq 60}$ fullerenes: A comparative study by computer simulation, *J. Phys. Chem. B* 107 (2003) 276–281.

[5] L. A. Girifalco: Interaction potential for carbon (C_{60}) molecules, *J. Phys. Chem.* 95 (1991) 5370.

[6] L. A. Girifalco: Molecular properties of fullerene in the gas and solid phases, *J. Phys. Chem.* 96 (1992) 858.

[7] J. M. Pacheco and J. P. P. Ramalho: First-principles determination of the dispersion interaction between fullerenes and their intermolecular potential, *Phys. Rev. Lett.* 79 (1997) 3873.

[8] M. Hasegawa and K. Ohno: Monte Carlo simulation study of the high-temperature phase diagram of model C_{60} molecules, *Journal of Chemical Physics* 111 (1999) 5955–5963.

[9] D. Costa, G. Pellicane, M. C. Abramo and C. Caccamo: Free energy determination of phase coexistence in model C_{60}: A comprehensive Monte Carlo study, *J. Chem. Phys.* 118 (2003) 304–310.

[10] C. Caccamo: Modified-Hypernetted-Chain determination of the phase diagram of rigid C_{60} molecules, *Phys. Rev. B* 51 (1995) 3387–3390.

[11] M. C. Abramo, C. Caccamo, D. Costa and G. Pellicane: Phase diagram of model $C_{n\geq 70}$ fullerenes, *Europhys. Lett.* 54 (2001) 468.

[12] P. V. Giaquinta and G. Giunta: About entropy and correlations in a fluid of hard spheres, *Physica A* 187 (1992) 145–158.

[13] D. Costa, G. Pellicane, C. Caccamo, E. Scholl-Paschinger and G. Kahl: Theoretical description of phase coexistence in model C_{60}, *Phys. Rev. E* 68 (2003) 021104.

[14] A. Cheng, M. Klein and C. Caccamo: Prediction of the phase diagram of rigid C_{60} molecules, *Phys. Rev. Lett.* 71 (1993) 1200–1203.

[15] D. Chandler, J. D. Weeks and H. Andersen: Van der Waals picture of liquids, solids, and phase transformations, *Science* 220 (1983) 787–794.

[16] B. Chen, J. I. Siepmann, S. Karaborni and M. L. Klein: Vapor-liquid and vapor-solid phase equilibria of fullerenes: The role of the potential shape on the triple point, *J. Phys. Chem. B* 107 (2003) 12320–12323.

[17] H. P. Diogo, R. C. Santos, P. M. Nunes and M. E. M. da Piedade: Ebulliometric apparatus for the measurement of enthalpies of vaporization, *Thermochim. Acta* 249 (1995) 113–120.

[18] P. J. Linstrom and W. G. Mallard (eds.): *NIST Chemistry WebBook, NIST Standard Database Number 69*, National Institute of Standards and Technology, Gaithersburg MD, 20899 (http://webbook.nist.gov) (2001), URL `http://webbook.nist.gov`.

[19] V. Y. Markov, O. V. Boltalina and L. N. Sidorov: Saturated vapor pressure and the enthalpy of sublimation of fullerenes, *Russian J. Phys. Chem.* 75 (2001) 1.

[20] W. G. Hoover and F. H. Ree: Melting transition and communal entropy for hard spheres, *J. Chem. Phys.* 49 (1968) 3609–3617.

[21] V. I. Zubov, I. V. Zubov and J. N. T. Rabelo: Theoretical study of thermodynamic properties of a family of fullerites from C_{36} to C_{96} in the equilibrium with their vapors, *J. Phys. Chem. B* 107 (2003) 10458–10463.

[22] M. H. J. Hagen, E. J. Meijer, G. C. A. M. Mooij, D. Frenkel and H. N. W. Lekkerkerker: Does C_{60} have a liquid phase?, *Lett. to Nature* 365 (1993) 425.

[23] W. B. Street, H. J. Raveché and R. D. Mountain: Monte Carlo studies of the fluid-solid phase transition in the Lennard-Jones system, *J. Chem. Phys.* 61 (1974) 1960–1969.

[24] J. Hansen and L. Verlet: Phase transitions of the Lennard-Jones system, *Phys. Rev.* 184 (1969) 151.

[25] M. Hasegawa and K. Ohno: Can the visual molecular configuration in computer simulations locate solid–fluid phase boundaries? the case of C_{60}, *J. Chem. Phys.* 113 (2000) 4315.

[26] P. G. Debenedetti: *Metastable Liquids. Concepts and Principles*, Princeton University Press (1996).

[27] F. M. S. S. Fernandes, R. P. S. Fartaria and F. F. M. Freitas: The starting state in simulations of the fluid-solid coexistence by Gibbs-Duhem integration, *Comp. Phys. Comm.* 141 (2001) 403.

[28] B. Chen, J. I. Siepmann and M. L. Klein: Direct Gibbs ensemble Monte Carlo simulations for solid-vapor phase equilibria: Applications to Lennard-Jonesium and carbon dioxide, *J. Phys. Chem. B* 105 (2001) 9840.

Capítulo 5

Adsorção e auto-montagem em eléctrodos de ouro

Neste capítulo encontram-se apresentados os resultados do estudo da interface etanol-Au(111) e adsorção de moléculas de 1-decanotiol nessa interface. Apresentam-se dois artigos, o primeiro, referente a um modelo inicial, e o segundo, referente ao desenvolvimento de um modelo mais refinado para a interacção etanol-Au(111):

- **A Study of 1-Decanethiol Self-Assembly on Gold Electrodes by Computer Simulation**
  Rui P.S. Fartaria, Filomena F.M. Freitas and Fernando M.S. Silva Fernandes
  Electroanal. Chem. 574 (2005) 321-331

- **A Force Field for Simulating Ethanol Adsorption on Au(111) Surfaces. A DFT Study**
  Rui P. S. Fartaria, Filomena F. M. Freitas and Fernando M. S. Silva Fernandes
  Int. J. Quantum Chem. 107 (2007) 2169-2177

No seguimento dos artigos apresentam-se, em duas secções, resultados ainda não publicados.

Electroanal. Chem. 574 (2005) 321-331

A Study of 1-Decanethiol Self-Assembly on Gold Electrodes by Computer Simulation

Rui P.S. Fartaria, Filomena F.M. Freitas and Fernando M.S. Silva Fernandes[1]
Laboratory of Molecular Simulation and CECUL, Department of Chemistry and Biochemistry, Faculty of Sciences, University of Lisboa, Rua Ernesto de Vasconcelos, Bloco C8, 1749-016 Lisboa, Portugal

Abstract

This work is a preliminary study towards the understanding of the adsorption and self-assembly mechanisms of alkylthiols on gold electrodes. Canonical Monte Carlo simulations were performed at 298 K. The simulated model consisted of diluted solutions of 1-decanethiol in ethanol inside two gold electrodes, at the potential of zero charge. Three potentials for the oxygen-gold surface interaction were used. The liquid phase molecules were taken as rigid. The average tilt-angle of the thiol molecule adsorbed on a Au(111) flat surface and the density profiles were determined. The approach of the thiol to the electrode was analyzed by calculating the variation of the Helmholtz energy along the normal to the surface. The average tilt-angle is in good agreement with experimental data. Finally, we suggest possible improvements to the present model.

Keywords: self-assembly, alkylthiol, gold electrode, tilt angle, mean force potential, Monte Carlo

[1]To whom correspondence should be addressed (e-mail: fsilva@fc.ul.pt)

1 Introduction

Since the end of the last century, special attention has been given to the way of selectively modifying the surface properties of metals and semiconductors by the adsorption of organic molecules, which form a film of organized structures.

Self-assembly provides an attractive method for the preparation of organized, stable and versatile organic molecular monolayers onto metallic surfaces, with a defined composition and a close-packed structure. The self-assembly process consists of chemisorption of species onto surfaces followed by their spontaneous organization, and the resulting films are known as self-assembled monolayers (SAMs) [1–3]. SAMs hold great promise for applications in different areas. Research in this field started in the 1980s and is ongoing. It has been one of the major research fields which has expanded its applications from biosensors to corrosion prevention and lubrication.

Self-assembled monolayers can be prepared using different types of molecules and different substrates. To occur, the process needs the following: a molecule that is normally an alkane chain, with $\geq$10 methylene units, and a head group with a strong preferential adsorption to the substrate. Thiol (S-H) head groups and Au(111) substrates are usually used since they work well. The thiol molecules adsorb readily from solution onto gold, creating a dense monolayer with the tail chain pointing outwards from the surface. By using thiol molecules with different tail chains, the resulting chemical surface functionality can be varied within wide limits. It is also possible to functionalize the tail chains chemically by performing reactions after the SAMs are formed.

Using surface analytical methods such as infrared spectroscopy [4,5], ellipsometry [6–8] and others techniques to characterize SAMs, it has been shown that alkane chains with a length of 12 or more methylene units form well-ordered and dense monolayers on Au(111) surfaces [9].

Due to the strong bond between gold and sulphur, the adsorption of alkylthiols on gold has become one of the most extensively studied systems in the field of self-assembled monolayers.

Computer simulation is a powerful tool for studying many problems of chemical interest [10]. The Monte Carlo (MC) and Molecular Dynamics (MD) methods have successfully been applied to systems with interest for Electrochemistry since 1970. The MD and MC calculations of water by Rahman and Stillinger [11], of electrolyte solutions by Heinzinger and Vogel [12, 13], Card and Valleau [14], Rasaiah et al. [15], Turq et al. [16] and of molten electrolytes by Woodcock and Singer [17] and

Lantelme et al. [18] are the pillars of the progress in this field. Since then, very many applications have been accomplished, ranging from electrolyte solutions and molten electrolytes to the electrical double layer, specific adsorption, nucleation, polymers, electrical conductivity, metal oxides, insulator-metal transitions, the positions of counter-ions in zeolites, molecule-metal potential surfaces and self-assembly [19–28]. For the particular case of self-assembly, which is of interest in the present work, the simulations carried out hitherto have mainly started from monolayers already assembled on the electrodes and the interaction between the thiolate and the metal. They have mainly focused on the study of the structural, dynamical and interfacial properties [28–33] of SAMs. Other have studied the nature of the bond formed between the thiolate and the Au(111) surface [34–37].

Simulation studies based on various models have been able to predict tilt angles in the range 20-30 degrees, in good accordance with values obtained by experimental techniques [38]. *Ab initio* calculations, mainly directed toward the study of the chemisorbed state (thiolate - gold bonding), led to the conclusion that the preferential site for physisorption and later chemisorption is the fcc surface-site on the Au(111) surface [35].

Our general objective is to carry out a detailed study starting from the adsorbate, dispersed into the solvent, following its approach to the electrode, the physical adsorption and, finally, the reaction between the thiol tail and the metal.

In this paper, we present preliminary results aimed at the analysis of a simple model for the physical adsorption. We should emphasize that, at this stage, we are more concerned with the feasibility of the model, and how it responds to the differences in the interaction potentials used, rather than with the reality of the potentials.

Starting from two limiting potentials for the O-surface interaction, the thiol tilt angles, the ethanol density profiles and the solvent potentials of mean force were analysed and are presented in sections 3.1 and 3.2. Simultaneously *ab initio* calculations were carried out to establish a more realistic ethanol-surface interaction, suggesting a new reparametrization of the O-surface interaction potential. Additional Monte Carlo simulations were performed to estimate the thiol tilt angles from the new potential. The results are presented in section 3.2.

In future articles, we shall report further improvements of the present model, including full *ab initio* calculations of the interactions between all the species in solution and the electrode.

2 Model

2.1 Computational details

The system was set up in a parallelepiped simulation box, 23.4 Å×23.4 Å base area and 51.5 Å height. It was composed by two flat Au(111) electrodes located at the top and bottom of the box (parallel to the xy plane). Between the electrodes, were placed 250 molecules of ethanol, when simulating pure ethanol, or else 250-3n molecules of ethanol and n molecules of 1-decanethiol, when simulating the mixture. The system dimensions were chosen to match the ethanol density at 298 K and 1 atm. In the case of the mixture, the substitution ratio of 3 ethanol molecules by 1 thiol molecule was found appropriate in order to maintain the ethanol density. Periodic boundary conditions (PBC) were applied in all simulations, but only in the x and y directions, the z direction being confined by the electrodes. In the initial configuration, the ethanol molecules were placed in a cubic lattice arrangement, and the thiol molecules in the vacant space left by elimination of some (3EtOH:1C10H21SH) ethanol molecules. From this starting point, the system was relaxed by equilibration runs with 5000 to 10000 Monte Carlo cycles followed by 5000 to 20000 production cycles. One cycle consisted of random trials to rotate and translate each molecule with an acceptance rate of ±50%. All simulations were performed in the canonical ensemble (NVT) at potential of zero charge (pzc) conditions. Further computational details will be given subsequently, according to the calculations in question.

2.2 Molecule-molecule interactions in the liquid phase

The intermolecular interactions in the liquid phase were modeled by a site-site potential resulting from the combination of Lennard-Jones (LJ) and Coulomb interactions according to the following equation,

$$U_{\mathrm{i,j}} = \sum_{\alpha\in \mathrm{i}} \sum_{\beta\in \mathrm{j}} \frac{A_{\alpha,\beta}}{r^{12}_{\alpha,\beta}} - \frac{B_{\alpha,\beta}}{r^{6}_{\alpha,\beta}} + \frac{q_\alpha q_\beta}{r_{\alpha,\beta}}, \tag{1}$$

where r, the distance between sites, q, the partial charges of the sites, and A and B the resulting Lennard-Jones parameters obtained by the combination rules of Lorentz and Berthelot [39]. The Lennard-Jones part of the interaction was truncated to half-side of the box but no cutoffs were applied to the Coulomb interaction. No intramolecular interactions were considered in this model since all molecules were taken as rigid. The potential parameters for the site-site interactions were

Table 1: OPLS parameters for the liquid phase.

Atom or group	q/e	σ/Å	ϵ/ kJ mol^{-1}
O (OH)	-0.70	3.070	0.170
S (SH)	-0.45	3.550	0.250
H (COH)	0.44	0.000	0.000
H (CSH)	0.27	0.000	0.000
CH_2 (COH)	0.27	3.905	0.118
CH_2 (CSH)	0.18	3.905	0.118
CH_2	0.00	3.905	0.118
CH_3	0.00	3.905	0.175

obtained from the so called Optimized Potentials for Liquid Simulations (OPLS) by Jorgensen [40, 41] and are presented in Table 1.

2.3 Molecule-electrode interactions

The molecule-electrode interactions were modeled by a 12-3 LJ potential. This potential was derived by Hautman and Klein's method [28] for the simulation of self-assembled thiol monolayers on flat Au(111) gold electrodes. In this method, the 12-6 LJ potential is integrated over the half space representing the Au(111) surface. The resulting form is a 9-3 LJ interaction. This form, however, cannot fit accurately the binding energy, the distance from the surface and the dispersion coefficient, C_3 [28,42,43]. Thus we have adopted the 12-3 form as used by Hautman and Klein [28]:

$$U(z) = \frac{C_{12}}{(r_z - r_{z_0})^{12}} - \frac{C_3}{(r_z - r_{z_0})^3}, \tag{2}$$

where, U is the potential energy, $C_n \propto \sqrt{\varepsilon\sigma^n}$, r_{z_0} is a limit approach distance to the electrode and r_z is the distance between each molecule site and the electrode. The C_{12} and C_3 parameters for the various sites are presented in Table 2 and Figure 1 shows the U vs. r_z plots for the S and O site-electrode potentials in the different approximations used.

It is well-known that the potential form $(c/r)^n$, to describe the short-range interactions, has no quantum mechanical basis. Therefore, the choice of the n value may be justified only by the quality of the fittings produced and by the accordance of the results, drawn from it, with experimental data. Incidentally, in very recent work [44] on the adsorption of phenol, from aqueous solutions, on gold electrodes,

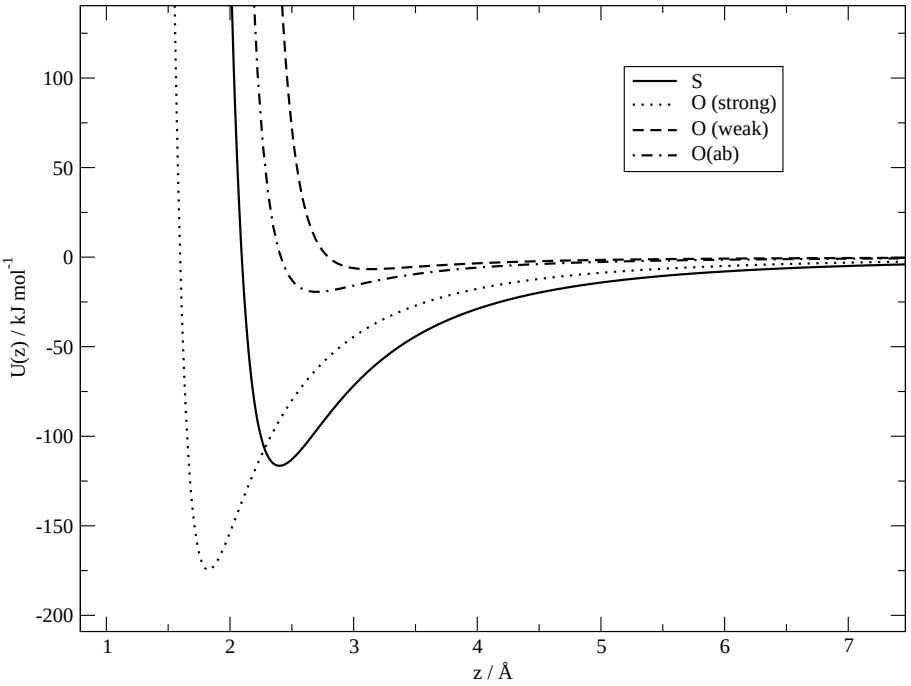

Figure 1: Surface potentials for the S and O sites.

we have used the 9-3 form for the water-gold interactions and the 12-3 form for the phenol-gold interactions. The simulation results are in good agreement with experiment.

For the interaction of the CH_3, CH_2 and S sites with the surface we used the same parameters as Hautman and Klein [28], but for the O site we did not find any reference value in the literature. Therefore, using the same method of Hautman and Klein for deriving the S interaction we used two approximations: one from the interaction of the O site in the liquid based on OPLS and the other from *ab initio* calculations describing the interaction of the OH^- group on the Au(111) surface [45]. As can be seen in Table 2 and Figure 1 these approximations result in two very distinct interactions for the O site. Nevertheless, at that stage and in order to see their influence on the system, they were used to model the ethanol-electrode interaction. We will refer to them as the O_{weak} and O_{strong} interactions, the strong interaction being that derived from the OH^-/Au(111) interaction. The potential referred to as O(ab) in Figure 1, came to light as the result of our *ab initio* calculations to estimate the ethanol-gold surface interaction energy and will be discussed later, in section 3.3.

It is worth mentioning that the S-surface interaction derived by Hautman and Klein, and used in the present work, is in fact parametrized for a binding energy cor-

Table 2: Parameters for the 12-3 LJ surface interaction.

	C_{12} / kJ mol^{-1} Å^{12}	C_3 / kJ mol^{-1} Å^3	r$_{z0}$ / Å	r$_{zm}$ / Å	U_m / kJ mol^{-1}
S	339698.96	1502.06	0.27	2.40	-116.32
O (strong)	16137.69	949.77	0.23	1.80	-173.64
O (weak)	65964.94	117.15	0.78	3.11	-6.82
O(ab)	31900.1	216.725	0.67	2.7	-19.4
CH_2	232722.45	142.26	0.86	3.51	-5.69
CH_3	283419.98	171.54	0.86	3.51	-6.90

responding to the chemisorption of the thiolate (that is, the Au-S bond is implicit). However, in this preliminary study, we used it just to analyse the solvent influence on the thiol tilt angles in the early stages of the physical adsorption. The effects of partial charge transfer due to the thiol adsorption, the constraints to the Au-S-CH_2 angles and the fate of the proton were not considered. They are the objective of our simulations on the chemisorption phenomena, presently in progress, and will be reported in future articles.

3 Results and discussion

Taking the two limiting ethanol-surface interactions, O_{weak} and O_{strong}, a set of simulations was carried out for each case. The structural and thermodynamic results are presented and compared for the two models and the effects of the different interactions are interpreted in parallel. The snapshots in Figure 2 give a general view of the system.

3.1 Structural results

The structural information is presented in the form of density profiles for the two systems in Figures 3 , 4 , 5 and 6 . From them we can see that for the O_{strong} interaction the ethanol molecules are strongly attached to the electrode. Due to the strong attraction of the O site towards the electrode the molecules of ethanol form a compact layer (0 - 5 Å) near the electrode with the CH_3 and CH_2 groups turned to the bulk of the solution. This can be seen in Figure 3 where the position of the peaks for the O and CH_3 sites, situated at 1.7 Å and 3.5 Å respectively, suggests the above orientation. Moreover, the sharpness of these peaks shows that the ethanol molecules should have a somewhat reduced mobility in this layer. In the second

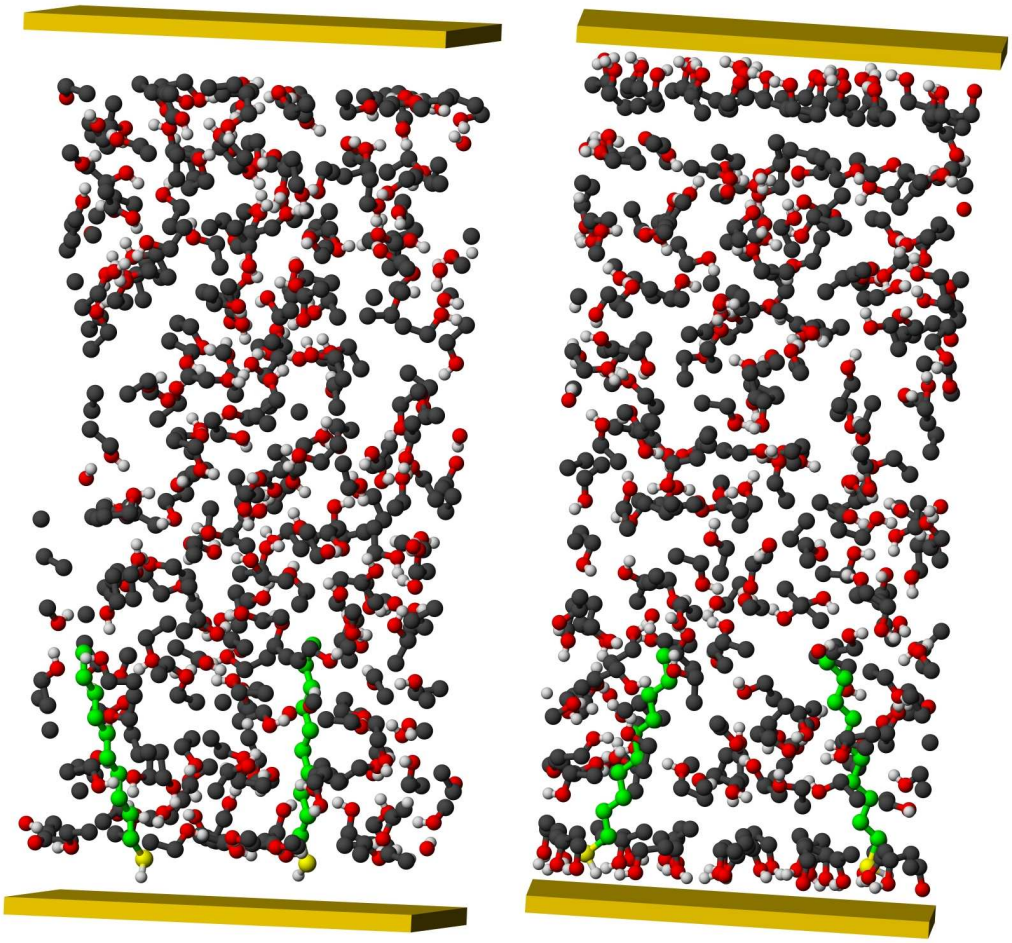

Figure 2: Snapshots of the simulated systems. On the left, the O_{weak} model and on the right, the O_{strong} model.

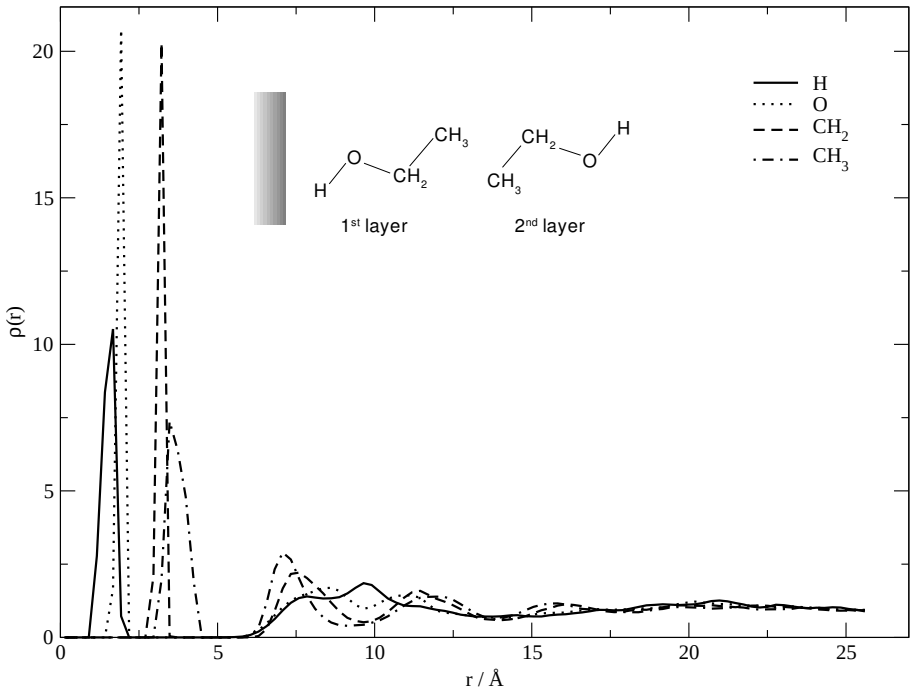

Figure 3: Density profile for ethanol with the O_{strong} interaction in the absence of thiol.

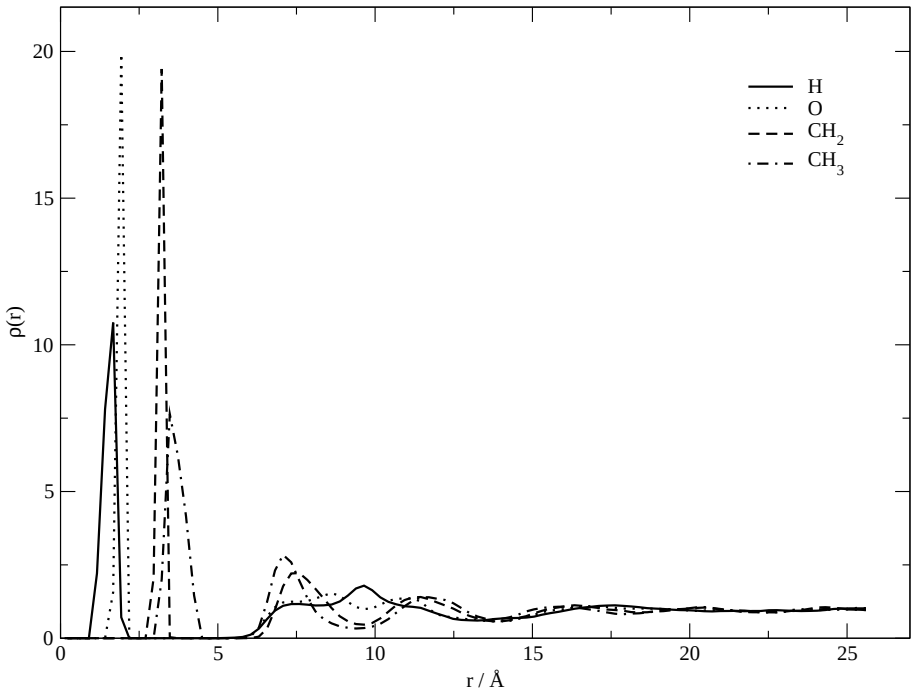

Figure 4: Density profile for ethanol with the O_{strong} interaction in the presence of thiol.

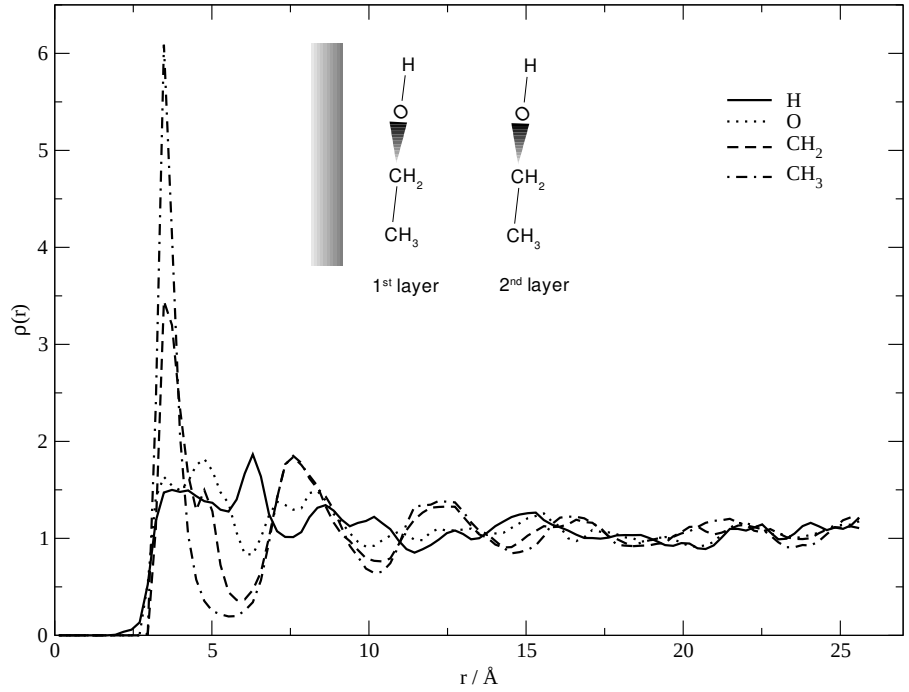

Figure 5: Density profile for ethanol with the O_{weak} interaction in the absence of thiol.

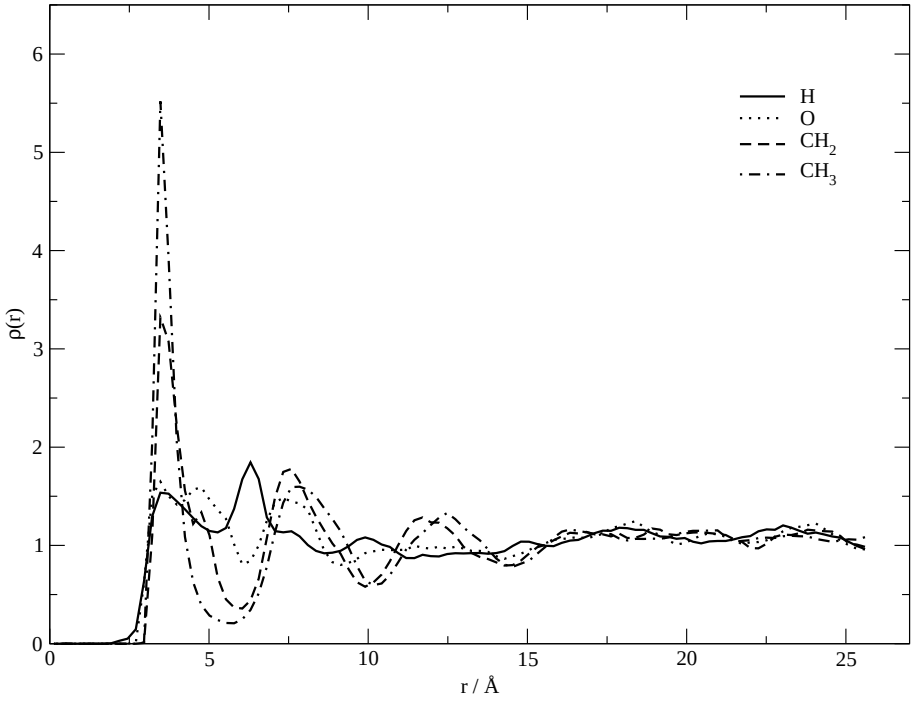

Figure 6: Density profile for ethanol with the O_{weak} interaction in the presence of thiol.

layer (5 - 10 Å) the ethanol molecules have the CH_3 site pointing to the CH_3 site of the molecules in the first layer as shown by the peaks at 7.1 Å (CH_3) and 8.5 Å (O). These peaks are broader and more superimposed with each other than those in the first layer which suggests that the mobility in this layer is greater than in the first one. On the other hand, in the system referred to as O_{weak} and according to the peaks at 3.44 Å (CH_3), 3.37 Å (CH_2), 3.48 and 4.77 Å (O) and 3.7 Å (H) the ethanol molecules are weakly attached to the electrode maintaining, on average, a parallel orientation on the first layer, either with all the sites at almost the same distance from the electrode or with the CH_2 and CH_3 near to the surface and the O and H sites pointing to the bulk. The second layer, retains the same orientation, with peaks at 7.62 Å (CH_3, CH_2), 7.14 and 8.44 Å (O) and 8.58 Å (H). The layers in this system are, of course, much more structureless when compared with the O_{strong} case since the peaks due to the weaker interactions are broader and greater in number.

The introduction of thiol molecules does not seem to produce significant alterations in solvent layers (the peaks do not change greatly), and the most significant ones seem to be located in the second layer of ethanol, the effect being more visible in the O_{weak} model.

The average tilt angles (relative to the normal to the surface), for the thiol molecules, were $26^o \pm 11^o$ for the O_{strong} model and $22^o \pm 8^o$ for the O_{weak} model. It is worth mentioning that these values are close to those obtained experimentally (20-30^o by Porter et al. [38]), and by simulation (30^o by Sellers et al. [34] and 29^o or 18^o by Hautman and Klein [28]), for the average tilt angle of thiol molecules in stable and organized SAMs.

3.2 Potentials of mean force

Based on the information provided by density profiles and average tilt angles, it was possible to draw the general disposition of the solvent along the normal to the surface (the z coordinate) and to predict the behavior of the thiol molecules, attached to the electrode by the sulphur site and waving around an average tilt angle of $\sim 26^o$.

We shall now look at the behavior of thiol molecules along the path of adsorption through the changes in the Helmholtz energy of the system during this process.

In this work, changes in Helmholtz energy were obtained by using a free-energy perturbation method, FEP [46–50]. The Helmholtz energy change associated with the displacement of a molecule along a coordinate of the system, taking into account the solvent effects, is called the potential of the mean force, PMF, acting on the

molecule. In the case in question the PMF can be divided into two contributions, one from the direct interaction of the thiol molecule and the electrode and the other from the interaction with the solvent surrounding the molecule. In the FEP method, the change in Helmholtz energy is calculated using the general equation:

$$\Delta A = -kT \ln \left\langle \exp \left[-\frac{U_1 - U_0}{kT} \right] \right\rangle \tag{3}$$

where U_0 and U_1 are the energies of the system before and after displacement of the thiol molecule. The brackets represent an ensemble average in the reference system.

An ensemble of configurations for the solvent is generated with the thiol molecule in a position R_0 and in a given orientation relative to the electrode (the reference system). The molecule is displaced by a very small distance δR towards the electrode, keeping the orientation constant (the perturbation). Then, the quantity $\exp\left[-\Delta U/kT\right]$ is averaged over all the solvent configurations of the reference system.

In the implementation of the FEP method, the adsorption path (coordinate z, defined by the distance of the sulphur atom from the electrode surface) was divided into a number of small windows of length δz. This number was chosen to match the requirement that in every window, $\Delta U = U_1 - U_0 \sim kT$ [49]. The Helmholtz energy change in each window, $\Delta A\left(z_\mathrm{i}, z_\mathrm{i} + \delta z\right)$, was evaluated using the equation:

$$\Delta A\left(z_\mathrm{i}, z_\mathrm{i} + \delta z\right) = \\ -kT \ln \left\langle \exp \left[-\frac{U_{z_\mathrm{i}+\delta z} - U_{z_\mathrm{i}}}{kT} \right] \right\rangle_{z_\mathrm{i}} \tag{4}$$

where U_{z_i} and $U_{z_\mathrm{i}+\delta z}$are the energies of the system before and after displacement of the thiol molecule. A double width sampling was used, thus, evaluating, in each simulation, $\Delta A\left(z_\mathrm{i}, z_\mathrm{i} + \delta z\right)$ and $\Delta A\left(z_\mathrm{i}, z_\mathrm{i} - \delta z\right)$. The change in Helmholtz energy between the initial position, z_initial, and the final position, z_final, was then computed by

$$\Delta A = \sum_\mathrm{i} \Delta A\left(z_\mathrm{i}, z_\mathrm{i} + \delta z\right) - \Delta A\left(z_\mathrm{i}, z_\mathrm{i} - \delta z\right). \tag{5}$$

For each window, equilibration runs of 1500 MC cycles were followed by 5000 MC cycles of production. The initial position for the molecule of thiol was chosen to be $R_{\mathrm{S-electrode}} \sim 11$ Å and the final position was $R_{\mathrm{S-electrode}} \sim 2$ Å. The path in between was subdivided in windows $2 \times \delta z$, with $\delta z = 0.1$ Å.

For each of the $\mathrm{O_{weak}}$ and $\mathrm{O_{strong}}$ systems, three orientations of the thiol molecule were studied: tilt angles of 0°, 26° and 45°. These were chosen to span the range of

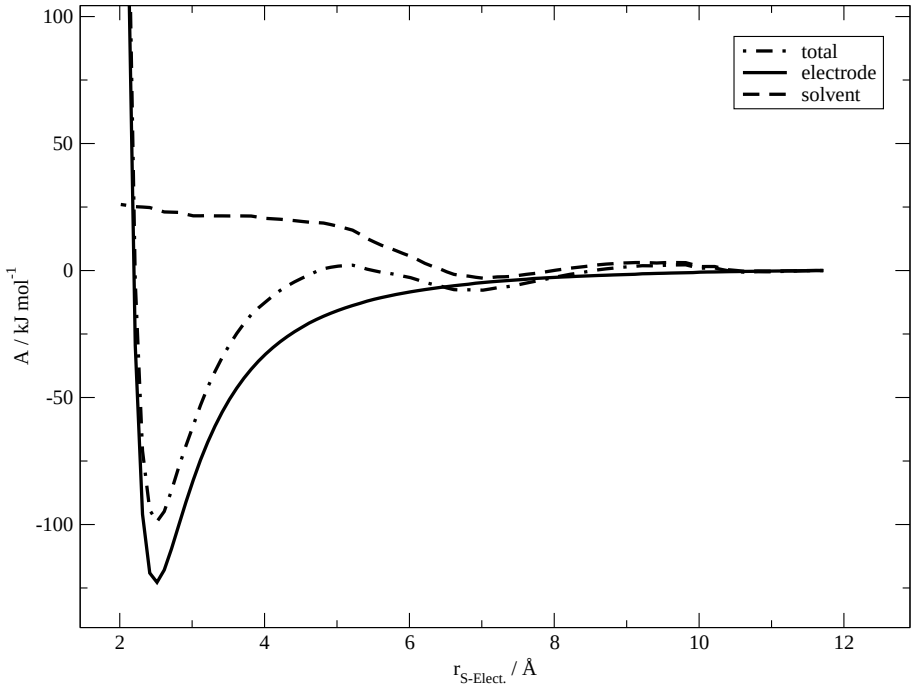

Figure 7: Total, solvent and electrode PMFs on thiol with a 26° tilt angle in the O_{strong} model.

values of tilt angles that the thiol molecules assumed during the simulations.

In order to show the relation between the total Helmholtz energy change, and the solvent and electrode potentials of mean force, the complete set of results for the 26° tilt angle in the O_{strong} model is presented in Figure 7. The main contribution for the Helmholtz energy change comes from the electrode and this is always a strongly negative change until the superposition takes place. This shows that the electrode is the main driving force for the adsorption. On the contrary, the solvent potential of mean force is always positive, showing the difficulties inherent to the movement of the thiol molecules through the solvent layers in the interface.

The results obtained for the solvent potential of mean force are presented in Figures 8 and 9. It turns out that in the system O_{strong}, as the thiol molecule starts to move through the second layer of ethanol molecules, the preferred tilt angle starts at 45° and then gradually changes to 26-0° when the thiol head enters the first layer of ethanol and the chain is between the first and second layers. In the O_{weak} system, as the thiol group moves through the second layer, the preferred orientation is the 0° tilt angle, which then changes gradually to the 45° tilt angle and finally, when the molecule is attached to the surface, the 0° and the 26° orientations are the preferred ones. The solvent potential of mean force reaches a maximum of $\sim$+30

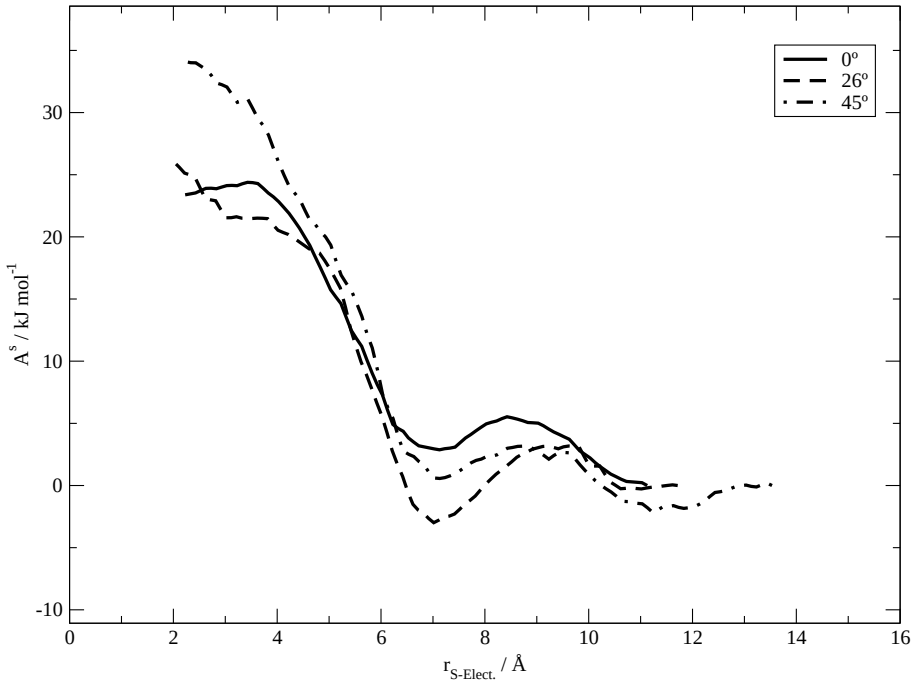

Figure 8: Solvent PMF in the O_{strong} model.

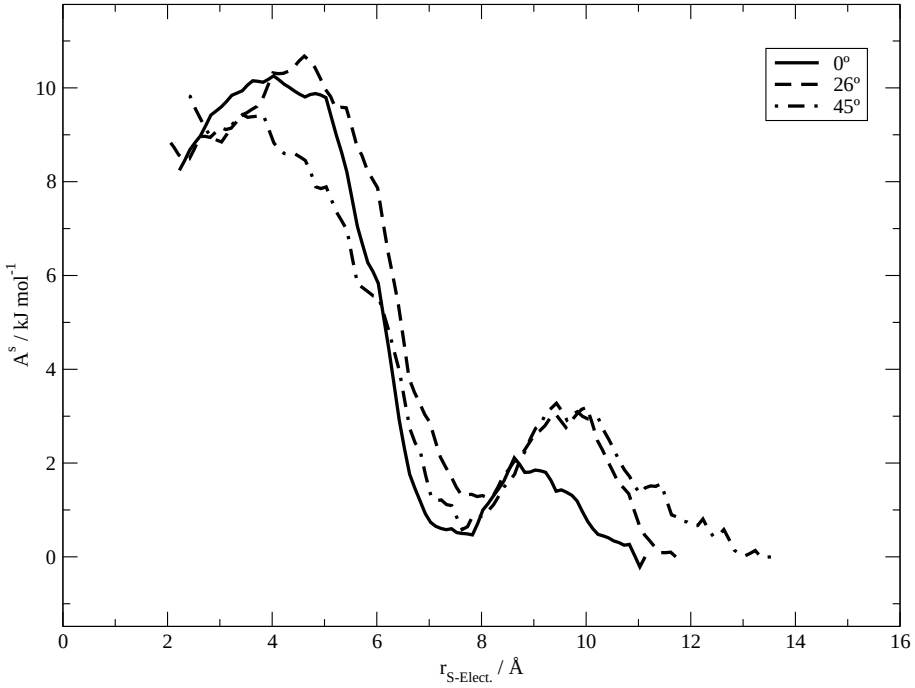

Figure 9: Solvent PMF in the O_{weak} model.

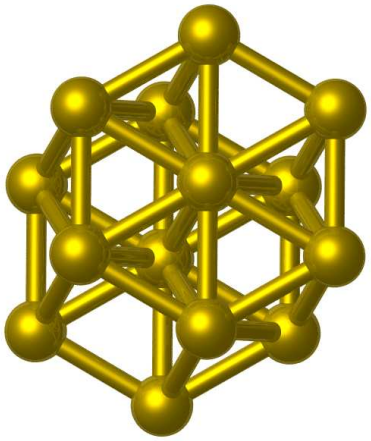

Figure 10: Gold cluster used in the *ab initio* calculations.

kJ mol^{-1}in the O_{strong} system and $\sim$+10 kJ mol^{-1} in the O_{weak} system, showing that the repulsion, by the solvent, affecting the thiol molecule is much greater in the O_{strong} system. This is a consequence of the very dense and organized layer of ethanol near the electrode, as displayed in Figure 4. The strong preference for the 0^o and 26^o final orientations in the O_{strong} system can also be interpreted as a consequence of the existence of this compact layer of ethanol molecules that will strongly reduce the thiol head and tail mobility.

3.3 Some improvements based on *ab initio* calculations

In order to pave the way for a more elaborate description of this system we have performed some *ab initio* calculations for the molecule of ethanol adsorbed in the Au(111) surface. We used the Gaussian98 program with B3LYP theory level. The basis sets were 6-31G, for H, C, and O atoms, and LanL1MB for gold atoms. As a model for the Au(111) surface we used the 14 Au cluster presented in Figure 10. The choice of this cluster size was a compromise between a reasonable amount of Au(111) surface and the best computing time/quality relation in view of the available computing facilities. Small cluster models are always a crude approximation to the real surface, but at this stage we were essentially concerned with obtaining a more realistic value for the EtOH-Au(111) binding energy than the values of the two limiting O_{weak} and O_{strong} interactions.

A minimum interaction energy of $\sim$20 kJ mol^{-1} was estimated. Taking into account this energy the surface interaction potential was reparametrized to meet the required *ab initio* value yielding the interaction potential referred to as O(ab)

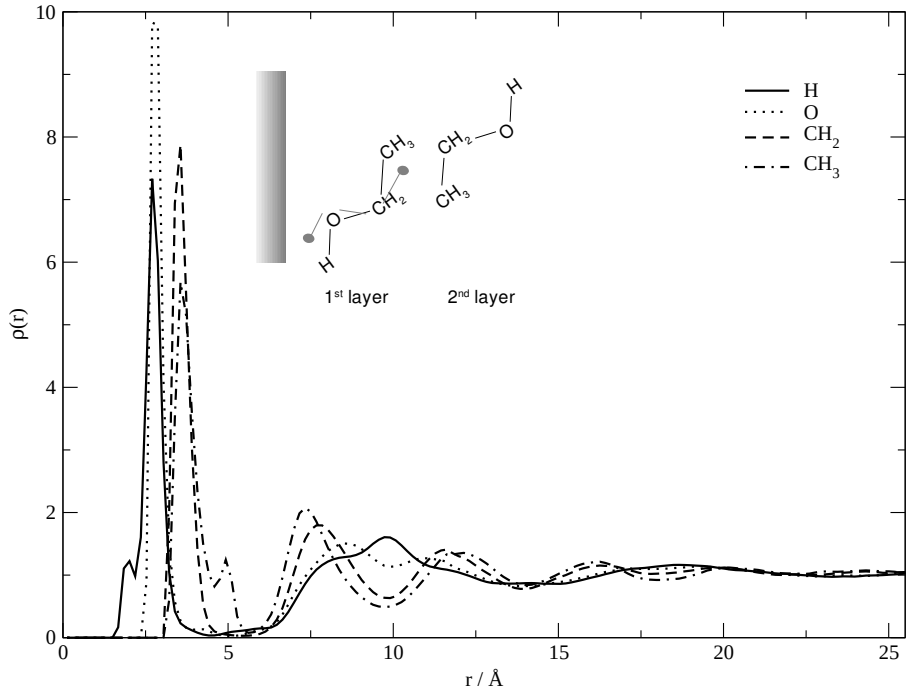

Figure 11: Density profile for ethanol with the O-surface interaction re-parametrized from our *ab initio* calculations (O(ab)) in the absence of thiol.

in Figure 1 and Table 2.

The simulations performed with this interaction potential revealed an intermediate situation relatively to the O_{weak} and O_{strong} interactions as shown by the density profiles in Figure 11. In the first solvent layer, the strongest hydrogen peak is at ∼2.7 Å with a smaller one at ∼2.0 Å, the oxygen peak is at ∼2.8 Å, the CH_2 peak at ∼3.5 Å and the CH_3 strongest peak at ∼3.6 Å with a minor one at ∼4.9 Å meaning that almost all the ethanol molecules are orientated, on average, with the plane of the molecule perpendicular to the electrode and the O-H bond almost parallel to the surface. The H and CH_3 smaller peaks, in the first layer, are possibly correlated showing that a small proportion of these molecules is more vertically orientated towards the electrode as illustrated in the inset of Figure 11. The second layer is localized at about 7.5 Å with molecular orientations correlated to those of the first layer. The average tilt angle, estimated in this new solvent distribution was 38 ± 14^{o} covering a range of 10^{o} to 70^{o}. This value is also close to that of the thiol tilt angle in a complete SAM.

4 Conclusions

We have presented a simple model for the physisorption of 1-decanethiol molecules on Au(111) surfaces using ethanol as the solvent. None of the effects related to chemisorption phenomena, such as partial charge transfer and the presence of reaction subproducts at the interface, were considered. A more complete study should include these effects and take into account the subproducts of chemisorption [51]. The nonexistence of a more elaborate description of the interaction between ethanol molecules and the gold surface led to the application of two limiting approximations. An improvement to the ethanol-surface potential based in *ab initio* calculations, with a relatively small gold cluster (14 atoms), was added. The problems involving cluster calculations were considered (by testing a number of clusters with variable numbers of gold atoms and structures), but not thoroughly investigated since, at this stage, we were essentially concerned with obtaining a more realistic estimate of the ethanol-Au(111) binding energy to compare with the two limiting approximations. The limiting approximations revealed two different structural organizations of the ethanol molecules at the interface. This suggested that those approximations for the ethanol-Au(111) interaction were unrealistic and a more refined interaction model was necessary. Indeed, our *ab initio* calculations indicate interaction energies between these two approximations. The average tilt angle (of just one adsorbed thiol molecule) was analyzed for the interaction models used. The tilt angles ($26^o \pm 11^o$ for the O_{strong} model, $22^o \pm 8^o$ for the O_{weak} model and 38 ± 14^o for the model based on our *ab initio* calculations), seem to be, apparently, independent of the structure of the solvent in the interface. It is also worth mentioning that the average thiol tilt angles, calculated with the three approximations, are close to those either verified experimentally, or obtained by simulations on already assembled monolayers. Will the close values of these angles be indicative of their importance in the monolayer organisation? The potentials of mean force, calculated with the two limiting approximations, show the orientational preference, in terms of tilt angles, of the thiol molecules along the path to adsorption indicating that in the final stage of the approach to the gold surface the preferred tilt angle is within $\sim 0^o$-30^o.

It should be emphasized that the potential interactions used in the present work are very simple regarding a full description and interpretation of self-assembly. Nonetheless, as stated in the introduction, at this stage we were more concerned with the feasibility of the model and how it responds to the differences in the interaction potentials rather than with the reality of such potentials. The present results

suggest that the model works well and can be improved.

Regarding the interactions in question, *ab initio* calculations are still in progress to determine the full ethanol-Au(111) and thiol-Au(111) interactions in order to make more realistic simulations of the adsorption and formation of SAMs. Further improvements include the consideration of the structure of the electrode and its influence on the preferential sites for adsorption of thiol and ethanol molecules, as well as the introduction of torsion and bending degrees of freedom. Also, it is of the utmost importance to consider long range contributions (calculated by Ewald's sum for example) to the Coulomb interaction. Work along these lines is in progress and will be reported soon.

Acknowledgements

Rui P. S. Fartaria gratefully acknowledges the support of Fundação para a Ciência e a Tecnologia (PhD grant SFRH/BD/10405/2002). This work was performed within the scope of the projects: COST D15 BBW Nº C99.0106/99 and POCTI 36457/QUI/2000.

References

[1] R. G. Nuzzo, F. A. Fusco and D. L. Allara: Spontaneously organized molecular assemblies. 3. Preparation and properties of solution adsorbed monolayers of organic disulfides on gold surfaces, *J. Am. Chem. Soc.* 109 (1987) 2358–2368.

[2] J. D. Swalen, D. L. Allara and J. D. A. et al.: Molecular monolayers and films, *Langmuir* 3 (1987) 932–950.

[3] A. S. Viana, A. H. Jones, L. M. Abrantes and M. Kalaji: Redox induced orientational changes in a series of short chain ferrocenyl alkyl thiols self-assembled on gold(111) electrodes, *J. Electroanal. Chem.* 500 (2001) 290–298.

[4] R. G. Nuzzo, L. H. Dubois and D. L. Allara: Fundamental-studies of microscopic wetting on organic-surfaces. 1. Formation and structural characterization of a self-consistent series of polyfunctional organic monolayers, *J. Am. Chem. Soc.* 112 (1990) 558–569.

[5] R. G. Nuzzo, E. M. Korenic and L. H. Dubois: Studies of the temperature-dependent phase-behavior of long-chain normal-alkyl thiol monolayers on gold, *J. Chem. Phys.* 93 (1990) 767–773.

[6] C. D. Bain, E. B. Troughton and Y.-T. T. et al.: Formation of monolayer films by the spontaneous assembly of organic thiols from solution onto gold, *J. Am. Chem. Soc.* 111 (1989) 321–335.

[7] G. M. Whitesides and P. E. Laibinis: Wet chemical approaches to the characterization of organic-surfaces - self-assembled monolayers, wetting, and the physical organic-chemistry of the solid liquid interface, *Langnuir* 6 (1990) 87–96.

[8] S. D. Evans, E. Urankar, A. Ulman and N. Ferris: Self-assembled monolayers of alkanethiols containing a polar aromatic group - effects of the dipole position on molecular packing, orientation, and surface wetting properties, *J. Am. Chem. Soc.* 113 (1991) 4121–4131.

[9] Y. V. Sukhinin: Phase transitions in self-assembled monolayers of alkanethiols containing the polar group, *J. Experimental and Theoretical Physics* 87 (1998) 115–122.

[10] F. M. S. S. Fernandes and P. C. R. Rodrigues: Molecular simulation. the state of the art., *Portugaliae Electrochimica Acta* 17 (1999) 61–90.

[11] A. Rahman and F. H. Stillinger: Molecular dynamics study of liquid water, *J. Chem. Phys.* 55 (1971) 3336.

[12] K. Heinzinger and P. C. Vogel: A molecular dynamics study of aqueous solutions. i. First results for LiCl in H_2O., *Z. Naturforch* 29a (1974) 1164–1171.

[13] P. C. Vogel and K. Heinzinger: A molecular dynamics study of aqueous solutions. ii. cesium chloride in H_2O., *Z. Naturforch* 30a (1975) 789–796.

[14] D. N. Card and J. P. Valleau: Monte-Carlo study of thermodynamics of electrolyte solutions, *J. Chem. Phys.* 52 (1970) 6232–6240.

[15] J. C. Rasaiah, D. N. Card and J. P. Valleau: Calculations on restricted primitive model for 1-1 electrolyte solutions, *J. Chem. Phys.* 56 (1972) 248–255.

[16] P. Turq, F. Lantelme and H. L. Friedman: Brownian dynamics - its application to ionic-solutions, *J. Chem. Phys.* 66 (1977) 3039–3044.

[17] L. V. Woodcock and K. Singer: Thermodynamic and structural properties of liquid ionic salts obtained by Monte Carlo computation .1. Potassium chloride, *Trans. Faraday Soc.* 67 (1971) 12–30.

[18] F. Lantelme, P. Turq, B. Quentrec and J. W. E. Lewis: Application of molecular-dynamics method to a liquid-system with long-range forces (molten NaCl), *Mol. Phys.* 28 (1974) 1537–1549.

[19] J. Barthel: *Portug. Electrochem. Acta* 9 (1991) 287–309.

[20] A. Ignaczak: *The Specific Adsorption of Halide Ions on Noble Metals. A theoretical approach.*, Ph.D. thesis, University of Porto, Portugal (1997).

[21] D. J. Tildesley: Molecular simulation: A view from the bond, *Faraday Discuss.* 100 (1995) C29–C45.

[22] E. Spohr: Computer simulations of electrochemical interfaces, in R. C. Alkire and D. M. Kolb (eds.), *Advances in Electrochemical Science and Engineering - vol. 6*, Wiley-VCH, New York (1999) pages 1–75.

[23] I. Benjamim: Molecular dynamic simulations in interfacial electrochemistry, cap.3, in J. O. M. Bockris (ed.), *Modern Aspects of Electrochemistry,n. 31*, Plenum Press (1997) pages 115–179, new York.

[24] A. J. Pertsin and M. Grunze: Computer simulation of water near the surface of oligo(ethylene glycol)-terminated alkanethiol self-assembled monolayers, *Langmuir* 16 (2000) 8829–8841.

[25] H. Sellers, A. Ulman, Y. Shnidman and J. E. Eilers: Structure and binding of alkanethiolates on gold and silver surfaces: Implications for self-assembled monolayers, *J. Am. Chem. Soc.* 115 (1993) 9389–9401.

[26] R. Mahaffy, R. Bhatia and B. J. Garrison: Diffusion of a butanethiolate molecule on a Au{111} surface, *J. Phys. Chem. B* 101 (1997) 771–773.

[27] Z. Zhang, T. L. Beck, J. T. Young and F. J. Boerio: Molecular structure of monolayers from thiol-terminated polyimide model compounds on gold. 2. Molecular dynamics simulations, *Langmuir* 12 (1996) 1227–1234.

[28] J. Hautman and M. L. Klein: Simulation of a monolayer of alkyl thiol chains, *J. Chem. Phys.* 91 (1989) 4994–5001.

[29] J. I. Siepmann and I. R. McDonald: Monte-Carlo study of the properties of self-assembled monolayers formed by adsorption of $CH_3(CH_2)_{15}SH$ on the (111) surface of gold, *Mol. Phys.* 79 (1993) 457–473.

[30] A. F. Sadreev and Y. V. Sukhinin: Phase transitions in a system of $CH_3(CH_2)_{n-1}$ self-assembled on the Au(111) crystal surface, *Phys. Rev. B* 54 (1996) 17966–17973.

[31] A. J. Pertzin and M. Grunze: Computer simulation of water near the surface of oligo(ethilene glycol)-terminated alkanethiol self-assembled monolayers, *Langmuir* 16 (2000) 8829–8841.

[32] S. Jiang: Molecular simulation studies of self-assembled monolayers of alkane thiols on Au(111), *Mol. Phys.* 100 (2002) 2261–2275.

[33] N. Gronbech-Jensen, A. N. Paikh, K. M. Beardmore and R. C. Desai: Rigid molecular model for the assembly characteristics and optimal structure in molecular monolayers of alkanethiols on Au(111), *Langmuir* 19 (2003) 1474–1485.

[34] H. Sellers, A. Ulman, Y. Shnidman and J. E. Eilers: Structure and binding of alkanethiolates on gold and silver surfaces: Implications for self-assembled monolayers, *J. Am. Chem. Soc.* 115 (1993) 9389–9401.

[35] Y. Yourdshahyan, H. K. Zhang and A. M. Rappe: n-alkyl thiol head-group interactions with the Au(111) surface, *Phys. Rev. B* 63 (2001) 081405.

[36] M. C. Vargas, P. Giannozzi, A. Selloni and G. Scoles: Coverage-dependent adsorption of CH_3S and $(CH_3S)_2$ on Au(111): A density functional theory study, *J. Phys. Chem. B* 105 (2001) 9509–9513.

[37] Y. Yourdshahyan and A. M. Rappe: Structure and energetics of alkanethiol adsorption on the Au(111) surface, *J. Chem. Phys.* 117 (2002) 825–833.

[38] M. D. Porter, T. B. Bright, D. L. Allara and C. E. D. Chidsey: Spontaneously organized molecular assemblies. 4. Structural characterization of n-alkyl thiol monolayers on gold by optical ellipsometry, infrared spectroscopy, and electrochemistry, *J. Am. Chem. Soc.* 109 (1987) 3559.

[39] M. Allen and D. Tildesley: *Computer Simulation of Liquids*, Claredon Press, Oxford, U.K., 1st ed. (1987).

[40] W. Jorgensen: Optimized intermolecular potential functions for liquid alcohols, *J. Phys. Chem.* 90 (1986) 1276–1284.

[41] W. Jorgensen: Intermolecular potential functions and Monte-Carlo simulations for liquid sulfur-compounds, *J. Phys. Chem.* 90 (1986) 6379–6388.

[42] W. Steele: *The Interaction of Gases with Solid Surfaces*, Pergamon, New York (1974).

[43] G. Cardini, S. F. O'Shea and M. L. Klein: Gas-surface potentials and the dynamics of overlayers, *J. Chem. Soc. Faraday Discuss.* 80 (1985) 227.

[44] R. S. Neves, A. J. Motheo, F. M. S. S. Fernandes and R. P. S. Fartaria: Monte Carlo simulation of the adsorption of phenol on gold electrodes. A simple model, *J. Braz. Chem. Soc.* 15 (2004) 224–231.

[45] M. T. M. Koper and R. A. van Santen: Interaction of H, O and OH with metal surfaces, *J. Electroanal. Chem.* 472 (1999) 126–136.

[46] C. A. Reynolds, P. M. King and W. G. Richards: Free energy calculations in molecular biophysics, *Mol. Phys.* 76 (1992) 251–275.

[47] E. Spohr: A computer-simulation study of iodide-ion solvation in the vicinity of a liquid water metal interface, *Chem. Phys. Lett.* 207 (1993) 214–219.

[48] E. Spohr: Computer modeling of interfaces between aqueous and metallic phases, *Acta Chem. Scandinav.* 49 (1995) 189–202.

[49] M. Mezei and D. L. Beveridge: Free energy simulations, *Annals of the New York Academy of Sciences* 482 (1986) 1–23.

[50] A. Ignaczak, J. A. N. F. Gomes and S. Romanowski: The potential of mean force on halide ions near the Cu(100) surface, *J. Electroanal. Chem. Interfacial Electrochem* 450 (1998) 175–188.

[51] A. S. Viana: *Preparation, Electrochemical and Optical Characterization of Modified Electrodes by Self-Assembled Monolayers*, Ph.D. thesis, Univesity of Lisbon (2002).

Int. J. Quantum Chem. 107 (2007) 2169-2177

A Force Field for Simulating Ethanol Adsorption on Au(111) Surfaces. A DFT Study

Rui P. S. Fartaria, Filomena F. M. Freitas and Fernando M. S. Silva Fernandes[1]
Department of Chemistry and Biochemistry, Faculty of Sciences, University of Lisboa, Campo Grande, Bloco C8, 1749-016 Lisboa, Portugal

Abstract

The development of a DFT force field to describe the adsorption of ethanol on Au(111) surfaces is presented. An analytical potential energy function is proposed based on fitting the DFT results by means of genetic algorithms. A preliminary test of the force field by Monte Carlo simulations shows a good consistency between the DFT and simulation results. They are also related to previous theoretical and spectroscopic studies on the adsorption of methanol and ethanol on gold clusters.

Keywords: ethanol, gold, adsorption, force-field, DFT, genetic algorithms

[1]corresponding author: fsilva@fc.ul.pt

1 Introduction

Potential Energy Surfaces (PES) are crucial to study reactive and non-reactive chemical systems by molecular simulations. For example, to investigate the mechanisms involved in the adsorption and self-assembly of solvated organic molecules on noble-metal electrodes, the PES should describe the interactions between the different molecular species present in the liquid phase, as well as the interactions between those species and the electrodes, in terms of distances and orientation angles.

Presently, we are interested in the study of the adsorption and self-assembly of alkylthiols, solvated by ethanol, on gold electrodes, regarding the mechanisms of physisorption and chemisorption, the formation of self-assembled monolayers and the structure of the double layer [1]. To the best of our knowledge, though, there is a lack of force fields, based on quantum mechanical calculations, for the interaction of ethanol with gold electrodes, in particular relatively to the Au(111) surface.

The main objective of this work is to set up such a force field, from Density Functional Theory (DFT) calculations, for the simulation of those heterogeneous systems by Monte Carlo and molecular dynamics.

The DFT calculations are described in the next section. Section 3 presents the fitting of the quantum results to an analytical function by means of genetic algorithms. Section 4 reports preliminary Monte Carlo simulations using the proposed PES. Finally, Section 5 presents the concluding remarks.

2 DFT Calculations

The starting point for building the ethanol-Au(111) PES was the calculation of interaction energy values by DFT [2–6]. This method has emerged as a promising approach to deal with the electronic correlation effects, which play an important role specially in systems containing transition metal atoms. One of its advantages, relatively to *ab initio* methods that also include electronic correlation, is to turn the computations more efficient for many electron systems. The theory level chosen for the present calculations was the hybrid B3LYP method with the LanL1MB basis set [7] applied to the Au atoms and the 6-31G basis set [8] for the H, C and O atoms. The LanL1MB belongs to a family of basis sets using the Hay and Wadt [7, 9, 10] effective-core potentials (ECP) to describe the core electrons and a minimal (MB), or double zeta (DZ), basis for the outermost (valence) electrons. Relativistic effects are of the utmost importance for elements of the 2nd and 3rd transitions series and

are folded, on average, in the ECPs constructs. In the case of gold, the LanL1MB specifies the use of a relativistic ECP for the electrons of the [Xe] $4f^{14}$ core and a MB for the remaining valence electrons ($5d^{10}$ $6s^1$). B3LYP is a hybrid method, implemented and parametrized by A. D. Becke [6,11], combining *ab initio* and DFT approximations. It uses the Hartree-Fock exchange potential and DFT exchange terms, namely the corrected correlation functional gradient developed by Lee *et al.* [4].

The above choice has been found adequate to model, for example, the interaction of water with transition metal surfaces [12] and it is assumed to work well for the ethanol adsorption. Studies of the interaction of methanol [13–15] and ethanol [16] with gold clusters showed that these molecules adsorb on the clusters through the O atom, similarly to water. All the calculations were performed using the GAUSSIAN98 software package [17].

To model the ethanol-Au(111) PES we used a cluster of 14 Au atoms, representing the surface, and one ethanol molecule in the equilibrium gas phase configuration calculated by a geometry optimization. A systematic search for the appropriate cluster size and geometry, in order to approach the Au(111) surface, was carried out with the compromise between the consistency of the yielded interaction energies and computing time. To this end a set of clusters with 8, 12, 14, 16, and 24 atoms was tested. We shall comment ahead on the chosen ethanol configuration.

The representation of an infinite surface by a small cluster is a common approximation in order to minimize the heavy computational requirements. Nevertheless, several studies, (see, for example, the review of Knickelbein [18]), with transition metal clusters suggest that the interactions between infinite metal surfaces and other species may be approached by using representative clusters. This does not mean, of course, that all the chemistry of bulk systems can be reproduced by small clusters. Gold, in particular, is quite unreactive in the bulk but it has significant catalytic activity in the form of nanoparticles [19–21]. This is, certainly, an important issue, which we do not address in the present paper. In fact, we assume that the interactions between bulk gold and ethanol can be approached by small gold clusters. The assessment of how far we can go with this assumption is one of the goals of our study.

Experimental and theoretical works on the adsorption of methanol, and more recently of ethanol on gold clusters [13–15] showed that methanol and ethanol adsorb intact on gold clusters. Furthermore, the binding occurs through the O atom of the hydroxyl group and always with the less coordinated available Au atom of the cluster.

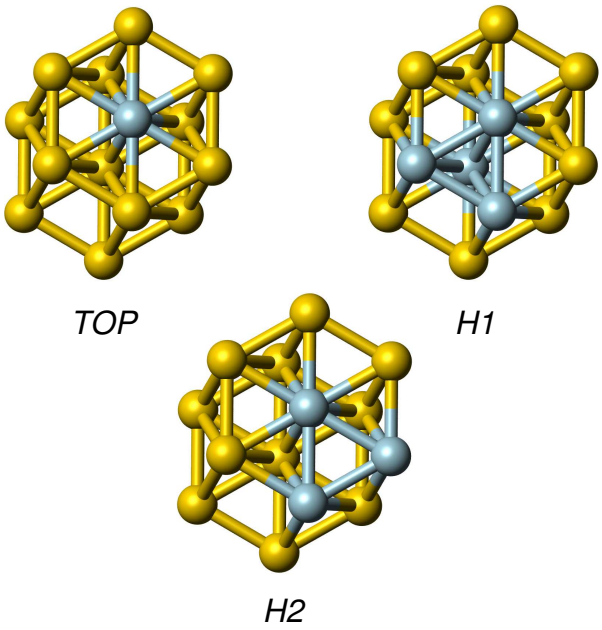

Figure 1: Surface sites, top, hollow1 and hollow2, chosen to set up the ethanol-Au surface interaction.

Although there is not much experimental work [22] on the interactions in this family of molecules with gold surfaces, the studies carried out hitherto lead to the relevant insight that the binding should be weaker for strongly packed surfaces and stronger for more open ones (which have less coordinated surface atoms).

Three sites have been selected to probe the ethanol-surface interaction, as shown in Figure 1: the top (*TOP*) site where the O atom approaches the surface directly over an Au atom of the 1st layer; the hcp site, named hollow1 (*H1*), and the fcc site, named hollow2 (*H2*) where the O atom approaches the surface in the direction of the center of a triangle formed between three Au atoms of the 1st layer. For site *H1* the triangle presents an Au atom of the second layer at the center.

The ethanol-Au$(111)_{14}$ cluster interaction energy as a function of the distance and orientation, relatively to the cluster Au(111) surface, is defined as

$$U_{\text{ethanol}-\text{Au}(111)_{14}}(r,\alpha,\beta) = U_{\text{Au}(111)+\text{ethanol}}(r,\alpha,\beta) - U_{Au(111)_{14}} - U_{\text{ethanol}} \quad (1)$$

where $U_{\text{Au}(111)+\text{ethanol}}$ is the energy of the system composed by the ethanol molecule and the cluster; $U_{\text{Au}(111)}$ and U_{ethanol} are, respectively, the energies of the isolated cluster and ethanol molecule; r is the distance from the ethanol O atom to the plane of the first layer of the Au(111) surface; α is the angle between the O-H bond and the normal to the surface and β is the angle between the H-O-C plane and the

H-O-(normal to the surface) plane. The orientations for the ethanol molecule were selected to span a wide range of situations, as presented in Figure 2 with the notation α/β. For each orientation, several values of r (about 30), spanning the interval 0-10 Å, were chosen and the $U_{\text{ethanol}-\text{Au(111)}_{14}}$ was evaluated. The interaction energy profiles are displayed in Figure 3. Table 1 presents the numerical values of the potential energy minima location, for each ethanol molecule orientation over each of the three selected adsorption sites.

The effect of restricting the ethanol molecule to the gas phase configuration was evaluated by computing the interaction energy with the molecule fully optimized at various distances of approach to the gold surface. The value obtained with the full optimization for the 90/180 orientation is of ∼-21 kJ mol^{-1} at the potential minimum. Also, a similar calculation was made using the LanL2DZ basis set, giving an interaction energy of ∼-18 kJ mol^{-1}. These values are within ∼2 kJ mol^{-1} from the value of ∼-19 kJ mol^{-1} (see Table 1) obtained for the model chosen in the present work. In view of these results, it seems that the present model constitutes a reasonable approximation not excluding, of course, the need for a more extensive study on this important aspect.

The results presented in Table 1 show that, in general, the strongest binding occurs for the orientations where the O atom is towards the surface and the CH_3 group away from it. The orientations 180/180 and 90/0, with the ethyl group turned to the surface, are always the most repulsive ones. The preferential site for the adsorption is the *TOP* one, at the 90/180 orientation where the O-H bond is parallel to the surface, with a minimum energy of ∼-19 kJ mol^{-1} at r ∼2.4 Å. Outka and Madix [22] reported an enthalpy of adsorption for methanol on an Au(110) surface of 56 kJ mol^{-1}. Considering that this is a more opened surface than the Au(111) one (thus, with less coordinated surface atoms) it seems consistent to find a weaker interaction with the Au(111) surface since it is the most closed surface of all. In the TOP site, the 90/180 orientation is also distinctly stronger in binding than the other ones, in contrast to the other sites for which there is some intermixing on the binding energy of different orientations. After the *TOP* site, in decreasing order of interaction strength, comes the *H1* and then the *H2* sites, with minimum binding energies of ∼-17 kJ mol^{-1} and ∼-15 kJ mol^{-1}, respectively.

In the *H1* site the preferential orientation is the 45/180 although the 90/180 one (with a minimum of ∼4 kJ mol^{-1} higher but ∼0.2 Å nearer to the electrode) crosses the repulsive part of the first one being the less repulsive at the end. This is interpreted as being the effect of the strong repulsion due to the *H* atom that in the

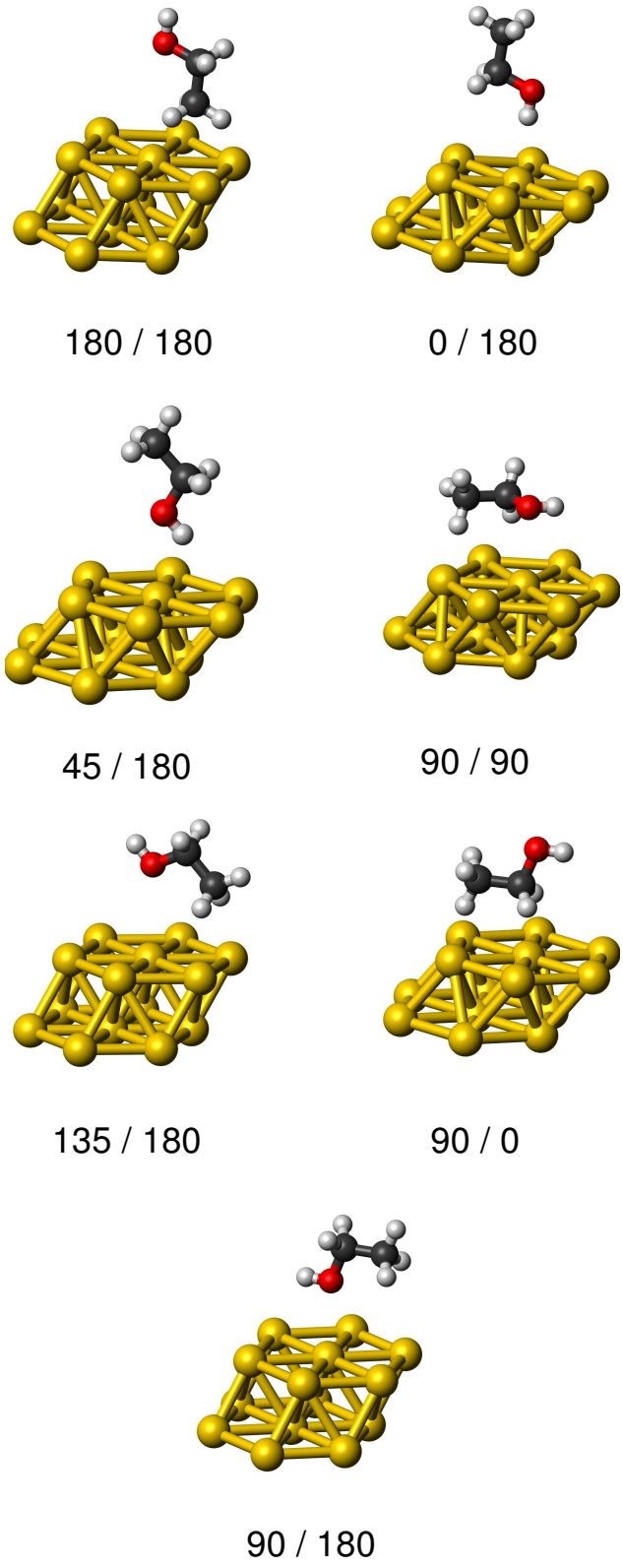

Figure 2: Selected orientations of the ethanol molecule relative to the Au(111) surface (notation: α/β, see text).

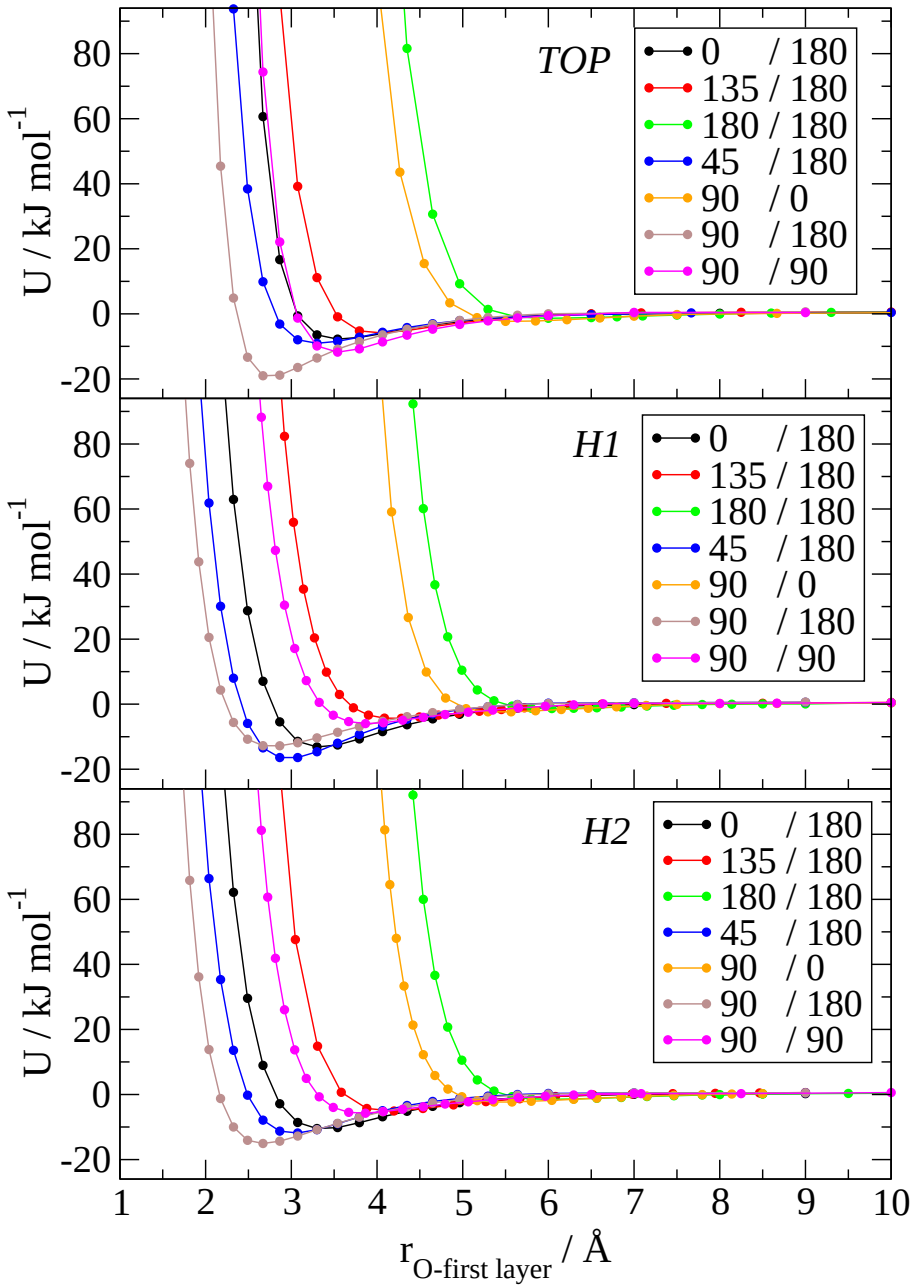

Figure 3: Potential energy values for the ethanol - $Au(111)_{14}$ interaction. The lines are guides for the eye.

Table 1: Potential energy minima location for each orientation and surface site.

Ethanol orientation		Distance O-surface	Potential Energy
α / degrees	β / degrees	r / Å	$-U$ / kJ mol^{-1}
Top (T) site			
0	180	3.6	7.9
135	180	4.0	6.0
180	180	6.1	1.7
45	180	3.3	9.2
90	0	5.7	2.4
90	180	2.8	19.5
90	90	3.6	11.9
Hollow1 (H1) site			
0	180	3.4	13.3
135	180	4.2	4.1
180	180	6.2	1.2
45	180	3.0	16.6
90	0	5.5	2.6
90	180	2.8	12.7
90	90	3.9	6.1
Hollow2 (H2) site			
0	180	3.4	10.4
135	180	4.2	5.1
180	180	6.1	1.7
45	180	3.0	12.0
90	0	5.5	2.4
90	180	2.7	15.2
90	90	3.8	5.8

45/180 orientation (as well as in the 0/180 one) goes into the electrode hindering the *O* approach. For the H2 site the preferential orientation is at 90/180, as in the TOP site. The main difference between this site and the *H1* and *TOP* ones is that there is no Au atom directly below the O atom, to which it can be attached. On the other hand, there are, on average, more Au atoms in the neighborhood (3 from the 1st layer and another 3 from the 2nd one). This leads to an interaction behavior comparable to an electrostatic one, with the binding character evenly distributed among the neighbor gold atoms, resulting in smoother and "better behaved" interaction curves.

3 Fitting the Potential Energy Surface

The molecular orientation and the energetic relation between the sites for adsorption, obtained from the interaction energy curves, only indicate the preferential behavior for the adsorption of ethanol molecules on the electrode in contact with the liquid phase. The global behavior, however, will depend greatly on the thermodynamic conditions imposed upon the system and the multiple ethanol-ethanol and ethanol-electrode interactions. To study these effects it is necessary to perform simulations using a force field describing all the interactions.

To this end, we developed an analytical force field for the interaction of ethanol molecules with Au(111) surfaces. The strategy was to fit an analytical function to the whole set of DFT interaction energy points presented in the previous section. A fitting of this kind of data is often complicated due to the existence of multiple local minima for the fitting function. A method specially suitable to overcome this difficulty is the use of Genetic Algorithms (GA) [23]. This technique generates a population of individuals in each iteration in a way that the best individuals of the forthcoming populations approach an optimal solution. The software used for this work was developed by the authors using the package GALib [24]. In this application an "individual" is a set of parameters taken from the trial function in the fitting process. Initially the populations were filled with random generated sets of parameters (with boundaries for each parameter) and then evolved using a GA until the convergence of the best scores was observed.

The elements chosen for the fitting were an Au(111) double layered surface of 74 Au atoms and an united atom model of the ethanol molecule (with H, O, CH_2 and CH_3 interaction sites). The size of the Au(111) surface was chosen so that the minimum distance between an Au atom, belonging to the periphery, and an ethanol site was at least 8 Å. This choice was based on the observation that at ∼8 Å the

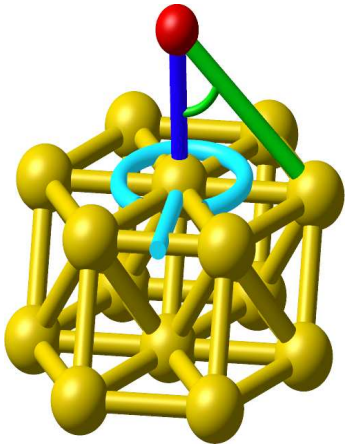

Figure 4: Chosen degrees of freedom for the ethanol-Au(111) interaction. The angular dependence θ is represented by the angle in green and the angular dependence ϕ is represented in light blue with the reference direction indicated by the cylinder of the same color.

energy curves asymptotically approach zero. The basis for the construction of the ethanol-Au analytical PES was to consider it as the sum of the interactions between each Au atom and the sites of the ethanol molecule, and two angular contributions, one related to the *TOP* site surface symmetry and the other to the O-Au interaction relative direction. Consequently, the variables used for the description of the interactions are: the distance, r, from each Au atom to each of the ethanol sites; the angle, θ, between the $\mathbf{r}_{\mathrm{O-Au}}$ vector and the normal to the surface; and the angle, ϕ, between the projection of the $\mathbf{r}_{\mathrm{O-Au}}$ vector on the surface plane and a reference surface vector beginning in a *TOP* site and pointing in the direction of a *H1* site, as shown in Figure 4. The selected function to represent the interaction between an ethanol molecule and a gold atom is

$$\begin{aligned} U_{EtOH-Au} &= U_H\left(r_{H-Au}\right) + \left(1 + B_0 \cos\left(\theta/rad\right)^{20} / r_{O-Au}^3\right) \cdot U_O\left(r_{O-Au}\right) + \\ & U_{CH_2}\left(r_{CH_2-Au}\right) + U_{CH_3}\left(r_{CH_3-Au}\right) + V\left(r_{O-Au}, \theta, \phi\right) \end{aligned} \quad (2)$$

where

$$U_i\left(r_{i-\mathrm{Au}}\right) = A_{0,i} \exp\left[A_{1,i}\left(r_{i-\mathrm{Au}} + A_{2,i}\right)\right] - A_{3,i} \exp\left[A_{4,i}\left(r_{i-\mathrm{Au}} + A_{5,i}\right)\right] \quad (3)$$

Table 2: Parameters for $U_i\left(r_{i-\mathrm{Au}}\right)$ in equation (3).

	A_0 (kJ mol^{-1})	A_1 (Å^{-1})	A_2 (Å)	A_3 (kJ mol^{-1})	A_4 (Å^{-1})	A_5 (Å)
H	74534.5	-4	0.0	111996	-2.2	2.7
O	29633.0	-2.6	0.4	17852.9	-1.2	3.5
CH_2	18594.0	-3.7	-1.2	85932.8	-3.6	8.7
CH_3	76040.5	-3.3	-0.5	63929.7	-1.4	4.5

Table 3: Parameters for the angular dependencies in equations (2) and (4).

B_0 (Å^3)	C_0 –	C_1 (Å)	C_2 (Å^2)
12.64	2000	1.05	-0.11
C_3 (kJ mol^{-1})	C_4 (kJ mol^{-1})	C_5 –	C_6 (kJ mol^{-1})
1.5	-0.27	1.4	0.2

is the site-site interaction energy and

$$V\left(r_{O-Au},\theta,\phi\right) = C_0 \sin\left(\theta/rad\right)^6 \cdot \exp\left[\left(r\sin\left(\theta/rad\right)-C_1\right)^2/C_2\right] \cdot \left(C_3 - C_4\cos\left(3\left(\phi/rad - C_5\right)\right) + C_6\cos\left(6\left(\phi/rad-C_5\right)\right)\right) \quad (4)$$

is the referred to contribution due to the surface symmetry around a *TOP* site. The values for the parameters $A_{\ldots,i}$, B_j, and C_k are presented in Tables 2 and 3. The cosine term with exponent of 20, in eq. 2, can be expressed in other forms (e.g. $\exp(-10x^2)$). The interaction energy between the ethanol molecule and the surface is calculated as the sum of $U_{EtOH-Au}$ over all the Au atoms in the surface. The fitting results for the main orientations in each site are presented in Figure 5. The fit for the *TOP* 90/180 and *H2* 90/180 curves is very good with less than 1 kJ mol^{-1} of deviation from the reference (DFT) curve at the minima region. In the H1 case the most favorable orientation is the 45/180 one. However, the fitting curve is not able to fully reproduce this situation since it gives the 90/180 configuration as the most favorable. In the fit, the 45/180 minimum is -13 kJ mol^{-1} (-16 kJ mol^{-1} in DFT) and the 90/180 one is -15 (-13 kJ mol^{-1} in DFT). As this is not the most important site for the adsorption and the role of these two orientations does not change in a great extent, this effect should have a minor influence in the molecular simulation results.

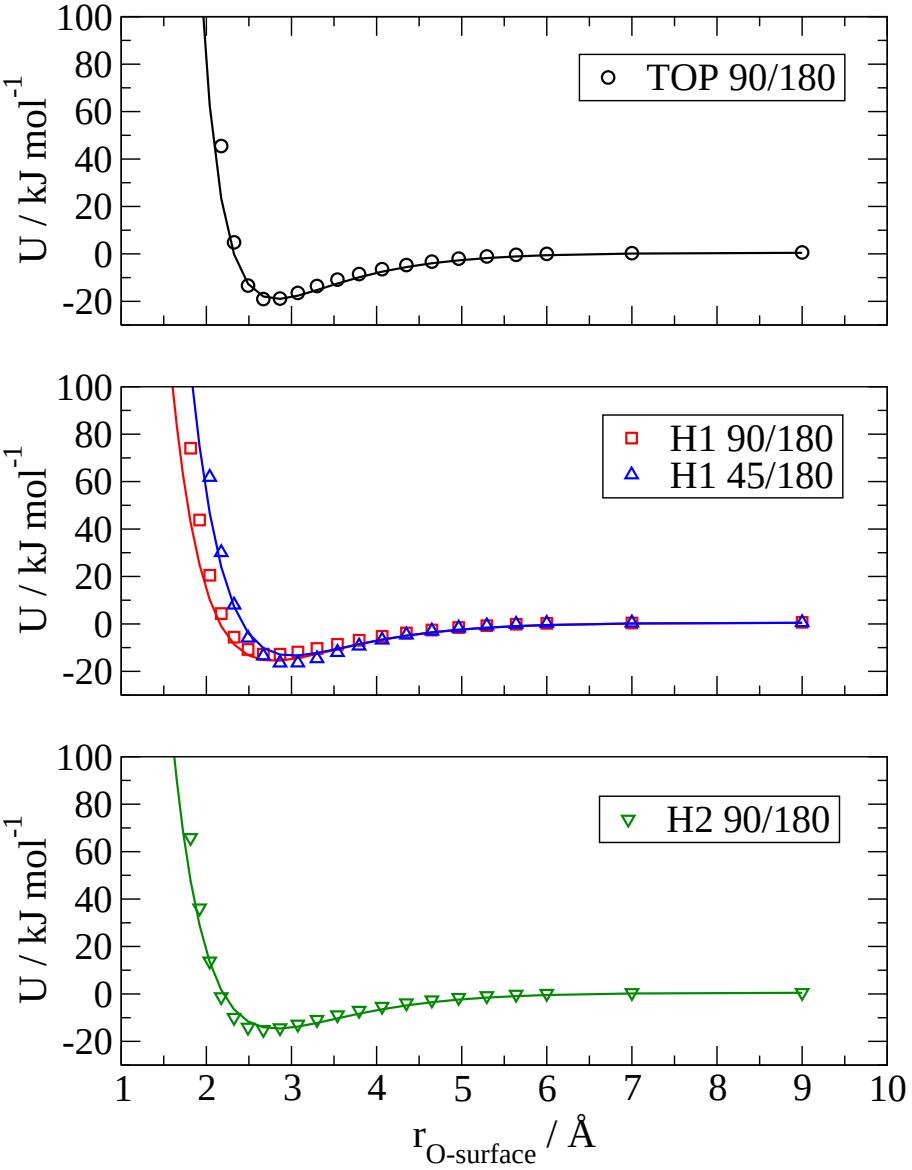

Figure 5: Fitting of the DFT results for the most attractive orientations in each site. The DFT values are presented as symbols and the fitting as lines.

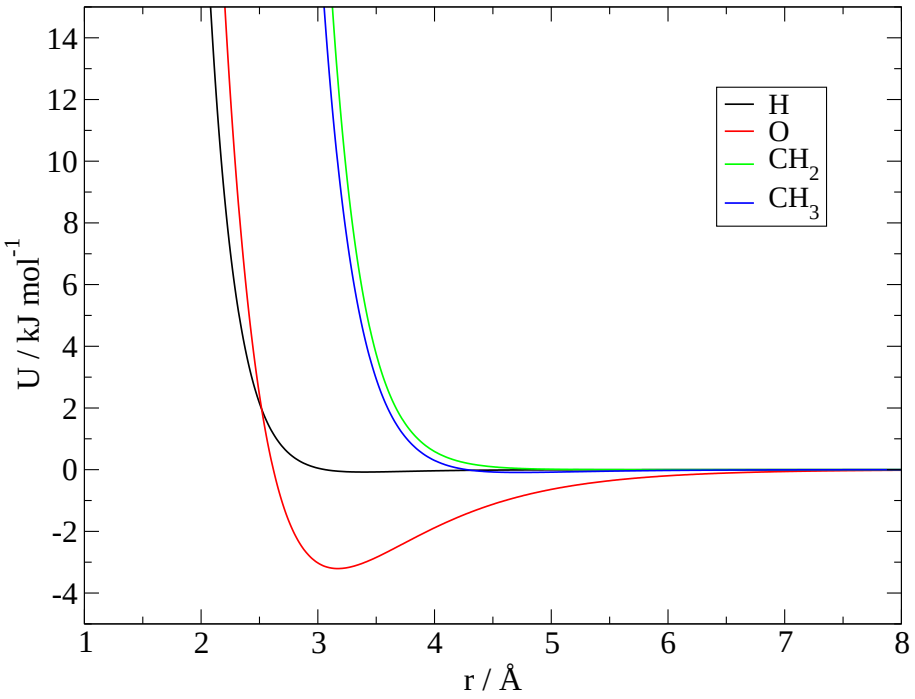

Figure 6: Individual ethanol site-Au interactions (equation 3).

It is also important to analyze the potential description of the individual ethanol site-Au interactions. It will give an idea of how these single interactions contribute to the whole ethanol-surface interaction and the relative importance of each ethanol site in the adsorption process. The plots of $U_i\left(r_{i-\mathrm{Au}}\right)$, in equation 3, are presented in Figure 6. They clearly show that, in this force field, the molecule should adsorb on the electrode from the O site and the other sites have repulsive contributions in order to control the allowed molecule orientations. However, the repulsive contributions of the CH_2 and CH_3 sites are felt at greater distances from the Au atoms, than for the H site, due to their bigger size. The behaviors described are in accordance with the insights provided by *ab initio*, DFT and experimental studies [13–15, 22].

4 Monte Carlo Simulations

To test the developed force field, preliminary Monte Carlo (MC) simulations were performed in the canonical ensemble (NVT) at 298 K. The sample was composed by 960 molecules of ethanol placed between a double layered 416 Au atoms electrode and a soft-wall surface. The electrode and soft-wall were placed parallel to the XY plane. The soft-wall is intended to constrain the ethanol molecules in order to maintain constant density conditions with the least perturbation of the system.

Periodic boundary conditions were used only in the X and Y directions since in the Z direction the system is confined by the two "walls". The simulation box dimensions were 37.5×40.0×65.6 Å. The system size was chosen taking into account the density of liquid ethanol at 298 K and 1 atm so that at half way between the two "walls" the ethanol molecules behavior should correspond to the bulk liquid. Each MC cycle consisted of trial moves for translation, rotation and dihedral torsion for each ethanol molecule. Equilibrium runs were performed with ∼ 5000 cycles and production runs took ∼ 20000 cycles divided in 5000 cycles blocks. The ethanol-ethanol intermolecular and ethanol intramolecular interactions were modeled by OPLS potentials of Jorgensen *et al.* [25]. These are parametrized combinations of a Lennard-Jones (LJ) and Coulomb potentials for liquid phases. The ethanol-soft-wall interactions were only repulsive and acted on the center of mass of the ethanol molecule. They were modeled by the Lennard-Jones truncated and shifted potential

$$u(r) = \begin{cases} u^{LJ}(r) - u^{LJ}(r_{min}) & r \leq r_{min} \\ 0 & r > r_{min} \end{cases} \tag{5}$$

where r_{min} is the value of r at the minimum of the LJ potential curve. Finally, the ethanol-electrode interactions were modeled by the herewith developed interaction potential.

The interfacial structure for ethanol adsorption was analyzed by calculating the ethanol density profiles, presented in Figure 7, along the normal to the electrode surface. These give the relative density of each ethanol site as a function of the distance to the electrode. The density profiles clearly show the existence of a well defined first adsorption layer, from ∼2 - 6 Å and two more diffuse layers, from ∼6 - 9 Å and ∼9 - 13 Å. Also, apart from minor fluctuations, for distances beyond ∼ 15 Å the relative density approaches unity as it would be expected in a bulk environment with no surface influence whatsoever. The first ethanol adsorption layer can also be observed in the snapshot of Figure 8. In this layer, the intense and narrow peaks (see Figure 7) indicate that this is a well organized layer, with the hydroxyl group attached to the electrode and the CH_2 and CH_3 sites turned to the bulk liquid. The position of the peaks for the H and O sites also shows that ethanol adsorbs with the OH bond parallel to the electrode, in accordance to the most favorable orientation suggested by the DFT calculations for the TOP site. The second adsorption layer has the CH_2 and CH_3 sites turned to the same sites of the first layer showing an obvious influence of the polar - polar and non-polar - non-polar groups affinities. The

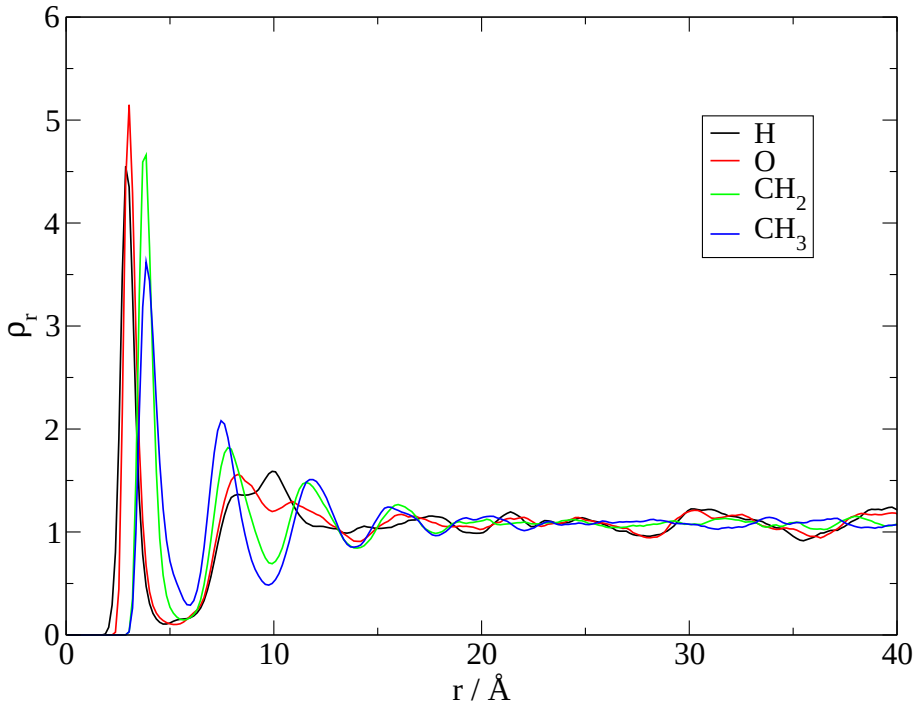

Figure 7: Ethanol density profiles along the normal to the electrode surface. r is the distance to the electrode surface.

third and most diffuse layer has again a structure correlated (in a minor degree) with the second layer. Therefore, according to these results, the interfacial region for the ethanol adsorption on Au(111) gold electrodes covers the range of 2 to 15 Å with increasingly disorganization as one moves towards the bulk liquid.

Finally, it is worth mentioning that although the DFT calculations were carried out up to the distance of 10 Å, where the ethanol-Au potential asymptotically approaches zero, the density profiles displayed in Figure 7 show up correlations beyond that distance. Indeed, they reflect the ethanol-ethanol interactions modeled by OPLS. Nonetheless, it is clear that up to ∼6 Å a major contribution is from the ethanol-Au potential.

5 Conclusions

We have presented the development and implementation of a force field for the ethanol - Au(111) surface interactions. According to the DFT calculations, ethanol adsorption should occur preferentially on the TOP site of the Au(111) surface with the O atom directly adsorbed on the Au atom, and with the OH bond parallel to the electrode surface. The implementation of the force field in MC simulations repro-

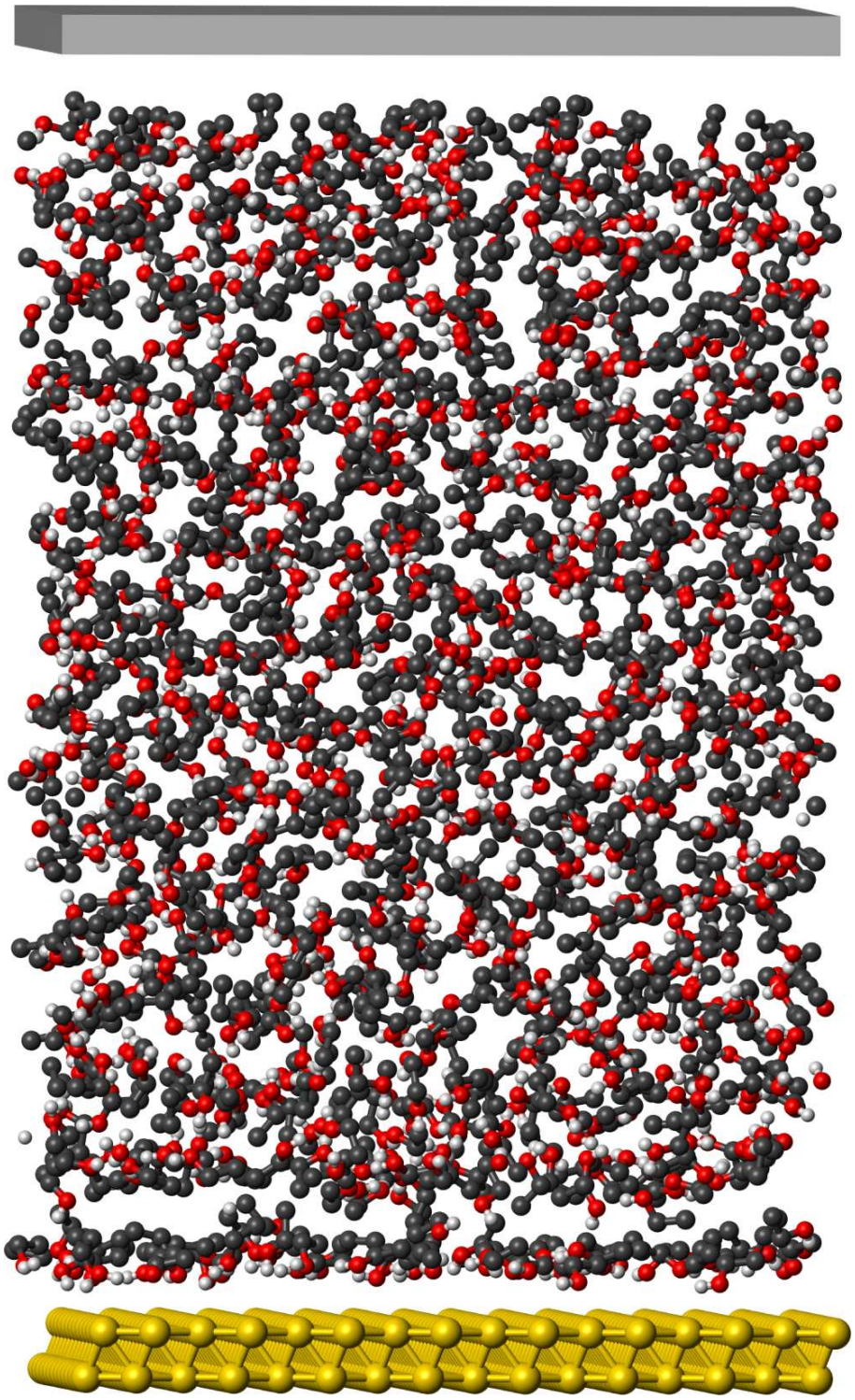

Figure 8: Last configuration of the production run for the ethanol + gold-electrode + soft-wall system.

duces the behaviors indicated by DFT calculations as shown by the density profiles. The interfacial region for the adsorption of ethanol extends up to 15 Å from the electrode, and is organized in three adsorption layers. The simulations demonstrate that the force field herewith presented produces well behaved results with no singularities. The structure and behavior of the interface have to be further analyzed by performing simulations with a more refined model, including 2D Ewald sum [26, 27] and, eventually, charge-image contributions [28, 29] for a better description of the electrostatic effects. Density profiles, surface covering and potentials of mean force should be calculated and compared with available experimental data, in order to completely validate the model.

Finally, the use of other basis sets (e.g. LanL1DZ, LanL2MB and LanL2DZ) for the DFT calculations, concerned with gold, as well as a full geometry optimization of the ethanol molecule at different distances from the surface are important aspects to be further analyzed. Work along these lines is in progress and will be reported soon.

Acknowledgements

The authors thank Professor Natália Cordeiro, University of Porto, Portugal, for the fruitful discussion on ECPs. Rui P. S. Fartaria gratefully acknowledges the support of Fundação para a Ciência e a Tecnologia (PhD. grant SFRH/BD/10405/2002).

References

[1] R. P. S. Fartaria, F. F. M. Freitas and F. M. S. S. Fernandes: A study of 1-decanethiol self-assembly on gold electrodes by computer simulation, *J. Electroanal. Chem.* 574 (2005) 321–331.

[2] P. Hohenberg and W. Kohn: Inhomogeneous electron gas, *Phys. Rev.* 136 (1964) B864.

[3] W. Kohn and L. J. Sham: Self-consistent equations including exchange and correlation effects, *Phys. Rev.* 140 (1965) A1133.

[4] C. Lee, W. Yang and R. G. Parr: Development of the colle-salvetti correlation-energy formula into a functional of the electron-density, *Phys. Rev. B* 37 (1988) 785–789.

[5] R. G. Parr and W. Yang: *Density-Functional Theory of Atoms and Molecules*, Oxford University Press, New York (1989).

[6] A. D. Becke: Density-functional thermochemistry. 3. The role of exact exchange, *J. Chem. Phys.* 98 (1993) 5648–5652.

[7] P. J. Hay and W. R. Wadt: Ab initio effective core potentials for molecular calculations - potentials for the transition-metal atoms Sc to Hg, *J. Chem. Phys.* 82 (1985) 270–283.

[8] W. J. Hehre, R. Ditchfield and J. A. Pople: Self-consistent molecular-orbital methods. 12. Further extensions of gaussian-type basis sets for use in molecular-orbital studies of organic-molecules, *J. Chem. Phys.* 56 (1972) 2257.

[9] P. J. Hay and W. R. Wadt: Ab initio effective core potentials for molecular calculations. Potentials for main group elements Na to Bi, *J. Chem. Phys.* 82 (1985) 284.

[10] P. J. Hay and W. R. Wadt: Ab initio effective core potentials for molecular calculations. Potentials for K to Au including the outermost core orbitals., *J. Chem. Phys.* 82 (1985) 299.

[11] A. D. Becke: A new mixing of Hartree-Fock and local density-functional theories, *J. Chem. Phys.* 98 (1993) 1372–1377.

[12] A. Ignaczak and J. A. N. F. Gomes: A theoretical study of the interaction of water molecules with the Cu(100), Ag(100) and Au(100) surfaces, *J. Electroanal. Chem.* 420 (1997) 209–218.

[13] M. B. Knickelbein and G. M. Koretsky: Infrared studies of the interaction of methanol with Cu_n, Ag_n, and Au_n, *J. Phys. Chem. A* 102 (1998) 580–586.

[14] R. Rousseau, G. Dietrich, S. Krückeberg, Lützenkirchen, D. Marx, L. Schweikhard and C. Walther: Probing cluster structures with sensor molecules: methanol adsorbed onto gold clusters, *Chem. Phys. Lett.* 295 (1998) 41–26.

[15] R. Rousseau and D. Marx: The interaction of gold clusters with methanol molecules: Ab initio molecular dynamics of $Au_n^+CH_3OH$ and Au_nCH_3OH, *J. Chem. Phys.* 112 (2000) 761.

[16] G. M. Koretsky, M. B. Knickelbein, R. Rousseau and D. Marx: A combined infrared photodissociation and theoretical study of the interaction of ethanol with small gold clusters, *J. Phys. Chem. A* 105 (2001) 11197–11203.

[17] M. J. Frisch, G. W. Trucks, H. B. Schlegel, G. E. Scuseria, M. A. Robb, J. R. Cheeseman, V. G. Zakrzewski, J. A. Montgomery, R. E. Stratmann, J. C. Burant, S. Dapprich, J. M. Millam, A. D. Daniels, K. N. Kudin, M. C. Strain, O. Farkas, J. Tomasi, V. Barone, M. Cossi, R. Cammi, B. Mennucci, C. Pomelli, C. Adamo, S. Clifford, J. Ochterski, G. A. Petersson, P. Y. Ayala, Q. Cui, K. Morokuma, D. K. Malick, A. D. Rabuck, K. Raghavachari, J. B. Foresman, J. Cioslowski, J. V. Ortiz, B. B. Stefanov, G. Liu, A. Liashenko, P. Piskorz, I. Komaromi, R. Gomperts, R. L. Martin, D. J. Fox, T. Keith, M. A. Al-Laham, C. Y. Peng, A. Nanayakkara, C. Gonzalez, M. Challacombe, P. M. W. Gill, B. G. Johnson, W. Chen, M. W. Wong, J. L. Andres, M. Head-Gordon, E. S. Replogle and J. A. Pople: *Gaussian 98*, Gaussian Inc., Pittsburgh PA (1998).

[18] M. B. Knickelbein: Reactions of transition metal clusters with small molecules, *Annu. Rev. Phys. Chem.* 50 (1999) 79–115.

[19] P. Schwerdtfeger: Gold goes nano - from small clusters to low-dimensional assemblies, *Angew. Chem. Int. Ed.* 42 (2003) 1892–1895.

[20] L. M. Molina and B. Hammer: Oxygen adsorption at anionic free and supported Au clusters, *J. Chem. Phys.* 123 (2005) 161104.

[21] P. Pyykko: Theoretical chemistry of gold, *Angew. Chem. Int. Ed.* 43 (2004) 4412–4456.

[22] D. A. Outka and R. J. Madix: The chemistry of atomic oxygen on the Au(110) surface, *J. Vac. Sci. Technol. A* 3 (1985) 1680.

[23] M. Mitchell: *An Introduction to Genetic Algorithms*, MIT Press, Cambridge, MA (1996).

[24] M. Wall: *GAlib - A C++ Library of Genetic Algorithm Components*, Massachusetts Institute of Technology (MIT) (1995), URL `http://lancet.mit.edu/ga/`.

[25] W. L. Jorgensen: Optimized intermolecular potential functions for liquid alcohols, *J. Phys. Chem.* 90 (1986) 1276–1284.

[26] E. Spohr: Effect of electrostatic boundary conditions and system size on the interfacial properties of water and aqueous solutions, *J. Chem. Phys.* 107 (1997) 6342–6348.

[27] I.-C. Yeh and M. L. Berkowitz: Ewald summation for systems with slab geometry, *J. Chem. Phys.* 111 (1999) 3155–3162.

[28] J. Hautman, J. W. Halley and Y.-J. Rhee: Molecular-dynamics simulation of water between 2 ideal classical metal walls, *J. Chem. Phys.* 91 (1989) 467–472.

[29] M. R. Philpott and J. N. Glosli: Molecular-dynamics simulation of the adsorption of benzene on charged metal-electrodes in the presence of aqueous-electrolyte, *Chem. Phys.* 198 (1995) 53–61.

5.1 Comparação de modelos computacionais para a interface etanol - Au(111)

Apresentámos, até ao momento, um estudo sobre o efeito dos modelos básicos de interacção etanol-Au(111) na descrição da aproximação do 1-decanotiol à superfície metálica, e o desenvolvimento de um campo de forças melhorado para a interacção etanol-Au(111). Estudaremos agora o comportamento da interface etanol-Au(111), tendo em conta os efeitos de estrutura da superfície Au(111) e a transição de modelos de moléculas rígidas para moléculas flexíveis, com introdução de graus de liberdade intramoleculares. Por fim, analisaremos o modelo "completo" com a introdução da soma de Ewald para o cálculo das interacções de longo alcance.

Recorreu-se a uma série de simulações pelo método MC no ensemble *NVT*. Os sistemas simulados eram constituídos por 980 moléculas de etanol, uma superfície plana, na parte superior, representando uma "soft-wall" (tal como já apresentado anteriormente [1]) e uma superfície Au(111), na parte inferior. Cada uma das superfícies apresentava como dimensões $37,5 \times 39,9$ Å. A superfície Au(111) era composta por 416 átomos de ouro, dispostos em duas camadas de acordo com a estrutura de uma superfície (111). As interacções inter- e intramoleculares utilizadas para a fase líquida do sistema foram descritas por potenciais OPLS [2,3], já apresentadas anteriormente [1,4]. As interacções etanol-Au(111), no caso da superfície não estruturada, foram representadas por um potencial 12-3 do tipo Lennard-Jones [5] reparametrizado para os valores do mínimo de energia de interacção, obtido por cálculos DFT, já apresentados por Fartaria et al. [4] (pag. 159). No caso da superfície estruturada a sua interacção com as moléculas de etanol foi modelada pelo campo de forcas já apresentado, também, por Fartaria et al. [1] (pag. 183). Sobre a interacção etanol-"soft-wall" é ainda de referir que esta interacção foi aplicada apenas no centro de massa da molécula de etanol podendo as moléculas em contacto com a superfície rodar independentemente desta. Adoptou-se esta estratégia com a intenção de minimizar os efeitos da superfície, de modo a que se dissipassem rapidamente em direcção ao interior do sistema. Os sistemas foram equilibrados com 2×10^4 ciclos de MC e os resultados obtidos com corridas de 2×10^5 ciclos de produção.

De modo a obter informação relativamente às características estruturais da interface, no estudo sobre a influência da estruturação da superfície e introdução de graus intramoleculares nas moléculas de etanol, calcularam-se, para cada um dos centros de interacção da molécula de etanol (H, O, CH_2 e CH_3): os perfis de densidade em função da distância à superfície (Figuras 5.1 e 5.2) e os perfis bi-dimensionais

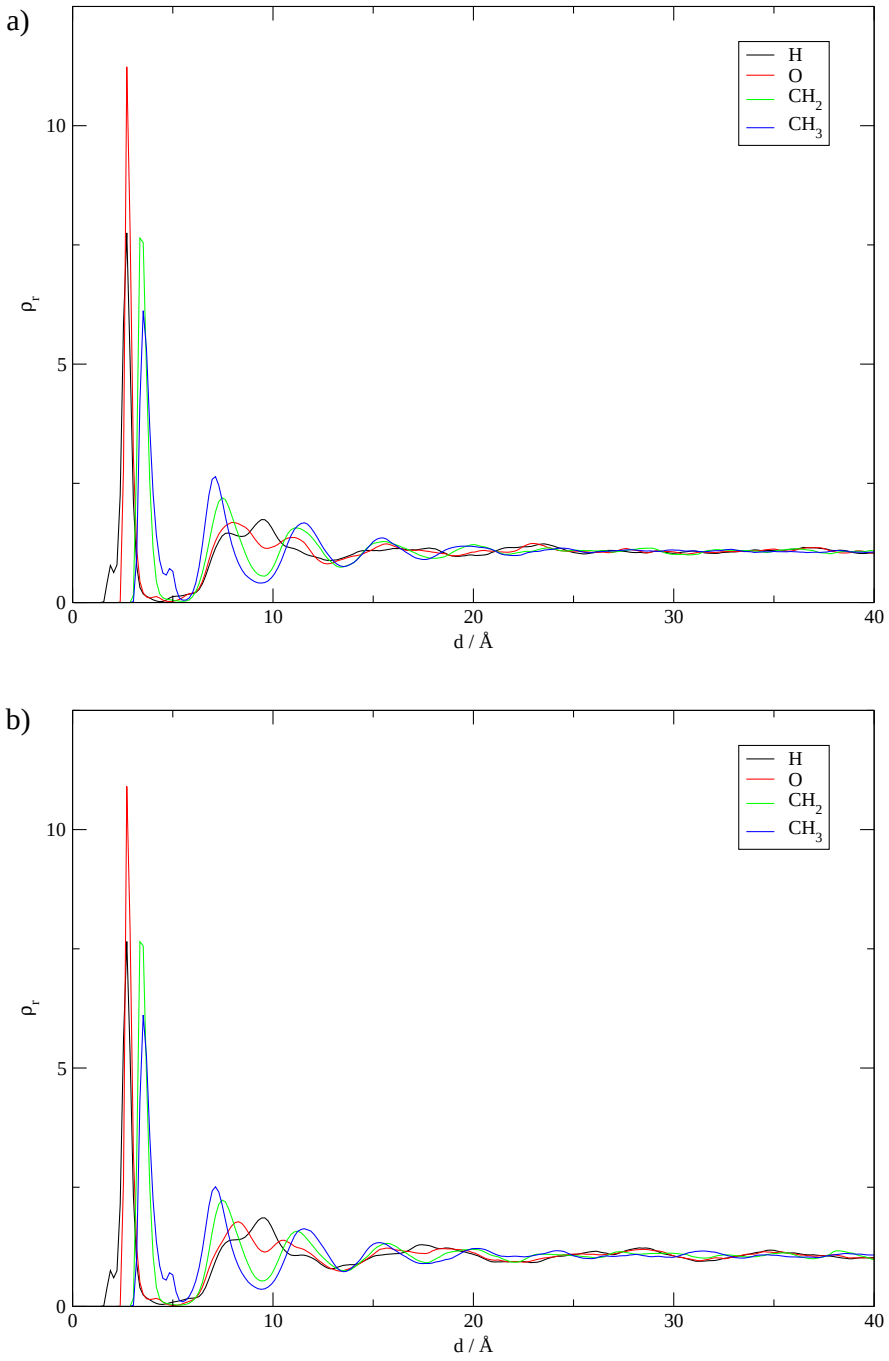

Figura 5.1: Perfis de densidade para o modelo com eléctrodo plano: a) com moléculas rígidas e b) com moléculas flexíveis.

Tabela 5.1: Identificação de picos e camadas de adsorção para os perfis de densidade da Figura 5.1 (eléctrodo plano). Valores em Å, excepto para o número de moléculas.

a) moléculas rígidas					
Camada	Centros	Picos	Loc. Camada	Espessura	Nº Molec.
1	H	2,7; 2,0	1,3 a 5,6	4,3	67
	O	2,7			
	CH2	3,4			*66±1*
	CH3	3,5; 4,9			
2	H	7,7	5,6 a 9,6	4,0	66
	O	8,1			
	CH2	7,5			
	CH3	7,1			
3	H	9,5; 11,0	9,6 a 13,3	3,7	63
	O	11,0			
	CH2	11,2			
	CH3	11,5			
b) moléculas flexíveis					
Camada	Centros	Picos	Loc. Camada	Espessura	Nº Molec.
1	H	2,7; 1,9	1,3 a 5,5	4,2	67
	O	2,7			
	CH2	3,4			*66±1*
	CH3	3,5; 4,9			
2	H	7,9	5,5 a 9,5	4,0	66
	O	8,2			
	CH2	7,5			
	CH3	7,1			
3	H	9,5; 11,5	9,5 a 13,4	3,9	63
	O	10,5			
	CH2	11,1			
	CH3	11,6			

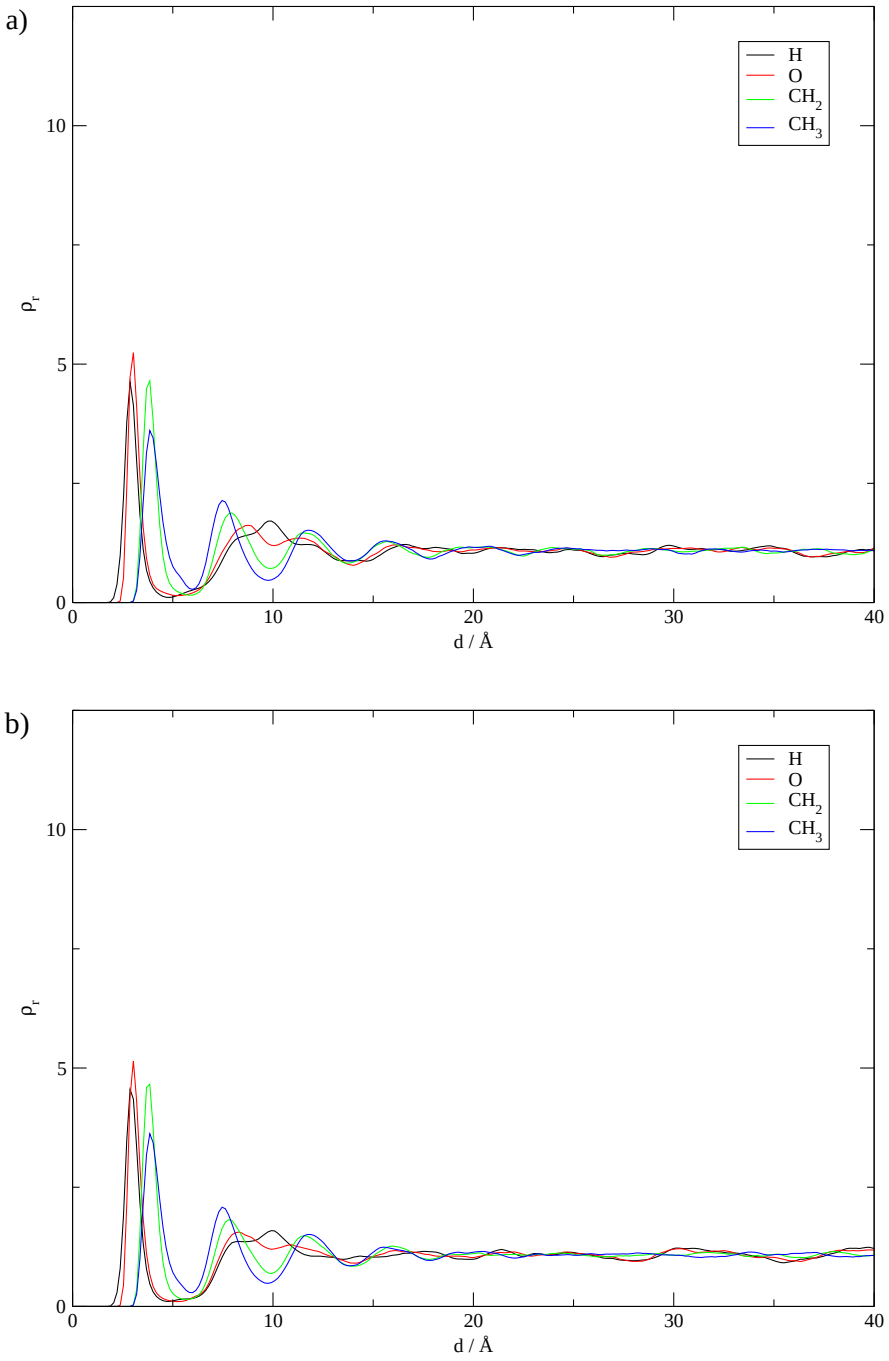

Figura 5.2: Perfis de densidade para o modelo com eléctrodo estruturado: a) com moléculas rígidas e b) com moléculas flexíveis.

Tabela 5.2: Identificação de picos e camadas de adsorção para os perfis de densidade da Figura 5.2 (eléctrodo estruturado). Valores em Å, excepto para o número de moléculas.

a) moléculas rígidas					
Camada	Centros	Picos	Loc. Camada	Espessura	Nº Molec.
1	H	2,9	1,6 a 5,5	3,9	60
	O	3,0			
	CH2	3,8			*59±2*
	CH3	3,9			
2	H	8,5	5,5 a 10,0	4,5	68
	O	8,7			
	CH2	7,9			
	CH3	7,5			
3	H	9,8; 11,8	10,0 a 14,0	4,0	67
	O	11,5			
	CH2	11,6			
	CH3	11,8			
b) moléculas flexíveis					
Camada	Centros	Picos	Loc. Camada	Espessura	Nº Molec.
1	H	2,8	1,6 a 5,7	4,1	61
	O	3,0			
	CH2	3,8			*59±2*
	CH3	3,9			
2	H	8,2	5,7 a 9,9	4,2	66
	O	8,3			
	CH2	7,8			
	CH3	7,5			
3	H	10,0	9,9 a 13,8	3,9	64
	O	11,0			
	CH2	11,5			
	CH3	11,8			

da densidade superficial relativa para as moléculas da primeira camada de adsorção (Figuras 5.3, 5.4, 5.5 e 5.6). A identificação dos picos principais e a localização aproximada das camadas de adsorção dos perfis de densidade das Figuras 5.1 e 5.2 encontram-se nas tabelas 5.1 e 5.2, respectivamente. O número, aproximado, de moléculas de etanol em cada camada de adsorção, também incluído nestas tabelas, foi calculado por integração dos perfis de densidade dos centros de interacção O e CH_3 através da fórmula

$$n\left(z_f\right) = \frac{N}{Z}\int_0^{z_f} g\left(z\right) dz \tag{5.1}$$

onde N é o número total de moléculas no sistema, Z é a distância entre os eléctrodos e $g\left(z\right)$ é a densidade relativa em função da distância ao eléctrodo, z. No caso da primeira camada de adsorção o número médio de moléculas adsorvidas foi também registado por amostragem configuracional e vem apresentado em itálico nas tabelas.

Analisando os perfis de densidade da Figura 5.1, para a superfície não estruturada, dos quais o perfil a), com moléculas rígidas, foi já parcialmente apresentado e analisado [4], verifica-se que o perfil b), para as moléculas flexíveis, mantém basicamente as mesmas características que o anterior. As camadas de adsorção encontram-se na mesma posição e permanecem basicamente inalteradas. Nota-se apenas que no caso das moléculas flexíveis a influência do eléctrodo se estende, de forma muito suave, um pouco para além dos 20 Å. A distribuição dos picos na primeira camada, com {O, H} e {CH_2, CH_3} separados por ∼0,8 Å, é consistente com uma orientação média das moléculas de etanol em que a ligação OH se encontra praticamente paralela à superfície e com o plano da molécula a formar um ângulo de ∼45° com esta. Observando a distribuição dos picos da segunda e terceira camadas, conclui-se que os centros CH_2 e CH_3 da segunda se encontram virados para a primeira enquanto que os mesmos centros da terceira se encontram virados para o interior da solução, ficando assim os picos O e H a fazer a ligação entre estas duas camadas como se pode ver na representação esquemática da Figura 5.7, onde se apresentam as orientações gerais das moléculas de etanol nas três primeiras camadas de adsorção. Esta observação, reforçada pela maior intensidade do pico H da terceira camada, sugere fortemente a formação de pontes de hidrogénio entre estas duas camadas, e ao mesmo tempo que a interacção entre a primeira e segunda camadas se faz através dos grupos hidrofóbicos da molécula de etanol, não parecendo existir, portanto, formação de pontes de hidrogénio. Um outro detalhe importante, já referido anteriormente em [4], são os pequenos picos a ∼2,0 Å, para o H, e a ∼4,9 Å, para o CH_3, da primeira camada. Estes traduzem a existência de alguns desvios da orientação principal nesta camada,

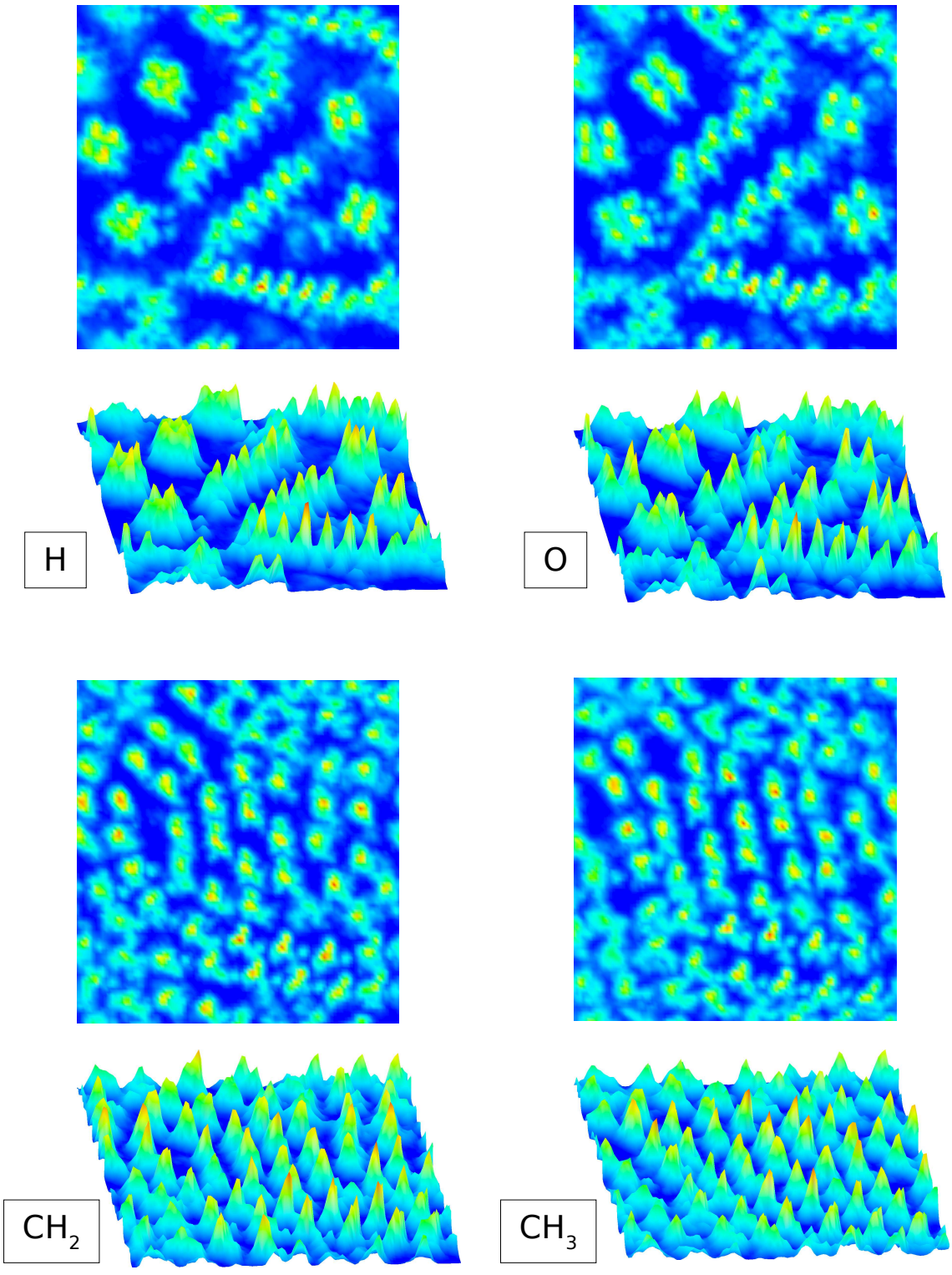

Figura 5.3: Densidade superficial relativa de cada um dos sítios, H, O, CH_2 e CH_3 das moléculas de etanol da primeira camada de adsorção. Sistema com eléctrodo plano e moléculas de etanol rígidas.

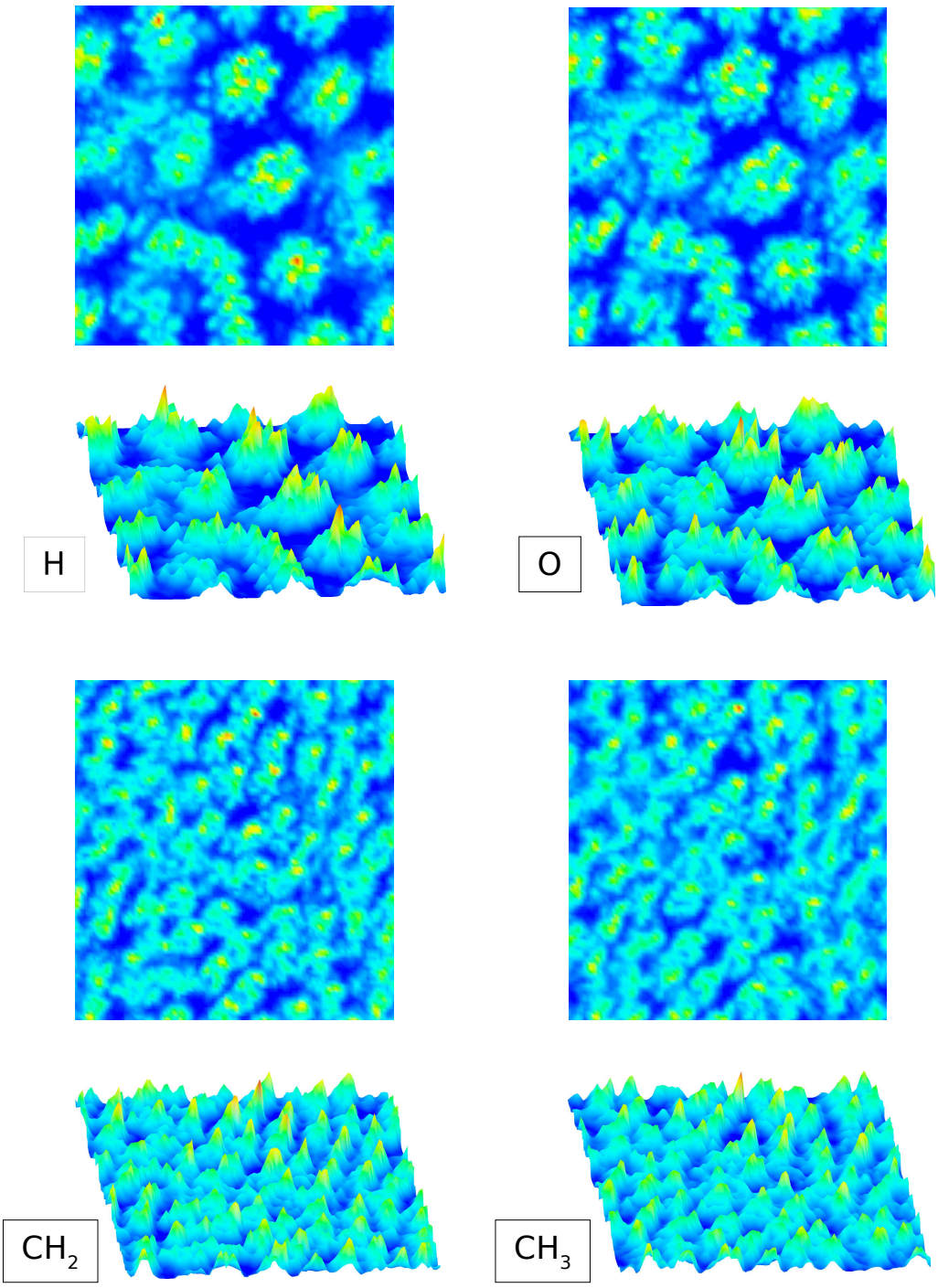

Figura 5.4: Densidade superficial relativa de cada um dos sítios, H, O, CH_2 e CH_3 das moléculas de etanol da primeira camada de adsorção. Sistema com eléctrodo plano e moléculas de etanol flexíveis.

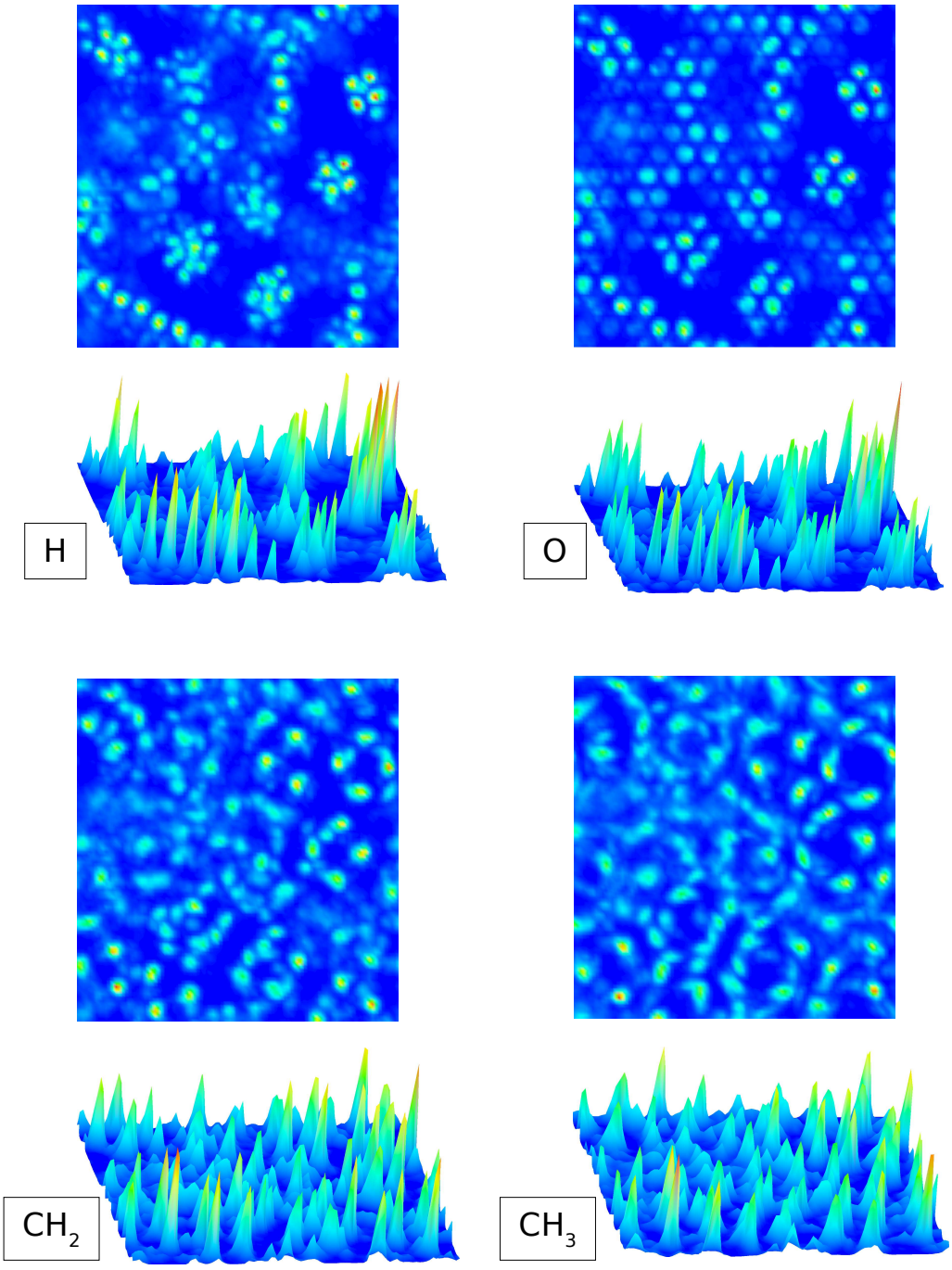

Figura 5.5: Densidade superficial relativa de cada um dos sítios, H, O, CH_2 e CH_3 das moléculas de etanol da primeira camada de adsorção. Sistema com eléctrodo estruturado e moléculas de etanol rígidas.

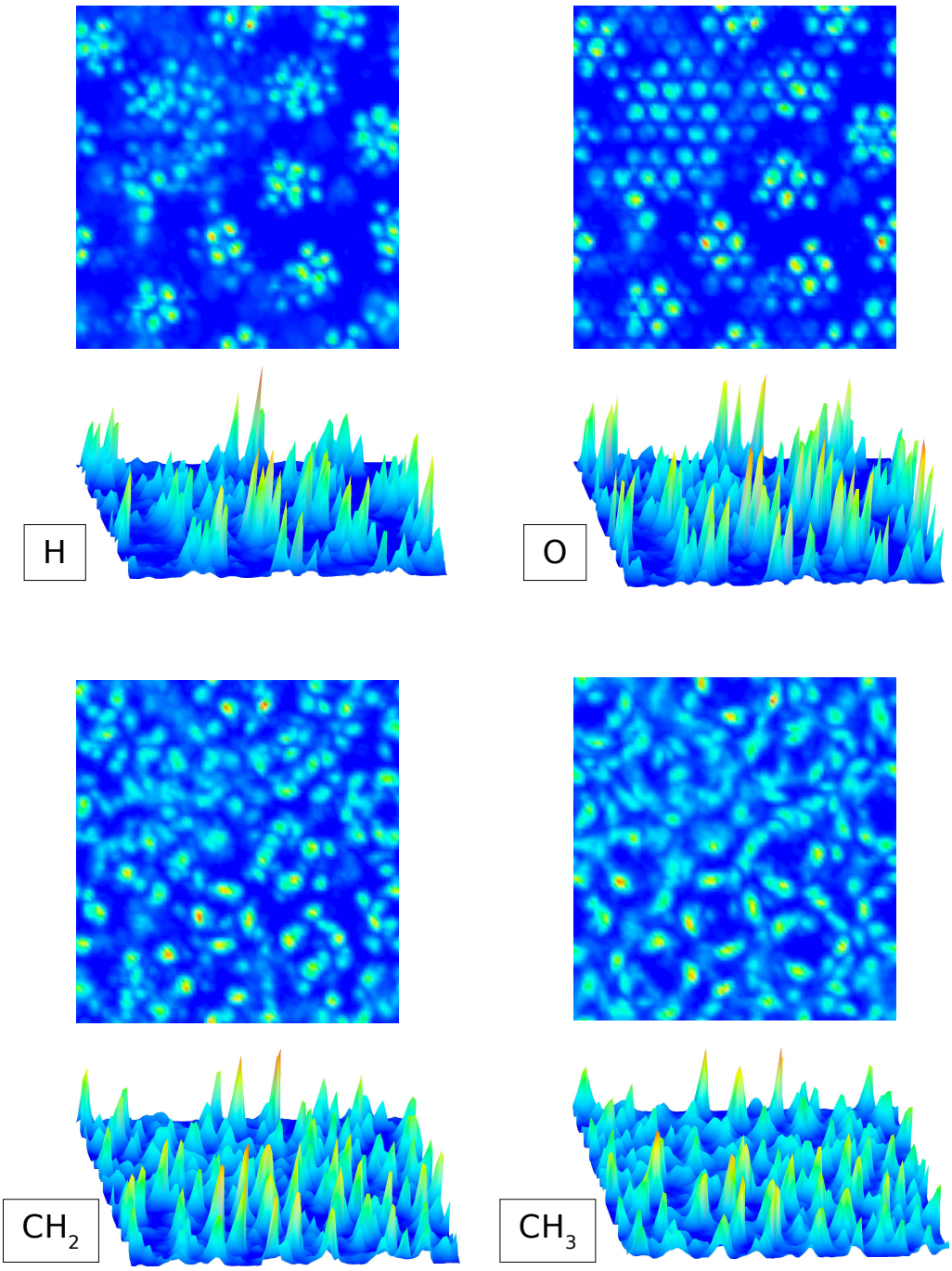

Figura 5.6: Densidade superficial relativa de cada um dos sítios, H, O, CH_2 e CH_3 das moléculas de etanol da primeira camada de adsorção. Sistema com eléctrodo estruturado e moléculas de etanol flexíveis.

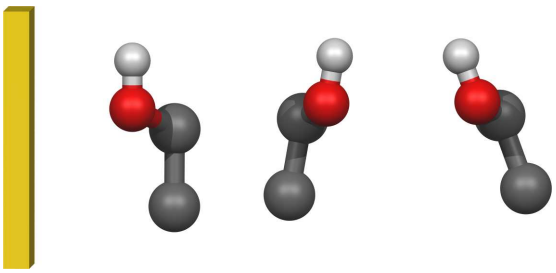

Figura 5.7: Orientações gerais das moléculas de etanol. Da esquerda para direita: primeira, segunda e terceira camadas.

com as moléculas numa posição "mais perpendicular" em relação à superfície (ver Figura 11 de [4]).

Observando os perfis de densidade da Figura 5.2 para o eléctrodo estruturado, conclui-se que a estrutura da interface etanol-Au(111), no que diz respeito às orientações das moléculas relativamente à superfície, mantém essencialmente as mesmas características, conservando-se a distribuição geral apresentada na Figura 5.7. No entanto, com este novo campo de forças, em que as interacções etanol-Au(111) são calculadas explicitamente para cada átomo de ouro na superfície, observa-se uma diminuição considerável da intensidade dos picos da primeira camada de adsorção. Esta, está associada a uma diminuição, de ∼67 para ∼60 (ver Tabelas 5.1 e 5.2 respectivamente), do número de moléculas de etanol na primeira camada de adsorção. Este efeito observa-se tanto nos sistemas de moléculas rígidas como nos de moléculas flexíveis, sendo portanto, consequência apenas da mudança da interacção etanol-Au(111).

Os perfis bi-dimensionais (2D), apresentados nas Figuras 5.3, 5.4, 5.5 e 5.6, mostram a densidade superficial das moléculas de etanol na primeira camada de adsorção, relativamente à densidade superficial média para esta camada (calculada durante as simulações). Através destes perfis pode-se retirar, de uma forma qualitativa, informação sobre a distribuição e mobilidade das moléculas sobre a superfície. Assim, no sistema com o eléctrodo plano e moléculas rígidas (Figura 5.3) observa-se a existência de conjuntos de quatro moléculas de etanol e também de estruturas em cadeia, com várias moléculas de etanol. Em volta dos conjuntos de quatro moléculas verifica-se, nos perfis para H e O, a inexistência de outros centros, H e O, adsorvidos em volta deles. Este vazio resulta, tendo em conta as orientações retiradas dos perfis de densidade "verticais", do impedimento esterioquímico provocado pelos centros CH_2 e CH_3. No que diz respeito aos perfis 2D para os centros CH_2 e CH_3, observa-se um empacotamento mais uniforme e com picos mais largos, indicando uma maior

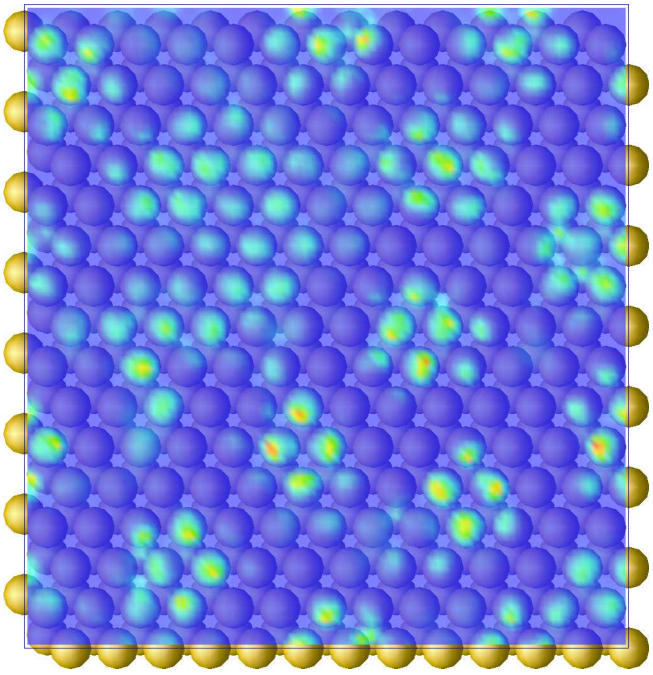

Figura 5.8: Projecção do perfil de densidade superficial do O sobre a superfície Au(111) no modelo mais completo.

mobilidade para estes centros da molécula de etanol. Ao introduzir flexibilidade nas moléculas de etanol, mas continuando com a superfície não estruturada (ver Figura 5.4), observa-se a intensificação da formação de conjuntos de quatro moléculas de etanol em detrimento da formação de cadeias. O alargamento geral dos picos para os quatro centros, comparativamente aos correspondentes na Figura 5.3, indica que as moléculas têm maior mobilidade, sendo esta consequência da introdução dos graus de liberdade intramoleculares.

A mudança da interacção etanol-Au(111) do potencial de superfície 12-3 para o campo de forças apresentado nesta tese, vem introduzir alterações substanciais na distribuição e mobilidade superficiais das moléculas de etanol. De acordo com o que foi discutido anteriormente, a influência desta mudança na distribuição "vertical" das moléculas não é muito importante, verificando-se apenas uma diminuição do número de moléculas na primeira camada de adsorção. Dos perfis 2D da Figura 5.5, conclui-se que as moléculas de etanol, adsorvem na superfície, através do átomo de O, com preferência pelos sítios TOP (ver [1]) da superfície como se mostra na Figura 5.8. Ainda se observa a formação de alguns conjuntos de quatro moléculas e alguma tendência para formação de cadeias. O afilamento dos picos dos centros H e O revela, no entanto, uma menor mobilidade "horizontal" das moléculas adsorvidas.

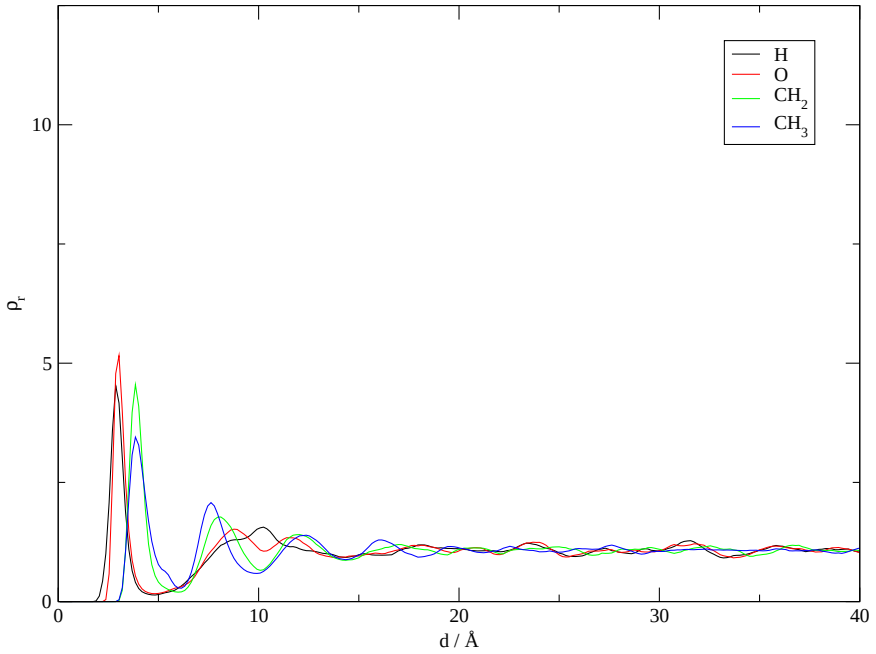

Figura 5.9: Perfis de densidade para o modelo com eléctrodo estruturado com moléculas flexíveis e com as interacções de longo alcance calculadas por somas de Ewald.

Ao passar para a Figura 5.6, verifica-se, com a introdução dos graus de liberdade intramoleculares, o desaparecimento das cadeias e uma maior incidência na formação de conjuntos moleculares. Estes perfis apresentam uma distribuição de picos mais difusa indicando que as moléculas apresentam maior mobilidade.

Nos casos até agora apresentados, o cálculo das interacções de Coulomb foi feito directamente, incluindo todas as distâncias no sistema (sem raio de corte). Para um cálculo mais rigoroso deste tipo de interacções, num sistema com condições de fronteira periódicas (apenas em duas direcções), é necessário utilizar uma técnica que inclua as denominadas contribuições de longo alcance inerentes a este tipo de potencial. Introduziram-se, então, as somas de Ewald para duas dimensões [6]. Os resultados obtidos, análogos aos anteriormente apresentados para os outros modelos, encontram-se nas Figuras 5.9 e 5.10. Na Tabela 5.3 encontram-se registadas as localizações dos picos dos perfis de densidade deste sistema, assim como a localização das camadas de adsorção e o número médio de moléculas em cada camada de adsorção. Comparando os perfis de densidade das Figuras 5.2b) e 5.9 observa-se que, de facto, os perfis são muito similares, apresentando basicamente o mesmo traçado para os quatro centros da molécula de etanol. No entanto, no caso dos perfis 2D das Figuras 5.6 e 5.10, em relação à distribuição "horizontal" das moléculas de etanol,

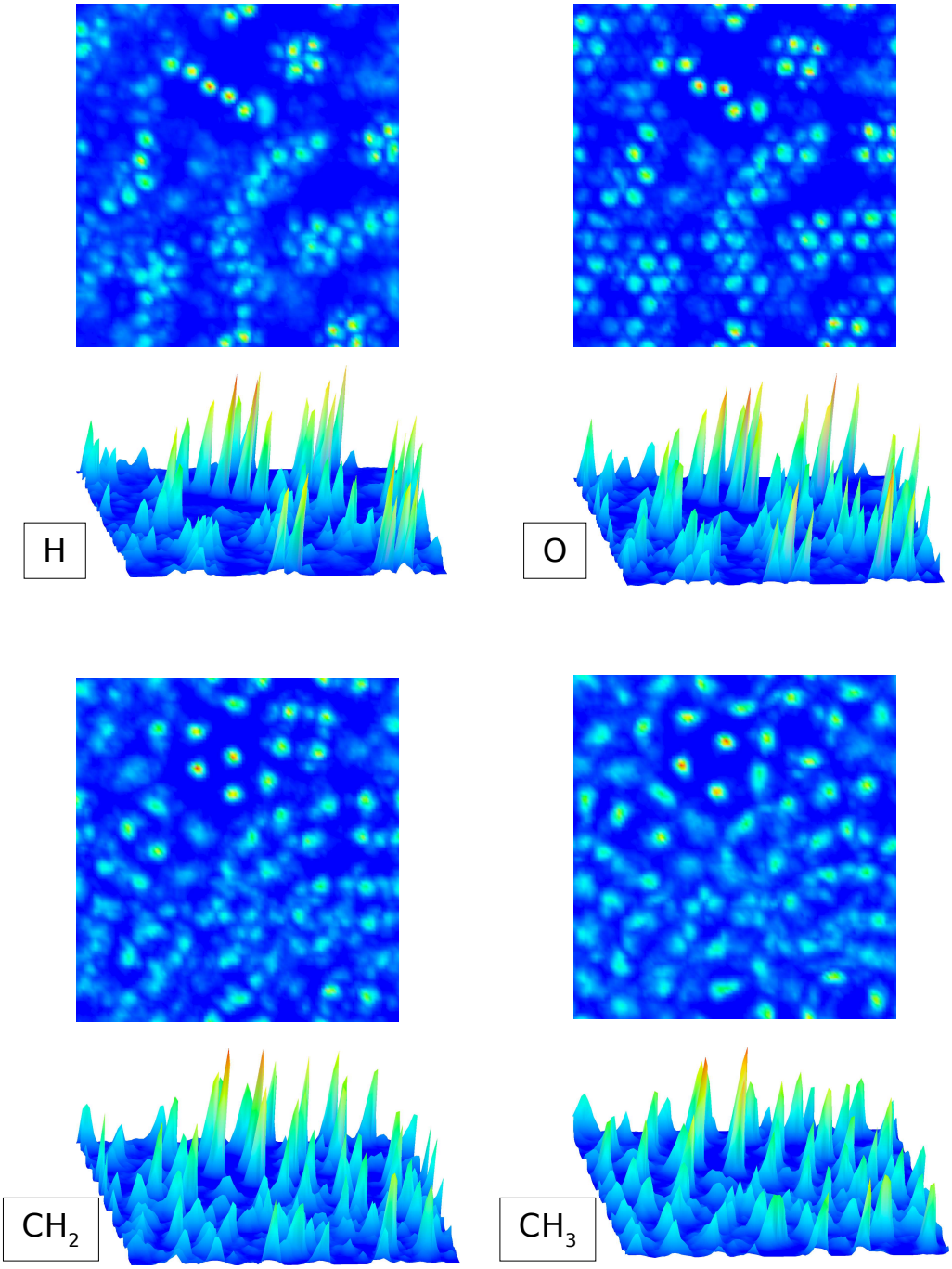

Figura 5.10: Densidade superficial relativa de cada um dos sítios das moléculas de etanol (H, O, CH_2 e CH_3) da primeira camada de adsorção. Sistema com eléctrodo estruturado e moléculas de etanol flexíveis e interacções de longo alcance calculadas por somas de Ewald.

Tabela 5.3: Identificação de picos e camadas de adsorção para o perfis de densidade da Figura 5.9. Valores em Å, excepto para o número de moléculas.

Camada	Centros	Picos	Loc. Camada	Espessura	Nº Molec.
	H	2,9			
1	O	3,0	1,5 a 5,5	4,0	60
	CH2	3,8			*58±2*
	CH3	3,9			
	H	8,7			
2	O	8,8	5,5 a 10,3	4,8	70
	CH2	8,0			
	CH3	7,6			
	H	10,2			
3	O	11,5	10,3 a 14,3	4,0	65
	CH2	11,9			
	CH3	12,3			

notam-se algumas diferenças. A formação de aglomerados de quatro e cinco moléculas, no sistema com somas de Ewald, parece diminuir um pouco, ou pelo menos os que se formam não mantém uma estrutura tão bem definida. Nota-se, também, a formação de uma pequena cadeia com quatro ou cinco moléculas de etanol. Estas diferenças em relação ao modelo sem soma de Ewald não são muito acentuadas podendo considerar-se que o comportamento dos dois sistemas é bastante similar.

Da análise dos resultados, apresentada nesta secção, pode concluir-se que os principais efeitos, causados pelas alterações sucessivas, introduzidas nos modelos da molécula de etanol e sua interacção com a superfície Au(111) são:

- Em geral, a organização "vertical" das moléculas de etanol é pouco sensível às modificações introduzidas, o que implica que esta depende principalmente das características da interacção directamente dependentes da distância à superfície do eléctrodo.

- A introdução de flexibilidade nas moléculas de etanol provoca uma maior mobilidade das moléculas na interface tendo pouca influência na organização "vertical" das camadas de adsorção.

- A estruturação da superfície, através do campo de forças apresentado, não exerce grande influência na distribuição "vertical" das camadas de adsorção,

mas altera, consideravelmente, a distribuição "horizontal" das moléculas adsorvidas. É a esta modificação na interface, que influencia radicalmente o empacotamento das moléculas de etanol, que se deve atribuir a diminuição do número de moléculas localizadas na primeira camada de adsorção.

A discussão destes efeitos serve de suporte para a interpretação dos resultados da secção seguinte, sobre o estudo da adsorção física do 1-decanotiol na interface etanol-Au(111).

5.2 Adsorção do 1-decanotiol na interface etanol - Au(111). Potenciais de força média

No estudo inicial do comportamento da molécula de 1-decanotiol na sua aproximação à superfície Au(111), apresentado nesta tese em Fartaria et al. [4] (pag. 159), utilizou-se um modelo simples com moléculas rígidas e interacções molécula-eléctrodo do tipo Lennard-Jones 12-3. Nesta secção apresentar-se-ão os resultados das simulações efectuadas para o mesmo tipo de estudo mas com um modelo mais refinado em que se consideram os graus de liberdade intramoleculares das moléculas de etanol e 1-decanotiol (através da aplicação do método MCCB [7]). A interacção etanol-Au(111) é modelada pelo campo de forças já referido [1] (pag. 183).

Os efeitos da introdução de uma molécula de 1-decanotiol na interface foram estudados através de simulações de MC com 30000 ciclos de produção. Calcularam-se os perfis de densidade para as moléculas de etanol, em função da distância ao eléctrodo, apresentados na Figura 5.11, e também os perfis de densidade superficial para a primeira camada de adsorção, apresentados na Figura 5.12 sob a forma de projecção sobre a superfície do eléctrodo. Na Figura 5.13 apresenta-se ainda um modelo de uma configuração da primeira camada de adsorção das moléculas de etanol incluindo uma molécula de 1-decanotiol adsorvida na superfície do eléctrodo.

Comparando os perfis da Figura 5.11 com os da 5.10, para o mesmo modelo mas sem a molécula de 1-decanotiol, observa-se o mesmo tipo de comportamento na orientação geral das camadas de adsorção. Nota-se, no entanto, que os picos da primeira camada de adsorção apresentam menor intensidade, o que leva a concluir que o número de moléculas de etanol na primeira camada de adsorção diminuiu, como seria de esperar, com a introdução do 1-decanotiol. De facto, o número médio de moléculas de etanol na primeira camada de adsorção, calculado por média configuracional, é de 46 ± 2. O número de moléculas de etanol deslocadas por uma

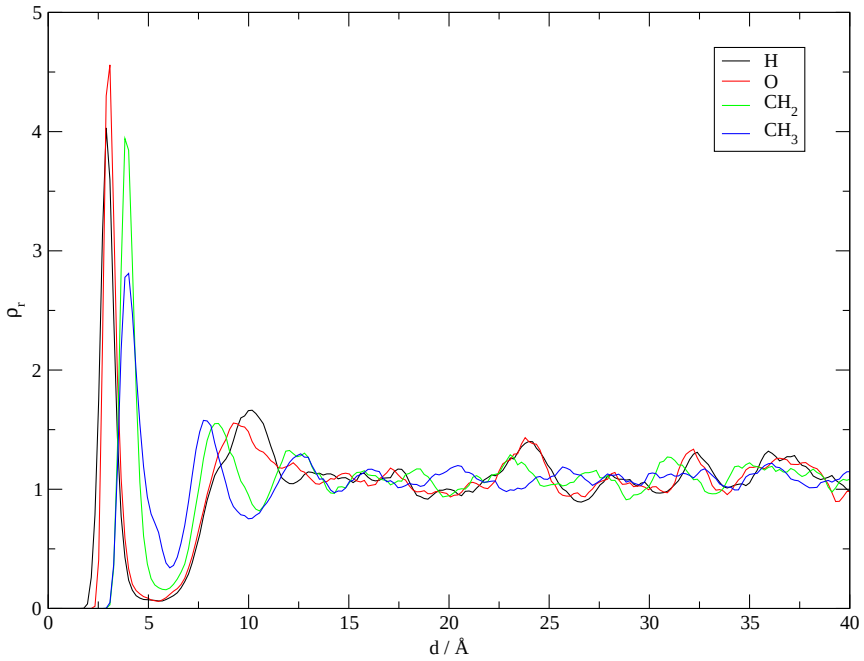

Figura 5.11: Perfis de densidade das moléculas de etanol num sistema com uma molécula de 1-decanotiol adsorvida na interface etanol-Au(111).

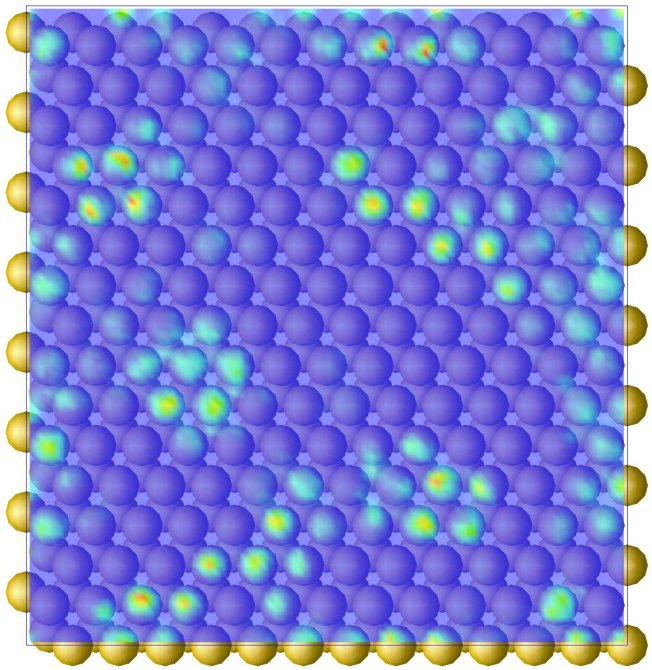

Figura 5.12: Projecção, sobre a superfície de ouro, do perfil de densidade superficial para o centro O das moléculas de etanol da primeira camada de adsorção. Sistema com o modelo mais completo.

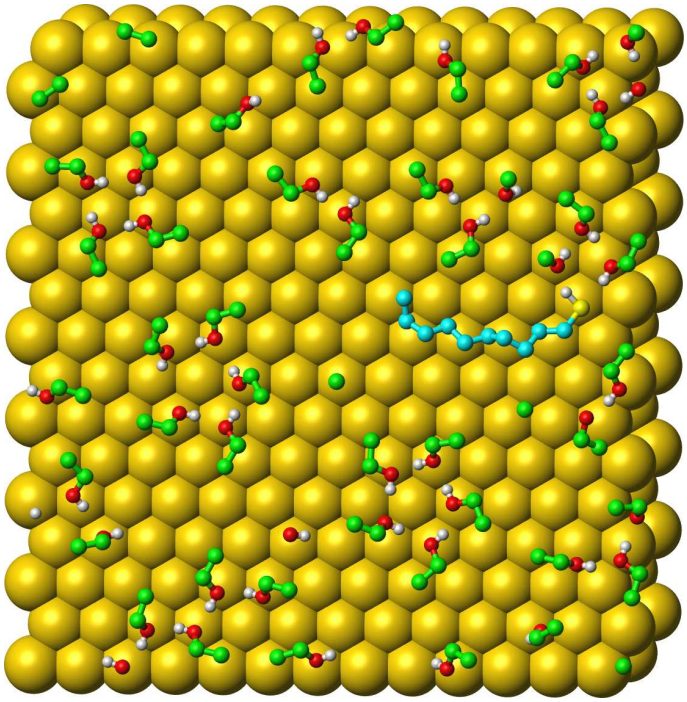

Figura 5.13: Uma configuração da primeira camada de adsorção com uma molécula de tiol adsorvida na superfície.

molécula de 1-decanotiol será, portanto, de ∼10. Este número deve estar relacionado não só com o espaço ocupado pela molécula de 1-decanotiol mas, também, com o impacto que esta possa ter na estrutura da interface etanol-Au(111). É possível visualizar o efeito da introdução desta molécula através das Figuras 5.12 e 5.13. No perfil de densidade superficial pode ver-se, nitidamente, a área ocupada pela molécula de 1-decanotiol, identificada pela maior área em azul que corresponde ao valor mínimo de densidade de centros O. No instantâneo da Figura 5.13 podemos observar que a molécula de 1-decanotiol (com a cadeia hidrofóbica representada a ciano) se encontra numa posição bastante horizontal em relação à superfície. O ângulo de inclinação médio da molécula de tiol foi determinado calculando o ângulo entre a normal à superfície e a recta que passa pelo átomo de enxofre e o centro de massa dos últimos quatro centros da cadeia (CML4), contados a partir do átomo de enxofre. Adoptou-se esta estratégia de forma a obter valores mais consistentes para o ângulo de inclinação. O valor calculado foi de 74±18º. Este valor revela que a configuração apresentada na Figura 5.13 é um caso particular e que na realidade o ângulo de inclinação é bastante variável, sendo comum a molécula apresentar-se com inclinações bem diferentes da que está representada nesta configuração. Um efeito a salientar e que está bem patente nesta configuração é a orientação relativa

das moléculas de etanol que rodeiam a molécula de 1-decanotiol. Todas as moléculas que estão dispostas em volta da cadeia alifática estão orientadas de modo a que os centros CH_2 e CH_3 estejam virados para ela. Por outro lado observa-se nitidamente que os centros O e H do etanol se encontram voltados para os centros S e H do tiol, evidenciando a possível formação de pontes de hidrogénio. Quanto à distribuição própria das moléculas de etanol, observa-se a formação de algumas estruturas de quatro e cinco moléculas, de forma anelar, de acordo com os perfis de densidade superficial, com os centros O e H, voltados para o interior do anel, com provável formação de pontes de hidrogénio, e os centros CH_2 e CH_3 voltados para o exterior. Na área acima da cadeia alifática evidencia-se a formação de uma cadeia de cinco ou seis moléculas de etanol, também observável no perfil de densidade superficial.

A aproximação da molécula de 1-decanotiol à superfície do eléctrodo foi estudada através do cálculo do potencial de forca média (PMF - "potential of mean force") [8–12] analogamente ao apresentado no estudo do modelo simples [4]. Através do PMF do solvente, ou seja, da variação de energia livre de Helmholtz provocada pela interacção solvente - 1-decanotiol, pode estudar-se o efeito do solvente na aproximação da molécula ao eléctrodo. Assim, procedeu-se a uma série de 57 simulações, cobrindo a distância que vai dos 2,7 aos 13,9 Å, medida a partir da superfície do eléctrodo segundo a normal à mesma. Em cada simulação, de 30000 ciclos de produção, calculou-se o PMF do solvente e o comprimento e ângulo de inclinação médios da molécula de 1-decanotiol. Os resultados encontram-se apresentados nas Figuras 5.14, 5.15 e 5.16 , respectivamente.

Comparando o gráfico do PMF da Figura 5.14 com os apresentados em [4] verifica-se que, no modelo presente, o efeito do solvente é análogo ao do modelo O_{strong}. A variação de energia livre reflecte a dificuldade crescente que o 1-decanotiol sente ao penetrar as camadas de adsorção do solvente. No entanto, no modelo O_{strong}, observa-se um abrandamento na repulsão da molécula de tiol, ao passar da segunda para a primeira camada. No modelo mais refinado, esse abrandamento quase não se verifica observando-se uma subida constante da energia livre ao longo de todo o processo de aproximação. Este efeito pode atribuir-se ao facto de no modelo O_{strong} a aproximação da molécula se fazer numa orientação fixa, com a molécula rígida, enquanto que no modelo presente a molécula segue adoptando um leque variado de configurações, observando-se, portanto, o comportamento do conjunto de orientações possíveis nessa situação.

Os gráficos das Figuras 5.15 e 5.16 revelam alguns aspectos do comportamento da molécula de 1-decanotiol à medida que se aproxima da superfície do eléctrodo.

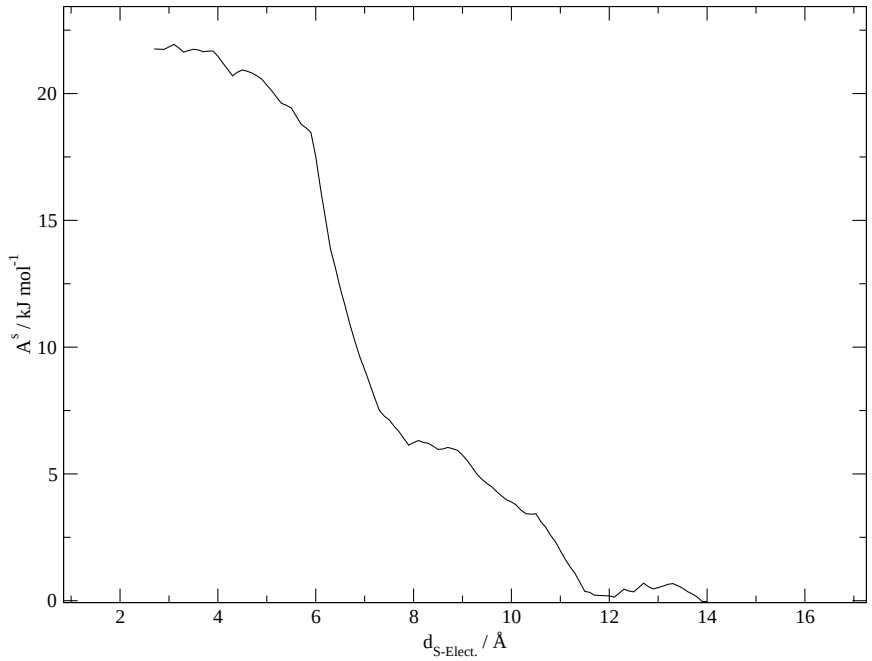

Figura 5.14: PMF do solvente em função da distância ao eléctrodo.

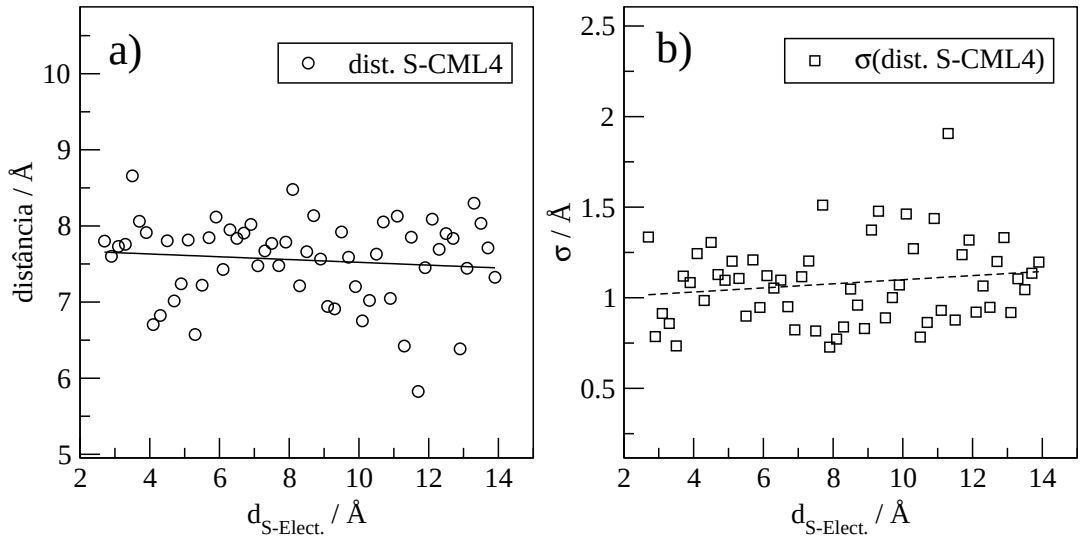

Figura 5.15: a) Comprimento médio da molécula de tiol em função da distância ao eléctrodo. b) Desvios padrões dos valores apresentados em a).

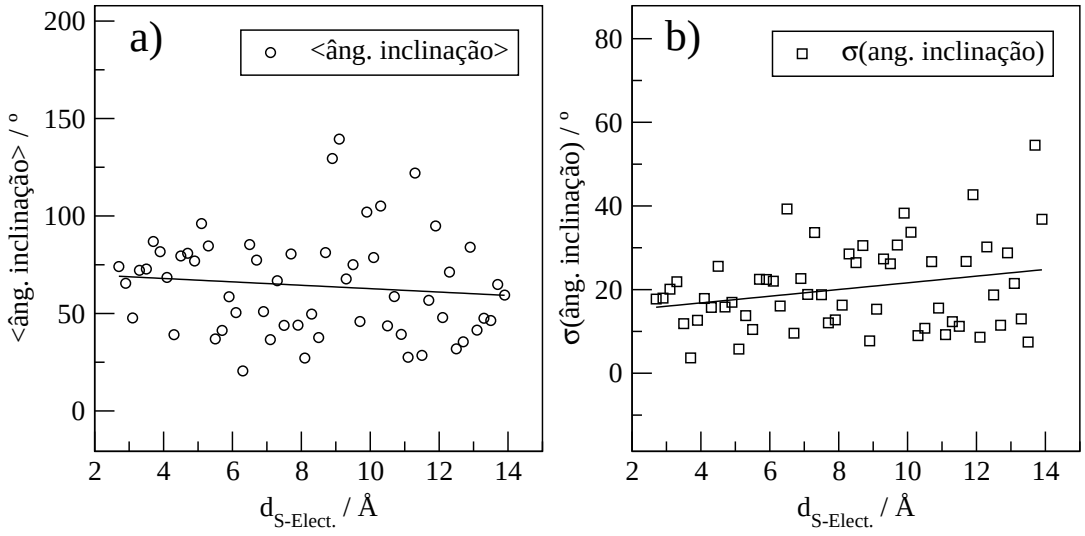

Figura 5.16: a) Ângulo de inclinação médio da molécula 1-decanotiol em função da distância ao eléctrodo. b) Desvios padrões dos valores apresentados em a).

A dispersão e o desvio padrão dos valores de comprimento da molécula (S-CML4) e ângulo de inclinação apresentados indicam o grau da variedade de configurações que a molécula de tiol pode assumir nestas condições. Seria necessário muito maior estatística, nas simulações, para se conseguir obter um comportamento mais refinado destas propriedades. No entanto, fazendo uma regressão linear dos valores apresentados podem retirar-se alguns comportamentos gerais. Assim, verifica-se, pelos gráficos da Figura 5.15, que o comprimento da molécula de 1-decanotiol tende a aumentar com a aproximação ao eléctrodo. Além disso, o desvio padrão desta propriedade, tende a diminuir o que leva a concluir que esse comprimento tende a estabilizar. Analogamente, pelos gráficos da Figura 5.16, o ângulo de inclinação da molécula tende a aumentar e a tornar-se mais estável à medida que esta se aproxima da superfície. O valor do ângulo de inclinação do 1-decanotiol, neste modelo, é de 74 ± 18^{o}. Este valor difere substancialmete do obtido com os modelos de moléculas rígidas,$\sim26^{o}$. É de salientar que os valores calculados são para a adsorção de uma única molécula de tiol. O ângulo de inclinação é, neste caso, muito influenciado pelo tipo de interacções entre a cadeia alquílica e as moléculas de solvente que são, obviamente, diferentes das interacções entre as cadeias numa camada já auto-montada, em que o valor do ângulo de inclinação, determinado experimentalmente e computacionalmente, é de $\sim30^{o}$ [5, 13, 14]. Sendo o último modelo, o mais elaborado, sugere-se que o valor de $\sim26^{o}$ é uma característica dos modelos rígidos e que o de $\sim74^{o}$ é o mais realista. A molécula de tiol parece, portanto, adsorver oscilando em

relação à superfície do eléctrodo sob uma forma relativamente alongada. Os cálculos com várias moléculas de tiol, que serão efectuados futuramente, poderão mostrar se as interacções conjuntas entre as diferentes moléculas de tiol e o etanol, obtidas através do presente modelo, reproduzirão o valor experimental para o ângulo médio de inclinação.

Bibliografia

[1] R. P. S. Fartaria, F. M. S. S. Fernandes and F. F. M. Freitas: A force field for simulating ethanol adsorption on Au(111) surfaces. A DFT study, *Int. J. Quantum Chem.* 107 (2007) 2169–2177.

[2] W. Jorgensen: Intermolecular potential functions and Monte-Carlo simulations for liquid sulfur-compounds, *J. Phys. Chem.* 90 (1986) 6379–6388.

[3] W. Jorgensen: Optimized intermolecular potential functions for liquid alcohols, *J. Phys. Chem.* 90 (1986) 1276–1284.

[4] R. P. S. Fartaria, F. F. M. Freitas and F. M. S. S. Fernandes: A study of 1-decanethiol self-assembly on gold electrodes by computer simulation, *J. Electroanal. Chem.* 574 (2005) 321–331.

[5] J. Hautman and M. L. Klein: Simulation of a monolayer of alkyl thiol chains, *J. Chem. Phys.* 91 (1989) 4994–5001.

[6] I.-C. Yeh and M. L. Berkowitz: Ewald summation for systems with slab geometry, *J. Chem. Phys.* 111 (1999) 3155–3162.

[7] D. Frenkel and B. Smit: *Understanding Molecular Simulations: From Algorithms to Applications*, Academic Press, 2nd ed. (2002).

[8] C. A. Reynolds, P. M. King and W. G. Richards: Free energy calculations in molecular biophysics, *Mol. Phys.* 76 (1992) 251–275.

[9] E. Spohr: A computer-simulation study of iodide-ion solvation in the vicinity of a liquid water metal interface, *Chem. Phys. Lett.* 207 (1993) 214–219.

[10] E. Spohr: Computer modeling of interfaces between aqueous and metallic phases, *Acta Chem. Scandinav.* 49 (1995) 189–202.

[11] M. Mezei and D. L. Beveridge: Free energy simulations, *Annals of the New York Academy of Sciences* 482 (1986) 1–23.

[12] A. Ignaczak, J. A. N. F. Gomes and S. Romanowski: The potential of mean force on halide ions near the Cu(100) surface, *J. Electroanal. Chem. Interfacial Electrochem* 450 (1998) 175–188.

[13] M. D. Porter, T. B. Bright, D. L. Allara and C. E. D. Chidsey: Spontaneously organized molecular assemblies. 4. Structural characterization of n-alkyl thiol monolayers on gold by optical ellipsometry, infrared spectroscopy, and electrochemistry, *J. Am. Chem. Soc.* 109 (1987) 3559.

[14] H. Sellers, A. Ulman, Y. Shnidman and J. E. Eilers: Structure and binding of alkanethiolates on gold and silver surfaces: Implications for self-assembled monolayers, *J. Am. Chem. Soc.* 115 (1993) 9389–9401.

Capítulo 6

Trabalhos em colaboração com outros grupos

Neste capítulo apresentam-se resultados de trabalhos efectuados em colaboração com um grupo experimental brasileiro. Estes trabalhos incidem sobre o desenvolvimento de modelos para a adsorção da molécula do fenol e da água em superfícies Au(210). As colaborações do autor abrangem o desenvolvimento do software de simulação e ajustes por GAs, a realização de alguns cálculos e uma participação activa no tratamento e interpretação dos resultados. O capítulo contém dois artigos:

- **Monte Carlo simulation of the adsorption of phenol on gold electrodes. A simple model**
  Rodrigo S. Neves and Artur J. Motheo
  Fernando M. S. Silva Fernandes and Rui P. S. Fartaria
  J. Braz. Chem. Soc. 15 (2004) 224-231

- **Modelling water adsorption on Au(210) surfaces. I. A force field for water-Au interactions by DFT**
  Rodrigo S. Neves and Artur J. Motheo
  Rui P. S. Fartaria and Fernando M. S. Silva Fernandes
  J. Electroanal. Chem. *in press,* doi:10.1016/j.jelechem.2007.06.020

O autor colaborou, também, com o grupo de Electroquímica Interfacial do Centro de Química e Bioquímica da FCUL, liderado pela Professora Luísa Abrantes. Para além de todo o apoio, estímulo e sugestões da Professora Luísa Abrantes relativamente aos trabalhos sobre adsorção e auto-montagem, foram realizados alguns cálculos *ab initio* e DFT na área da electropolimerização, os quais conduziram a uma publicação

[Int. J. Quantum Chem. 99 (2004) 11-27]. Uma vez que o tema ultrapassa o âmbito desta dissertação não se inclui a cópia desse artigo.

J. Braz. Chem. Soc. 15 (2004) 224-231

Monte Carlo simulation of the adsorption of phenol on gold electrodes. A simple model

Rodrigo S. Neves[a], Artur J. Motheo[a], Fernando M. S. Silva Fernandes[b,1] and Rui P. S. Fartaria[b]

[a] *Laboratory of Interfacial Electrochemistry, Department of Physical Chemistry, Institute of Chemistry of São Carlos, University of São Paulo*
Avenida do Trabalhador Sancarlense, Caixa Postal 780, 13560-970 São Carlos Brazil

[b] *Laboratory of Molecular Simulation and CECUL, Department of Chemistry and Biochemistry, Faculty of Science, University of Lisbon*
Rua Ernesto de Vasconcelos, Bloco C8, 1749-016 Lisboa Portugal

Abstract

Canonical Monte Carlo simulations simulations, at 298 K, of the adsorption of phenol in a dilute aqueous solution on gold electrodes, at the potential of zero charge, are presented. The results suggest that the process occurs in two distinct and successive steps. Adsorption starts with the phenol oxygen atom pointing towards the gold surface and the aromatic ring in a quasi-perpendicular orientation relative to the surface. This is followed by the reorientation of the aromatic ring to a parallel configuration. The effect of the solvent is analyzed through the calculation of the potentials of mean force acting on phenol.

Despite the simplicity of the model and the interaction potentials used in the simulations, the results are in good agreement with experimental observations, giving insight into the microscopic details of the adsorption process of phenol at low concentrations.

Keywords: phenol adsorption, gold electrode, Monte Carlo simulation, mean force potential

Resumo

Neste trabalho são apresentadas simulações de Monte Carlo no ensemble canônico, a 298 K, da adsorção de fenol, a partir de uma solução aquosa diluída, em um

[1]Corresponding author. *E-mail address:* fsilva@fc.ul.pt (F. M. S. Silva Fernandes)

eletrodos de ouro no potencial de carga zero. Os resultados sugerem que o processo de adsorção ocorre em duas etapas distintas e consecutivas. A adsorção tem início com o átomo de oxigênio da molécula de fenol apontando em direção ao eletrodo, com o anel aromático adotando uma inclinação aproximadamente perpendicular em relação à superfície. Segue-se então a reorientação do anel, que adota a orientação paralela ao eletrodo. O efeito do solvente é analisado através do potencial de força média que atua no fenol.

Apesar da simplicidade do modelo e potenciais de interação utilizados nas simulações, os resultados estão de acordo com observações experimentais, fornecendo informações sobre os detalhes microscópicos do processo de adsorção do fenol em baixas concentrações.

Keywords: phenol adsorption, gold electrode, Monte Carlo simulation, mean forçe potential

1 Introduction

The acquisition of information at molecular level, for the adsorption of organic molecules on electrochemical interfaces composed by metalic electrodes in contact with a liquid phase is one of the main scopes of interfacial electrochemistry. Structural factors play a major role in the processes taking place in the interfacial region determining, for example, the resultant products of electron transfer reactions [1,2].

Computer simulation techniques, namely Monte Carlo (MC) and Molecular Dynamics (MD) [3, 4], have successfully been used in the study of different electrode/solution phenomena such as the molecular details concerning the structure of the liquid phase in the interfacial region [5–11] and charge and field distributions in the electrical double layer (edl) on the presenrce of specific and non specific adsorption of ionic and organic species [12–19]. The combination of such kind of information with experimental results strongly contribute to the understanding of the behaviour of interfacial systems.

Phase transitions in adsorbed layers is another topic of interest concerned with the main adsorption processes on metalic electrodes. For instance, MD and MC have been used with success to study the self-assembly of alkyl thiols monolayers on gold electrodes [20–23].

The objective of the present work is to simulate, by canonical Monte Carlo method, the adsorption of phenol in a dilute aqueous solution on gold electrodes, at the potential of zero charge (pzc), and to analyse how far we can go into the analysis of adsorption with a rather simple model. In an experimental investigation, Lezna et al. [24] concluded that, at pzc, the phenol molecule adopts a parallel orientation relative to electrode surface. However, when the potential across the interface is shifted to more positive values, this is followed by a reorientation of the molecule to a perpendicular orientation, the oxygen atom pointing to the surface and presenting a strong covalent interaction with the metal. Moreover, studies of the adsorption of phenol and correlated compounds on platinum show that for dilute solutions the same behaviour is observed, but for more concentrated ones, the adsorption occurs directly in the perpendicular orientation and no further reorientation of the molecule is detected [25,26]. Thus, the final orientation of the adsorbate relative to the electrode seems to depend on the solution concentration.

Two main aspects of the process are considered in the present study: the approximation of the phenol molecule to the surface and its behaviour thereafter. To analyse the contribution of the solvent, mean force potentials (MFP) were calculated for de-

termining the preferential orientation of the phenol molecule when it approaches the electrode surface. In the next section, we present the essential aspects of the model, the interaction potentials and some simulation details. The results are shown and discussed in Section 3. The final section contains the conclusions of this work.

2 Model

2.1 The electrochemical cell

The system was composed by a liquid phase, with 245 molecules of water and one molecule of phenol, encapsulated between two flat gold surfaces perpendicular to the z-direction. The use of one single phenol molecule corresponds to the condition of infinite dilution. The cell was of a rectangular shape, with 15.52 x 15.52 Å in the x-y plane parallel to the metal surface, and 31.04 Å in the z-direction. Periodic boundary conditions (PBC) were applied in the the x and y directions to replicate the cell in the directions parallel to the electrodes. PBC where not applied on the z-direction, which was confined by the electrodes. The size of the cell was chosen to reproduce the water density at the specified conditions of the simulations: 298.15 K and 1 atm.

The use of flat gold surfaces does not take into account the effects of the atomistic corrugation of the electrodes. These structural characteristics are, of course, of great relevance to the preferential adsorption on the hollow and top sites of the electrodes and are responsible for further degree of order in the surface solvation layers [8, 10, 19, 26] afecting also the dispersive character of interfacial phenomena [27–29]. Despite being a simple approximation, we shall see in the next section that the present model gives results in accordance with experimental evidence. Moreover, it paves the way to more elaborate models and simulations.

Equilibration runs of 10,000 Monte Carlo cycles were followed by production runs of 100,000 cycles. A MC cycle consisted of a random translation and rotation applied to each molecule of the system with an acceptance rate of $\pm$ 50%.

2.2 Models for the liquid phase

The interaction between the components of the liquid phase was modelled by Lennard - Jones (LJ) potentials between the sites of each molecule, combined with a coulomb interaction related to the partial charges on each site. For water molecules, the

Table 1: Interaction parameters for all the atoms on the liquid phase.

	ε (kJ·mol^{-1})	σ (Å)	q (e)
Water - TIP4P			
O	0.6490	3.15	0.0000
H	0.0000	0.00	0.5200
e	–	–	-1.0400
Phenol			
H(O)	0.000	0.00	0.4400
O	0.650	3.07	-0.6400
C_1	0.294	3.55	0.5400
$C_{2,6}$	0.294	3.55	-0.4125
$C_{3,5}$	0.294	3.55	-0.0300
C_4	0.294	3.55	-0.3000
$H_{1,5}$	0.126	2.42	0.2000
$H_{2,4}$	0.126	2.42	0.1430
H_3	0.126	2.42	0.1590

TIP4P interaction model [30] with a cutoff cut-off radius of 7.5 Å was adopted. This model consists of four interaction centers, related to the three atoms of the water molecule and to the electronic charge density on the oxygen atom. For the phenol, the potential proposed by Mooney et al. [31] was used. All the liquid phase molecules were considered as rigid species. The TIP4P model is rigid by itself, but the internal contributions of the potential used for phenol were constrained to the minimal energy molecular geometry. The LJ parameters for the different interaction centers were obtained by the combination rules of Lorentz and Berthelot. The potential parameters and site charges for each model are presented on table 1, where ε and σ are the common Lennard-Jones parameters and **q**, the charge on each atom. For the later molecule, the interaction site **e** represents the pair of electrons of the oxigem atom. The indexes indicated for the phenol atoms are related to figure 1.

2.3 Models for the liquid phase in contact with the electrodes

The interactions of the liquid phase molecules with the flat electrodes were modelled by the combination of a LJ potential, to describe the interaction with the non-

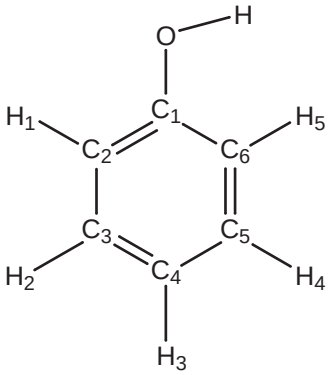

Figure 1: Representation of the phenol molecule.

conductive electrons of the metalic surface, with an electrostatic interaction berween each molecule in the solution and its image charge projected onto the electrodes, to describe the interaction with the conductive electrons.

In the case of the water molecules, the 9 - 3 LJ successfully used by Philpott et al. [18], for the solvent - electrode interaction in the simulation of benzene adsorption on gold electrodes, was adopted. For the phenol - electrode interaction, a 12 - 3 LJ potential was derived by the Hautman et al.'s method [20] used in the simulation of self-assembled alkyl thiols monolayers on gold electrodes. Both potentials are described by equations 1 and 2 respectively:

$$V(z) = \frac{A_9}{z^9} - \frac{A_3}{z^3} \tag{1}$$

$$V(z) = \frac{C_{12}}{(z - z_0)^{12}} - \frac{C_3}{(z - z_0)^3} \tag{2}$$

were $A_n = 4\varepsilon\sigma^n$, $C_n \propto \sqrt{\varepsilon\sigma^n}$, z is the distance between the interaction center and the surface and z_0 is a limit approach distance particular for each center. The parameters ε and σ are Lennard-Jones potential parameters.

Those potentials result from the integration of the 12 - 6 LJ potential over the half-space related to the electrode surface. The original result is the 9 - 3 LJ, but for some systems, such potential fails on the description of the interaction, mainly on the dispersion coefficient parameters [20]. Thus, the 12 - 3 LJ potential was used for the phenol - electrode interaction instead of the 9 - 3 LJ. The potential parameters related to equations 1 and 2 are listed on table 2. Both the potentials were truncated at a 15 Å distance cutoff cut-off.

Table 2: Interaction parameters for all the atoms on the liquid phase with the surface. * only hydrogen atoms bonded to carbon.

Water:	$A\ (10^3 kJ \cdot mol^{-1})$	$B\ (kJ \cdot mol^{-1})$	
O	17.4	76.2	
H	0.0	76.2	
Phenol:	$C_{12}\ (10^3 kJ \cdot mol^{-1})$	$C_3\ (kJ \cdot mol^{-1})$	$z_0\,(A)$
C	101.4	95.1	0.82
O	63.1	113.7	0.76
H*	6.7	35.0	0.68

The interactions of the liquid phase molecules with the conductive electrons of the metal were modelled by a self-image charge potential method without distance cutoff. In the original version, each charge in the liquid phase interacts with the projections of all their image charges, reflected inside the electrode. This total-image method for the simulation of the polarization effects in the metal has been commonly used for water near metalic electrodes and the adsorption of liquid phases on surfaces [5–7, 17, 18], however, some comments should be made. In the case of water near a polarizable surface, the induction effect due to a single molecule can be very large. Nonetheless simulation studies of pure water on the vicinity of metalic surfaces using the total-image charge approach have shown a high degree of cancellation of interactions due to the sum over all the images and molecules [10]. Thus, when only the self-image interactions are handled for the water-electrode interaction many body cancellations may not occur and an eventual overestimation of the interaction potential may take place, as pointed out by Shelley et al. [11]. The net cancellation itself could also result from an overestimation of the induction power of water molecules distant from the electrode and separated by several layers of molecules. Indeed, it seems reasonable that water molecules of the nearest hydration layers of the electrode present a higher degree of induction when compared with the distant ones.

In the simulations reported here, however, the self-image approach was applied with the reflection plane coincident with the electrode surface. The structural properties are in accordance to those obtained by Phipott et al. [18] in the simulation of the adsorption of benzene on gold, using the same 9 - 3 LJ potential and a total-image charge potential. This is worth mentioning due to the structural similarities

Table 3: Water density profile characteristics

	I	II	III	IV
Oxygen				
r (Å)	2.70	5.60	–	9.50
ρ_O	2.45	1.45	–	1.20
Hydrogen				
r (Å)	2.70	5.80	1.45	9.75
ρ_H	1.90	1.30	0.20	1.20

of benzene and phenol.

3 Results and Discussion

3.1 Structural Properties

The normalized density profiles for pure water hydrogens and oxygen relative to one of the electrodes, are presented in figure 2 and their main numerical characteristics are shown in Table 3. The peaks in region **I**, centered at 2.7 Å from the surface, show that in the first layer the water molecules, in contact with the electrode, mainly have the molecular plane parallel to the electrode surface, with just a few of them with the hydrogens hydrogen atoms pointing towards the surface (see sub-peak **III**).

The ordered structure of the first layer is a consequence of the equilibrium between the water-electrode potential and the hydrogen bonds between water molecules. It is observed in all simulations of water near metal surfaces either for flat surfaces [7] or structured ones [8, 11, 17]. A second solvent layer is observed in region **II**, centered at 5.6-5.8 A. The relative positions of the oxygen and hydrogen peaks indicate a small inclination of the molecular plane, with the hydrogen atoms pointing towards the solution bulk, but the molecular orientation is mainly parallel to the electrode and still reflects a high degree of organization. On region **IV**, between 8 and 11 Å , a small perturbation on the water distribution is also detected. This density fluctuation shows a weaker influence of the electrode at those distances. For distances from the electrode surface greater than 11 Å the presence of the electrode seems to be not relevant and the density profiles reach the normalized equilibrium value

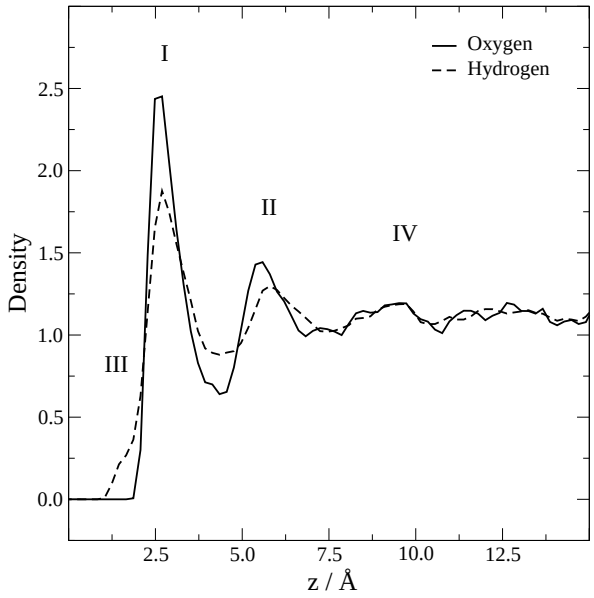

Figure 2: Density profiles (ρ) of pure water/electrode as a function of the distance (z) from the elctrode.

around the 1.10. These structural properties, obtained for pure water in contact with a flat gold electrode surface at pzc, are in accordance with results reported by Phipott et al. [18] and Hautman et al. [7]. Therefore, the water-metal potential adopted in the present model seems to be a suitable choice for the simulation of the phenol adsorption in aqueous solutions.

Figure 3 displays the density profiles for water in the presence of one phenol molecule (3a) and the mean position of the center of mass of the phenol molecule (3b). The main numerical values of the water distribution are in Table 4.

Table 4: Water density profile characteristics in the presence of adsorbed phenol

	I	II	III	IV
Oxygen				
r (Å)	2.80	5.70	–	9.00
ρ_O	2.11	1.45	–	1.35
Hydrogen				
r (Å)	2.80	6.11	1.55	9.20
ρ_H	1.53	1.35	0.20	1.25

The phenol molecule adsorbs at a distance of about 3.20 Å from the electrode, in-

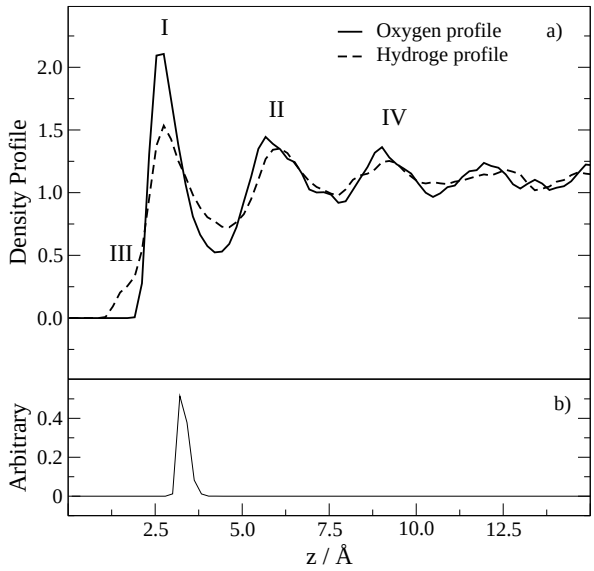

Figure 3: a) Density profiles (ρ) of water/electrode in the presence of one adsorbed phenol molecule as a function of the distance (z) from the elctrode. b) Average position of the mass center of the adsorbed phenol molecule.

side the first layer of water molecules, with an angle of 89 ± 4^0 between the aromatic ring plane and the normal to the electrode surface, in the so-called horizontal configuration. This agrees with the experimental results for the adsorption of phenol on gold electrodes [24]. The presence of the organic molecule causes some perturbations in the solvent layers at contact with the electrode. The analysis of the peak areas in region **I** of figures 2 and 3 indicate that the first solvent layer suffers a decrease of approximately 30% in the number of water molecules directly adsorbed on the surface, when phenol is adsorbed, with a small displacement of the mean distance of the solvent, from 2.7 to 2.8 Å. The preferential orientation of water molecules in the first layer still remains the same as observed for pure water. Region **III** is slightly affected by the phenol presence, in the same way as discussed for region **I**.

On the other hand, in the second solvent layer the second solvent layer, the oxygen density is weakly perturbed by the presence of phenol, but the hydrogen density is pushed to the solution direction approximately by 0.30 Å, with, no significant change is detected on the second solvent layer on the whole. In region **IV**, the presence of the adsorbate results in an increase of structural order, with a clear peak observed at 12 Å from the electrode. Despite the clear influence of the phenol presence in this region, a more complete analysis is inadequate due to the small size of the present model and it was postponed to future simulations**.**

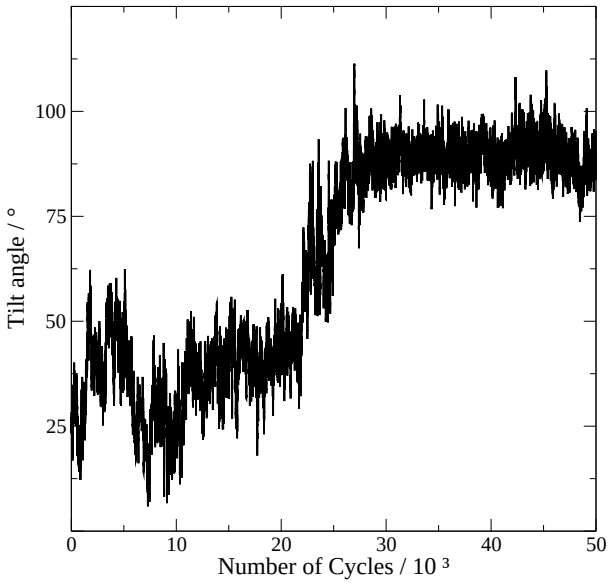

Figure 4: Evolution of the tilt angle between the aromatic ring of the adsorbed phenol molecule and the axis normal to the electrode surface during the MC simulation.

The final and more stable simulated configuration for phenol adsorption is the one with the aromatic ring parallel to the surface in accordance with the experimental observation of Lezna et al. [24] for the adsorption of phenol on gold polycrystalline electrodes. However, the present simulations of the evolution of the phenol tilt angle clearly show that the process take place in two steps, as can be seen in figure 4.

First, the phenol molecule adsorbs on the surface by the oxygen atom with the ring in a quasi-perpendicular orientation, oscillating around an angle of 25 ° with the normal to the surface. After ± 25,000 Monte Carlo steps, there is a reorentation of the molecule to a horizontal configuration, oscillating thereafter around an angle of 89 ± 4^0. A qualitative view of the two distinct events can be observed in the snapshots of Figure 5.

As already mentioned, there are experimental evidences that phenol, and some similar compounds, adsorbs on metalic surfaces at horizontal configurations for low concentrations solutions, but the same behaviour is not observed at high concentrations. In this situation, the adsorption persists in the quasi-perpendicular orientations with the negative center, the oxygen in the case of phenol, pointing towards the surface. The picture of the adsorption process from the simulations reported here, associated to experimental information, suggest that the approach of the phenol molecule to the surface, at the pzc, is always on a quasi-perpendicular orientation. In low concentration solutions, a reorientation occurs and the molecule reaches a final

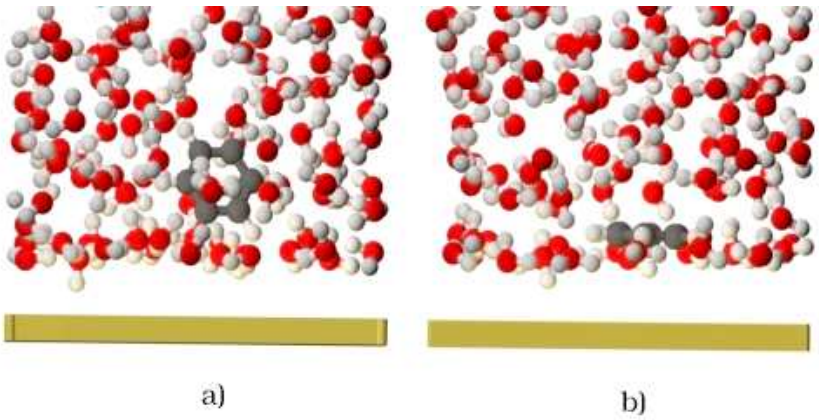

Figure 5: Snapshots of the phenol molecule adsorbed on gold electrode. a) Quasi-perpendicular configuration. b) After the reorientation to the horizontal configuration.

horizontal configuration. In high concentration solutions, the number of adsorbate molecules near the electrode surface is high and lateral interactions will presumably hinder a further reorientation to a final horizontal configuration.

3.2 Potentials of Mean Force

The structural properties are fundamental to understand the mechanism of the processes taking place in the interfacial region. Behind them, however, it is the powerful hand of free-energy. Thus, the knowledge of the free-energy changes is invaluable for the full comprehension of the problem. The changes can be obtained by the so-called free-energy perturbation (FEP) method [10, 15, 19, 32].

The total free-energy change, that is, the reversible work necessary to approach the adsorbate molecule to the electrode, has two contributions: the mean force potential (MFP) due to the solvent and the direct interaction of the adsorbate with the surface. Thus, the solvent contribution is can be calculated by the general FEP equation 3:

$$\Delta A = -kTln \left\langle exp \left[-\frac{(U_1 - U_0)}{kT} \right] \right\rangle_0 \tag{3}$$

where U_0 is the potential energy of one configuration of the reference system, U_1 is the potential energy of the perturbed system calculated on the basis of that configuration for the unperturbed one, k is the Boltzmann constant and T the temperature of the system. The brackets represent an ensemble average over the assembly of configurations generated for the reference system.

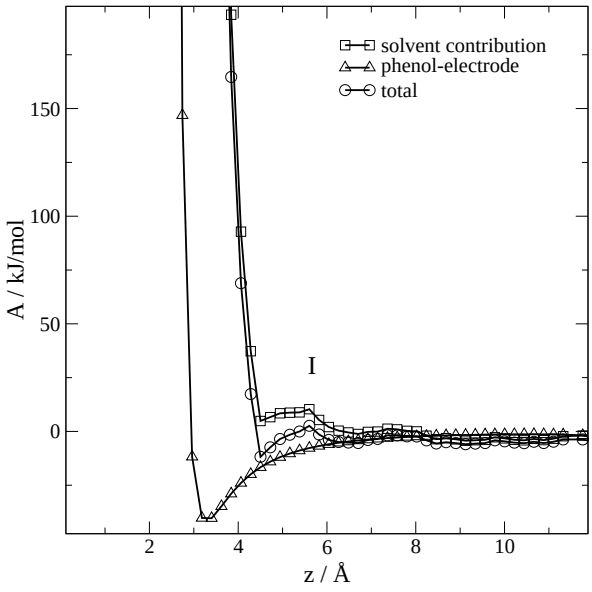

Figure 6: Free energy changes associated to the phenol approach to the surface in the flat orientation.

In the present case, a reference system is composed by the phenol molecule at a fixed distance (z_i), measured from its mass center to the surface, the water molecules and the electrodes. The assembly of configurations for this system is generated by randomly translating and rotating the water molecules, taking into account only the solvent-solvent, solvent-adsorbate and solvent-electrode interactions. The assemby of configurations for the perturbed system is the same as the preceding one as far as the water molecules are concerned, but now with the phenol molecule in a new fixed distance $z_i + dz_i$, where dzi is the displacement applied to generate a perturbed state.

As the reference and perturbed states differ only in the position of the phenol molecule, equation 3 can be recasted in the form:

$$\Delta A_i = -kTln \left\langle exp \left[-\frac{\left(U_{(z_i+dz)} - U_{(z_i)} \right)}{kT} \right] \right\rangle_{z_i} \tag{4}$$

The term, $U(z_i+dz_i)$ - $U(z_i)$, is just the difference of the phenol-water interaction energies. The MFP of the solvent can then be added to

the phenol-electrode interaction energy, at coordinate z_i, to obtain the total free energy change.

The main requirement for the use of the FEP method is that the energy difference

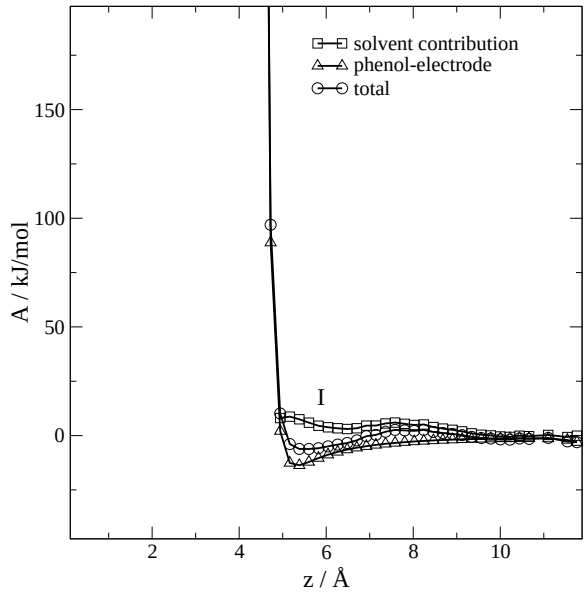

Figure 7: Free energy changes associated to the phenol approach to the surface in the perpendicular orientation.

between states 0 and 1, $\Delta U = U(z_1) - U(z_2)$, must be $<<$ kT for proper convergence. Therefore, the distance z1-z0 must be divided into a number of windows, each one characterized by the coordinate zi. An assembly of reference states is generated for each window and a perturbation is applied to them, displacing the phenol mass center by dzi . The free-energy difference between states 0 and 1 is obtained by summing the results for the corresponding windows.

For each window, equilibration runs of 15,000 MC cycles were followed by production runs of 10,000 cycles. The first window was chosen at a distance of 13.5 Å between the phenol mass center and the electrode surface. The following windows were located at successive displacements of 0,22 Å towards the surface. The perturbation distance, dz_i, was 0.1 Å. and a double-wide sampling was used. Additionally, during the production runs, the phenol molecule was allowed to move in the x and y directions for a better relaxation of the solvent in the vicinity.

Two orientations of the phenol molecule were tested: case 1, with the aromatic ring parallel to the electrode and case 2 with the ring perpendicular to the surface and the oxygen pointing towards the metal. They are the most interesting geometries considering the structural properties showed in the last section.

The contribution of the solvent, the interaction of the phenol with the electrode and the total free energy change for cases 1 and 2 can be seen in figures 6 and 7, respectively.

Region **I** of both figures, at about 5.5 Å from the electrode, is the onset of penetration of the phenol molecule in the first solvation layer of the electrode. In case 1, the solvent contribution to the free-energy is approximately 10 $kJ \cdot mol^{-1}$ higher than in case 2. When the phenol molecule approaches the first water layer, with the ring parallel to the electrode, it finds that small energy barrier which is presumably due to the compression of the solvent layer against the electrode surface. In case 2, at approximately the same distance, the phenol molecule experiences a small energy minimum. For this geometry, when the center of mass is at 5.5 Å from the electrode, the oxygen atom is at ± 2.8 Å, inside the first water layer and physically adsorbed on the surface. It seems, therefore, that the difference of 10 $kJ \cdot mol^{-1}$, in the solvent contributions to the free-energy, favours the perpendicular approach.

Additionally, the analysis of the remarkable energy barriers to the approach of the phenol molecule, for distances less than 5 Å, shows that they have different origins. In case 1, the barrier arises from the further compression of the solvent layer in the direction of the electrode, caused by the parallel approach of the ring. This will disable the adsorption of the phenol molecule directly on the horizontal configuration. In case 2, the energy barrier results from the direct interaction of the phenol oxygen with the electrode surface. In this situation, no significant structural changes of the first solvent layer occur and the phenol will adsorb by the oxygen atom, in a quasi-perpendicular configuration, performing the first adsorption step. Then, the transition to the horizontal configuration is driven by the interaction of the aromatic ring with the electrode (see Figures 6 and perpendicular). Indeed, the horizontal configuration has an interaction energy of -40 $kJ \cdot mol^{-1}$, whilst whilst the interaction energy for the perpendicular configuration is -15 $kJ \cdot mol^{-1}$. The transition process is smooth and allows the first solvent layer to successively relax, as was observed in the evolution of the tilt angle on figure 4.

4 Conclusions

We have presented canonical Monte Carlo simulations of the adsorption of phenol, in a dilute aqueous solution, on flat gold electrodes at the potential of zero charge.

The results clearly show that the adsorption process occurs in two distinct and successive steps. The first one is the physical adsorption of the phenol oxygen and the aromatic ring pointing towards the bulk of the solution. This is followed by a second step consisting of the reorientation of the molecule to a horizontal configuration, at

a distance of approximately 3.20 Å from the surface, and a mean angle of 89 $\pm 4^0$ with the axis normal to the surface. The final configuration is in agreement with the experimental studies of Lezna et al. [24].

The potentials of mean force indicate that the perpendicular approach is favorable to the penetration of the organic molecule across the first solvent layer on the electrode. A horizontal approach would result in the compression of that layer and in a considerable energy barrier obstructing the adsorption process. For the perpendicular approach, the barrier energy is mainly due to the direct interaction of the phenol oxygen with the electrode surface.

Experimental evidence, obtained from the study of the adsorption of aromatic molecules on platinum electrodes [25, 33], show that for low concentration solutions the adsorption process ends in a horizontal orientation, but at high concentrations the quasi-perpendicular orientation is the preferred one. The behaviours observed in the present work for the adsorption on gold, suggest that in the case of a greater number of phenol molecules on the surface, lateral interactions will difficult the reorientation and the perpendicular adsorption should indeed persist.

Despite the simplicity of the model, the structural properties, and the consistency of the respective thermodynamic behaviour, suggest that the present model represents the main characteristics of the phenol adsorption on gold, giving insight into the microscopic details.

The reported results constitute the starting point to a more refined model, which should consider the structural properties of the electrode surface to detect preferential top and hollow adsorption sites and their influence on the adsorption process. The introduction of intramolecular degrees of freedom and the developement of accurate *ab-initio* potential surfaces, mainly for the interactions between the molecules and gold, are also of the utmost importance regarding the full understanding of the whole process, in particular of the chemisorption. Work along these lines is in progress and will be reported soon.

References

[1] M. P. Soriaga, J. L. Stickney and A. T. Hubbard: Electrochemical oxidation of aromatic-compounds adsorbed on platinum-electrodes - the influence of molecular-orientation, *J. Electroanal. Chem.* 144 (1983) 207–215.

[2] J. H. White, M. P. Soriaga and A. T. Hubbard: Effect of surface-roughness on the adsorption, orientation and anodic-oxidation of hydroquinone at platinum-electrodes, *J. Electroanal. Chem.* 177 (1884) 89–96.

[3] M. Allen and D. Tildesley: *Computer Simulation of Liquids*, Claredon Press, Oxford, U.K., 1st ed. (1987).

[4] D. Frenkel and B. Smit: *Understanding Molecular Simulations: From Algorithms to Applications*, Academic Press, 1st ed. (1996).

[5] E. Spohr: Computer simulations of electrochemical interfaces, in R. C. Alkire and D. M. Kolb (eds.), *Advances in Electrochemical Science and Engineering - vol. 6*, Wiley-VCH, New York (1999) .

[6] I. Benjamim: Molecular dynamic simulations in interfacial electrochemistry, cap.3, in J. O. M. Bockris (ed.), *Modern Aspects of Electrochemistry,n. 31*, Plenum Press (1997) pages 115–179, new York.

[7] J. Hautman, J. W. Halley and Y.-J. Rhee: Molecular-dynamics simulation of water between 2 ideal classical metal walls, *J. Chem. Phys.* 91 (1989) 467–472.

[8] E. Spohr: Computer simulation of the water/platinum interface., *J. Phys. Chem.* 93 (1989) 6171–6180.

[9] J. I. Siepmann and M. Sprik: Influence of surface-topology and electrostatic potential on water electrode systems, *J. Chem. Phys.* 102 (1995) 511–524.

[10] E. Spohr: Computer modeling of interfaces between aqueous and metallic phases, *Acta Chem. Scandinav.* 49 (1995) 189–202.

[11] J. C. Shelley, G. N. Patey, D. R. Bérard and G. M. Torrie: Modeling and structure of mercury-water interfaces, *J. Chem. Phys.* 107 (1997) 2122–2141.

[12] D. A. Rose and I. Benjamim: Solvation of Na^+ and Cl^- at the water platinum (100) interface, *J. Chem. Phys.* 95 (1991) 6856–6865.

[13] D. A. Rose and I. Benjamim: Adsorption of Na^+ and Cl^- at the charged water platinum interface, *J. Chem. Phys.* 98 (1993) 2283–2290.

[14] J. N. Glosli and M. R. Philpott: Adsorption of hydrated halide-ions on charged electrodes - molecular-dynamics simulation, *J. Chem. Phys.* 98 (1993) 9995–10008.

[15] E. Spohr: A computer-simulation study of iodide-ion solvation in the vicinity of a liquid water metal interface, *Chem. Phys. Lett.* 207 (1993) 214–219.

[16] M. T. M. Koper: Monte Carlo simulations of ionic adsorption isotherms at single-crystal electrodes, *Electrochim. Acta* 44 (1998) 1207–1212.

[17] D. I. Dimitrov and N. D. Raev: Molecular dynamics simulations of the electrical double layer at the 1M KCl solution vertical bar Hg electrode interface, *J. Electroanal. Chem.* 486 (2000) 1–8.

[18] M. R. Philpott and J. N. Glosli: Molecular-dynamics simulation of the adsorption of benzene on charged metal-electrodes in the presence of aqueous-electrolyte, *Chem. Phys.* 198 (1995) 53–61.

[19] A. Ignaczak, J. A. N. F. Gomes and S. Romanowski: The potential of mean force on halide ions near the Cu(100) surface, *J. Electroanal. Chem. Interfacial Electrochem* 450 (1998) 175–188.

[20] J. Hautman and M. L. Klein: Simulation of a monolayer of alkyl thiol chains, *J. Chem. Phys.* 91 (1989) 4994–5001.

[21] R. P. S. Fartaria, F. F. M. Freitas and F. M. S. S. Fernandes: Abstracts of the XV Congresso da Sociedade Ibero-americana de Electroquímica, Évora (2002) .

[22] P. Nikitas and F. Moumtzis: A Monte-Carlo test of the mean field approximation used for the modeling of the adsorption of organic compounds on electrodes. Evidences for existence of peculiar phase transitions, *Electrochimica Acta* 47 (2002) 1765–1775.

[23] A. J. Pertsin and M. Grunze: Computer simulation of water near the surface of oligo(ethylene glycol)-terminated alkanethiol self-assembled monolayers, *Langmuir* 16 (2000) 8829–8841.

[24] R. O. Lezna, N. R. Tacconi, S. A. Centero and A. J. Arvia: Adsorption of phenol on gold as studied by capacitance and reflectance measurements, *Langmuir* (1991) 1241–1246.

[25] V. K. F. Chia, M. P. Soriaga and A. T. Hubbard: Kinetics of oriented adsorption - hydroquinone on platinum, *J. Phys. Chem.* 91 (1987) 78–82.

[26] A. Ignaczak and J. A. N. F. Gomes: A theoretical study of the interaction of water molecules with the Cu(100), Ag(100) and Au(100) surfaces, *J. Electroanal. Chem.* 420 (1997) 209–218.

[27] A. J. Motheo, A. Sadkowski and R. S. Neves: Electrochemical immittance spectroscopy applied to the study of the single crystal gold/aqueous perchloric acid interface, *J. Electroanal. Chem.* 430 (1997) 253–262.

[28] A. Sadkowski, A. J. Motheo and R. S. Neves: Characterisation of Au(111) and Au(210) aqueous solution interfaces by electrochemical immittance spectroscopy, *J. Electroanal. Chem.* 455 (1998) 107–119.

[29] A. J. Motheo, R. M. P. Saldanha, R. S. Neves, E. D. Robertis and A. Sadkowski: Characteristics of pyridine adsorption on Au(111) and Au(210) by EIS parameters fitting procedure, *Eclect. Quim.* 28 (2003) 29–40.

[30] W. L. Jorgensen, J. Chandrasekhar and J. D. Madura: Comparison of simple potential functions for simulating liquid water, *J. Chem. Phys.* 79 (1983) 926–935.

[31] D. A. Mooney, F. Müller-Plathe and K. Kremer: Simulation studies for liquid phenol: properties evaluated and tested over a range of temperatures, *Chem. Phys. Lett.* 294 (1998) 135–142.

[32] C. A. Reynolds, P. M. King and W. G. Richards: Free energy calculations in molecular biophysics, *Mol. Phys.* 76 (1992) 251–275.

[33] M. P. Soriaga and A. T. Hubbard: Determination of the orientation of aromatic-molecules adsorbed on platinum-electrodes - the effect of solute concentration, *J. Am. Chem. Soc.* 104 (1982) 3937–3945.

J. Electroanal. Chem. *in press*

doi:10.1016/j.jelechem.2007.06.020

Modelling water adsorption on Au(210) surfaces. I. A force field for water-Au interactions by DFT

Rodrigo S. Neves[a], Artur J. Motheo[a], Rui P. S. Fartaria[b], Fernando M. S. Silva Fernandes[b,1]

[a] *Laboratory of Interfacial Electrochemistry, Department of Physical Chemistry, Institute of Chemistry of São Carlos, University of São Paulo, Avenida do Trabalhador Sancarlense, CP 780, 13560-970 São Carlos-SP Brazil*

[b] *Molecular Simulation Group, Department of Chemistry and Biochemistry, and CCMM, Faculty of Science, University of Lisboa, Campo Grande, Bloco C8, 1749-016 Lisbon Portugal*

Abstract

A force field for the adsorption of water on Au(210) surfaces is presented, based on Density Functional Theory (DFT) calculations of a single water molecule interacting with a gold cluster of 16 atoms, in a configuration representing the Au(210) crystal surface. The potential energy surface presents the typical behaviour of the water-noble metals interactions. The preferential adsorption on Au occurs at atomic sites of the first layer of the surface, usually referred to as âtop sitesâ, followed by sites of the second and third sub-layers, respectively. For all the sites, the preferential orientation has the water hydrogen atoms pointing outwards the metallic surface. An analytical function, fitted to the DFT results, expresses the interaction between the water atoms and the entire surface, considering its topography though not explicitly discriminating the orientation angles and the interactions with each of the gold atoms. These are implicitly taken into account through the interactions of the water atoms and the whole surface. The proposed function has been used in Monte Carlo simulations of water adsorption on Au(210) surfaces whose results will be reported in another paper.

Keywords: Au(210), water, DFT, ab initio, B3LYP

[1]To whom correspondence should be adressed: fsilva@fc.ul.pt

1 Introduction

The molecular structure and dynamics of electrode/solution interfaces are of fundamental importance in electrochemistry [1, 2]. The microscopic properties of water, for example, are crucial to understand the molecular behaviour at the interface. Indeed, solvent molecules are the predominant species in this region, being involved in a large number of processes, from the adsorption of ions and organic molecules [3–5], to the mechanism of charge transfer reactions, as in the case of the bi-functional mechanism of alcohols oxidation by metallic electrodes [6, 7].

In the last decades, Monte Carlo (MC) and molecular dynamics (MD) methods, have been used to simulate metal/water interfaces [8–10]. For instance, relevant molecular information has been obtained for different metal/solution systems concerned with the solvent properties at the interfacial region [11–16], and the adsorption of halide ions [11, 13, 17–22] and some organic molecules [23–27]. Apart from the interactions between the species in the fluid phases, it is necessary to develop models for the interaction of those species with the metallic atoms. In a first approximation, models describing the metal by a smooth and flat non-structured surface [28, 29] have been used. These models have evolved to more sophisticated ones in which the surface structure is explicitly considered by means of oriented atomic crystallographic surfaces [12, 14, 30].

In the smooth surface models, the potential function usually combines soft wall and charge-image potentials. The last one describes the polarisation of the surface, induced by the point charges present in the liquid phase [28, 29, 31]. Despite their simplicity, these models have produced fairly good qualitative results, specially when applied to describe water-metal interactions in the presence of organic molecules [25, 27]. Such models, however, do not account for preferential site adsorption, which directly depends upon the atomic arrangement of the metallic phase [12, 32]. The structure of the metallic surface has been considered in some water-metal interaction models, based on quantum mechanical calculations involving clusters of various metals like platinum [12, 16, 30, 33] and copper [20, 34], with different low-index crystallographic orientations. As electronic correlation effects are considerable, DFT methods are commonly used [32, 35–38].

Simulations based on metallic clusters have indicated the strong influence of the surface structure on the properties of the adsorbed water layer. For example, Yeh and Berkowitz [12] showed that in a Pt(100) surface, water molecules adsorb at every top site, with a square lattice packing, whereas in a Pt(111) surface the

molecules still adsorb at top sites, but forming rings of six and five molecules around an unoccupied site. This study indicates that the introduction of surface corrugation not only strongly affects the structure of the adsorbed layer but also the distribution of water molecules in the direction normal to the surface, yet in a minor degree.

The simulation of water in contact with high-index crystallographic surfaces, which present a higher degree of corrugation than the low-index ones, can yield interesting information on the relation between the surface structure and the solvent properties at the interfacial region. The Au(210) surface, for instance, has a considerable degree of corrugation but still presents short range two-dimensional symmetry. The last feature turns the development of the water-surface interaction function less complicated.

The objective of this work is to develop an analytical potential function for the interaction between water molecules and Au(210) surfaces, to be used in MC or MD simulations of the adsorption process. To this end, Density Functional Theory (DFT) calculations for the interaction of one water molecule with a metallic cluster representing the Au(210) surface have been performed. The analytical function has been obtained by fitting the DFT results so that the interaction of water molecules with an infinite Au(210) surface is approached.

Section 2 presents the methodology and models used in the DFT calculations, with special attention to the metallic cluster characteristics and the choice of the basis sets. Section 3 reports the DFT results and the development of the potential analytical function. Finally, section 4 contains the concluding remarks of this work.

2 Methodology and Models

In order to deal with electron correlation effects, which play an important role specially on systems containing transition metal atoms, all the calculations involving the interaction of the water molecule with the gold cluster have been performed using the B3LYP method, implemented and parameterised by Becke [39, 40]. It combines the Hartree-Fock exchange potential with DFT exchange terms, including the corrected correlation functional gradient developed by Lee et al. [41]. The LanL1MB basis set [42] has been used for the gold atoms and the 6-31G basis set [43] for the water molecule atoms. This choice was shown to be an adequate one to describe the interactions of water with transition metallic clusters by Ignaczak and Gomes [32].

The present model consists of one 16-atom gold cluster, fixed in the geometry corresponding to the Au(210) crystallographic orientation, and one rigid water

molecule with the O-H-O angle at 104.52º and the O-H bond length at 0.9572 Å. These values correspond to the geometry of the TIP4P model [44], which is often used in simulations of water in contact with metallic surfaces [13, 25, 45–47].

The representation of an infinite surface by small clusters is a common approximation to face the heavy computational requirements. As the quantum results are affected by the cluster size [32], its influence should be reduced as much as possible. Thus, a systematic search for an appropriate cluster size and geometry, in order to approach the Au(210) surface, was carried out considering the consistency of the DFT interaction energies and minimisation of border effects, the reproduction of the work function (Φ) of the macroscopic surface, which corresponds to the HOMO energy of the cluster used in the DFT calculations as well as, of course, the computing time. The value of Φ determined in this work for the $Au(210)_{16}$ cluster is 4.85 eV, in excellent accordance with the experimental value of 4.9 eV for the Au(210) surface [48].

Several studies [49] on transition metal clusters suggest that the interactions between infinite metal surfaces and other species may be approached by using representative clusters. This does not mean, though, that all the chemistry of bulk systems can be reproduced by small clusters. Gold, in particular, is quite unreactive in bulk but it has significant catalytic activity in the form of nanoparticles [50–52]. Another alternative to represent infinite surfaces is, certainly, the use of periodic slabs [48]. These important aspects are not addressed, however, in the present paper. In fact, we shall assume that the interactions between bulk gold and water can be approached by small gold clusters. The assessment of how far we can go with this assumption is one of the goals of our study.

The representations of a section of the Au(210) surface and the $Au(210)_{16}$ cluster are displayed in Fig. 1(a) and Fig. 1(b), respectively.

Fig. 1(b) also shows the three sites selected for the study of the water–$Au(210)_{16}$ interactions: *T* (the top site), *H1* (the hollow1 site) and *H2* (the hollow2 site), which are related, respectively, to the atoms of the first, second, and third and fourth surface layers. This selection intends to span the energies associated to very different site geometries of the metallic surface.

The water–$Au(210)_{16}$ cluster interaction energy as a function of the distance and orientation, relatively to the cluster surface, is defined by:

$$U_{Water-Au(210)_{16}}(z,\theta) - U_{water} - U_{Au(210)_{16}} \quad (1)$$

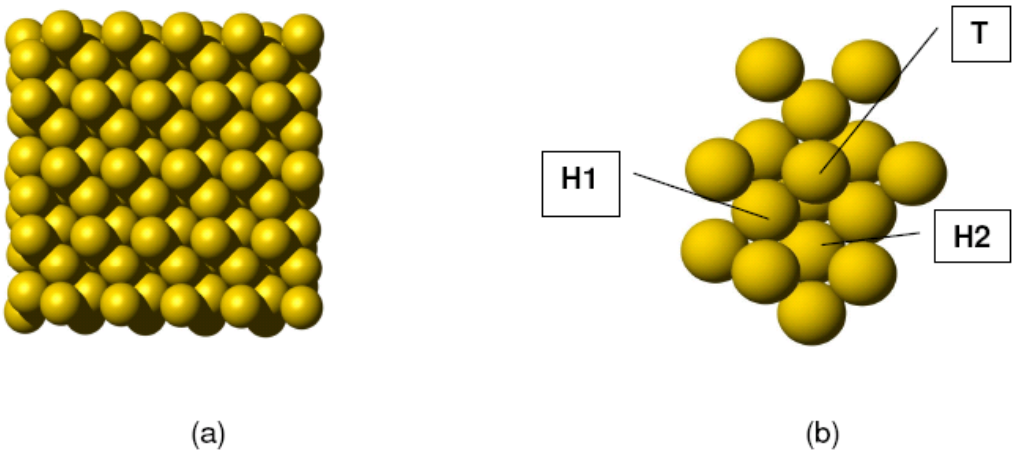

Figure 1: a) Section of an Au(210) surface. b) Metallic cluster composed by 16 atoms used in the DFT calculations.

where $U_{Water-Au(210)_{16}}$ is the energy of the system composed by the gold cluster and the water molecule; U_{water} and $U_{Au(210)}$ are, respectively, the energies of the isolated water molecule and cluster; z is the distance from the mass centre of the water molecule to the plane of the first atomic layer of the Au (210) surface; and θ is the angle between the molecular plane and the axis normal to the surface.

The orientations for the water molecule ($\theta = 0^o, 45^o, 90^o, 180^o$) were also chosen to span a wide range of situations. At each orientation and the centre of mass of the molecule over one of the selected sites, the interaction energy, given by equation (1), was evaluated for several values of z. The DFT calculations were performed by the GAUSSIAN-98 package [53].

3 Results and Fits

Fig. 2 displays the DFT interaction energies for the selected sites and orientations as a function of the distance, z. The numerical values of the energy minima and respective locations are in Table I.

The results indicate that the water molecule presents the strongest binding energy, -49.8kJ mol^{-1}, at $\theta = 0^o$ and z = 2.4 , for site T via the oxygen atom.

As for the *H1* and *H2* sites, the stronger binding energies are also at $\theta = 0^o$, respectively: -33.2 kJ mol^{-1} at z = 1.75 Å, and -25.2 kJ mol^{-1} at z = 1.55 Å. That is, the preferential orientation has the water hydrogen atoms pointing outwards the metallic surface. The same tendency is observed for the orientations $\theta = 45^o$ and

Table 1: Dependence of the characteristics of the water-$Au(210)_{16}$ interaction in the energy minima on the molecular plane orientation.

θ	T	$H1$	$H2$
	Minima of Energy (kJ mol^{-1})		
0 º	-49.8	-33.2	-25.2
45 º	-47.6	-32.8	-22.5
90 º	-37.7	-24.3	-20.7
180 º	-12.5	-15.1	-17.3
	Distance z at the Minimum of Energy (Å)		
0 º	2.40	1.75	1.55
45 º	2.45	1.77	1.60
90 º	2.56	1.97	1.90
180 º	3.27	2.65	2.38

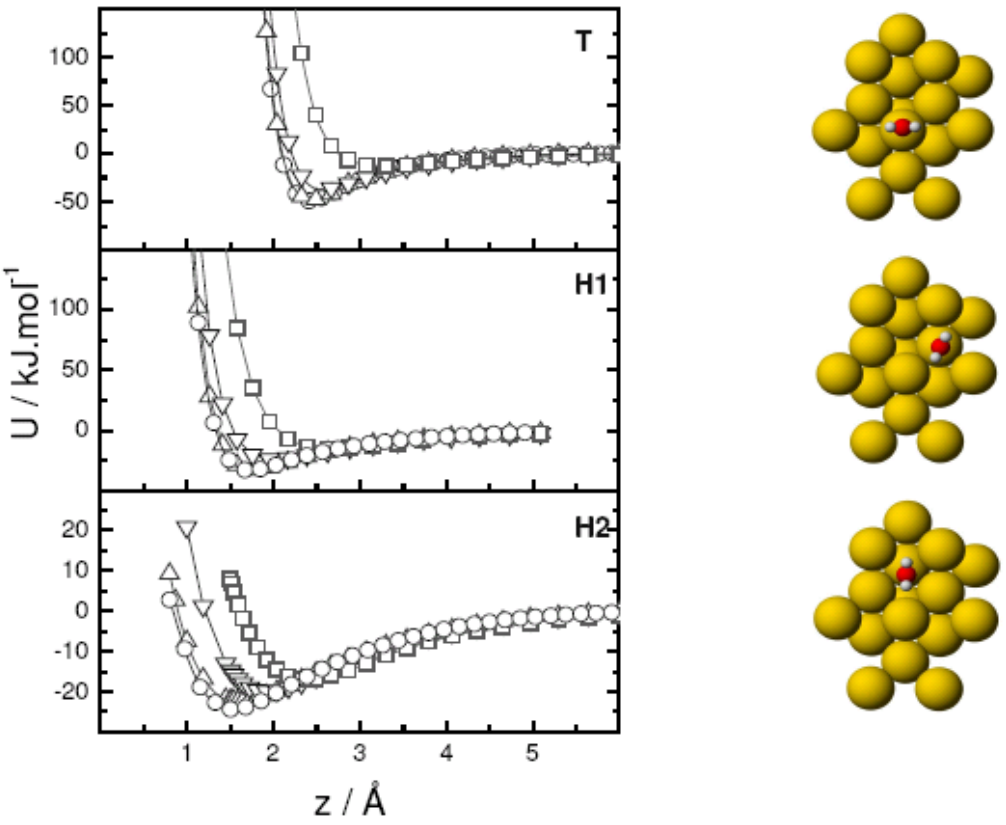

Figure 2: DFT interaction energy of the water molecule with the cluster $Au(210)_{16}$ as a function of the distance from the surface and the molecular plane orientation: 0º(◯), 45º (△), 90º (▽) and 180º(□). The lines are guides to the eye.

$\theta = 90^{o}$. The decrease of the binding energies for sites *H1* and *H2* is consistent with the fact that the distances of approach of the water molecule to these sites are less than the ones for site *T*, giving rise to a considerable repulsion.

The dependence of the interaction energy on orientation changes the previous order when the hydrogen atoms point towards the cluster surface ($\theta = 180^{o}$). In such case, the repulsion between the hydrogen atoms and the surface affects the energy more effectively than in the other orientations, and site *H2* presents the strongest binding energy: -17.3 kJ mol^{-1} at z = 2.38 Å.

The general trend of the water â $Au(210)_{16}$ interactions, concerning the preferred molecular orientation, is in agreement with the one found by Ignaczak and Gomes [32] from quantum calculations of water adsorption on copper, gold and silver (100) surfaces. In that study, the preferred orientation of the molecular plane also is, approximately, perpendicular to the cluster surface ($\theta = 0^{o}$). However, this was not observed in the molecular simulations, where in the equilibrated ensemble, the majority of the water molecules are adsorbed with the molecular plane parallel to the surface. Such simulation outcome is certainly due to the equilibrium between the water–water and water–surface interactions.

Aiming at the simulation of an ensemble of water molecules in contact with Au(210) surfaces, we have developed an analytical potential function by fitting the DFT results discussed above. The chosen strategy was similar to the one of Yeh and Berkowitz [12] for water on platinum crystal surfaces. In this approach, the function describes the interaction of each water atom with the entire surface, considering its topography, though not explicitly discriminating the interactions of the water atoms with every atom of the gold surface, and the orientation angles. These are implicitly taken into account through the following constructs.

The general form of the function is:

$$U_{H_2O-Au(210)}(x,y,Z) = U_T(Z) + U_{H1}(Z)\,A(x,y) + U_{H2}(Z)\,B(x,y); \quad (2)$$

$$Z \in \{z_O, z_{Ha}, z_{Hb}\}$$

where U_T is the interaction energy when the water molecule is over the TOP site, which is taken as the reference energy. U_{H1} and U_{H2} are the energetic contributions, relatively to the TOP, of the sites *H1* and *H2* respectively. These functions, only depend on the distances (z_O, z_{Ha}, z_{Hb}) between each one of the water atoms and

the plane of the first atomic layer of the surface:

$$U_{site}Z = U_{O-Au}\left(z_O\right) + U_{Ha-Au}\left(z_{Ha}\right) + U_{Hb-Au}\left(z_{Hb}\right) \tag{3}$$

The functions A(x,y) and B(x,y) in eq. 2 are concerned with the periodicity of the surface structure:

$$A(x,y) = f(x)\left[\sin\left(\frac{1.9+by}{2}\right)\right]^8 + [1-f(x)]\left[\cos\left(\frac{1.9+by}{2}\right)\right]^8 \tag{4}$$

$$B(x,y) = f(x)\left[\cos\left(\frac{1.25+by}{2}\right)\right]^8 + [1-f(x)]\left[\sin\left(\frac{1.25+by}{2}\right)\right]^8 \tag{5}$$

where x and y are the co-ordinates of the centre of mass of the water molecule in the respective directions (which define the surface plane perpendicular to z direction), and the constants 1.9 and 1.25 are *ad hoc* fitting parameters. The function *f(x)* and the constant b depend on the parameter of the gold cell (a = 4.0786 Å):

$$f(x) = \left(\sin\frac{\pi x}{a}\right)^2 \tag{6}$$

$$b = \frac{2\pi}{a\sqrt{5}} \tag{7}$$

When the centre of mass of a water molecule is over a site *T*, A(*x,y*) and B(*x,y*) are equal to zero. Then, interaction potential of eq. 2 is reduced to U_T. If the centre of mass is over a site *H1*, A(*x,y*) = 1 and B(*x,y*) = 0, and the interaction energy is $U_T + U_{H1}$. When it is over a site *H2*, A(*x,y*) = 0 and B(*x,y*) = 1, and the energy is $U_T + U_{H2}$. The co-ordinates x and y should be measured relatively to a site *T*. Since the surface structure is periodic, any site *T* can be used.

In the fit procedure, following the scheme of Yeh and Berkowitz, it is assumed that the functions A(*x,y*) and B(*x,y*) represent the lateral variation of the corrugation energy, based on the periodic geometry of the macroscopic surface. In this paper we do not address the consequences of this assumption. A better strategy would be, for example, to do calculations for non-symmetry sites (e.g. along the lines between the *T* and *H1* sites) at different values of z and θ. The analysis of this important issue is presently in progress and will be reported soon. Meanwhile, we have recently used another fit strategy concerned with the interactions of ethanol with Au(111) surfaces [54].

The application of eq. 2 requires the knowledge of the functions U_T, U_{H1} and

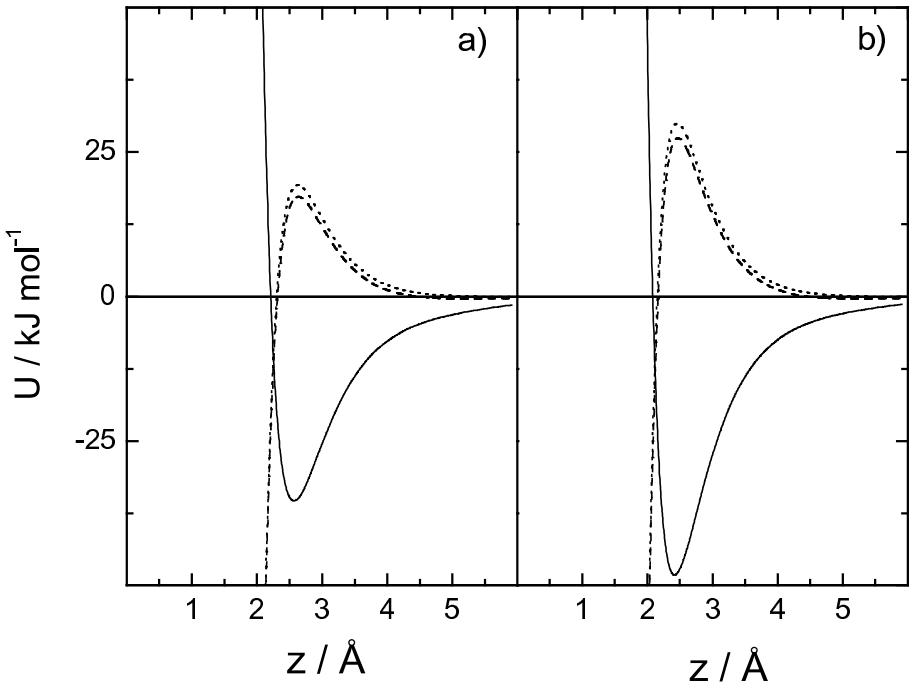

Figure 3: Dependence of the functions U_T, U_{H1} and U_{H2} on the distance from the surface: a) $\theta = 90^o$, b) $\theta = 0^o$. U_T (——), U_{H1} (— —) and U_{H2} (– – –).

U_{H2}. They are written as the sum of the interactions between each water atom and the surface:

$$U_{O-Au}(z_O) = c_0 \exp(c_1 z_O) - c_2 \exp(c_3 z_O) - c_4 \exp(c_5 z_O) \tag{8}$$

$$U_{H-Au}(z_H) = c_6 \exp(c_7 z_H) - c_8 \exp(c_9 z_H) \tag{9}$$

The fitting coefficients for eqs 8 and 9 are in Table II.

The dependence of the functions U_T, U_{H1} and U_{H2} on the distance from the surface, for the configurations $\theta = 90^o$ and $\theta = 0^o$, can be seen in Figs 3a and 3b, respectively. The functions U_{H1} and U_{H2} represent pure repulsive contributions, in contrast to the U_T profiles, reflecting the "less attractive" character of the sites *H1* and *H2*. It is worth mentioning, however, that U_{H1} and U_{H2} should not be interpreted as the water interaction energies with those sites but just as the respective deviations relatively to the *reference* interaction energy with theTOP site. Therefore, the attractive oxygen/metal interactions are maintained throughout the three surface sites, decreasing their strength on the *H1* and *H2* sites, as shown in Fig. 4.

The fit quality of the function in eq. 2 to the DFT results, can be seen in Fig. 5 for all the interaction energy curves. The maximum average deviation in the fitting,

Table 2: Values of the constants for the potential function for the different sites.

Constant	*T*	*H1*	*H2*
c_0 (kJ mol^{-1})	4.774×10^6	4,136.72	7,642.4
c_1 (Å^{-1})	-5.12	-1.67	-1.66
c_2 (kJ mol^{-1})	4,015.23	4.709×10^6	4.773×10^6
c_3 (Å^{-1})	-1.69	-5.12	-5.12
c_4 (kJ mol-$^{-1}$)	0.00	341.73	3,214.1
c_5 (Å^{-1})	0.00	-1.11	-1.50
c_6 (kJ mol^{-1})	43,994.8	5,900	3,888.21
c_7 (Å^{-1})	-3.48	-3.24	-3.09
c_8 (kJ mol^{-1})	3.33798	46,500	47,771.9
c_9 (Å^{-1})	-0.16	-3.44	-3.45

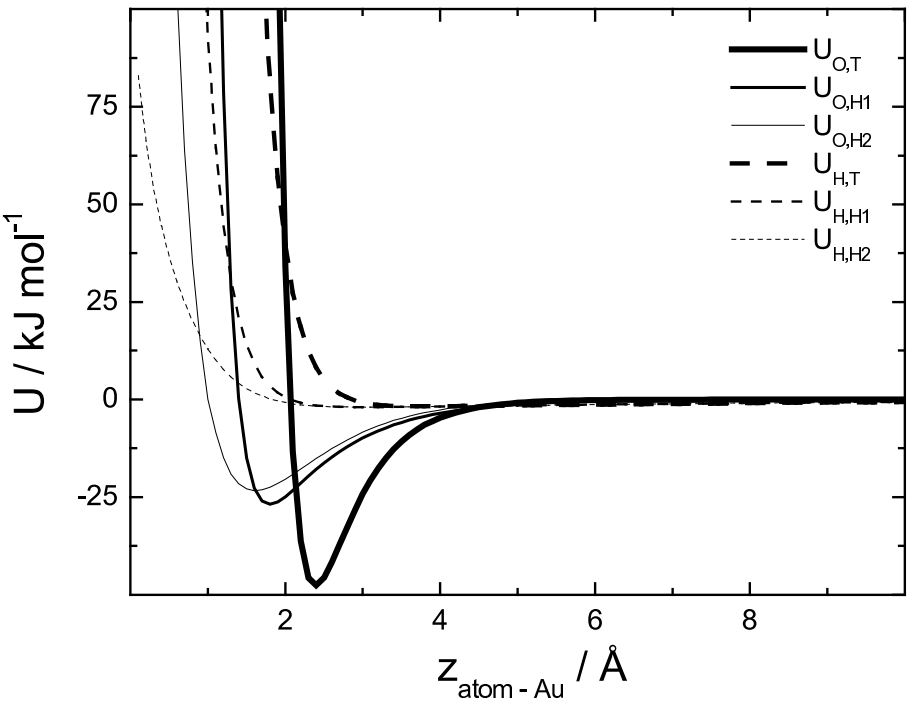

Figure 4: Interactions between the water atoms and the Au surface.

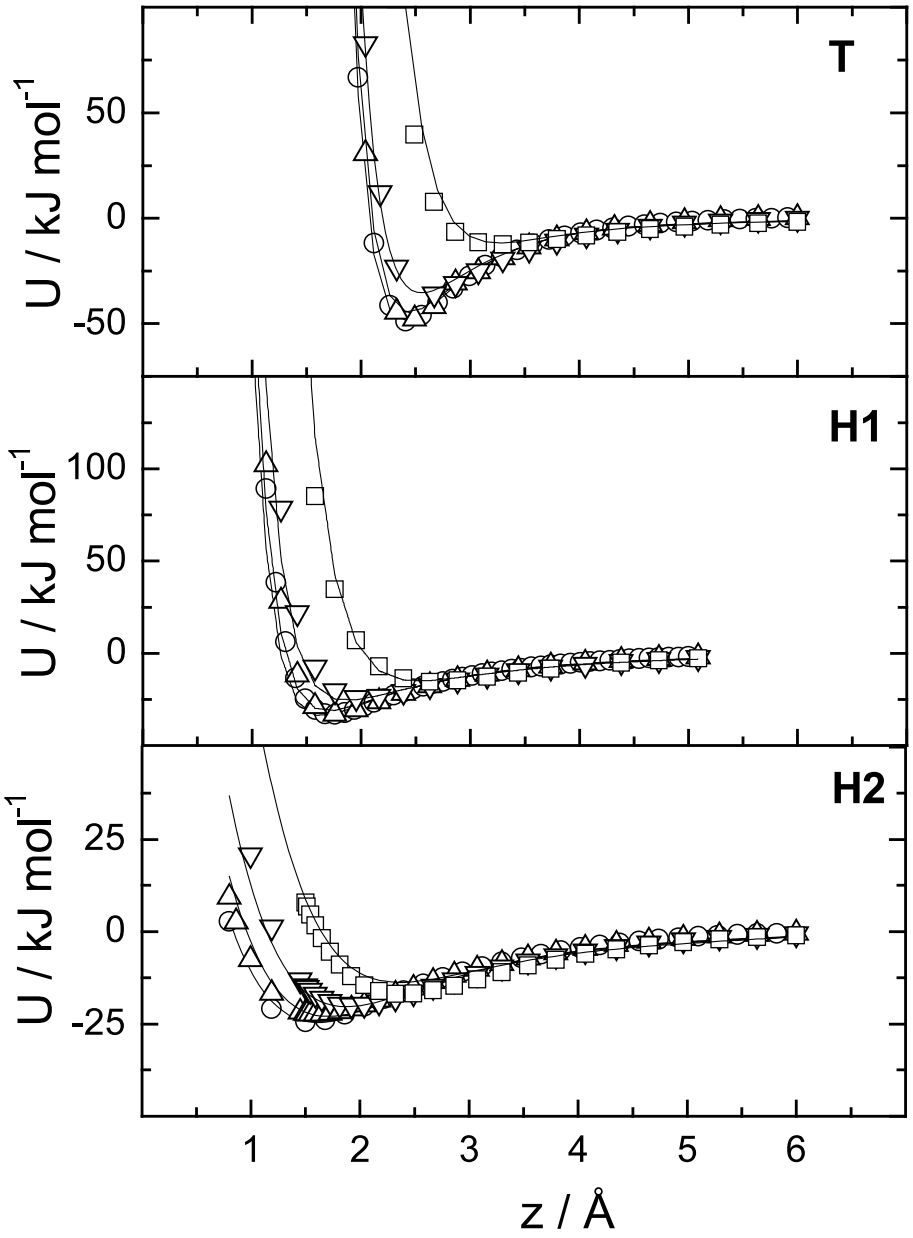

Figure 5: Fit of the developed analytical function. The symbols correspond to the DFT results and the lines to equation 2; 0º(◯), 45º (△), 90º (▽) and 180º(□).

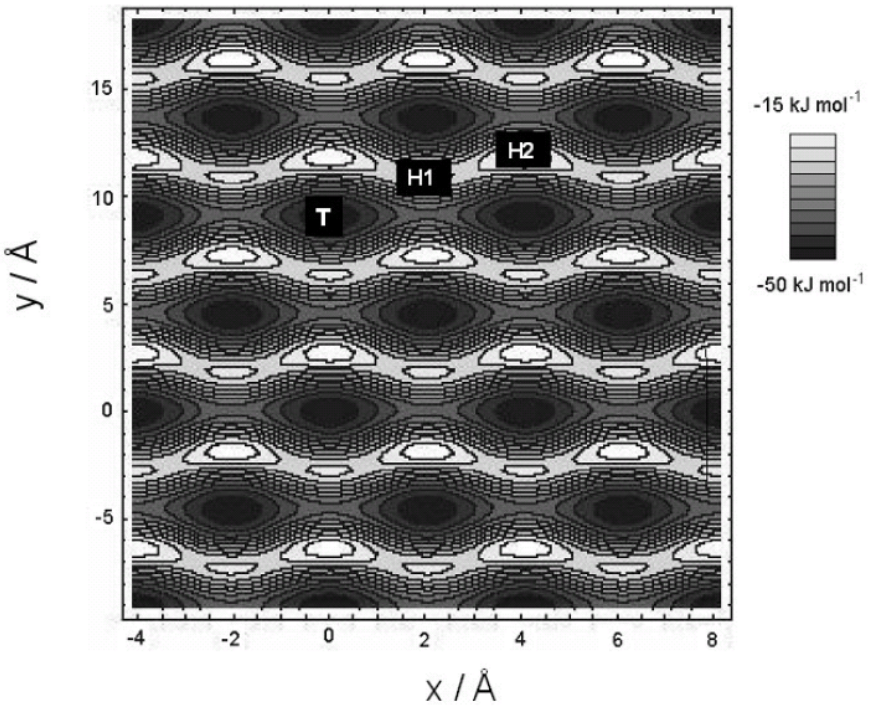

Figure 6: Map of adsorption energies of a water molecule on the surface, obtained from equation. 2 ($z = 2.4$Å and $\theta = 0^{o}$).

on the minima energy regions, is ˜2.5 kJ mol^{-1}. The only situation where the deviation is a little higher is for the site *H2* at $\theta = 180^{o}$. As this orientation is not much relevant regarding the interaction energies (see Table I), this presumably has negligible effects in the application of the analytical function to molecular simulations of the water/Au(210) interface.

A map of adsorption energies for a single water molecule on the Au(210) surface, obtained from eq. 2 at $z = 2.4$Åand $\theta = 0^{o}$, is represented in Fig. 6. The darkest colours correspond to the more negative energies.

A fundamental aspect related to the present development should be stressed. The chosen DFT model does not take into account the many body effects resulting from the influence of neighbour water molecules on the interaction of a water molecule and the surface. A common approach to deal with this problem is the parameterisation of the potential function in order to turn it into an effective potential. Yet, this is not usual in the case of interactions involving metallic surfaces and molecules. Nonetheless, many body effects are, in a certain way, implicit in the model since the main criteria used has been the reproduction of coherent adsorption energies and the work function of the metallic surface. In fact, the consistency of metallic

surface-water potential functions developed with the present approach is observed in many studies [9, 12, 55].

Another important point is that this model does not include the contribution from the polarisation effect of the point charges of the water molecules on the metal surface, the so called charge-image effect [9, 18, 27, 28, 56]. However, a study of this effect on low index crystallographic surfaces of Pt, Ni, Cu and Ag, by Siepmann and Sprik [56], showed that the induction process contributes with energies less than ˜10% of the total interaction energy. Also, the image induction by a great number of water molecules seems to result in a considerable cancellation of such effect, producing only a small global induction [57]. Based on this arguments, the charge-image effect can be neglected with minor effects in the molecular simulations of such kind of systems, as pointed out by Yeh and Berkowitz [12].

4 Concluding remarks

We have presented the development of a force field for the simulation of water molecules in contact with an Au(210) surface, based on a potential surface generated by DFT calculations.

The potential surface exhibits the main features normally associated to the interaction of water molecules with noble metal surfaces. In this respect, the preferential adsorption occurs at the top sites of the surface, followed by the second and third layer sites. In the preferential orientation the hydrogen atoms point outwards the metallic surface.

The developed analytical potential function reproduces very well the DFT results for the water-$Au(210)_{16}$ cluster interactions, regarding the preferential adsorption sites and orientations. This potential function enables the realization of molecular simulations (by Monte Carlo or molecular dynamics) for water molecules in contact with the Au(210) surface. Such simulations are of great importance to understand the behaviour of the solvent in the interfacial region.

Canonical Monte Carlo simulations of water near to Au(210) surfaces using the present force field will be reported in another paper [58].

Acknowledgements

F. Fernandes and R. Fartaria are grateful to Fundação para a Ciência e Tecnologia (FCT) within the project POCTI/QUI/36457/2000. R. Fartaria also gratefully

acknowledges the support of FCT within the Ph.D. grant SFRH/BD/10405/2002.

R. S: Neves and A. J. Motheo are grateful to CAPES within the project BEX0532/00-2, CNPq within the project 140250/00-0 and FAPESP within the project 06/04122.

References

[1] R. Parsons: The electrical double layer: recent experimental and theoretical developments, *Chem. Rev.* 90 (1990) 813 – 826.

[2] R. Parsons: The metal-liquid electrolyte interface, *Solid State Ionics* 94 (1997) 91–98.

[3] R. D. Levie, A. V. Shlepakov, B. B. Damaskin and I. A. Bagotskaya: Metal-solvent interaction and ion adsorption : Influence of solvent and metal nature, *J. Electroanal. Chem.* 138 (1982) 1–27.

[4] I. A. Bagotskaya, C. H. Hai, V. G. Boitsov and V. E. Kasarinov: Solvent effects in halide ion adsorption on different metals, *Soviet Electrochem.* 24 (1988) 248–253.

[5] R. Guidelli: *Adsorption of molecules at metal electrodes*, page 1, VHC,New York (1992) .

[6] A. Hamnett: Mechanism and electrocatalysis in the direct methanol fuel cell, *Catal. Today* 38 (1997) 445–457.

[7] C. Lamy, A. Lima, V. LeRhun, F. Delime, C. Coutanceau and J. M. Léger: Recent advances in the development of direct alcohol fuel cells (DAFC), *J. Power Sources* 105 (2002) 283–296.

[8] E. Spohr: Some recent trends in computer simulations of aqueous double layers, *Electrochim. Acta* 49 (2003) 23–27.

[9] E. Spohr: Computer simulations of electrochemical interfaces, in R. C. Alkire and D. M. Kolb (eds.), *Advances in Electrochemical Science and Engineering - vol. 6*, Wiley-VCH, New York (1999) pages 1–75.

[10] E. Spohr: Computer simulation of the structure of the electrochemical double layer, *J. Electroanal. Chem.* 450 (1998) 327–334.

[11] E. Spohr: Molecular dynamics simulations of water and ion dynamics in the electrochemical double layer, *Solid State Ionics* 150 (2002) 1–12.

[12] I. C. Yeh and M. L. Berkowitz: Structure and dynamics of water at water vertical bar Pt interface as seen by molecular dynamics computer simulation, *J. Electroanal. Chem.* 450 (1998) 313–325.

[13] E. Spohr, G. Tóth and K. Heinzinger: Structure and dynamics of water and hydrated ions near platinum and, mercury surfaces as studied by MD simulations, *Electrochim. Acta* 41 (1996) 2131–2144.

[14] K. J. Schweighofer, X. Xia and M. L. Berkowitz: Molecular dynamics study of water next to electrified Ag(111) surfaces, *Electrochim. Acta* 12 (1996) 3747–3752.

[15] J. Bocker, Z. Gurskii and K. Heinzinger: Structure and dynamics at the liquid mercury-water interface, *J. Phys. Chem.* 100 (1996) 14969–14977.

[16] X. Xia, L. Perera, U. Essmann and M. L. Berkowitz: The structure of water at platinum/water interfaces - molecular-dynamics computer-simulations, *Surf. Sci.* 335 (1995) 401–415.

[17] M. T. M. Koper, J. J. Lukkien and N. P. Lebedeva: Adsorbate interactions and phase transitions at the stepped platinum/electrolyte interface: experiment compared with Monte Carlo simulations, *Surf. Sci.* 478 (2001) L339–L344.

[18] D. I. Dimitrov and N. D. Raev: Molecular dynamics simulations of the electrical double layer at the 1M KCl solution vertical bar Hg electrode interface, *J. Electroanal. Chem.* 486 (2000) 1–8.

[19] P. S. Crozier, R. L. Rowley and D. Henderson: Molecular dynamics calculations of the electrochemical properties of electrolyte systems between charged electrodes, *J. Chem. Phys.* 113 (2000) 9202–9207.

[20] A. Ignaczak, J. A. N. F. Gomes and S. Romanowski: The potential of mean force on halide ions near the Cu(100) surface, *J. Electroanal. Chem. Interfacial Electrochem* 450 (1998) 175–188.

[21] J. N. Glosli and M. R. Philpott: Adsorption of hydrated halide-ions on charged electrodes - molecular-dynamics simulation, *J. Chem. Phys.* 98 (1993) 9995–10008.

[22] D. A. Rose and I. Benjamim: Adsorption of Na^+ and Cl^- at the charged water platinum interface, *J. Chem. Phys.* 98 (1993) 2283–2290.

[23] R. P. S. Fartaria, F. F. M. Freitas and F. M. S. S. Fernandes: A study of 1-decanethiol self-assembly on gold electrodes by computer simulation, *J. Electroanal. Chem.* 574 (2005) 321–331.

[24] U. Reimer, M. Wahab, P. Schiller and H. Mogel: Monte Carlo study of surfactant adsorption on heterogeneous solid surfaces, *Langmuir* 21 (2005) 1640–1646.

[25] R. S. Neves, A. J. Motheo, F. M. S. S. Fernandes and R. P. S. Fartaria: Monte Carlo simulation of the adsorption of phenol on gold electrodes. A simple model, *J. Braz. Chem. Soc.* 15 (2004) 224–231.

[26] M. R. Philpott, J. N. Glosli and S. Zhu: Molecular-dynamics simulation of adsorption in electric double-layers, *Surf. Sci.* 335 (1995) 422–431.

[27] M. R. Philpott and J. N. Glosli: Molecular-dynamics simulation of the adsorption of benzene on charged metal-electrodes in the presence of aqueous-electrolyte, *Chem. Phys.* 198 (1995) 53–61.

[28] J. Hautman, J. W. Halley and Y.-J. Rhee: Molecular-dynamics simulation of water between 2 ideal classical metal walls, *J. Chem. Phys.* 91 (1989) 467–472.

[29] M. Watanabe, A. M. Brodsky and W. P. Reinhardt: Dielectric-properties and phase-transitions of water between conducting plates, *J. Phys. Chem.* 95 (1991) 4593–4596.

[30] K. Raghavan, K. Foster, K. Motakabbir and M. Berkowitz: Structure and dynamics of water at the Pt(111) interface - molecular-dynamics study, *J. Chem. Phys.* 94 (1991) 2110–2117.

[31] E. Spohr and K. Heinzinger: Computer-simulations of water and aqueous-electrolyte solutions at interfaces, *Electrochim. Acta* 33 (1988) 1211–1222.

[32] A. Ignaczak and J. A. N. F. Gomes: A theoretical study of the interaction of water molecules with the Cu(100), Ag(100) and Au(100) surfaces, *J. Electroanal. Chem.* 420 (1997) 209–218.

[33] E. Spohr: Computer simulation of the water/platinum interface., *J. Phys. Chem.* 93 (1989) 6171–6180.

[34] A. Ignaczak: *The Specific Adsorption of Halide Ions on Noble Metals. A theoretical approach.*, Ph.D. thesis, University of Porto, Portugal (1997).

[35] B. S. de Bas, M. J. Ford and M. B. Cortie: Low energy structures of gold nanoclusters in the size range 3-38 atoms, *J. Mol. Struc. (THEOCHEM)* 686 (2004) 193–205.

[36] A. Vivoni, R. L. Birke, R. Foucoult and J. R. Lombardi: Ab initio frequency calculations of pyridine adsorbed on an adatom model of a SERS active site of a silver surface, *J. Phys. Chem. B* 107 (2003) 5547–5557.

[37] P. R. N. de Souza, D. A. G. Aranda, J. W. N. Carneiro, C. S. B. Oliveira, O. A. C. Antunes and F. B. Passos: Theoretical study on the adsorption of aromatic compounds on platinum clusters, *Int. J. Quantum Chem.* 92 (2003) 400–411.

[38] A. Ignaczak: DFT calculations of the interaction of alkali ions with copper and silver, *J. Electroanal. Chem.* 495 (2001) 160–168.

[39] A. D. Becke: Density-functional thermochemistry. 3. The role of exact exchange, *J. Chem. Phys.* 98 (1993) 5648–5652.

[40] A. D. Becke: A new mixing of Hartree-Fock and local density-functional theories, *J. Chem. Phys.* 98 (1993) 1372–1377.

[41] C. Lee, W. Yang and R. G. Parr: Development of the colle-salvetti correlation-energy formula into a functional of the electron-density, *Phys. Rev. B* 37 (1988) 785–789.

[42] P. J. Hay and W. R. Wadt: Ab initio effective core potentials for molecular calculations - potentials for the transition-metal atoms Sc to Hg, *J. Chem. Phys.* 82 (1985) 270–283.

[43] W. J. Hehre, R. Ditchfield and J. A. Pople: Self-consistent molecular-orbital methods. 12. Further extensions of gaussian-type basis sets for use in molecular-orbital studies of organic-molecules, *J. Chem. Phys.* 56 (1972) 2257.

[44] W. L. Jorgensen, J. Chandrasekhar and J. D. Madura: Comparison of simple potential functions for simulating liquid water, *J. Chem. Phys.* 79 (1983) 926–935.

[45] J. A. N. F. Gomes and A. Ignaczak: A theoretical approach to the adsorption of ions on metal surfaces, *J. Mol. Struc. (THEOCHEM)* 463 (1999) 113–123.

[46] E. Spohr: Computer modeling of interfaces between aqueous and metallic phases, *Acta Chem. Scandinav.* 49 (1995) 189–202.

[47] J. Böcker, R. R. Nazmutdinov, E. Spohr and K. Heinzinger: Molecular-dynamics simulation studies of the mercury-water interface, *Surf. Sci.* 335 (1995) 372–377.

[48] J. Lecoeur, J. P. Bellier and C. Koehler: Comparison of crystallographic anisotropy effects on potential of zero charge and electronic work function for gold (111), (311), (110) and (210) orientations, *Electrochim. Acta* 35 (1990) 1383–1392.

[49] M. B. Knickelbein: Reactions of transition metal clusters with small molecules, *Annu. Rev. Phys. Chem.* 50 (1999) 79–115.

[50] P. Schwerdtfeger: Gold goes nano - from small clusters to low-dimensional assemblies, *Angew. Chem. Int. Ed.* 42 (2003) 1892–1895.

[51] P. Pyykko: Theoretical chemistry of gold, *Angew. Chem. Int. Ed.* 43 (2004) 4412–4456.

[52] L. M. Molina and B. Hammer: Oxygen adsorption at anionic free and supported Au clusters, *J. Chem. Phys.* 123 (2005) 161104.

[53] M. J. Frisch, G. W. Trucks, H. B. Schlegel, G. E. Scuseria, M. A. Robb, J. R. Cheeseman, V. G. Zakrzewski, J. A. Montgomery, R. E. Stratmann, J. C. Burant, S. Dapprich, J. M. Millam, A. D. Daniels, K. N. Kudin, M. C. Strain, O. Farkas, J. Tomasi, V. Barone, M. Cossi, R. Cammi, B. Mennucci, C. Pomelli, C. Adamo, S. Clifford, J. Ochterski, G. A. Petersson, P. Y. Ayala, Q. Cui, K. Morokuma, D. K. Malick, A. D. Rabuck, K. Raghavachari, J. B. Foresman, J. Cioslowski, J. V. Ortiz, B. B. Stefanov, G. Liu, A. Liashenko, P. Piskorz, I. Komaromi, R. Gomperts, R. L. Martin, D. J. Fox, T. Keith, M. A. Al-Laham, C. Y. Peng, A. Nanayakkara, C. Gonzalez, M. Challacombe, P. M. W. Gill, B. G. Johnson, W. Chen, M. W. Wong, J. L. Andres, M. Head-Gordon, E. S. Replogle and J. A. Pople: *Gaussian 98*, Gaussian Inc., Pittsburgh PA (1998).

[54] R. P. S. Fartaria, F. M. S. S. Fernandes and F. F. M. Freitas: A force field for simulating ethanol adsorption on Au(111) surfaces. A DFT study, *Int. J. Quantum Chem.* 107 (2007) 2169–2177.

[55] C. G. Sánchez: Molecular reorientation of water adsorbed on charged Ag(111) surfaces, *Surf. Sci.* 527 (2003) 1–11.

[56] J. I. Siepmann and M. Sprik: Influence of surface-topology and electrostatic potential on water electrode systems, *J. Chem. Phys.* 102 (1995) 511–524.

[57] J. C. Shelley, G. N. Patey, D. R. Bérard and G. M. Torrie: Modeling and structure of mercury-water interfaces, *J. Chem. Phys.* 107 (1997) 2122–2141.

[58] R. S. Neves, A. J. Motheo, R. P. S. Fartaria and F. M. S. S. Fernandes: Modelling water adsorption on Au(210) surfaces. II. Monte Carlo simulations, *J. Electroanal. Chem. (under review)* .

Capítulo 7

Conclusões e perspectivas futuras

Foi apresentado um estudo sistemático, por simulação molecular, dos diagramas de fase de fulerenos, com especial ênfase no C_{60}. Os primeiros cálculos, reportados na literatura, do diagrama de fases do C_{60} revelaram-se inconsistentes levantando a dúvida sobre a existência de uma fase líquida estável para este sistema. Deste modo, numa primeira fase, utilizando os métodos de Gibbs-ensemble (GEMC) e Gibbs-Duhem (GD), foi traçado o diagrama de fases do C_{60} com os potenciais PRP e GP. Os pontos críticos do C_{60}, com estes modelos, foram estimados recorrendo à lei do escalamento do parâmetro de ordem e diâmetros rectilíneos. As temperaturas críticas determinadas foram, respectivamente, 2006±27 K e 1951±28K em concordância com os valores determinados por outros autores, utilizando métodos diferentes. A determinação do ponto triplo foi feita utilizando dois métodos. O primeiro, uma adaptação do método de Agrawal e Kofke, inspirado na integração de Gibbs-Duhem, resultou num ponto triplo à temperatura de 1858±32K para o modelo PRP e 1898±21K para o modelo PRP, concordante com os valores obtidos por outros autores que utilizaram uma combinação de métodos de simulação e cálculos de energia livre. O segundo, proposto por nós, é baseado unicamente em simulações pelo método de GEMC, em que o ponto triplo é identificado com a temperatura a que a fase líquida desaparece espontaneamente surgindo no seu lugar uma fase sólida cristalina sem imperfeições. O método foi previamente desenvolvido e testado para o Lennard-Jonesium revelando uma boa capacidade da determinação do ponto triplo numa faixa muito estreita de temperaturas. Analisaram-se e integraram-se as funções de distribuição radial que confirmaram a formação de redes cristalinas perfeitas a partir da fase líquida. A aplicação deste método ao sistema C_{60} resultou na determinação do ponto triplo a 1570±20K e 1529±36K para os modelos PRP e

GP, respectivamente. Estes valores estão de acordo com os obtidos por outros autores através de métodos teóricos (HMSA e MHNC) e cálculos de dinâmica molecular e Monte Carlo. A partir dos pontos triplos de "baixa-temperatura" calcularam-se, utilizando o método de Gibbs-Duhem, as linhas de coexistência líquido-sólido, denominadas "GD-up". Estas têm um comportamento semelhante às linhas denominadas "GD-down" para os pontos triplos de "alta-temperatura". De acordo com estes cálculos o C_{60} deveria ter uma fase líquida estável que se estenderia por ∼450K. Posteriormente, calcularam-se os diagramas de fase dos fulerenos C_{70}, C_{76} e C_{84}, utilizando o modelo GP. Estes fulerenos revelaram, essencialmente, o mesmo tipo de comportamento que o C_{60}. As relações entre os pontos críticos e triplos calculados encontram-se de acordo com as relações entre as profundidades dos potenciais para cada um destes fulerenos e são consistentes com os resultados reportados por outros autores utilizando a teoria MHNC. Determinaram-se as entalpias de sublimação destes fulerenos e os seus valores encontram-se em boa concordância com os valores experimentais. Considerando os resultados, baseados principalmente no cálculo de energias livres, que apontavam para a realidade dos pontos triplos de "alta-temperatura", foram efectuadas novas simulações. O estudo conjunto das isotérmicas supercríticas do modelo Lennard-Jonesium e GP (para o C_{60}) e das linhas de coexistência líquido-sólido "GD-up", revelou uma instabilidade relativamente à fase líquida que, com a subida da temperatura e pressão, colapsa para densidades próximas das do sólido. Ao mesmo tempo, a observação de que a pressão para o equilíbrio sólido-vapor, nas gamas de temperaturas entre ∼1850 e ∼1400K, é mais baixa do que a pressão para o equilíbrio líquido-vapor, na mesma gama de temperaturas, mostra que o potencial químico deste último equilíbrio tem que ser superior ao anterior, representando, portanto, um equilíbrio meta-estável. Isto veio reforçar a realidade dos pontos críticos de "alta-temperatura". Desta forma, foi feita uma revisão crítica dos resultados obtidos anteriormente apontando agora para a meta-estabilidade dos pontos críticos de "baixa-temperatura". Estima-se, portanto, que o C_{60} possua uma fase líquida estável, que cobre uma gama de temperaturas de ∼150K com um ponto triplo a ∼1850K e um ponto crítico a ∼2000K.

Foi estudado e desenvolvido um algoritmo baseado num "repositório de energia" de forma a acelerar as simulações de MC. O método já havia sido utilizado anteriormente por outros autores, mas nunca enunciado ou discutido com o presente detalhe, como nos foi gentilmente referido pelo Dr. Silvano Romano [Comp. Phys. Comm. 176 (2007) 250]. De facto, foi efectuada uma pesquisa bibliográfica exaustiva em que não se identificou qualquer referência a esta técnica. As capacidades do "repo-

sitório" foram testadas para vários potencias de interacção, modelos moleculares e acoplamento com outras técnicas de aceleração como as listas de vizinhos e as listas ligadas. Esta técnica revelou-se mais eficaz para potencias de interacção computacionalmente mais dispendiosos com reduções no tempo das simulações da ordem dos 30% a 45%. Estes valores são excelentes tendo em conta que o valor máximo será de 50%.

O estudo das camadas auto-montadas iniciou-se com a realização de simulações, pelo método de MC no ensemble *NVT*, de um modelo simplificado, com moléculas rígidas, para a interface etanol-Au(111) e para a adsorção de moléculas de 1-decanotiol nessa interface. Perante a inexistência na literatura de potenciais intermoleculares adequados à descrição da interacção das moléculas de etanol com a superfície, recorreu-se ao potencial de Hautman et al. (um potencial do tipo LJ 12-3) também utilizado para a interacção tiol-superfície. Utilizando a estratégia destes autores foram delineados dois potenciais: um, baseado nos parâmetros de interacção dos campos de forças OPLS, utilizados na simulação de fases condensadas, com o mínimo da curva de potencial a -6,82 kJ mol^{-1}, foi denominado de O_{weak}; o outro, baseado em cálculos *ab intio* para a interacção do ião hidróxido com a superfície Au(111), com o mínimo da curva de potencial a -173.64 kJ mol^{-1}, foi denominado de O_{strong}. Dos resultados obtidos com estes modelos concluiu-se que seria necessário um modelo mais realista para a descrição desta interacção. Uma primeira aproximação consistiu na previsão da energia de interacção etanol-Au(111), recorrendo a cálculos DFT com uma molécula de etanol e um cluster de 14 átomos de Au. Obteve-se a energia de interacção de $\sim$20 kJ mol^{-1}. Foram efectuadas simulações com o potencial 12-3 reparametrizado com base na energia de interacção calculada por DFT. Este modelo foi denominado de O_{ab}. Contudo, este modelo, apesar de mais realista, continuava a não ter em conta a influência explícita da estrutura superficial do eléctrodo. Seguiu-se, então, a construção de um campo de forças que traduzisse essa influência. Efectuou-se, para o efeito, por DFT, o cálculo das curvas de energia de interacção etanol-14Au para várias distâncias, e orientações, de aproximação da molécula ao plano (111) do cluster. Foram considerados três sítios de adsorção, denominados de *top*, *hollow1*, e *hollow2*. Estes cálculos indicam que a adsorção das moléculas de etanol se faz preferencialmente nos sítios *top*, de acordo com o sugerido em estudos efectuados para a adsorção de etanol em nano-clusters de ouro. Recorrendo a algoritmos genéticos ajustou-se uma função analítica a estas curvas construindo-se um novo campo de forças para a interacção etanol-Au(111). Neste campo de forças, a energia de interacção depende da distância de cada um dos

centros (H, O, CH_2 e CH_3) da molécula de etanol a cada um dos átomos de ouro da superfície, e de dois ângulos referentes à orientação da interacção O–Au em relação à normal à superfície e à posição superficial da molécula relativamente aos átomos de ouro, respectivamente. Deste modo, neste campo de forças a estrutura do eléctrodo influencia explicitamente o comportamento das moléculas de etanol adsorvidas, não só na distribuição "vertical" das moléculas, mas também na distribuição superficial (ou "horizontal"). Os modelos foram sucessivamente melhorados com a introdução de graus de liberdade intramoleculares e somas de Ewald. Cada um dos modelos foi sistematicamente analisado por determinação dos perfis de densidade "verticais" e "horizontais" (de superfície). A adsorção da molécula de tiol em cada um destes modelos foi também analisada através do cálculo de ângulos de inclinação, potenciais de força média e comprimento médio da molécula, ao longo do processo de aproximação ao eléctrodo.

Da análise dos perfis de densidade "vertical" das moléculas de etanol foi possível identificar as camadas de adsorção e a orientação média das moléculas em relação ao eléctrodo. Assim, na primeira camada de adsorção, entre os $\sim$2Å e os $\sim$5Å, as moléculas encontram-se adsorvidas com os átomos O e H voltados para a superfície e os grupos CH_2 e CH_3 voltados para o interior da fase líquida. Isto apenas não se verifica para o modelo O_{weak} em que as moléculas adoptam uma orientação quase paralela à superfície. Os perfis de densidade superficial permitiram estudar a influência da introdução explícita da estrutura do eléctrodo com o novo campo de forças. Nos modelos de superfície plana, não estruturada, as moléculas de etanol rígidas ou flexíveis, conforme o modelo utilizado, organizam-se principalmente em função das interacções com as moléculas vizinhas, observando-se a formação de cadeias e agregados de quatro e cinco moléculas de etanol. No modelo com a superfície estruturada embora se continue a observar a existência destas estruturas, verifica-se que elas se formam em menor quantidade. Este efeito deve-se à limitação da mobilidade superficial das moléculas de etanol que são atraídas pelos sítios *top* da superfície. Adicionalmente, o número de moléculas de etanol adsorvidas também diminui com a introdução do modelo de superfície estruturada.

A adsorção do 1-decanotiol na interface etanol-Au(111) revelou-se bastante distinta, quando se compararam os modelos iniciais, com a molécula rígida, sem graus de liberdade intramoleculares, com o modelo final, com a molécula flexível. Assim, enquanto que no modelo rígido se verifica a adsorção com um ângulo de inclinação de $\sim$26º, no modelo flexível a molécula adopta um ângulo de inclinação de 74$\pm$18º. Considera-se que este valor, calculado com o modelo mais completo, é porventura

o valor mais realista para a adsorção de uma única molécula de tiol. Os potenciais de forca média do solvente para a adsorção do 1-decanotiol revelam o mesmo tipo de comportamento em todos os modelos. No modelo mais completo, com moléculas flexíveis, eléctrodo estruturado e soma de Ewald, a aproximação da molécula ao eléctrodo faz-se contra a barreira de solvente adsorvido na interface. O solvente oferece uma resistência à adsorção do tiol, que vai aumentando à medida que este atravessa as camadas de adsorção, tendendo a estabilizar na parte final da aproximação em que o tiol já se encontra incorporado na primeira camada de adsorção do solvente. Os valores do ângulo de inclinação e do comprimento médio da molécula de tiol tendem, também, a estabilizar durante a adsorção.

Apesar do número de publicações sobre estudos da adsorção dos tiois e da formação e propriedades de monocamadas auto-montadas ser já muito vasto e continuar a aumentar, consideramos que o estudo teórico deste fenómeno se encontra apenas no seu início. É necessário continuar o desenvolvimento dos campos de força para descrição das interacções envolvidas nestes sistemas, de modo a que as simulações se tornem progressivamente mais próximas dos sistemas reais, possibilitando um estudo mais refinado dos seus comportamentos. O desenvolvimento de um modelo da interacção tiol-Au(111) que tenha em conta a estrutura explícita da superfície é, neste âmbito, fulcral, não menosprezando as interacções entre os grupos funcionais que se pretendam introduzir nas cadeias orgânicas. É importante, também, introduzir várias moléculas de tiol no sistema de modo a esclarecer cabalmente o comportamento do ângulo médio de inclinação. Complementarmente, é nossa intenção estudar a reactividade da molécula de tiol com o ouro analisando os mecanismos de adsorção química deste sistema, ainda por clarificar.